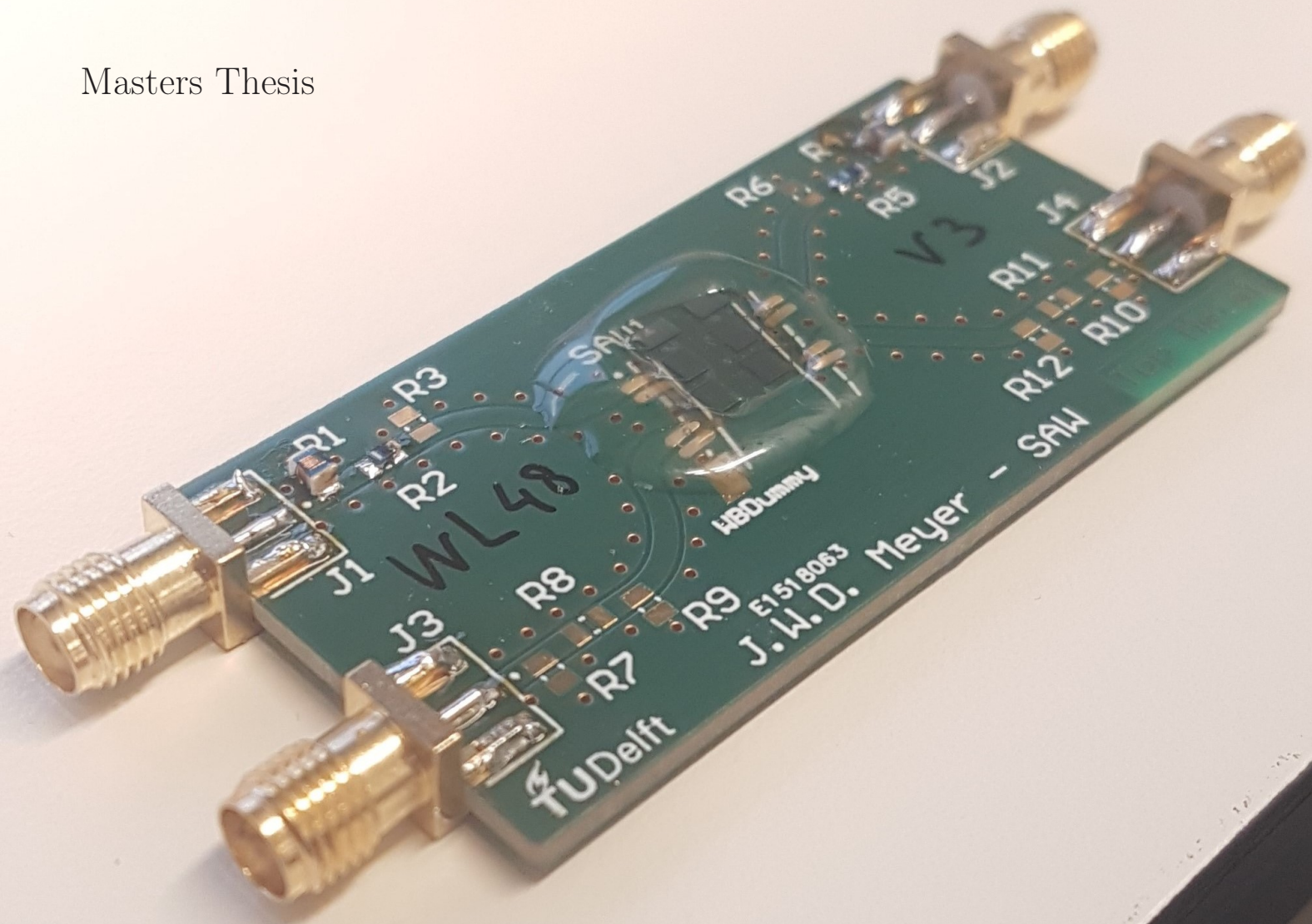


# A Love-mode Surface Acoustic Wave Based Sensor

For Gravimetric Detection of Extracellular Vesicles in Liquid Samples

J.W.D. Meyer

Masters Thesis



# A Love-mode Surface Acoustic Wave Based Sensor

For Gravimetric Detection of Extracellular  
Vesicles in Liquid Samples

To obtain the degree of Master of Science  
at the Delft University of Technology,  
to be defended on December 12<sup>th</sup>, 2023 at 11:00  
by

**J.W.D. Meyer**

Student number	4587103	
Project duration	March 2021 - December 2023	
Thesis committee	Prof. dr. P.J. French	TU Delft
	dr. T. Manzaneque	TU Delft
	dr. ir. E. Korkmaz	The Hague University of Applied Sciences
	dr. A.S. Sisman	TU Delft, daily supervisor

# Abstract

Prostate cancer is the most prevalent form of cancer among men, increasing in annual prevalence. Often, the disease progression is less intrusive than treatment. Sensitive and low-intrusive diagnosis methods exist but these are not specific. Causing the need for biopsy, an intrusive and high risk for complication procedure.

This thesis sets out to design, fabricate and test a low cost, maximum sensitivity for surface mass loading Love-mode surface acoustic wave (SAW) based sensor. The thesis goal and requirements build up to answer the research question: Can the biomarker CD9 in a liquid sample be detected by means of a Love-mode surface acoustic wave device?

SAW based sensors utilise the modulation of acoustic vibrations to detect an analyte. In this thesis, the change is caused by the immobilisation of a biomarker on a delay line between an input and output transducer. The method, more often referred to as gravimetric sensing, is based on the shift of the passband frequency by a change in surface mass density due to selective immobilisation of the biomarker. The change in passband frequency is detected by the change in phase at the fixed frequency. In this work, the fixed frequency within the passband is around 620MHz.

The Love-mode SAW is transceived by  $8\mu\text{m}$  wavelength spaced interdigitated transducers on piezoelectric crystalline ST-cut quartz utilising Y propagating waves. The wave mode becomes Love-mode by capturing the wave energy using a slower shear horizontal wave speed 900nm polyimide waveguide layer.

The biomarker is the transmembrane protein CD9, present on extra cellular vesicles. These CD9 positive extracellular vesicles are well accessible as they are present in body fluids including urine. In this work, in vitro cell culture derived CD9 positive extracellular vesicles are used.

After an extensive study to the design of a Love-mode SAW based sensor and micro fabrication, using the high frequency probe station device characterisation method, it can be concluded Love-mode SAWs were excited. The devices show sensitivity for different liquids and are proven to be able to immobilise CD9 utilising covalent immobilised streptavidin and biotinylated monoclonal anti-CD9. The devices show a response to CD9 containing samples but are not proven to be sufficiently sensitive for CD9 in liquid sample detection.

It is recommended the sensor achieved sensitivity is first more systematically determined. Then a more robust measurement setup must be designed, less prone to cross sensitivity to environmental changes and experimental variations. Then a next generation sensor for better sensitivity to surface mass loading in liquid samples can be designed.

# List of Figures

1.1	Currently most often applied diagnosis procedure for PCa and prospected role in diagnosis for new test . . . . .	2
1.2	Thesis contents, showing the distribution between biological topics for design relevance and engineering topics and how they fit in the structure. . . . .	3
2.1	A) Incidence (new diagnoses per year) for a large selection of common cancer types in the Netherlands for both sexes. PCa is very prevalent among men considering most other cancer types occur in both sexes. Data from IKNL. B) Incidence of PCa in the Netherlands per age group divided of five year intervals. PCa incidence increases hugely with age. Data from IKNL. . . . .	4
2.2	Schematic representation of the lower pelvic region with the prostate pointed out. . . . .	5
2.3	Schematic cross section of a tubuloalveolar prostatic gland showing the three major present cell types. . . . .	5
2.4	Sandwich Enzyme-linked Immunosorbent Assay (ELISA) diagram with steps. 1 coat plate with antibody, 2 allow target antigen (if present) to bind, 3 add enzyme labelled antibody to bind to target antigen, 4 add substrate causing change of colour detectable by plate reader giving quantitative or qualitative result dependent on kit setup. . . . .	7
2.5	Schematic representation of a trans-perineum biopsy with echo device anally inserted for locating the biopsy needle. The method reduces infection risk, is less painful and more accurate. . . . .	7
2.6	The Gleason score is made up of two parts. All samples from a prostate biopsy get a grade. The most prevalent grade is the first part and the second most prevalent grade is the second part. . . . .	8
2.7	Comparison of incidence and mortality of PCa in the Netherlands. The large increase in incidence and relatively stable mortality is an indication of overdiagnosis. Data from IKNL. . . . .	8
3.1	Different forms of PSA, some derivatives more detectable then others and some more present in PCa then in BHP. The year of detection is included. Also the definition of the phi is included. . . . .	9
3.2	CD9 fixed to EV. . . . .	10
4.1	Linear source plane excitation for surface and bulk wave propagation modelling. . . . .	11
4.2	Relation of SH, SV L and $\phi$ wave velocity and the effect when they couple . . . . .	12
4.3	Love mode SAW based sensor schematic representation. . . . .	12
4.4	Bi-directional IDT schematic representation with labels for the dimensions. . . . .	15
4.5	Metalization ratio ideally at 0.5 to avoid higher harmonics to be excited. . . . .	15
4.6	Bi-directional IDT, SPUDT and reflector layout. . . . .	16
4.7	The maximum L for a certain W before the SAW wavefront enters the Fraunhofer region where the wavefront becomes circular. . . . .	17
4.8	Influence of w <sub>gth</sub> and L on IL. . . . .	18
4.9	Measured change of signal transfer amplitude on a quartz device with a Novolac overlayer as performed by Gizeli et. al. . . . .	19
4.10	Bender et al., 2000, measured IL while changing PMMA WG thickness. . . . .	19
4.11	Optimum WG thickness for PI and PS by Branch et al. . . . .	19
4.12	Several BAW causing spurious response in a SAW device. . . . .	20
4.13	Equivalent circuit for a SAW sensor. . . . .	21
4.14	Schematic setup for an oscillator readout scheme. . . . .	21
4.15	Typical transfer characteristic of a SAW device. . . . .	22
4.16	Mixer based phase detector. . . . .	22
4.17	Variables and parameter relation and resulting design order. . . . .	23

5.1	Showing the differences in mesh size and the effect on the displacement and electric field distribution after solving. Clearly, the very coarse mesh on the left causes a deterioration of information, but the middle (applied mesh in all other simulations) and extremely fine mesh on the right do not show clear differences in the results. . . . .	25
5.2	Effect of mesh size on found eigenfrequency with and without electrodes. The simulation with electrodes always stays quite accurate. When the electrodes are removed, large deviations from the most accurate simulations are observed. For both cases, the simulation time increases exponentially with increased resolution as can be seen on the logarithmic scale. As the impulse response simulations must sustain the wave over the delay line without electrodes, the latter without electrodes is the better simulation to adhere to. So the minimum mesh size element is chosen to obtain 9 points per period and the maximum size 5 points per period. . . . .	25
5.3	Example of the application of Euler angles Z-X-Z sequence by rotating over $\alpha, \beta, \gamma$ respectively. .	26
5.4	Practical example of the conversion between the historically used RH-IEEE 1978 ST-cut quartz definition and the corresponding Euler angles. The drawn crystals are aligned with the axis so a clear indication can be found of how the ST-cut wafer is oriented in a quartz crystal. . . . .	26
5.5	Visually checking if displacement matches Love mode SAW . . . . .	27
5.6	Resulting voltages on the sensor side after a 1 sample impulse on a slice. Clearly, the direct voltage feedthrough, the substrate bulk waves and waveguide waves can be distinguished. The zones were also investigated with separate FFTs to investigate their contribution to the total frequency response. . . . .	28
5.7	FFT of the time impulse signal. The direct coupled impulse is removed before FFT. Also, the first and last 20 samples are attenuated with a Hanning window. . . . .	28
5.8	Comparing the found eigenfrequencies . . . . .	29
5.9	DFT magnitude plot of same geometry with differing crystal orientation definitions. . . . .	29
5.10	Dimensions for the capacitance conformal mapping based MATLAB calculation and COMSOL model calculation. . . . .	30
5.11	Decomposition of the geometry used to estimate the capacitance of a coplanar capacitor in multiple dielectric layers. . . . .	30
6.1	Design order sections . . . . .	31
6.2	Surface displacement in ST-quartz . . . . .	32
6.3	Selection of materials with potential use as waveguide material showing a clear trade-off between acoustic velocity (low as possible) and mechanical loss (also as low as possible). The figure is created with Granta Edupack materials database. . . . .	35
6.4	Slice time impulse model results for 6 PI thicknesses. . . . .	37
6.5	Slice time impulse model results PI. . . . .	37
6.6	Eigen frequency and maximum WG displacement for the unit wavelength model using ST-quartz substrate, PMMA WG, pure-Al metal and a 8um wavelength for several electrode thicknesses. Increasing electrode thickness increases eigenfrequency at the cost of displacement. . .	39
6.7	Effect of device capacitance, set by W and N, on reflection coefficient using electrical equivalent model. . . . .	40
6.8	Smith chart based on electrical equivalent model sweeping N and W . . . . .	41
6.9	Series and shunt single element matching circuit schematic. . . . .	41
6.10	Influence L on IL for several $\Gamma$ . . . . .	43
6.11	Constant IL contour lines for different W and L for N=75 . . . . .	43
6.12	Using diffraction equation 4.12, a maximum delayline length is found for any aperture. The diffraction is clearly no limiting factor in the directionally constant (or isotropic along the wave plane of propagation) ST-cut quartz. Also constant area lines are shown corresponding to the area required for a droplet with a volume as shown in the legend. It shows that for even very small volumes, quite a large area is required. . . . .	43
6.13	Summary of previous plots combined to show trade-off between area and IL together with the maximum L before diffraction and the reflection coefficient with the SAW devices that are planned to be fabricated pointed out. . . . .	44

6.14	On wafer example of effect removing PI from dicing line. Both attenuation (SSBW instead of Love wave) and shift of wave propagation so part of energy misses next IDT. However, part of energy is reflected by next IDT and has a return path to original IDT, finally arriving at receiving IDT. . . . .	46
6.15	The model by Simons used to check the dimensions of the copper trace on the PCB as calculated by Altium. . . . .	47
6.16	Render of designed PCB in Altium . . . . .	47
6.17	Wells lasercut from acrylic plate from left to right: wells melted stuck in 8mm thickness acrylic, 500nm wall thickness 4mm high well, 1mm wall thickness 4mm high well, well on SAW device after functionalisation process showing red discolouring and particles. . . . .	48
7.1	Complete fabrication flowchart schematic. . . . .	49
7.2	Functionalisation protocol. . . . .	51
8.1	Setup used for the probe station wafer level device characterisation. . . . .	52
8.2	Setup used for the mass loading experiments. . . . .	53
8.3	Matching artificially using MATLAB. . . . .	54
8.4	Example of data selection and processing to extract less noisy phase at some selected frequency. . . . .	54
9.1	Finalised PCB. . . . .	55
9.2	Metal showing many holes after Al wet etch. Picture taken after PI develop. . . . .	56
9.3	Example of very well defined metal without defects after PI cure step. . . . .	56
9.4	Microscope photo of a 1um CD structure. . . . .	56
9.5	HRP staining of PCB 1 and PCB 2 where goat-anti-mouse antibodies conjugated with horse radish peroxidase (GaM-HRP) are added to PCB 1. Both PCBs are functionalised and used for EV capture in timed measurements. After adding horse radish in buffer solution to both samples, only PCB 1 shows a clear brown colour. This indicates the colour is due to GaM-HRP, binding to mouse derived anti-CD9. It is then proved the anti-CD9 is successfully immobilised on PCB1. Here PCB 2 serves as a negative control. It is assumed the capture of CD9 by anti-CD9 is a highly reliable process. . . . .	57
9.6	Full wafer probe station measurement of devices with different aperture, S21 magnitude. . . . .	57
9.7	Full wafer probe station measurement of devices with different aperture, S21 magnitude zoomed in around resonance band. . . . .	58
9.8	Full wafer probe station measurement of device W1.3, S21 phase. . . . .	58
9.9	Full wafer probe station measurement of devices with different aperture, S11 Smith chart for the frequency band around the resonance band. . . . .	59
9.10	Full wafer probe station measurement of decreasing wavelength devices showing decreasing the wavelength increases the resonant band to higher frequencies. . . . .	59
9.11	Full wafer probe station measurement of several device versions placed 90°rotated on the wafer so the quartz crystal orientation should now support Rayleigh-mode. Included to check if other measurements are indeed likely to be Love-mode and as backup if an error is made in wafer orientation. . . . .	60
9.12	Passband centre frequencies calculated without waveguide, modeled in COMSOL with and without 900nm PI WG and measured in the probestation with 900nm PI WG. For big wavelengths and low frequency, measurement and simulation are in good agreement. At thinner WG thickness, deviation starts. . . . .	60
9.13	Full wafer probe station measurement of all devices. . . . .	61
9.14	Full wafer probe station measurement of all devices, artificially matched. . . . .	62
9.15	Full wafer probe station measurement of all WL devices. . . . .	62
9.16	On wafer S21 IL probe station measurement and PCB placed measurement of the W1.3 version. . . . .	63
9.17	By loading several PBS volumes with in between wash steps on the delay line the influence of sample volume on the phase is determined. The measurements are taken at t=30s after deposition of the test volume PBS sample. . . . .	63
9.18	Subsequently, the device is measured dry (Dry 1), with DI water (DI water 1), then 50/50 PBS and DI water, then only PBS, then again DI water after a DI wash (DI water 2) and finally the dried device (Dry 2). . . . .	64

9.19	The consistency between measurements is tested by loading the delay line with 15uL of PBS for 4 times with wash steps in between. Every measurement is taken at t=30s after the next PBS 15uL volume is pipetted on the delay line. . . . .	64
9.20	S11 Smith chart for the W1.3 str device on a PCB in dry and DI loaded conditions. . . . .	65
9.21	S21 insertion loss for the W1.3 str device on a PCB in dry and DI loaded conditions showing decreased received signal when the SAW device is loaded with a fluid and matching improves the received signal. . . . .	65
9.22	S21 phase for the W1.3 str device on a PCB in dry and DI loaded conditions. . . . .	66
9.23	Microscope image of PCB 9 after 16 hours passe since the HMDA step (during the day long dry period) showing some crystallised material (expected to be HMDA) on the IDT. . . . .	66
9.24	S21 magnitude data for three time points showing very little visible change. . . . .	67
9.25	S21 phase data for three time points showing very little visible change. . . . .	68
9.26	S11 of three time points plotted in a Smithchart to indicate the seen impedance by the transmitter is constant through the measurement. . . . .	68
9.27	S21 phase with error bars showing the consecutive loading of the delay line with PBS and two concentrations of EVs containing sample applied in 15uL and again a sample of 70uL. . . . .	69
9.28	S21 phase, normalised with the initial measurement to zero degrees to observe the relative phase shift during the time the EVs can bind to the sensor surface with error bars. Indicating the consecutive loading of the delay line with PBS and two concentrations of EVs containing sample applied in 15uL and finally a sample of 70uL. . . . .	69
9.29	S21 phase vs frequency slope with error bars showing the consecutive loading of the delay line with PBS and two concentrations of EVs containing sample applied in 15uL and finally a sample of 70uL. . . . .	69
9.30	S21 phase vs frequency slope, normalised with the initial measurement to zero degrees/Hz to observe the relative change of slope during the time the EVs can bind to the sensor surface. Indicating the loading of the delay line with PBS and two consecutive concentrations of EVs containing sample applied in 15uL and finally a sample of 70uL. . . . .	70
9.31	S21 phase, normalised with the initial measurement to zero degrees to observe the relative phase shift during the time the EVs can bind to the sensor surface with error bars. Indicating the consecutive loading of the delay line with PBS before functionalisation in 'PBS Noise test' and loading with PBS and 4 concentrations of EVs containing sample applied in 15uL volumes. . . . .	70
9.32	S21 phase vs frequency slope, normalised with the initial measurement to zero degrees/Hz to observe the relative change of slope during the time the EVs can bind to the sensor surface. Indicating the loading of the delay line with PBS before functionalisation in 'PBS Noise test' and loading with PBS and 4 consecutive concentrations of EVs containing sample applied in 15uL volumes. . . . .	70
11.1	Example of method to integrate microfluidics automatism and standardisation on SAW device. . . . .	75
A.1	Streptavidin-biotin binding used to detect the binding of antibodies to antigen in analyte. . . . .	89
A.2	Biotin bicyclic structure with spacer arm which can be made hydrophobic or hydrophilic and a reactive group to biotinylate a molecule of interest to later be detected using streptavidin. . . . .	89
B.1	Obtaining monoclonal antibodies. . . . .	90
C.1	The origin of Extracellular Vesicles (EV) involving the transmembrane glycoprotein availability on the cell membrane, the forming of an endosome, the formation of an endosome with vesicles (a multi-vesicular body) and the excretion of these vesicles (containing the glycoprotein) so the EV can move through the body. . . . .	92
C.2	Low CD9 expression (indicated with the 27kD arrow) in advanced prostate cancer (PCa) while levels are normal for Benign Hyperplasia (BHP) and localised PCa in western blot analysis. . . . .	93
C.3	Comparing sensitivity and specificity for CD9, CD63, Urinary PSA and serum PSA. . . . .	93
C.4	Antibody shape and functioning. . . . .	93
D.1	Decomposition of the geometry used to estimate the capacitance of a coplanar capacitor in multiple dielectric layers. . . . .	95

D.2	Dimensions for the capacitance conformal mapping based MATLAB calculation and COMSOL model calculation. . . . .	96
E.1	Equivalent circuit for a SAW sensor. . . . .	99
E.2	Field lines between IDT fingers and the crossed field and in-line model assumptions. . . . .	99
F.1	All parameters and materials that can be chosen independently have no arrow into them. From bottom up, the influence of each material of parameter on eventually the sensitivity is represented. Notice this is a simplified diagram where several blocks can be further subdivided. All red blocks are dependent on material choices. All blue blocks are determined by IDT design. Finally, all green blocks are defined by both material and IDT design. As the material choices influence many variables, they have been represented with circles to avoid an unreadable amount of interconnections. . . . .	100
F.2	All parameters and materials that can be chosen independently have no arrow into them. From bottom up, the influence of each material of parameter on eventually the sensitivity is represented. Notice this is a sub-block for the IL or magnitude of the transfer H. It is still a simplified diagram where several blocks can be further subdivided. All red blocks are dependent on material choices. All blue blocks are determined by IDT design. Finally, all green blocks are defined by both material and IDT design. As the material choices influence many variables, they have been represented with circles to avoid an unreadable amount of interconnections. . . . .	101
H.1	Soft bake spin curves from datasheet by manufacturer, Fujifilm. . . . .	104
H.2	Flowchart for PI spinning thickness tests with indicated process steps. . . . .	105
H.3	Measured points on spin curve. A) Measurements with a 75 second spin time and the calculated corresponding spin curve. B) Measurements at 6000rpm for several spin times to determine time related thickness dependency. . . . .	106
H.4	A) Spread in measured points per wafer. B) Dependency of thickness on distance to centre showing a slight dependency for most wafers. . . . .	106
H.5	Locations of Dektak measurements. . . . .	106



# List of Tables

- 2.1 Specificity comparison of Prostate Specific Antigen (PSA) derivatives for equal sensitivity. . . . . 6
- 4.1 Signal degeneration causes to be kept in consideration in design. . . . . 20
- 4.2 State of the Art design variables comparison. . . . . 23
- 5.1 Geometry eigenmode model . . . . . 27
- 5.2 Compare the derived capacitance from the CAD equations and from COMSOL. The dimensions are explained in Figure 5.10. For parallel plate, square area chosen to reduce fringing inaccuracy. Dimensions chosen close to single finger area to stay in the same order of magnitude. In COMSOL, 1 plate connected to ground, the other to 1V. Then using  $Q=C*V$ , follows  $C=Q/1$ , the charge on 1 plate is taken. The parallel plate contribution of the CPW capacitance is added at a 50nm electrode thickness to show its value is neglectible compared to the total capacitance. This indicates most energy will be in the field lines travelling through the elliptic field lines, half of which perturbate the Quartz, exciting the piezoelectric effect. . . . . 30
- 6.1 Substrate material options and summary of most relevant material properties. . . . . 32
- 6.2 The most relevant materials and their parameters for the SAW device waveguide design. . . . . 33
- 6.3 Relevant material parameters for the IDT material. . . . . 36
- 6.4 Solutions for single element matching . . . . . 42
- 6.5 Summary of mask design considerations. . . . . 46
- 9.1 Fabricated wavelengths and measured resonance band centre frequencies and calculated wave speed . . . . . 59
- 11.1 Materials to be considered to make, low-ohmic, re-configurable connections between a small PCB with wire bonded SAW sample and another PCB with matching and connectors for interfacing with the measurement equipment. . . . . 74
- 11.2 Thesis dependencies . . . . . 75
- D.1 Compare the derived capacitance from the CAD equations and from COMSOL. The dimensions are explained in Figure D.2. For parallel plate, square area chosen to reduce fringing inaccuracy. Dimensions chosen close to single finger area to stay in the same order of magnitude. In COMSOL, 1 plate connected to ground, the other to 1V. Then using  $Q = C V$ , follows  $C = Q/1$ , the charge on 1 plate is taken. The parallel plate contribution of the CPW capacitance is added at a 50nm electrode thickness to show its value is negligible compared to the total capacitance. This indicates most energy will be in the field lines travelling through the elliptic field lines, half of which perturbate the Quartz, exciting the piezoelectric effect. . . . . 97
- H.1 Summary of found processing parameters with results from previous works and own conducted process. . . . . 108

# Acronyms

**BHP** Benign Hyperplasia. v, 92, 93

**DRE** Digital Rectal Examination. 1, 5, 6

**EKL** Else Kooi Lab, the cleanroom facility available at TU Delft. 2, 38

**ELISA** Enzyme-linked Immunosorbent Assay. ii, 2, 6, 7

**EV** Extracellular Vesicles. v, 92, 93

**IDT** Interdigital Transducer. 16, 38, 39

**PCa** prostate cancer. v, 1, 5, 6, 8, 9, 92, 93

**PCA3** Prostate Cancer gene 3. 6

**phi** Prostate Health Index. 6

**PI** polyimide. 35

**PSA** Prostate Specific Antigen. vii, 1, 4–6, 8, 9

**SAW** Surface Acoustic Wave. 27

**ST-cut quartz** Stable Temperature cut quartz. 32, 73

**TMP-biopsy** Template Prostate Mapping biopsy. 6

**TRUS-biopsy** Trans Rectal Ultrasound Guided biopsy. 6

**WG** Wave Guide. 18, 24

# Contents

Abstract	i
List of Figures	ii
List of Tables	vii
1 Introduction	1
1.1 Current diagnosis strategy	1
1.2 Current diagnosis shortcomings	1
1.3 Proposed analyte	1
1.4 Current analyte detection strategies	2
1.5 Proposed analyte detection method	2
1.6 Thesis aim, requirements and research question	2
1.7 Contents	3
2 Prostate Cancer Prevalence, Anatomy and Diagnosis	4
2.1 Prostate cancer prevalence	4
2.2 Prostate Cancer Anatomy	4
2.3 Currently Practised Diagnosis Methods	5
2.4 Discrepancies in PSA and Biopsy Diagnosis Method	8
3 Biomarkers for PCa and capturing them	9
3.1 Common practise biomarkers: PSA and derivatives	9
3.2 Other FDA approved biomarkers	9
3.3 The biomarker used in this work, CD9	9
3.4 Biomarker immobilisation	10
3.5 Concluding on biomarkers and immobilisation	10
4 Surface acoustic wave devices	11
4.1 SAW introduction	11
4.2 Acoustic wave excitation and propagation	11
4.3 Love mode	12
4.4 Sensitivity as Performance Measure	12
4.5 Variables Determining Performance	13
4.5.1 Material properties based variables	13
4.5.2 Transducer considerations	15
4.5.3 Wave guiding layer considerations	18
4.5.4 Spurious response	20
4.6 SAW Electrical model	21
4.7 Readout	21
4.8 Parameter dependence and design order	23
4.9 State of the Art	23
5 Design methods	24
5.1 FEM modeling in COMSOL	24
5.1.1 Meshing	24
5.1.2 Crystal orientation	25
5.1.3 Unit wavelength eigenmode model	27
5.1.4 Time impulse simulation	27
5.2 Capacitance estimation	29
5.2.1 Static capacitance COMSOL model	29
5.2.2 Static capacitance calculation	30

6	Design	31
6.1	Requirements	31
6.2	Substrate Materials	31
6.2.1	Substrate material conclusion	33
6.3	Waveguide materials	33
6.3.1	Metals	33
6.3.2	Ceramics	33
6.3.3	Polymers	34
6.3.4	Waveguide material conclusion	35
6.3.5	Interconnect and IDT metal materials	35
6.4	Materials selection conclusion	36
6.5	Waveguide thickness	36
6.6	IDT geometry	38
6.6.1	IDT Layout	38
6.6.2	IDT width	38
6.6.3	Metallisation ratio	38
6.6.4	IDT thickness	38
6.6.5	Transducer and delay line considerations	40
6.6.6	Final device versions	43
6.7	Mask design considerations	45
6.7.1	Wafer orientation and Euler angles	45
6.7.2	Free dicing lines	45
6.7.3	Dice under angle	45
6.7.4	Bond wire reach	45
6.7.5	The final wafer and die layout	45
6.8	Peripherals	46
6.8.1	PCB considerations	46
6.8.2	Fluid well	48
6.9	Design conclusion	48
7	Fabrication	49
7.1	Process flowchart	49
7.2	Functionalisation Protocol	51
8	Experimental Methods	52
8.1	Measurement protocols	52
8.1.1	Probe station wafer level device characterisation protocol and setup	52
8.1.2	PCB mass loading protocol and setup	53
8.2	Data processing	53
8.2.1	MATLAB artificial matching	54
8.2.2	Full wafer device characterisation measurements IL data	54
8.2.3	PCB measurements phase shift	54
9	Results and Discussion	55
9.1	Fabrication	55
9.1.1	Floating in sputter coater	55
9.1.2	Feature size	56
9.1.3	Flat alignment	56
9.1.4	Dice blade	56
9.1.5	Dice markers	56
9.2	Functionalisation	57
9.3	Full wafer device characterisation measurements interpretation	57
9.3.1	Typical full wafer device characterisation measurement result	57
9.3.2	Wavelength and measured frequency	59
9.3.3	Spurious pass bands	59
9.3.4	Full wafer device characterisation measurement result deviation from simulation	60

9.4	Full wafer device characterisation measurement optimal devices. . . . .	61
9.4.1	Best performing fabricated device . . . . .	61
9.4.2	Best performing lower frequency device . . . . .	61
9.5	PCB characterisation . . . . .	63
9.5.1	DI, 50/50 DI/PBS, PBS loading PCB1. . . . .	63
9.5.2	PCB2 volumes . . . . .	63
9.5.3	PCB3 PBS 15uL repeatability. . . . .	64
9.5.4	On PCB Matching . . . . .	64
9.5.5	Love mode wave . . . . .	66
9.5.6	PCB characterisation conclusion. . . . .	67
9.6	Mass loading experiments . . . . .	67
9.6.1	S parameter plots of timed data . . . . .	67
9.6.2	Timed mass loading measurements PCB 2. . . . .	67
9.6.3	Timed mass loading measurements PCB 1. . . . .	68
10	Conclusions . . . . .	71
10.1	Research question . . . . .	71
10.2	Aim and requirements . . . . .	72
11	Future research and recommendations . . . . .	73
11.1	Design . . . . .	73
11.1.1	2d sim . . . . .	73
11.1.2	Include damping in model. . . . .	73
11.1.3	Automated time impulse model simulations. . . . .	73
11.1.4	Operation frequency and noise floor. . . . .	73
11.1.5	Operation frequency and WG thickness . . . . .	74
11.1.6	Matching. . . . .	74
11.1.7	PCB design. . . . .	74
11.1.8	Process dependencies . . . . .	74
11.1.9	Integrate automated microfluidics. . . . .	75
11.2	Fabrication . . . . .	75
11.2.1	Metal. . . . .	75
11.2.2	Standardisation of substrate . . . . .	76
11.2.3	Well for fluid containment . . . . .	76
11.3	Surface functionalisation . . . . .	76
11.3.1	Storage. . . . .	76
11.3.2	Sensor re-usability. . . . .	76
11.4	Sensor stability and durability . . . . .	77
11.5	Cross sensitivity. . . . .	77
11.6	Sensitivity for surface mass loading characterisation . . . . .	77
11.6.1	Initial sensitivity estimation . . . . .	78
11.6.2	Data acquirement equipment . . . . .	78
11.6.3	Noise analysis . . . . .	78
11.7	Conclusion . . . . .	79
	Bibliography . . . . .	80
A	(Strept)avidin-Biotin . . . . .	88
B	Obtaining antibodies . . . . .	90
C	CD9 and immobilisation . . . . .	92
C.1	CD9 background information. . . . .	92
C.2	Capturing CD9 . . . . .	93

---

D Conformal mapping based calculation of a coplanar capacitor capacitance	95
E Crossed-Field Model	98
F Parameter and Variable relation	100
G Smith chart	102
H PI spin test	104
H.1 Flowchart . . . . .	104
H.2 Profilometry Results . . . . .	105
H.3 Discussion . . . . .	106
H.4 Conclusion . . . . .	108
I Mask	118
J Flowchart	121
K Bonding Diagram	136
L Functionalisation Test	142
M Functionalisation Protocol	150

# 1 | Introduction

Amongst men, prostate cancer (PCa) is the most diagnosed cancer. Considering both sexes, together with gastrointestinal-tract-related cancer, breast cancer, respiratory-related cancer and skin cancer, PCa is among the cancers that are diagnosed most often on an annual basis. Moreover, PCa annual incidence is increasing in the Netherlands [1].

Monitoring the onset and progression of PCa is desired as not all PCa cases are life threatening. The survival rate in the Netherlands, 9 years after diagnosis, is over 80% [1]. Leading regularly to the decision that treatment will not improve the quality of life and is therefore not performed [2]. Methods of detection are required to make the decision of what treatment, if any, is best. Besides, non-intrusive, accessible (affordable for a large population) monitoring of the progression of PCa is required to check if treatment at a later stage becomes relevant.

## 1.1. Current diagnosis strategy

To stress the need for an additional low cost, less intrusive, lower risk diagnosis and monitoring method for the onset and progression of PCa, the currently most standardised procedure and its risks are explained. Currently, diagnosing PCa is conducted using several tests among which some are very intrusive. These tests include but are not confined to: score lists (like the International Prostate Syndrom Score), blood screening for the protein PSA, Digital Rectal Examination (DRE) and finally prostate biopsy [2][3][4]. Of these, the PSA blood test, DRE and biopsy are most intrusive. These methods are often performed in the aforementioned order.

## 1.2. Current diagnosis shortcomings

The shortcomings and risks for the current diagnosis methods, PSA blood screening, DRE and biopsy, are summarised. For blood screening for PSA, the subject has to visit a hospital which is considered intrusive. Furthermore, PSA blood test is sensitive to PCA, but also benign hyperplasia (BHP) [5]. This means the PSA test has low specificity as it is not exclusively sensitive for PCa, causing many subjects to have to undergo the unpleasant DRE. Then the physician rectally palpates the prostate with a digit to check on the size and consistency of the prostate and the presence of nodules [6]. And biopsy, the golden standard in PCa diagnosis [7]. This latter procedure introduces potential complications of which severe examples are erectile dysfunction and urinary tract infection [8].

Though PCa is diagnosed more frequently, the mortality rates do not follow this increase [1], indicating overdiagnosis. Where overdiagnosis is defined as diagnosing a condition that does not go on to cause symptoms or death [9].

## 1.3. Proposed analyte

The test can be an addition to the currently applied methods done before, or instead of, the PSA blood test as shown in Figure 1.1. For this reason and to enable the monitoring of disease progression, the device should be low cost. It should aid predominantly in reducing the need for biopsy.

To develop a new method to support the current PCa diagnosis methods, first a suitable, measurable quantity with high correlation to the condition must be found that must be unobtrusively detectable. If this measurable quantity is any biological substance, it can be called a biomarker. A suitable candidate for this biomarker is extracellular vesicles (EVs) positive for CD9, an active research topic at Erasmus MC [10]. The sensor will be designed to be sensitive to these CD9 positive EVs.

A system must be designed that is sensitive for any relevant change in this quantity; a sensor. CD9 positive EVs will only be available in very low quantities per sample [10], so a system highly sensitive for these EVs is required. And the sensitivity for any other substances in a sample or any environmental changes, in short, cross sensitivity, must be extremely low.

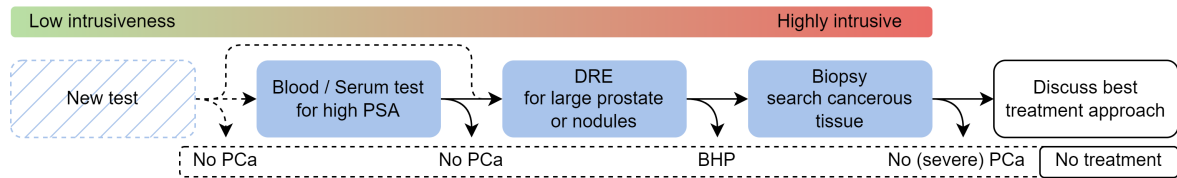


Figure 1.1: Currently most often applied diagnosis procedure for PCa and prospected role in diagnosis for new test

## 1.4. Current analyte detection strategies

At present, optically based techniques for detection are common practise. An example is the sandwich enzyme linked immunosorbent assay (ELISA), the most sensitive type of ELISA variants, where a surface is made sensitive to the biomarker, by coating it with an antibody specific for the antigen related to the biomarker. Then a substrate that can change colour is added which will bind to the captured antigens. A chemical to start the colour change is added and how much the colour changes then gives insights in the presence of the biomarker [11]. The two immobilisation steps and addition of colour changing chemical and need for optics, bulky equipment, make it a time consuming and expensive method.

## 1.5. Proposed analyte detection method

By finding another way of determining if a biomarker is captured to a surface, without the substrate and colour change detection steps, a cheaper sensor can be created that needs less bulky equipment. One such a method is to determine the change of mass attached to the surface due to the binding of a biomarker. This can be done by bringing the surface where binding occurs in to vibration with acoustic waves. Then the eigenmode of the acoustic wave is influenced when the surface mass changes, which can be detected by a change in frequency or phase of the wave. Multiple technologies exist that are based on this principle of a vibrating surface and one suitable for biocompatible sensing (or biosensing) is the surface acoustic wave or SAW. Several modes of vibration can be utilised. In this work, the Love-mode is used.

## 1.6. Thesis aim, requirements and research question

This thesis sets out to design, fabricate and test a Love-mode SAW based sensor with an as high as possible sensitivity for surface mass loading with low cost production in mind and with the material and equipment available at TU Delft.

This translates to the following two main requirements:

- Sensitivity sufficient to detect qualitatively the CD9 concentration in liquid samples.
- Make use of standard materials and processes within Else Kooi Lab, the cleanroom facility available at TU Delft (EKL).

Then, a secondary set of requirements to further refine the design goals are established. First, to verify the design process, multiple designs should be fabricated and a requirement is to enable rapid testing of several designs. As the CD9 is in a liquid solution, the SAW sensor should be designed with this in mind. And part of low cost is also the yield and robustness of the sensor. Robustness is referring to portability and reuse of the same sensor without emerging defects. Therefore a requirement on this topic is added. This leads to the following requirements:

- The SAW sensor fabrication process will allow for rapid device characterisation.
- A practical setup coping with liquid samples must be realised.
- The SAW sensor and measurement platform will be robust, allowing for repeated measurements and portability.

To achieve the thesis goal and requirements, the thesis aims to answer the research question: What properties can be achieved by a Love-mode SAW sensor, for gravimetric sensing for CD9, fabricated at EKL?



This is a proof of concept objective. Notice then that several important topics are left for future research due to limited time and resources. Topics including:

- Selectivity for CD9.
- Reusability of the sensor for CD9 detection.
- Long term stability of the sensor.
- Physical testing of the influence of design variables on the sensitivity.
- Design for upscaling.
- Integrated readout electronics.

## 1.7. Contents

This thesis can roughly be divided in biological (for research relevance) and engineering topics, distributed over several parts, in accordance with Figure 1.2. It is then ordered in chapters to first, elaborate on prostate cancer and the most common diagnosis methods (Chapter 2). Secondly, a discussion on relevant biomarkers and detection methods is given in Chapter 3. Thirdly, a background on surface acoustic wave devices and the state of the art of this technique is discussed in Chapter 4. Then, design methods and choices are expanded upon in Chapters 5 and 6. After this, in Chapter 7, the plan for fabrication is depicted. Next, in Chapters 8 and 9, the fabricated devices are characterised and the results of the optimal fabricated devices are given and the thesis conclusion is formulated in Chapter 10. And lastly, the future prospects and what challenged are left for future research is reviewed in Chapter 11.

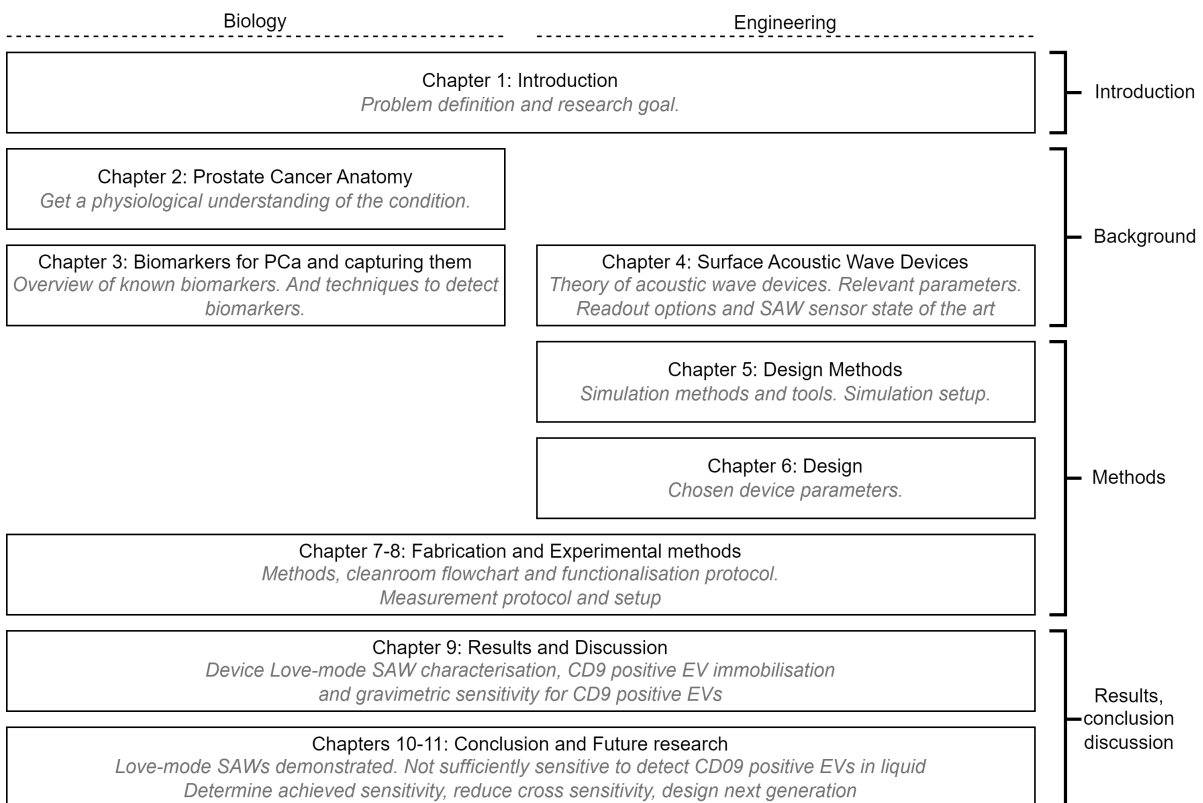


Figure 1.2: Thesis contents, showing the distribution between biological topics for design relevance and engineering topics and how they fit in the structure.

# 2 | Prostate Cancer Prevalence, Anatomy and Diagnosis

To understand the relevance of the design, in this chapter the prevalence, anatomy and diagnosis methods are described. It is meant to give a broad overview of PCa as a condition. It is important to realise where the device that is proposed fits in the state of the art and have an idea of the societal relevance. First the prevalence is presented. Second, a short overview of the anatomical implications of PCa is included. Third, the clinically used diagnosis methods are discussed extensively to get an idea how the proposed method fits in with the current procedures. Then the discrepancies of these methods are treated to indicate where the gap lies that could be solved with the proposed method.

## 2.1. Prostate cancer prevalence

As mentioned, PCa is a growing factor in an ageing society, making the search for additions to the diagnosis tool worthwhile. Figure 2.1 B indicates the increasing prevalence of PCa with age. Furthermore PCa is among the most prevalent forms of cancer in the Netherlands (Figure 2.1 A) and the most prevalent form of cancer among men [1].

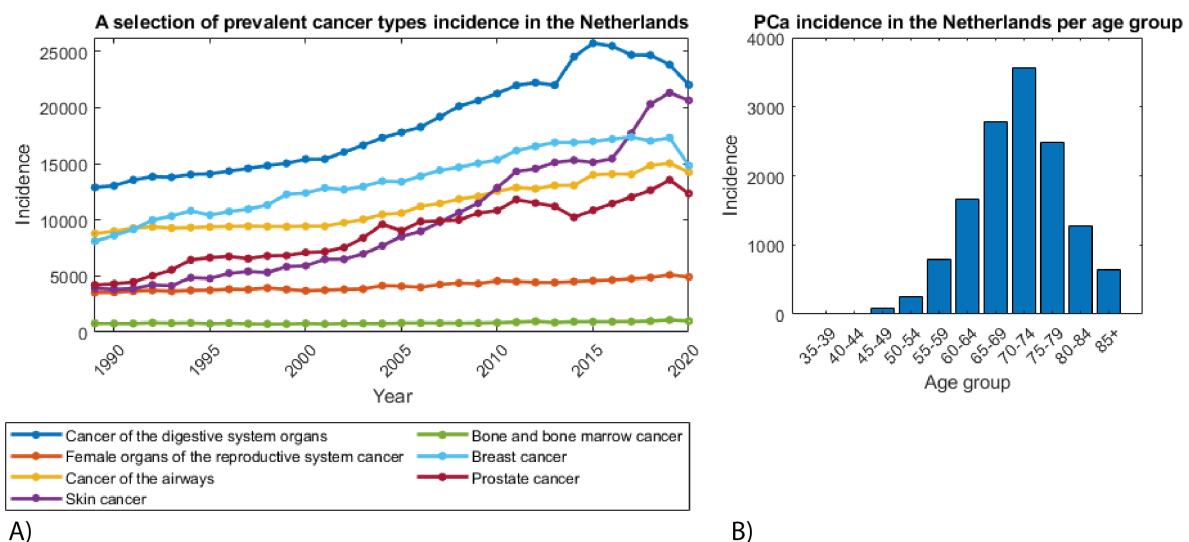


Figure 2.1: A) Incidence (new diagnoses per year) for a large selection of common cancer types in the Netherlands for both sexes. PCa is very prevalent among men considering most other cancer types occur in both sexes. Data from [1]. B) Incidence of PCa in the Netherlands per age group divided of five year intervals. PCa incidence increases hugely with age. Data from [1].

## 2.2. Prostate Cancer Anatomy

The prostate is located inferior to (below) the bladder, around the urethra (at that location called the prostatic urethra) against the rectum and in a grown man is approximately the size of a walnut. It is located between the internal (above) and external (below) sphincters of the urethra (Figure 2.2). The role of the prostate is for the smooth muscle to contract during ejaculation and squeeze prostatic secretion (nutrient source citrate, several enzymes and PSA) into the prostatic urethra via several ducts [12]. The prostate is made up of 20 to 30 compound tubuloalveolar glands embedded in smooth muscle and dense connective tissue.

The prostate tubuloalveolar glands are mainly built-up of three cell types, luminal cells (secretory function), basal cells (considered as protective for the luminal cells), and neuroendocrine cells (function not yet

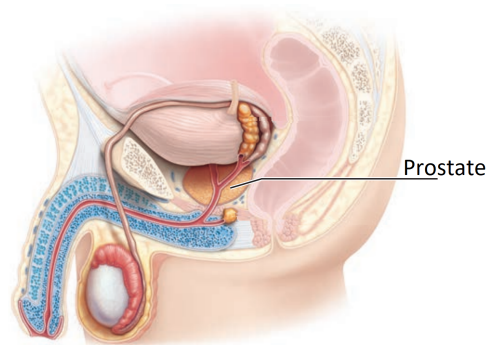


Figure 2.2: Schematic representation of the lower pelvic region with the prostate pointed out. Adapted from [12].

understood), as shown in Figure 2.3. In PCa, the cancerous tissue mainly have luminal cell phenotype, however, it is believed the cancerous tissue originates from basal cells, though this is still an active area of research [13]. The cause of PCa is not yet understood. Etiology studies indicate the largest riskfactor is age. Additionally, there is an indication family history with PCa increases the risk for the condition [14]. And African-American men have increased incidence and mortality compared to white American men [15].

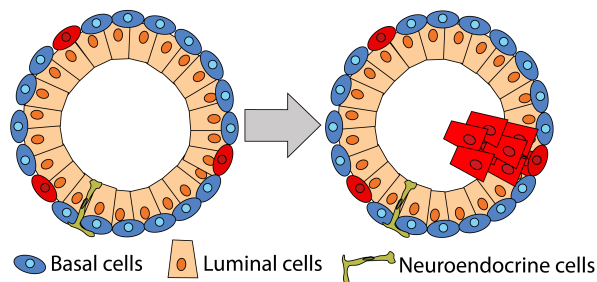


Figure 2.3: Schematic cross section of a tubuloalveolar prostatic gland showing the three major present cell types. Adapted from [13].

### 2.3. Currently Practised Diagnosis Methods

For the presently standard PCa diagnosis, procedures ranging from low-intrusive, low-specificity to highly intrusive, high-specificity are possible. Several procedures mentioned by Antoni van Leeuwenhoek [2], Erasmus MC [3] and UMC Utrecht [4] are summarised here:

- Score lists as IPSS (International Prostate Syndrome Score). This score is built up of seven questions, about holding urine and micturating, in a questionnaire. Every question is about the incidence of a phenomenon where higher incidence increases the score [16].
- Uroflowmetry and residue measurement to give information about the strength, duration and residue of urinating giving an indication of the functioning of the bladder and urethra.
- Blood (whole blood or serum) and/or urine screening for the protein PSA.
- DRE where the physician can feel for abnormalities on the consistency of the prostate with a digit. The procedure can be used to gather information on different conditions such as hemorrhoids, rectal prolapse or neuromuscular function of the external anal sphincter. When screening for PCa, attention is given to the size and consistency of the prostate, and the presence of nodules [6].
- Prostate biopsy with Gleason score or ISUP grading (as addition to the Gleason score) [17]
- Several imaging techniques as prostate ultrasound (for example, transrectal ultrasound), MRI, PET/CT PSMA and bone scintigraphy (last two mainly for metastasis screening). To prevent negative effects of biopsy experienced by some patients and to reduce the cost of care, in 2020, new guidelines on PCa

diagnosis were adopted in the Netherlands. These guidelines dictate that MRI can be applied after elevated PSA levels are detected to determine if the prostate shows any abnormal tissue. Potentially preventing numerous unnecessary biopsies [8][18].

Testing for PSA and biopsy are further elaborated upon as they combine to the most common practise in PCa diagnosis. The first step is to test for PSA in blood serum. And when the concentration is elevated, secondly, biopsy is performed. Though it becomes more common to first do a MRI to reduce unnecessary biopsies.

### Blood screening for PSA

Blood (whole blood or serum) and/or urine screening for the protein PSA. This kallikrein-like protease is produced and contained in the healthy prostate. It is confined to the prostate and only released during ejaculation as it plays a role in the liquefaction of semen by fragmenting proteins (gel-bound fibronectin and semenogelin) [19]. Normally, PSA only rarely leaks to the bloodstream and in healthy men, concentrations of less than 4ng/ml of PSA in the serum are typical. When abnormalities arise, however, PSA is allowed to leak to the bloodstream, and eventually to urine, due to discontinuities in the prostate epithelium. This makes PSA a biomarker for PCa, but also for other prostate conditions including benign hyperplasia [5].

PSA as a biomarker was approved by the Food and Drug Administration (FDA) in 1994 in conjunction with DRE in males over 50 years of age [20].

The sensitivity of PSA based tests can be set by lowering the threshold of detection. This, however, decreases the specificity and will lead to overdiagnosis. A review by Duffy (2019), reviewing the specificity of PSA and derivatives, reports that when the threshold is chosen such that a 95% sensitivity is achieved, then, total PSA has a specificity of 17.2%, Prostate Health Index (phi) a specificity of 36.0% and freePSA/totalPSA a specificity of 19.4% [21]. The same review found for Prostate Cancer gene 3 (PCA3) a lower sensitivity of 65% resulting in a relatively high specificity of 73%. This sensitivity can again be increased at the cost of specificity. In another study, reported in the same review, this resulted in a 91% sensitivity and 42% specificity for PCA3.

Table 2.1: The sensitivity for total PSA, phi and freePSA/totalPSA was chosen at 95% to compare specificity. Data from review [21].

Biomarker	Sensitivity	Specificity
total PSA	95%	17.2%
phi	95%	36.0%
freePSA/totalPSA	95%	19.4%
PCA3	91%	42%

Many methods to detect PSA are reported like Fluorescence, Chemiluminescence, Surface Plasmon Resonance, Optical scattering and Optical Absorbance [22]. However, the most reported method to detect PSA is an ELISA. In this method, usually a 96-well (polystyrene) plate is coated to strongly bind protein, this is a special type of absorbant plate. Several variations of the ELISA exist, these are: direct, indirect, sandwich and competitive ELISA where the sandwich variation is most sensitive. All ELISA variations have in common, some antigen is present, fixed to the substrate or free with an attached enzyme. The antibody of interest can then bind to this antigen. When the antibody of interest is fixed to the plate, in sandwich ELISA, a detection primary antigen can bind to the antibody. Then a complementary secondary antigen can bind to the primary detection antigen. Finally a substrate is added which can bind to the secondary antigen. This substrate causes a change of colour which can be detected by a plate reader [11] [23]. For the sandwich ELISA the steps are shown in Figure 2.4.

### Biopsy and Gleason Score

In a biopsy, using a needle, tissue is removed to undergo lab analysis. Several biopsy methods can be applied, examples are Trans Rectal Ultrasound Guided biopsy (TRUS-biopsy) and Template Prostate Mapping biopsy (TMP-biopsy). In the first method, a rectal ultrasound probe is used to locate suspicious tissue and with a needle, samples are taken as shown in Figure 2.5. This method reduces the amount of sample points to about twelve. In the second method, many more samples are taken as the prostate is sampled every 5mm. This is much more invasive but is also more accurate (more sensitive) as no part of the prostate is skipped [8]. Both these methods are transperineal. This is standard as transrectal is even more prone to infection risk [7].

Microscope lab evaluation of the samples leads to a Gleason score which is composed of a sum of two numbers. First, all samples from the biopsy get a grade according to Figure 2.6. The first number of the

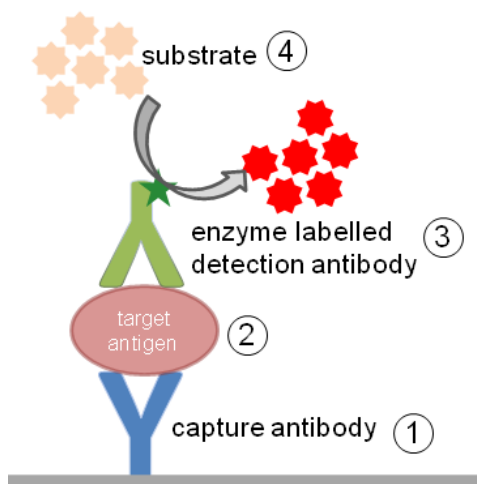


Figure 2.4: Sandwich ELISA diagram with steps. 1 coat plate with antibody, 2 allow target antigen (if present) to bind, 3 add enzyme labelled antibody to bind to target antigen, 4 add substrate causing change of colour detectable by plate reader giving quantitative or qualitative result dependent on kit setup. Used from [23]

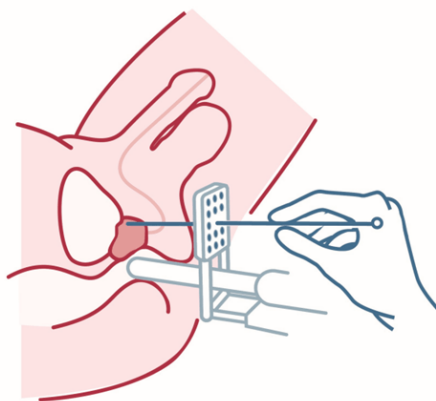


Figure 2.5: Schematic representation of a trans-perineum biopsy with echo device anally inserted for locating the biopsy needle. The method reduces infection risk, is less painful and more accurate [7].

Gleason-score then is the most prevalent grade from the samples, and the second number is the second most prevalent grade from the samples. As Gleason 1 and Gleason 2 are rarely given, this usually results in a Gleason-score between 6 and 10 [24].

To better differentiate between cancer stages, as for example the tumor behaviour of 3+4 and 4+3 is significantly different but both give a Gleason-score of 7. Therefore a need for an alternative representation of the score is obvious. So often the two numbers of the Gleason-score are represented as a sum (possibly with percentages of prevalence as additional information). Also an additional score system is used, the International Society of Urological Pathology grading or Grade Group. This is based on the Gleason-score in the following way [17]:

ISUP	Gleason-score
Group 1	Gleason-score $\geq 6$
Group 2	Gleason-score $3+4 = 7$
Group 3	Gleason-score $4+3 = 7$
Group 4	Gleason-score 8
Group 5	Gleason-score 9 or 10

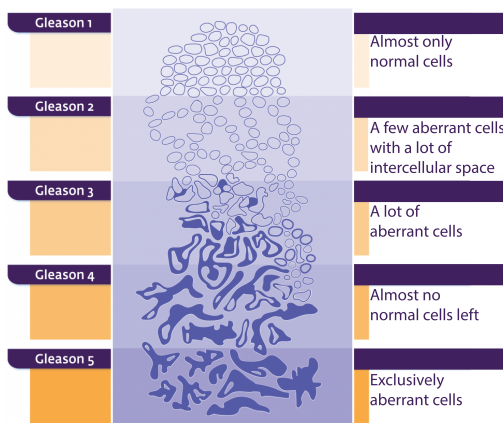


Figure 2.6: The Gleason score is made up of two parts. All samples from a prostate biopsy get a grade. The most prevalent grade is the first part and the second most prevalent grade is the second part [24].

### 2.4. Discrepancies in PSA and Biopsy Diagnosis Method

So far, ample diagnosis tools were presented and it was mentioned PSA testing followed by biopsy in case of increased blood PSA concentrations is the most common practised diagnosis method. However, there is still a gap in PCa diagnosis tools as PSA lacks specificity [20] and a biopsy introduces risk factors related to the procedure [8].

Until 2008, in the USA, it was recommended to screen for PCa using a PSA test [20]. However, due to the lack of specificity of the PSA test and the often latent behaviour of PCa, this advice was redrawn [20] [25]. Population wide screening led to overdiagnosis, which is the case when "a condition is diagnosed that would otherwise not go on to cause symptoms or death", Gilbert Welch et. al. [9]. Figure 2.7 gives an indication of overdiagnosis in PCA in the Dutch population.

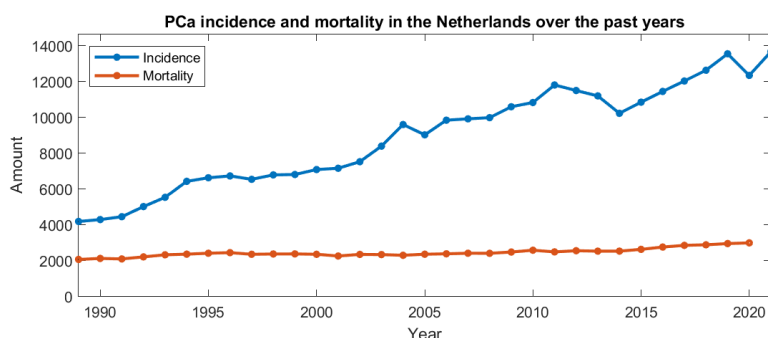


Figure 2.7: Comparison of incidence and mortality of PCa in the Netherlands. The large increase in incidence and relatively stable mortality is an indication of overdiagnosis. Data from [1].

A meta analysis from 2018 concludes screening for PSA does not reduce PCa mortality significantly. As when screening, per 1000 men screened in 10 years, one PCa related death is averted. However, using models, it was estimated per 1000 men screened, one would be hospitalised for sepsis, three would require pads for urinary incontinence and twenty five would report erectile dysfunction. Clearly illustrating the negative effects of the follow up research or treatment after screening for PSA [26].

Following the PSA results, due to the low specificity, biopsy must be done to avoid unnecessary treatment. Unfortunately, biopsy still brings large risks. From a study performing both earlier described biopsy methods on 576 patients, the side effects are listed together with percentage of incidence to indicate the risk of biopsy: pain/discomfort [64%], dysuria (painful urination) [46%], haematuria (blood in urine) [67%], haematospermia (blood in sperm) [55%], erectile dysfunction [14%], urinary tract infection [6%], systemic urosepsis [1%], acute urinary retention [10%], spinal/general anaesthetic related symptoms [4%] and other side effects [11%] [8]. It can be concluded, though many diagnosis tools exist, there still is a need to increase the specificity of non invasive diagnosis to reduce the need for biopsy.

# 3 | Biomarkers for PCa and capturing them

In this chapter, several biomarkers are discussed to demonstrate that if the proposed sensor efficacy can be demonstrated for one biomarker, it is in potency a very strong method as it can easily be adapted to other biomarkers. Then, shortly, the capture, or immobilisation, of biomarkers to a surface is discussed.

## 3.1. Common practise biomarkers: PSA and derivatives

An FDA approved and widely applied biomarker is PSA. Cancer in the prostate causes irregularities in the tubuloalveolar prostatic glands giving PSA a chance to leak to the bloodstream [13]. Other prostatic conditions as benign hyperplasia can, however, also cause PSA to leak to the bloodstream [5] making it impossible to use PSA as an independent test for diagnosis.

Many biomarkers derived from PSA, such as, total PSA, prostate health index (phi) and free PSA normalised to total PSA, are also FDA approved [5]. How these derived forms relate to each other is shown in Figure 3.1. These are all reported to have a high sensitivity to PCa, around 95%. Unfortunately, their specificities are all low, ranging from 17% to 36% [21].

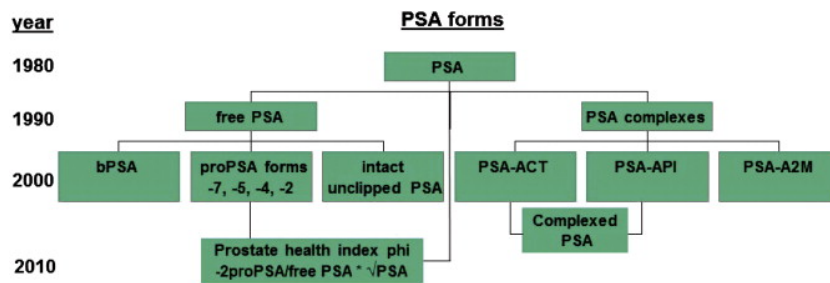


Figure 3.1: Different forms of PSA, some derivatives more detectable then others and some more present in PCa then in BHP. The year of detection is included. Also the definition of the phi is included. Figure from [5].

## 3.2. Other FDA approved biomarkers

Two urinary biomarkers are the FDA approved Prostate Cancer gene 3 (PCA3) and the TMPRSS2:ERG gene fusion. The latter is a frequently mentioned biomarker with potential to improve diagnosis in multivariate methods. This method is based on the detection of the alteration of the TMPRSS2 gene. The TMPRSS2:ERG fusion is a common genetic aberration in human tumors [27]. Using a urinary assay similar to PCA3, this fusion can be detected [28]. Used complementary to PCA3 detection, it can help improve specificity by increasing the PCA3 detection limit as TMPRSS2:ERG can detect the PCa cases missed out by PCA3 preserving the sensitivity and avoiding false negatives [5] [29].

It should be noted that for all biomarkers there is a trade-off between sensitivity and specificity. In Table 2.1 the sensitivity and specificity of FDA approved PCa biomarkers are summarised.

## 3.3. The biomarker used in this work, CD9

As mentioned, the cluster-of-differentiation antigen 9 (CD9) will be the biomarker used for testing the sensor. CD9 is a transmembrane glycoprotein involved in adhesion with other transmembrane molecules. It is expressed on a specific type of extracellular vesicle (EV) namely exosomes (50 to 100nm diameter) [30]. These EVs can spread freely through the body and can therefore end up in the urine [31]. When capturing a CD9 protein, the entire EV it is attached to is also captured [32], as illustrated in Figure 3.2. This is a huge advantage of CD9 as a biomarker, as the sensor is sensitive for changes in the attached surface mass, and the added mass due to the entire EV relaxes sensitivity requirements for detection.

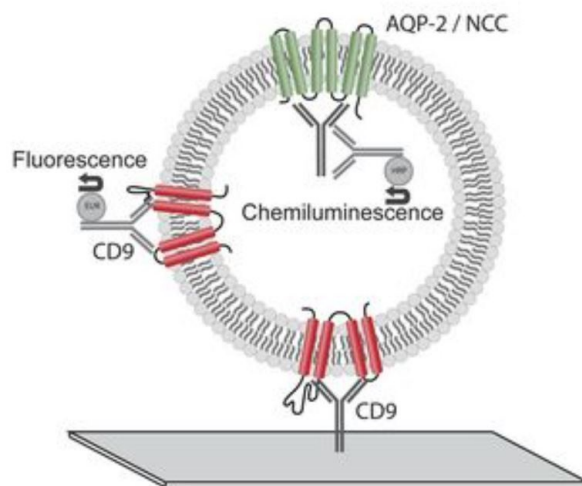


Figure 3.2: CD9 is a transmembrane glycoprotein present in urine fixed in extracellular vesicles. Therefore it is also captured while attached to an extracellular vesicle, not as a single protein. Adapted from [32].

### 3.4. Biomarker immobilisation

Capturing biomarkers has become easier since the discovery of how to obtain monoclonal antibodies [33]. A short description on this topic is included in Appendix B. These monoclonal antibodies are commercially available and can be attached to a biotin molecule, or be biotinylated. This biotin has an exceptionally strong binding with streptavidin becoming a biotin-streptavidin complex. Streptavidin can be immobilised to a surface due to its affinity for free OH groups [34]. So, firstly a high surface affinity for streptavidin must be created by ensuring free OH, or hydroxyl, groups. Secondly, streptavidin is allowed to bind to the surface. Thirdly, the biotinylated antibodies are exposed to the surface. Now the surface is active and sensitive for a very specific antigen, corresponding to a specific biomarker. A more complete description on the avidin-biotin interaction is given in Appendix A.

### 3.5. Concluding on biomarkers and immobilisation

In conclusion, PSA and several derivatives are FDA approved biomarkers with high sensitivity but unfortunately, low specificity. Numerous biomarkers that might have a predictive value for numerous types of conditions are currently a topic of active research, one of them is CD9 for PCa diagnosis, which will be used for this work. Using commercially available monoclonal, biotinylated antibodies, a surface can be functionalised to capture a specific antigen. With this method, a surface can be designed to capture any biomarker for which a biotinylated antibody is available.



## 4 | Surface acoustic wave devices

This thesis proposes to use a Love-mode SAW for gravimetric sensing in liquid samples for biomarkers. In this chapter, the theory behind the surface acoustic wave (SAW) is discussed. First, a short recap is given on what a SAW is, followed by, a very short historic overview on the discovery of the SAW for completeness. Then the fundamentals and different modes of surface acoustic waves is discussed. Useful performance parameters are identified. The variables that can be influenced are identified for both the material choices and geometric design options. Then the way the variables set the most central parameters is mapped to help determine a design order. Finally, readout options are presented.

### 4.1. SAW introduction

A SAW is a device that uses acoustic waves through a material that are confined to the surface. This differentiates them from other devices using acoustic waves, such as, the thickness shear mode devices that use acoustic waves through the entire material, or bulk [35]. When acoustic waves travel through a piezoelectric material, the deformation due to the waves creates electric fields, which can be used for sensing applications. In a piezoelectric material the link between deformation and the electric field is reciprocal, so an electric field can also be used to induce acoustic waves [36].

The first known research on acoustic waves in piezoelectric materials was performed by Lord Rayleigh around 1885 [37]. Later, White and Voltmer introduced a method to invoke surface acoustic waves using interdigital transducers (IDTs) [38]. But, due to lagging technology, only in 1977 the first commercial SAW devices were produced [39]. These commercial devices were radio frequency filters, now SAWs are used in more fields such as bio-sensing [40].

### 4.2. Acoustic wave excitation and propagation

To understand how acoustic waves are created and how they fundamentally behave, a material surface is considered upon which some force incident on the surface excites the material. The induced deformations in the material now have a longitudinal (L), shear vertical (SV) and shear horizontal (SH) component. The L and SV displacement components can not behave as such at the surface due to the material boundary, causing them to have non-uniform propagation patterns into the bulk and to combine to a new wave mode, or couple. Together, the L and SV components form a wave mode along the surface, evanescent into the bulk as illustrated in Figure 4.1, first described by and named after Lord Rayleigh [37]. This wave mode can be induced in all solids, including piezoelectric materials. In isotropic materials, the SH mode displacement is supported by the material, it is not impeded by the material boundary, and has a uniform propagation pattern [41].

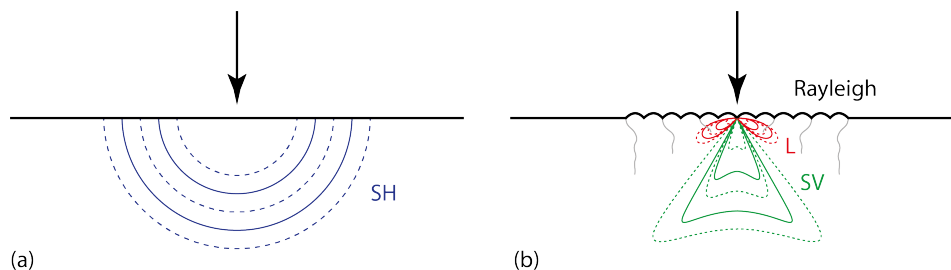


Figure 4.1: Linear source plane excitation for surface and bulk wave propagation modelling in an isotropic solid. (a) Propagation of SH waves along the surface and into the bulk. (b) Coupling of SV and L modes to a Rayleigh mode SAW. Both (a) and (b) are simultaneously at play but drawn separately for clarity. Figure based on [41][42][43].

In anisotropic materials with piezoelectric properties, the SH mode can couple to the electric potential  $\phi$  induced by the stress from deformation. This can confine the SH wave to the surface causing a SH-SAW,

which is slower than the original SH-BAW. The stronger the piezoelectric effect, the slower the SH-SAW and the better the confinement to the surface [41].

Alternatively, the SH-BAW can be confined to the surface by depositing a material with a lower SH-BAW velocity on top of the original material. This mechanism was first described by and is named after Augustus E.H. Love [44] and it was actually first observed in geodynamics [45].

When the created SAW wave is faster than a remaining BAW (SV or SH), then energy is allowed to leak into the bulk. The SAW mode is then known as a leaky-SAW mode [41]. The difference between leaky and non-leaky modes is shown in Figure 4.2. In some cases for quartz, the shear horizontal acoustic wave is not radiated into the bulk, but also does not adhere to the surface very well, this is known as the surface skimming bulk wave SSBW [46].

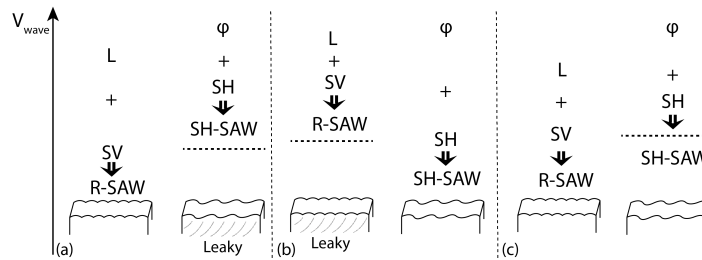


Figure 4.2: Relation of SH, SV, L and  $\phi$  wave velocity and the effect when they couple. When the coupled wave causing a SAW is faster than any present shear BAW component, a leaky SAW is created. Figure based on [41].

Another SAW mode, the Lamb wave, can be excited when the elastic solid material guiding the acoustic wave is made into a thin membrane with a thickness in the vicinity of the acoustic wavelength. This SAW has a symmetric zero order mode  $S_0$  converging to a longitudinal mode towards zero membrane thickness and has an asymmetric zero order mode  $A_0$  which converges to a Rayleigh mode at high frequencies [47].

### 4.3. Love mode

For this work, the Love mode SAW is considered. As already described in Section 4.2, the Love mode SAW is a SH-based mode in a piezoelectric substrate material with slower wave speed wave guiding layer as depicted in Figure 4.3. IDTs convert the electric signal to the acoustic domain and back to the electric domain.

This mode offers several advantages over the other modes such as:

- Natural protection of the interdigitated electrodes by the wave guiding layer.
- As the acoustic energy is confined to the surface by a wave guiding layer, the piezoelectric substrate thickness can be thick without loss of sensitivity, making it a robust design.
- Being SH-wave based, there is no displacement out of plane, so only viscous coupling with any liquid sample arises and little energy due to mode conversion is radiated into this sample [48].

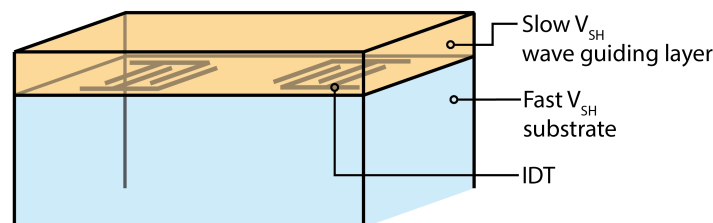


Figure 4.3: Love mode SAW based sensor schematic representation.

### 4.4. Sensitivity as Performance Measure

In this work, the most important measure of performance is sensitivity for mass loading in accordance with the aim stated in Chapter 1.6. The mass sensitivity turns out to be frequency dependent [49]. For a general

SAW device the change in mass loading of the surface causes a change in kinetic energy at the surface.

$$\Delta U_k = \frac{\rho_s}{4} (v_{x0}^2 + v_{y0}^2 + v_{z0}^2) \quad (4.1)$$

With  $v_{x0}, v_{y0}, v_{z0}$  the particle velocities along the respective  $x, y$  and  $z$  axis. And  $\rho_s$  the change in surface mass density. The particle velocities are related to their displacements by their derivatives so  $v_i = j\omega u_i$ . Taking a unit volume and assuming constant power density, equation 4.2 shows an increase in kinetic energy reduces the wave velocity.

$$\frac{\Delta v}{v_0} = -\frac{\Delta U}{U_0} \quad (4.2)$$

Where  $v_0$  and  $U_0$  are the unperturbed wave velocity and kinetic energy respectively.

Then these expressions can be combined to find the relation between the wave velocity and mass loading.

$$\frac{\Delta v}{v_0} = -\frac{\omega v_0 \rho_s}{4} \left( \frac{v_{x0}^2}{\omega P} + \frac{v_{y0}^2}{\omega P} + \frac{v_{z0}^2}{\omega P} \right) \quad (4.3)$$

with  $\omega$  the radial frequency and  $P$  the power transmitted by the acoustic wave. The surface particle velocities  $v_{x0}, v_{y0}$  and  $v_{z0}$  increase proportionally with  $\sqrt{\omega P}$  due to increased wave energy confinement at higher operating frequency. So the  $(v_{i0}^2)/(\omega P)$  terms are frequency independent. Then an expression is found indicating the mass induced change in SAW propagation velocity is operating frequency dependent.

$$\frac{\Delta v}{v_0} = -c_m f_0 \rho_s \quad (4.4)$$

With a mass sensitivity factor  $c_m$

$$c_m = \frac{\pi v_0}{2} \left( \frac{v_{x0}^2}{\omega P} + \frac{v_{y0}^2}{\omega P} + \frac{v_{z0}^2}{\omega P} \right) \quad (4.5)$$

Also, increasing frequency reduces acoustic wave penetration depth, improving surface capturing of the wave energy and thus increasing sensitivity [50].

Unfortunately, increasing the operating frequency will also increase noise, limiting the maximum sensitivity. Increasing the operating frequency will decrease the sensor geometry. Imperfections like surface roughness will not scale accordingly, causing noise [50].

It is concluded, that the operating frequency of the sensor should be designed as high as possible for maximum sensitivity. Though, a trade-off between sensitivity and noise is found.

## 4.5. Variables Determining Performance

In the next sections the variables that determine the device performance are discussed. These can be separated in material properties and transducer related variables. First the material property related variables are discussed. Then the transducer design related variables are elaborated upon.

### 4.5.1. Material properties based variables

As depicted in Figure 4.3, a Love mode SAW device has a piezoelectric substrate, slower wave speed wave guiding layer and conductive transducers. The materials used have a large impact on the final properties of the sensor. Therefore, the most important material properties having the most profound impact of device performance are discussed next.

#### Crystal orientation

First, the substrate material needs to be piezoelectric for the electrode transducers to cause any deformation in the substrate which can be guided by this material as acoustic wave. Piezoelectricity arises due to asymmetry in the crystal structure [36]. The orientation also determines what acoustic wave modes are supported. Though all materials support Rayleigh waves, special conditions are required to support non-leaky SH waves as was explained in 4.2.

### Electromechanical coupling coefficient

The electromechanical coupling coefficient,  $\kappa^2$ , gives the magnitude of the relation between an applied electric field and the resulting displacement of a piezoelectric material and vice versa. For this reason a high  $\kappa^2$  is desired. It can be approximated by the equation from Campbell and Jones 1968 [51].

$$\kappa^2 \approx 2 \frac{\Delta v}{v} = 2 \frac{v_{ph} - v_m}{v_{ph}} \quad (4.6)$$

It is defined as the change of velocity  $\Delta v$  caused by applying a highly conductive infinitely thin metal film on the surface of a piezoelectric material [52].  $\kappa^2$  is usually given in percent.

### Shear horizontal wave speed

The different acoustic wave modes that can travel through a solid have their own propagation speeds. The Love mode wave will be sustained by the SH-mode in the substrate (when a lower shear wave speed waveguide is deposited on top of the waveguide, see Section 4.3), which velocity  $v_s$  is depending on the density  $\rho$  and the shear-horizontal modulus  $G$ , relation given by equation 4.8. And  $G$  is set by the Youngs modulus  $E$  and the Poissons ratio  $\nu$ , which relation is given by equation 4.7, as can be derived from Hooke's law [53].

$$G(E, \nu) = \frac{E}{2(1 + \nu)} \quad (4.7)$$

$$G = \rho v_s^2 \quad (4.8)$$

Equivalently, the shear wave velocity is set by the material stiffness matrix, given by  $v_s = \omega/k = (G/\rho)^{1/2}$ , where  $k$  is the wave vector,  $G$  is the shear wave modulus, which is equal to the  $c_{44}$  element from the material stiffness matrix. Finally,  $\rho$  is the material density [54].

For the substrate, to allow for a high operating frequency and a wide choice of waveguide materials, a high as possible  $v_s$  for the substrate is beneficial.

For the wave guide, wave energy confinement at the substrate-waveguide interface increases with increasing difference between substrate and waveguide shear wave velocity, which implies the possibility to achieve better sensitivity for surface mass changes [55].

### Temperature coefficient of frequency

The temperature coefficient of frequency (TCF) relates the influence of the temperature to the resonance frequency of the piezoelectric crystal [47]. All used materials have their own TCF and they can enhance or cancel each other in the total device. So, the wave guide layer will also introduce a TCF which is layer thickness dependent making a zero TCF design with a nonzero TCF substrate possible by careful selection of the wave guiding layer thickness [56]. Preferably all materials should have a low and ideally zero TCF for design ease. Though it is the sum of all material TCFs that determines the total device TCF. If the total device TCF is not zero, compensation techniques are required to avoid influence of the TCF. These can include, but are not limited to, regulated operation temperature, calibration and compensation or differential readout methods using a reference sensor deprived from the measurand.

### $\tan \delta$

$\tan \delta$  is a measure for the conversion of vibrational energy to heat by a material [57]. The values in this report are found in the literature for 1Hz and around room temperature. As  $\tan \delta$  is highly temperature and frequency dependent for many materials, the given values can only be used comparatively and not as absolute values.

### Other material considerations

Finally, for a practical sensor, the actual ease of use and robustness of the device is relevant. Both for a substrate and optional waveguide, mechanical stability is required. Also, for all materials that are in contact with the sample, high chemical stability in chemically harsh environments is required. Moreover, to some extent, the materials in contact with the sample must be bio-compatible to avoid denaturing of protein (low cytotoxicity). Furthermore, the materials selected must be compatible with the mechanical stresses induced during the fabrication process and all materials must be cleanroom compatible. Some materials that are considered contaminants like gold are still possible to process, however, the process flow is complicated potentially increasing the design and fabrication cost. Therefore the use of any material that is not cleanroom compatible is avoided.

### 4.5.2. Transducer considerations

The excitation of the above discussed acoustic waves in piezoelectric materials can be done by electrodes in the form of an interdigital transducer (IDT) [38] as was mentioned before, because of the reciprocal coupling between the electric field and the material stress. The reciprocal relation also enables sensing with a similar or identical IDT [36]. For the IDT, the design parameters are as illustrated in Figure 4.4. With the electrode width or metalisation ratio,  $\eta$ . The electrode length or aperture,  $W$ . The amount of repeating electrode pairs,  $N$ . And finally, the length between the transmitting and receiving IDT, called the delayline length,  $L$ . Furthermore, the electrode geometry can also be altered to influence directionality [58] and reflection structures can be applied [59].

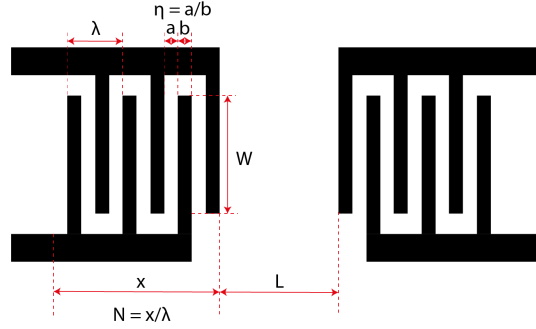


Figure 4.4: Bi-directional IDT schematic representation with labels for the dimensions.

#### Electrode width

The electrode width and separation determines the wavelength. This wavelength then determines the operation frequency following equation 4.9 [48].

$$f_r = \frac{c}{\lambda} \quad (4.9)$$

Here  $c$  is determined by material properties as discussed in Section 4.5.1.

In a Love mode SAW, the operating frequency is between the frequencies following from 4.9 of the substrate and waveguide where a thicker waveguide lowers the frequency as shown in equation 4.10 [54].

$$f_{0\text{waveguide}} < f_{0\text{Love}} < f_{0\text{substrate}} \quad (4.10)$$

#### Electrode metalisation ratio

The period of the IDT fingers sets, and is equal to, the wavelength, but the optimum metalisation ratio is set by the sensitivity for odd harmonics. Figure 4.5, by Campbell et al. [60], shows the harmonics that can be excited by the IDT. The figure indicates no higher harmonics are excited for a 0.5 metalisation ratio.

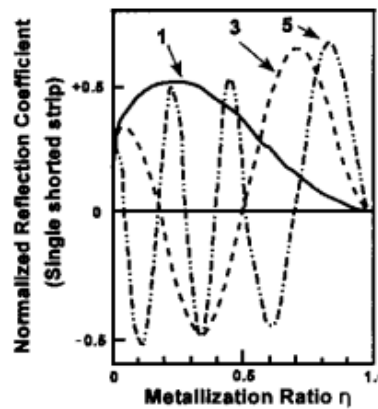


Figure 4.5: Metallization ratio ideally at 0.5 to avoid higher harmonics to be excited. Figure taken from [60].

### Electrode thickness

It is beneficial to decrease the electrode thickness to reduce the electrodes mass impeding surface acoustic waves. This will however increase the electrode series resistance which will also go on to cause increased noise [61]. The effects of these added noise sources have to be taken into account in the readout electronics design to mitigate its effects [40].

### Layout

The most recurring IDT layouts are the bi-directional IDTs with or without reflectors and the single phase unidirectional digitated transducer (SPUDT). These are illustrated in Figure 4.6. The most simple IDT is the two electrode per period straight IDT with  $\lambda/4$  electrode width. Unfortunately, this type of IDT has a bi-directional operation due to its electrical and mechanical symmetry. When using a transmitting and receiving IDT, this will cause fundamentally a 6dB insertion loss (IL) [62]. This IL can be mitigated by improving the directionality of the IDT.

The first method to improve directionality is to apply reflection structures, at the cost of SAW BW and required area. It was, however, shown the total IL is reduced more by adding an additional excitation pair than a reflection pair by Tran et. al. [59].

A second solution is to use uni-directional IDT structures like multiphase unidirectional IDT (UDT). However, generating the additional excitation phase signals increases design complexity and connecting the additional phases can be complicated in a 2D planar technology [41]. These challenges are avoided when applying a single phase uni-directional IDT or SPUDT. By using a  $\lambda/8$  excitation electrode and a  $3\lambda/8$  or  $\lambda/4$  reflector electrode per unit, a structure is made with non overlapping mechanical and electrical reflection centres [62]. This has as effect that the total transmitted wave can be made unidirectional. The smaller feature sizes do limit the operation frequency when only a limited fabrication equipment resolution is available [58].

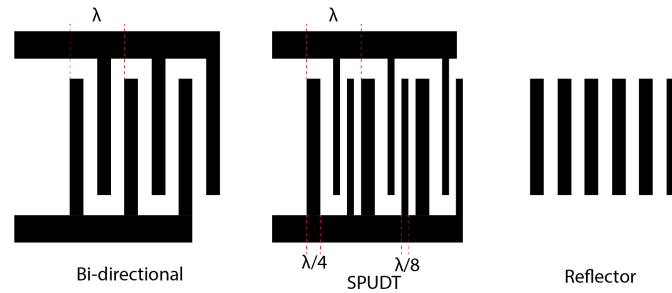


Figure 4.6: Bi-directional IDT, SPUDT and reflector layout.

### Electrode pairs $N$

The optimum number of electrode pairs  $N$  is a trade-off between electrical coupling to the piezoelectric substrate and bandwidth with both an upper and lower limit. The acoustic bandwidth of an IDT for a SAW device is inversely proportional to the number of finger pairs  $N$  [63][64].

$$\frac{\Delta\omega_a}{\omega_0} = \frac{1}{N} \frac{v_g}{v_{ph}} \quad (4.11)$$

It is recognised the reduction in bandwidth is practically limited as at around  $N=100$ , losses due to mass loading and scattering due to the very same electrodes begin to counteract the added value of the electrode pairs [49]. The bandwidth can also not be made infinitely large. A higher  $N$  results in more efficient SAW generation. This implies that when the number of finger pairs becomes low, relatively more BAW modes are excited. If  $N$  is reduced below a certain point, the power radiated into the bulk grows exponentially [65].

### Aperture $W$

The overlapping finger length or width of the delay line is called the aperture or  $W$  and it determines the sensitive area width and it has large influence on the IDT impedance.  $W$  can be chosen such that transducer impedance matches the driving and detection circuits [66] [49]. Furthermore, the aperture should be sufficiently wide so the delay line area has sufficient contact area with the sample.

The Interdigital Transducer (IDT) excites a plane wave. Due to diffraction, this plane wave will become a circular wavefront. Two regions can be distinguished, the Fresnel region where the wave propagates as plane

wave and the Fraunhofer region where the wave becomes circular. The aperture should also be chosen such that the propagation of the surface acoustic wavefront is still a plane wave. The length of propagation path  $x_c$  which distinguishes between the Fresnel and Fraunhofer regions is given by [67]

$$x_c = (1 + \gamma)w^2/\lambda, \quad (4.12)$$

where  $\gamma$  is a factor of anisotropy of the guiding media, with  $\gamma \rightarrow 0$  for isotropic materials, and is reported to be 0.378 for ST-cut quartz. And  $w$  is the width of the initial wavefront, which equals the aperture. Finally,  $\lambda$  is the wavelength [41].

With equation 4.12, a maximum delay line length  $L$  can be determined for some chosen aperture  $W$ .

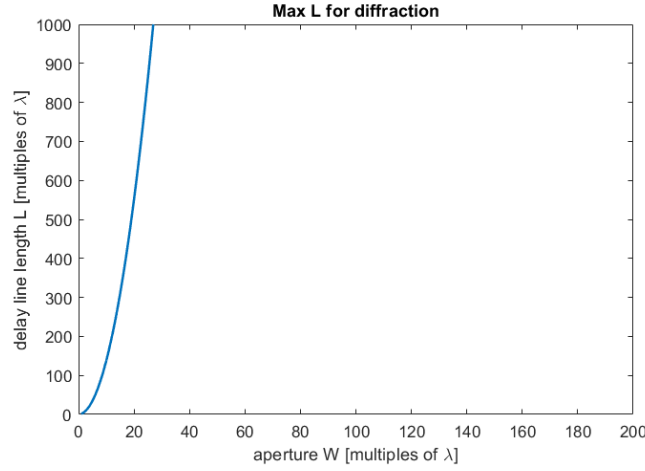


Figure 4.7: The maximum  $L$  for a certain  $W$  before the SAW wavefront enters the Fraunhofer region where the wavefront becomes circular.

#### Delay line length $L$

Together with the aperture  $W$ , the delay line length  $L$  determines the contact area between the sensitive area of the sensor surface and the sample.

Any acoustic wave travelling along will have a reducing pressure over distance. This is partly by spreading of the wave energy due to diffraction or transmission and, in non ideal media, for another part due to losses. These losses can be due to scattering or absorption. Scattering is the random redirection of wave energy due to material anisotropy with respect to the wave propagation direction. This anisotropy can be caused by grain structures or gas bubbles in a material. Absorption is the conversion of acoustic energy into heat due to various mechanisms. The acoustic pressure in a solid can be generally expressed with [68]

$$p = p_0 e^{-\alpha d}, \quad (4.13)$$

where  $p_0$  is the pressure at the source,  $\alpha$  is an attenuation constant and  $d$  is the distance travelled by the wave. The effects of scattering and absorption can be combined in the attenuation constant  $\alpha$ . Generally, attenuation due to scattering is dominant in metals while in polymers likewise materials absorption is dominant [68].

For polyimide, the attenuation per wavelength ( $IL/\lambda$ ) is linearly dependent on frequency  $f$  at constant waveguide thickness [69]

$$IL/\lambda \propto f. \quad (4.14)$$

Conversely, at higher frequencies the waveguide thickness ( $th$ ) is also decreased for optimal energy capture, as will be discussed in Section 4.5.3, reducing the acoustic absorption in the waveguide.

$$th \propto -f. \quad (4.15)$$

Furthermore, the following relations are found from Qian et al. 1991 [69] (Figure 4.8):

$$IL \propto th^2 \quad (4.16)$$

at constant  $f$  and  $L$ ,

$$IL \propto f^2 \quad (4.17)$$

at constant  $th$  and finally

$$IL \propto L_\lambda = L_m/\lambda \quad (4.18)$$

at constant  $f$  and  $th$ . The proper relation between the insertion loss (IL), delay line length (L) and operating frequency (f) at optimum waveguide thickness ( $th$ ) is hard to predict. It suffices to conclude, delay line lengths of state of the art literature are best compared in terms of wavelengths ( $IL \propto L_\lambda = L_m/\lambda$ ), giving a conservative comparison as the  $th$  is presumed constant though in reality it will decrease. When the decreased waveguide thickness  $th$  is taken into account, the IL decreases a bit, leaving room for additional wavelengths of delay line  $L_\lambda$ . Still the results must be treated with caution.

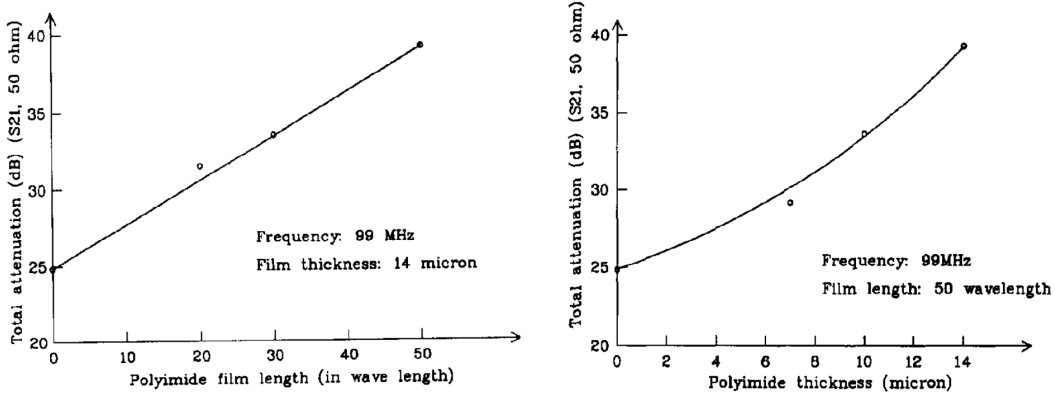


Figure 4.8: Influence of wght and L on IL from Qian et al. 1991 [69]. Used to derive the IL per wavelength per waveguide thickness.

### 4.5.3. Wave guiding layer considerations

By selecting the proper material properties and thickness of the wave guiding layer, the SAW can propagate in Love mode. For the wave guiding layer the Shear horizontal wave speed, TCE,  $\tan \delta$  and general properties as robustness, processability all play a similar role as described in Section 4.5.1.

#### Shear wave speed

Additionally, the shear horizontal wave speed of the wave guiding layer must be lower than the shear horizontal wave speed of the piezoelectric material [44] as mentioned in Section 4.2. Moreover, the shear wave speed of the waveguide and substrate be as low as possible as can be derived from Equation 4.19 by Wang et al. for the frequency sensitivity for mass-loading,

$$Sf \approx \frac{-4V_{sub}}{V_{wg}\rho_{wg}\lambda_{sub}} \quad (4.19)$$

[55], with  $V_{sub}$  and  $V_{wg}$  the shear horizontal wave speeds of the substrate and wave guiding layer respectively,  $\rho_{wg}$  the waveguide density and  $\lambda_{sub}$  the wavelength of the SAW in the substrate.

#### Thickness

The wave guiding layer thickness has an optimum for maximum energy transfer from input to output IDT. First, two coarse estimation methods for the optimum Wave Guide (WG) thickness are presented. Also, an estimation for the maximum WG thickness was found. These are included as quick estimators are valuable in design. Then measurement results proving this optimum for maximum energy transfer for several material combinations and operating frequencies are shown. These are valuable as reference for simulations.

A first coarse indication was determined by Stevenson et. al. (1993) [70], who relates optimum WG thickness to the WG material density. Empirically it is determined that materials with a density below  $10\,000\text{ kg/m}^3$  should be applied with a 3 to 12  $\mu\text{m}$  thickness while higher density materials should be applied more thin, 1 or 2  $\mu\text{m}$  thickness.



Wang et al. (1994) concluded, based on perturbation theory, that an optimal WG thickness exists for the 'quarter wavelength resonance' of the waveguide, leading to a WG thickness [55],

$$h_{wg-opt} = (1/4)(V/f)/\sqrt{V^2/V_{wg}^2 - 1} \approx (1/4)(V_{wg}/f) \tag{4.20}$$

with  $V$  the actual SH wave velocity,  $f$  the operation frequency,  $V_{wg}$  the wave guide layer SH wave speed.

The maximum thickness for mono-mode operation or zero order wave within the wave guiding layer can be estimated with equation 4.21 [48] from [71]:

$$h_0 = \frac{V_s V_l}{2f \sqrt{V_s^2 - V_l^2}} \tag{4.21}$$

with  $V_s$  and  $V_l$  the shear horizontal and longitudinal wave speeds of the wave guiding layer material respectively and  $f$  the excitation frequency.

In the literature, several experiments were done to determine the optimum in the wave guide thickness for maximum energy transfer from input to output IDT. For example the WG thickness vs insertion loss from Gizeli for a novolac WG on quartz is shown in Figure 4.9, from [72].

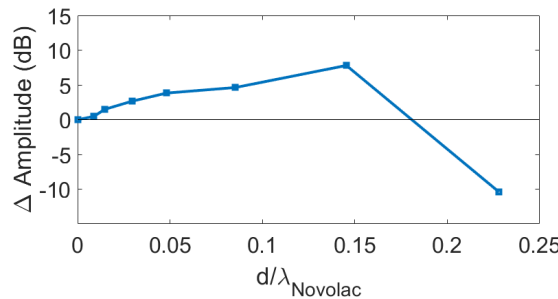


Figure 4.9: Measured change of signal transfer amplitude on a quartz device with a Novolac overlayer as performed by Gizeli et. al. [72]. The Novolac thickness ( $d$ ) is normalised to the acoustic wavelength in Novolac ( $\lambda_{Novolac}$ ). A clear optimum thickness is apparent where the signal transfer is largest.

Bender et al., measures an optimum PMMA WG thickness on a Love mode device with 40um wavelength, 100nm Cr/Au electrodes, 103MHz, metalised delay line path [73].

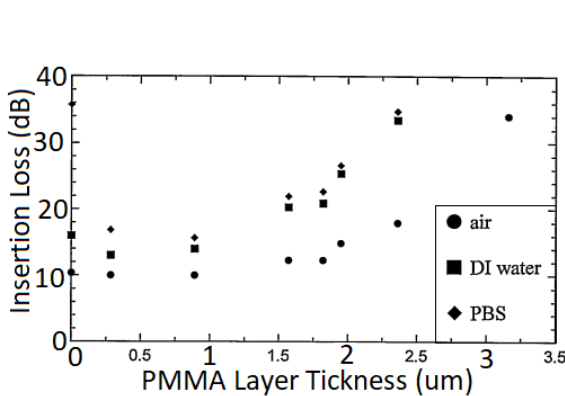


Figure 4.10: Measured IL while changing PMMA WG thickness [73].

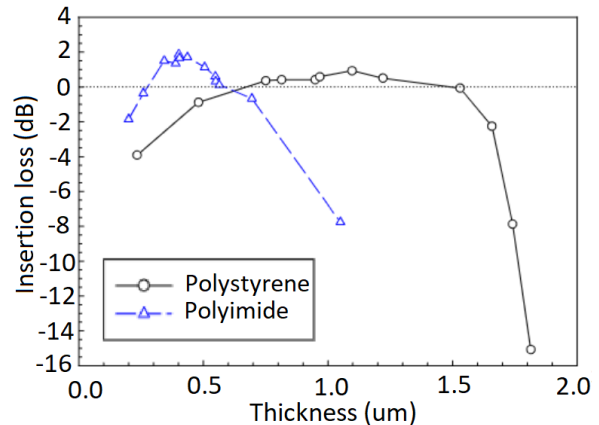


Figure 4.11: Optimum WG thickness for PI and PS at a fixed frequency of 103MHz [74].

Branch et al., measures at 103MHz, the optimum WGth for polyimide (PI) and polystyrene (PS) as in Figure 4.11 from [74].

#### 4.5.4. Spurious response

Additional wave modes, or spurious modes, can interfere with the signal of interest. On a SAW device, the input IDT excites the type of wave it was designed for as well as these spurious modes. Figure 4.12 gives graphical examples of deep bulk acoustic waves (DBAW) due to bulk acoustic waves (BAW), surface skimming BAW (SSBAW) or surface skimming bulk waves (SSBW), thickness resonance and leaked BAW modes. These and more signal detrimental effects are summarised in Table 4.1. The most relevant spurious modes and mitigation is discussed next. For a complete overview on this topic, the reader is referred to the book "Surface Acoustic Wave Devices and Their Signal Processing Applications" by Campbell et al, 1989.

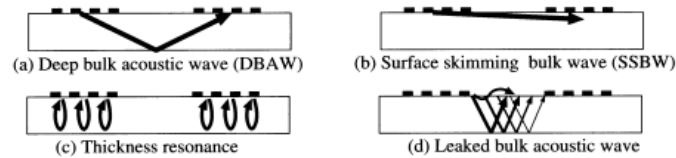


Figure 4.12: Several BAW causing spurious response in a SAW device. From [41].

#### BAW relates spurious response

To reduce the spurious response due to bulk waves, applying to DBAW and leaked BAW, it is common to roughen the substrate bottom surface [41]. The BAW energy is then scattered. Reflected BAW energy can be further reduced by attaching an absorbing material to the bottom. Applying a soft and electrically conducting material can even further reduce BAW reflections [65].

Also bulk related is thickness resonance, which occurs at integer multiples of  $2d_{\text{substrate}}/V_{\text{Bulkwavespeed}}$ . Usually this results in low frequencies not being picked up by the IDT with a set wavelength [41].

#### Signal path related spurious response

The substrate must ideally be terminated with low reflecting boundaries to avoid reflections from the substrate termination influencing the direct signal of interest. One option is to mould the die in a soft polymer holder [59]. Or a polymer stiff enough to acoustically match the substrate, as to avoid reflections, and allow high transmission from the substrate in the acoustically-lossy polymer to quickly dampen the acoustic wave. Another method to reduce the effect of substrate termination reflections is to ensure the SAW approaches the substrate termination under an angle other than  $90^\circ$ . The SAW is then reflected away from the IDTs [65].

Triple transit echo (TTE) occurs when a signal is reflected by the sensing IDT, then reflected by the actuating IDT and finally reaches the sensing IDT again. It can be reduced by placing oblique dummy electrodes or be eliminated by using 2 input IDTs and placing the output IDT between them [41].

Electrical feedthrough the direct electrical coupling of the excitation signal on the input IDT to the output IDT without acoustic propagation. It can be referred to as capacitive coupling. It can be reduced using guard electrode between IDTs, however, these guard electrodes induce additional reflections [41].

Beam steering is the effect that the SAW beam is not headed straight to the receiving IDT due to the anisotropic substrate. The SAW beam will have a tendency to align with a local maximum SAW velocity direction on a specific crystal cut. To prevent deterioration of device performance due to beam steering, the device should be designed to use a propagation direction along such a SAW velocity maximum [65].

Table 4.1: Signal degeneration causes to be kept in consideration in design.

Spurious response	Other signal degeneration
- Deep bulk acoustic waves	- Impedance matching
- Surface skimming bulk waves	- Interconnect parasitics
- Thickness resonance	- Diffraction
- Leaked BAW	- Beam steering
- Substrate termination reflections	
- Electromagnetic feedthrough	
- Triple transit echo	
- Electrode reflections	

## 4.6. SAW Electrical model

The crossed-field electrical equivalent model presented here was used to predict the optima for the aperture of the SAW device and peripheral (matching) circuit design. Several approaches to obtain an electrical equivalent circuit exist such as, but not limited to, the Butterworth-Van Dyke model [75], the Delta Function model [76], the Crossed-Field model [77] or the Impulse Response model [76].

These models differ mostly in how to evaluate the equivalent components, while the equivalent circuit topologies look similar. For the Butterworth van Dyke (BvD) model the equivalent circuit parameters are obtained from coupling of modes theory, perturbation theory or curve fitting from measurement data [75]. The Delta function model treats every single finger as a weighted delta function contribution to the transfer function. Summation of these delta functions gives the transfer function of an IDT [76]. The crossed-field model, derived from the Mason equivalent circuit treats each IDT as a three port network. Two ports are acoustic (to accommodate for the bidirectional function) and one port electric [76]. The derivation of this model that was originally described by Smith (et. al) 1969 [77] is given in Appendix E.

The resulting equivalent circuit of the crossed-field model, can be expressed by a static capacitance and a radiation conductance as is depicted in Figure 4.13. A, when the input and output IDTs are symmetrical, the equivalent circuit can be represented as shown in Figure 4.13. B, where the output IDT excitation source represents the arriving acoustic waves and is modelled with a current source causing a voltage over the output IDT and load [77].

The input admittance near the centre frequency is given by

$$Y_e(f_0) = \left. \frac{I_e}{V_e} \right|_{f_0} = G_a(f_0) + j2\pi f_0 C_T, \quad (4.22)$$

with the circuit elements, the total capacitance of an IDT  $C_T$ , the electrical characteristic impedance  $G_a(f)$  and  $B_a(f)$ . Near resonance,  $B_a(f_0) \approx 0$ , and

$$G_a(f_0) = 8\kappa^2 f_0 C_s N^2 \quad (4.23)$$

with the electromechanical coupling coefficient  $\kappa^2$ , centre frequency  $f_0$ , single finger pair capacitance  $C_s = C_0 * W$  (with  $C_0$  the single finger pair unit length capacitance) and the number of finger pairs  $N$  [77].

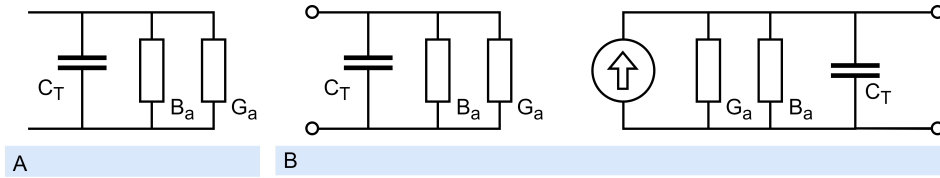


Figure 4.13: Equivalent circuit for a SAW sensor based on the crossed field model [77].

## 4.7. Readout

This work used an open-loop configuration to measure the phase shift at fixed frequency. The available measurands and measurement configurations are discussed here. The parameters that are available as measurand are frequency, phase, voltage amplitude and current amplitude. These measurands can be measured in open-loop or closed-loop configuration.

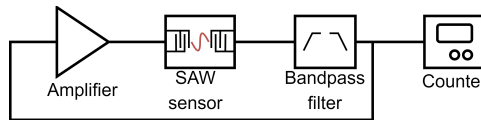


Figure 4.14: Schematic setup for an oscillator readout scheme, based on [78].

The most reported closed-loop solution is the oscillator, as in [78] for example. This solution feeds the sensor output signal back to the input via an amplifying component as in Figure 4.14. With careful design, the circuit starts to oscillate at a frequency where the total phase shift in the circuit is  $180^\circ$  and the total gain in the circuit is 0dB. This oscillation frequency must be set to the eigenfrequency of the SAW device. Any change

to the delay line (like mass loading) will cause a phase shift in the delay line. This phase shift will change the oscillation frequency. A drawback of the oscillator circuit is that only the frequency is directly detectable and it is hard to conclude anything on the insertion loss.

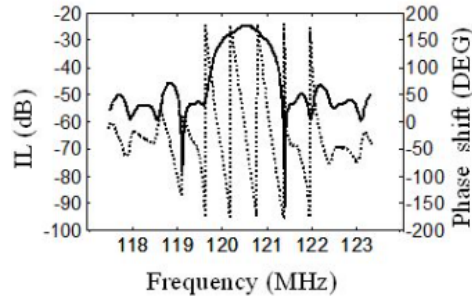


Figure 4.15: Typical transfer characteristic of a SAW device. At the resonance peak, where the insertion loss (IL) is smallest, the phase has a large shift. Taken from [40].

Phase noise limits the resolution of an oscillator circuit. As is shown in Figure 4.15, around the resonance frequency, where the insertion loss is minimal, the phase jumps several times. Phase noise can cause the circuit to jump to a different phase ramp, so that the same phase is achieved on a different frequency which makes interpreting the measurement impossible. When the SAW-device is designed for high frequency use for better sensitivity, phase shifts will jump more frequently (closer together) making the phase jumping due to phase noise more likely reducing the achievable resolution [40].

Open-loop solutions just give an input signal and measure the output signal, so no feedback to the SAW-component occurs. An often used open-loop technique is the vector network analyser (VNA) [40]. A large benefit of the vector network analyser is the abundance of information, all available measurands can be extracted. It comes at the cost of measurement speed. This abundance of information argument gives room to later reconsider the measurand after measurements were done. For this flexibility, the VNA was selected as measurement solution.

An alternative open-loop method using a mixer based phase detector to detect mass loading of the SAW-component delay line is described by Montagut [79] and is shown in Figure 4.16.

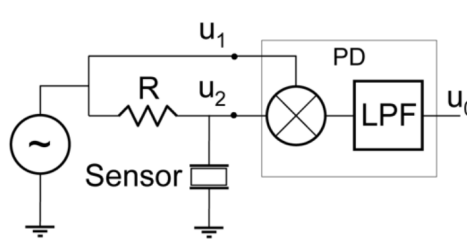


Figure 4.16: Mixer based phase detector to detect the phase shift of the SAW-component due to mass loading of the delay line. From [79].

### 4.8. Parameter dependence and design order

To enable a design phase that is avoiding design loops and iterations, the parameter dependence on variables is identified. Then, this is inverted to investigate how variables should be designed to satisfy the required parameter values.

The resulting design order is shown in Figure 4.17. Indicating for every variable, where design choices are based on and resulting in a design order for the following design phase. The figure can be read left to right for the design order. For every variable, the reasoning can be read from right to left by following the arrows leading to a variable in opposite direction. All influencing variables and output parameters can be identified. The figure is based on Figures F.1 and F.2 in Appendix F where the influence of variables on output parameters was identified. Figure 4.17 gives the designer a structured method to tackle design of a Love-mode SAW device.

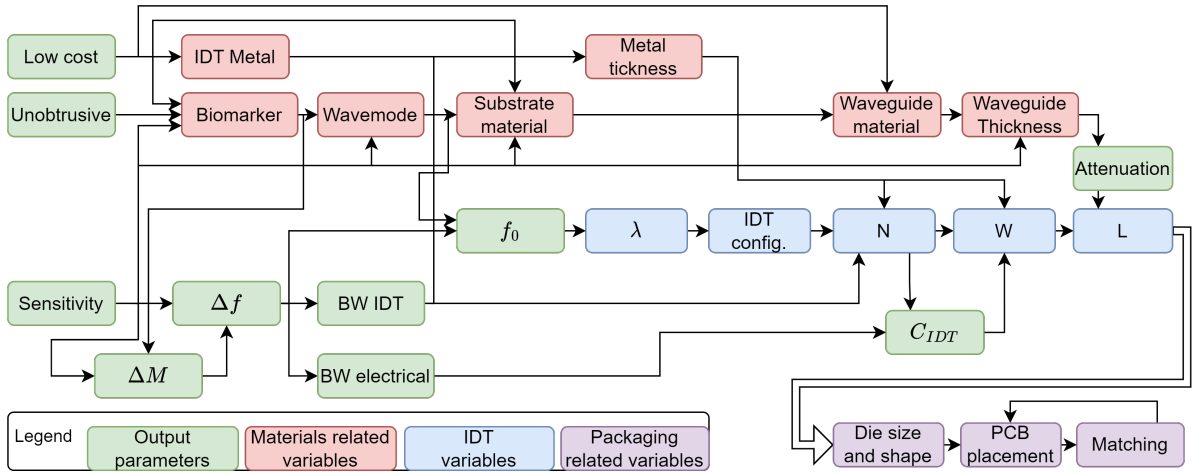


Figure 4.17: Variables and parameter relation and resulting design order. The parameters in green are set by the variables chosen. In design, this relation is inverted where the required parameter values are to be achieved by implementing the proper variable values. Resulting in a structured design order for this project.

### 4.9. State of the Art

The state of the art is summarised in Table 4.2, showing the most important variables as discussed previously in this chapter. In the table, works that use SH or Love-mode SAW have been included with an application in liquid or bio-sensing. Year or substrate and waveguide material were not selection criteria.

Previous work shows Love-mode sensors for biomarker detection have been attempted in the MHz frequency range. The number of finger pairs (N) is ranging from 40# to 80# with an exception using only 20#. The delay line length (L) is chosen most often around 100λ, though higher and lower values are both demonstrated. Aperture (W) is chosen broadly from 20λ to over 150λ.

Table 4.2: State of the Art design variables comparison.

Reference	Mode	Sub	State of the Art						
			WG	Biomarker	$f_0$ (MHz)	$\lambda$ (um)	N (#)	L (# * $\lambda$ )	W (# * $\lambda$ )
Alper 2017 [80]	SH	ST-Q	no WG	PSA	16.9	x	x	x	x
Alper 2012 [78]	SH	ST-Q	no WG	Bcl-2	16.8	300	20	40	20
Zijlmans 2021 [81]	Love	ST-Q	PMMA	CD-9	400	8	50	125	50
Raimbault 2007 [82]	Love	AT-Q	SiO2	viscosity	117.2	40	50	x	100
Johansson 2012 [83]	Love	LiNbO3	PDMS	flow	40	100	40	100	100
Gizeli 1992 [48]	Love	Y-Q	PMMA	no biomark	110	45	80	200	65
Tran 2014 [59]	SH	AlN	SiN	no biomark	211.25	24	45	104	167

## 5 | Design methods

For design, the finite element method (FEM) software with computer aided design (CAD) interface COMSOL 5.4 will be used to do predictions on device performance. Examples exist where the electrical equivalent model described in Section 4.6 is used using coupling of modes theory to do predictions on massloading and the effect of a waveguide. These models tend to be very complex. Using FEM software, after a good model is defined, much of the mathematical complexity is taken over by the software.

COMSOL is used to define a model for an eigenmodes study, very well suited for fast evaluation of the expected centre frequency, and a model for a time domain study giving a more complete view of the sensor input to output relation. Both are three dimensional models. The data generated by COMSOL is exported and data processing is done as much as possible in MATLAB to keep a better grip on what computations are exactly executed. A complete geometry model is not attempted as only the larger geometry already causes the computational cost to exceed the available budget. To gain more predictive value from a complete geometry model, the model complexity has to be increased much, adding studies on damping and reflections for example, even further adding to the computational cost.

Still for several design choices, mathematical models will be used for verification purposes or as main source. This refers mostly to capacitance calculations. And finally, the state of the art will be used, in some cases to put model results into respect to reality, or because models do not have proper predictive value for a specific case.

### 5.1. FEM modeling in COMSOL

First several aspects important to all COMSOL simulations are given attention. Then, the eigenmode model is set out. Afterwards, the time based model, that builds on from the eigenmode model, is presented.

#### 5.1.1. Meshing

To improve model accuracy and reduce computational complexity, the substrate and waveguide are defined using custom tetrahedral meshes. As the wave energy is supposed to be confined in the top part of the geometry, the degrees of freedom can be reduced by making a custom mesh with only high resolution where it is needed, at and near the waveguide layer. The Nyquist theorem states that any periodic signal must be sampled at least twice per period of the highest frequency component of the signal to enable recovery of the complete signal after sampling. This is often associated with time, but also true for signals in three dimensions. Therefore the mesh in COMSOL is set up respecting the Nyquist condition of having at least two sample points per wavelength.

To enable the envisioning of a higher excitation mode, the minimum mesh element size is chosen to obtain nine points per wavelength and the maximum element size must still contain five points per wavelength. These element sizes are applied to the free tetrahedral meshes of the WG and substrate.

For the electrodes, first a swept mesh is defined as it is more suitable for the high aspect ratio of these electrodes due to their extreme thinness in the nm order of magnitude. This swept mesh only has 1 element in the electrode thickness direction, which is fine as the electrode voltage is considered equal through the electrode. To ensure compliance with the WG and substrate, their meshes made next. The, by default, square swept mesh needs to have diagonals added by a convert mesh operator. This own designed mesh is more physically relevant than the standard meshing by COMSOL and gives a good understanding of the achieved model accuracy.

The maximum mesh size, that is still obtaining reliable eigenfrequency estimations, was tested by searching for eigenmodes using an extremely fine mesh and increasingly coarser meshes. A clear boundary on the mesh requirements was found as becomes clear in Figure 5.2 at a minimum mesh size of 5 points per wavelength. The effect of the mesh size on displacement and electric field is also visibly noticeable as in Figure 5.1.

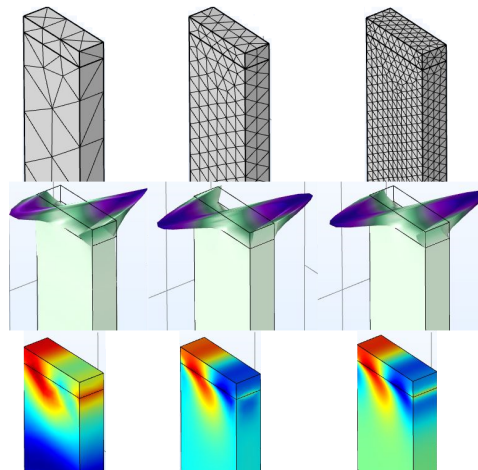


Figure 5.1: Showing the differences in mesh size and the effect on the displacement and electric field distribution after solving. Clearly, the very coarse mesh on the left causes a deterioration of information, but the middle (applied mesh in all other simulations) and extremely fine mesh on the right do not show clear differences in the results.

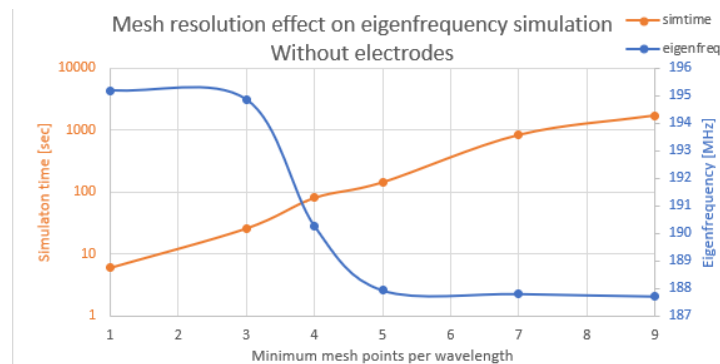


Figure 5.2: Effect of mesh size on found eigenfrequency with and without electrodes. The simulation with electrodes always stays quite accurate. When the electrodes are removed, large deviations from the most accurate simulations are observed. For both cases, the simulation time increases exponentially with increased resolution as can be seen on the logarithmic scale. As the impulse response simulations must sustain the wave over the delay line without electrodes, the latter without electrodes is the better simulation to adhere to. So the minimum mesh size element is chosen to obtain 9 points per period and the maximum size 5 points per period.

### 5.1.2. Crystal orientation

This section is paraphrased from the book 'Acoustic Technologies in Biology and Medicine' by A. Ozcelik, R. Becker and T.J. Huang (2023) [84] as the author of this work contributed the following section to the chapter 'Acoustic Biosensors' of the book.

The crystal orientation of some piezoelectric materials matters for their piezoelectric behaviour. As discussed in Section 4.5.1, this is the case for quartz. Euler identified one linear coordinate system can be converted to another with just three rotations about the origin [85] (referenced by Whittaker [86]). These three rotations can be around any of the original axis with as only constraint that two consecutive rotations are not about the same axis (two possibilities are a X-Y-Z or a Z-X-Z rotation). This leads to twelve ( $3 * 2 * 2$ ) possible conversion options who are equivalent but not equal [87].

A commonly used Euler rotation is Z-X-Z, which happens to also be applied in the rotated system function of the finite element method (FEM) computational software product COMSOL. In this Z-X-Z system, first a rotation about the Z axis in the XY plane is done. Secondly, a rotation about the new X axis is performed. Finally, a rotation about the new Z axis is done. To make clear the rotations are about the new axis every time, the Z-X-Z transformation can also be represented by z-x'-z''.

Common symbols for the Euler angles are  $\phi, \theta, \psi$ . Realise that these symbols do not reveal what Euler rotation set is used. Another set of symbols sometimes used is  $\alpha, \beta, \gamma$  as used in COMSOL and Figure 5.3. Specifically for SAW applications, the base orientation of the material of interest has to be rotated to its final orientation in the application.

The cut angle reasoned from the point of view of the crystal cutter is generally not coinciding with the

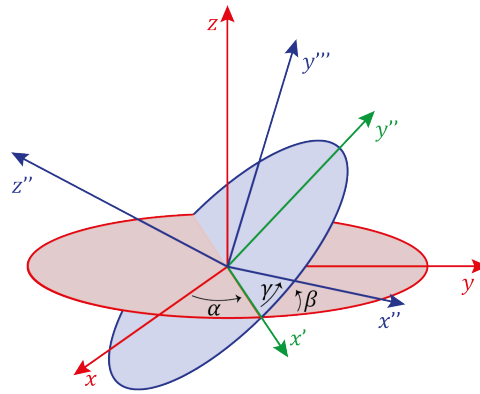


Figure 5.3: Example of the application of Euler angles Z-X-Z sequence by rotating over  $\alpha$  (rotate over the xy-plane),  $\beta$  (tilt the xy-plane),  $\gamma$  (rotate over the new xy-plane) respectively.

Euler angle system convenient for the engineer [88][89]. This implies caution is required when doing calculations or simulations with a piezoelectric material and the conversion from the material specific cut angles to Euler angles must be executed with care.

A practical example is the often applied piezoelectric material quartz. It has a crystalline structure that is build up from unit cells consisting of three SiO<sub>2</sub> molecules that are forming a helix [90]. This helix can be right-hand or left-hand rotating [91][92]. These, both naturally occurring, variants are referred to with RH-quartz and LH-quartz respectively. Then the cuts made in this crystal follow two conventions, the Institute of Radio Engineers 1949 (IRE 1949) [93] and the newer Institute of Electrical and Electronics Engineers 1978 (IEEE 1978) [94]. An example is the ST-cut quartz. This is, for RH-IEEE 1978 quartz, a Y-cut (XZ-cut plane) where the cut plane is 42.75° rotated over the X axis. To convert this to Z-X-Z Euler angles, no initial rotation over Z is required, then 90° rotation over the Z axis is required to get a XZ-cut plane and an additional 42.75° Z rotation is required to get to the ST-cut. And no final rotation over Z is done. This leads to Euler angles [0;90+42.75;0] [89] as illustrated in Figure 5.4.

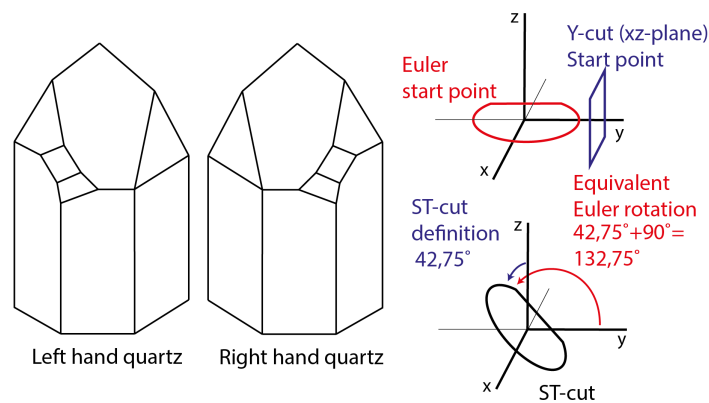


Figure 5.4: Practical example of the conversion between the historically used RH-IEEE 1978 ST-cut quartz definition and the corresponding Euler angles. The drawn crystals are aligned with the axis so a clear indication can be found of how the ST-cut wafer is oriented in a quartz crystal.

While for another often applied material, lithium niobate (LiNbO<sub>3</sub>), the cut angles are again defined differently. The crystal is oriented along the Cartesian axes according to the IRE 1949 convention [93]. An example of a cut is then the X-cut LiNbO<sub>3</sub>, which implies the crystal is cut perpendicular to the X axis (the same can be applied to the Y and Z axis). A second naming option for more freedom in cut definition is for example, XZ 30°-LiNbO<sub>3</sub>. Here, the cut plane, perpendicular to the first axis (X implies the YZ-plane) is rotated counter clockwise around the second axis (in this case Z). In this notation also any other combination of axes is possible like the XY-, YX-, YZ-, ZX- and ZY-cut [95]. With this knowledge, the Euler angles can be derived.



### 5.1.3. Unit wavelength eigenmode model

To determine a suitable operation frequency that supports the desired wave mode, an eigenmode simulation model is built. To reduce the degrees of freedom, only part of the geometry is simulated and artificially extended using periodic boundary conditions for all lateral surfaces [96]. The top is free and the bottom is fixed with a fixed constraint boundary. This also reduces possible modes, further increasing simulation efficiency. Perpendicular to the direction of propagation, the desired wave mode is invariant, so to reduce the number of unknowns and the number of supported (unwanted) wave modes, a width of only a fraction of the wavelength is chosen. As a Surface Acoustic Wave (SAW) amplitude decreases quickly into the substrate medium, even more so for a Love wave mode, the thickness of the substrate model only has to be several wavelengths instead of a wafer thickness. So for the 1978 IEEE RH Quartz with x-direction propagation, the eigenmode model geometry is given in Table 5.1. The included model physics for the unit wavelength eigenmode model is, the piezoelectric module. This is using the electrostatics and mechanical physics modules.

Then the model is set-up to find eigenmodes between the lowest and highest possible frequencies. After solving, manually, the found solutions are visually judged on being a Love-mode or not. Generally, two Love-modes are found at very close frequencies, one mode is shown in Figure 5.5, on the left. The other mode is a quarter wavelength shifted and thus deemed equivalent.

Table 5.1: Geometry eigenmode model

Length	$\lambda$	$8\mu\text{m}$
Width	$\lambda/3$	$2.7\mu\text{m}$
Thickness	$\lambda*10$	$80\mu\text{m}$

### 5.1.4. Time impulse simulation

Building on from the unit wavelength eigenmode model, a three dimensional slice of the delay line with IDTs is constructed. An impulse is given on one IDT and the resulting deformation and electric field is then monitored. The electric field is recorded on a second IDT, separated several wavelengths from the actuating IDT.

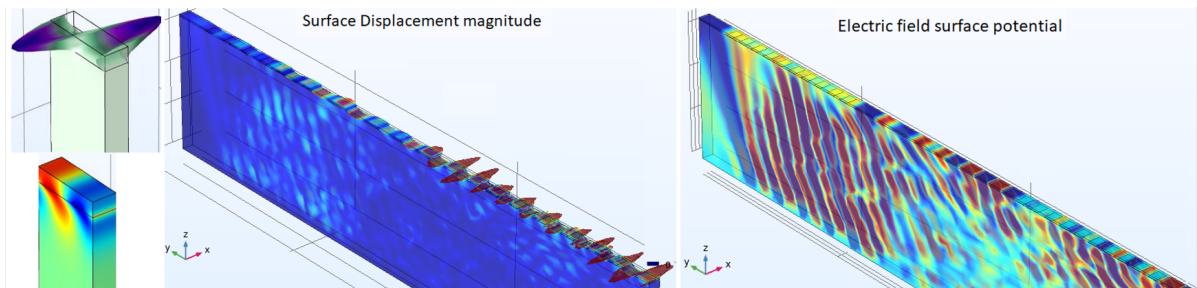


Figure 5.5: Visually checking if displacement matches Love mode SAW. Left shows the 'unit wavelength' model, up displacement, down electric field. Then the middle and right show the 'time impulse' model displacement and electric field respectively. Only horizontal, no out of plane, displacement is found. The waves have a wavelength of  $8\mu\text{m}$ . These findings support this mode found in the simulations behaves like a Love mode SAW.

The impulse is given as a single sample at unit voltage. The sample time interval or time step then determining the maximum detectable frequency according to Nyquist. The exact desired time steps should be forced, otherwise, COMSOL will make a too large time step causing an error which is not tolerable. Then the solver will take smaller steps but the error is not compensated anymore. So for the desired single frequency time simulations, the automatic Time-Dependent Solver setup is not suitable. Instead, for time varying or harmonic signals, strict time steps or manual time steps should be used. The measurement time then determines the lowest frequency measurable.

The meshing is just as unit wavelength model. Periodic boundary condition is still used for the planes parallel to the wave direction of propagation. Absorbing boundary condition are used on the lateral faces perpendicular to the wave direction of propagation. Terminals are used for electrical contacts. A voltage is forced on the actuating electrodes (0V and 1V for 1 time sample) and 0V for the ground electrodes on the actuating side (not differential actuation). The sensing electrodes all have a charge Q of 0C fixed on them. Then the changing electric field in the piezoelectric substrate causes voltage changes on the sensing

electrodes which are measured differentially. The mechanical and electrical waves can be seen travelling in Figure 5.5, right two renders.

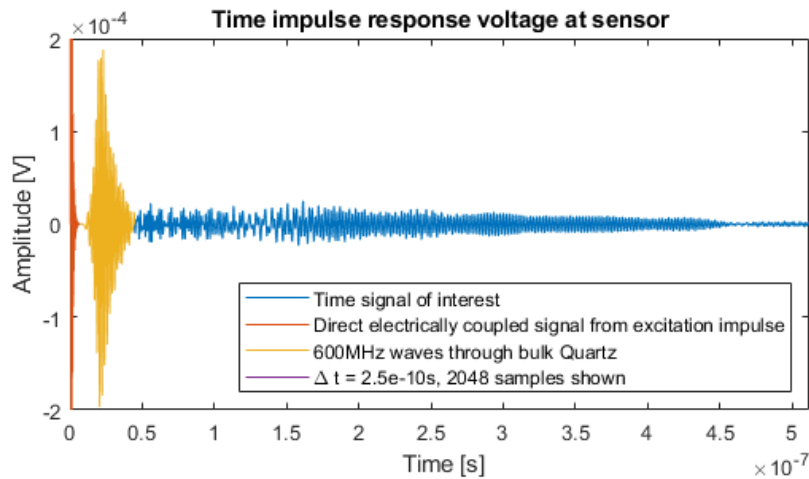


Figure 5.6: Resulting voltages on the sensor side after a 1 sample impulse on a slice. Clearly, the direct voltage feedthrough, the substrate bulk waves and waveguide waves can be distinguished. The zones were also investigated with separate FFTs to investigate their contribution to the total frequency response.

The resulting time data is exported and using an fast Fourier transform (FFT) algorithm in MATLAB, the frequency spectrum is determined after applying a time window to reduce high frequency artefacts. An example of the time data is shown in Figure 5.6. This results in a spectrum as Figure 5.7.

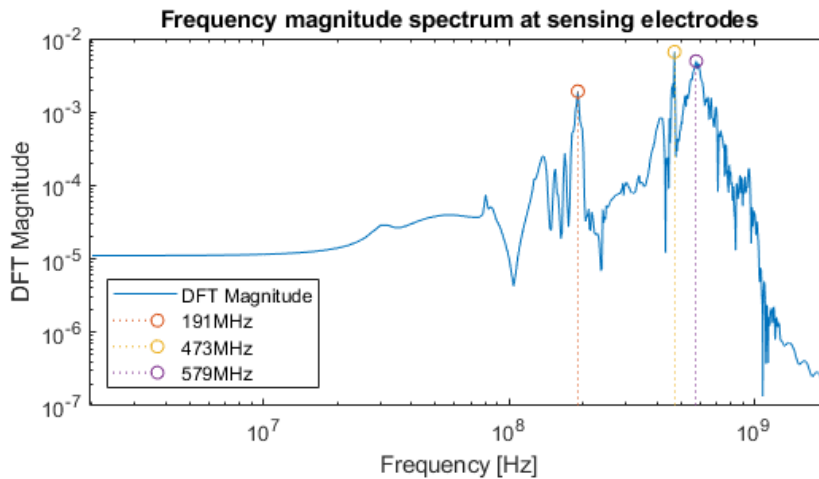


Figure 5.7: FFT of the time impulse signal. The direct coupled impulse is removed before FFT. Also, the first and last 20 samples are attenuated with a Hanning window.

Then manually, the transmission bands centre frequencies are identified and stored, together with their insertion loss. This data is then used for example in determining the effect of different waveguide thickness (Section 6.5).

#### Comparing unit model and time impulse model

The time impulse model results are verified to demonstrate Love-mode operation by comparing it to the unit model and by visual inspection. The 'unit wavelength eigenmode' COMSOL model results are compared to the passband frequencies found in the 'time impulse' model, and as Figure 5.8 shows, these coincide nicely, giving some support the found passbands correspond to the Love mode SAW. The simulations are also visually inspected as in Figure 5.5, where the displacement and electric field further confirm the likelihood of a Love mode SAW being simulated. The time impulse electric field does show a set of waves travelling through the quartz bulk and waves captured at the PI-Qz interface. This might give rise to the two separate passbands found in the time impulse simulation frequency spectrum for most WG thicknesses.

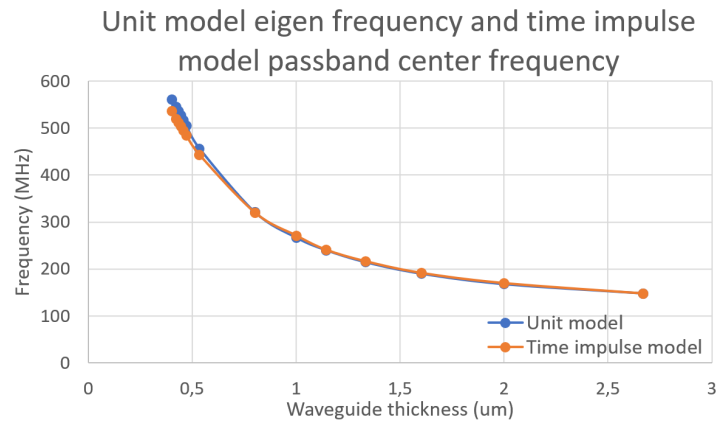


Figure 5.8: Comparing the found eigenfrequencies with the unit wavelength eigenmode model to the passbands found using the time impulse model. The good agreement in frequencies reinforce the time impulse model shows the Love mode pass band.

### Crystal orientation time impulse model

To indicate the influence of the crystal orientation, Figure 5.9 shows altering the crystal orientation has little influence on the first passband, whereas the second passband is much shifted in centre frequency. This reinforces the hypothesis in the previous section (Section 5.1.4) that a waveguide eigenmode and a SSBW are both travelling at different speeds (and thus frequency) in the simulation. The  $+42.5^\circ$  crystal definition corresponds best to the SSBW speed in the literature that predicts a SSBW mode in quartz around 600MHz (equation 4.9, evaluated in Section 6.5).

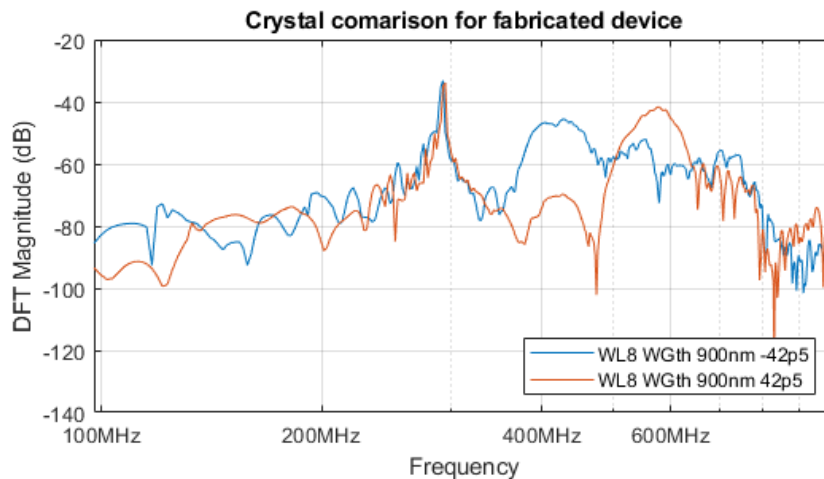


Figure 5.9: DFT magnitude plot of same geometry with differing crystal orientation definitions.

## 5.2. Capacitance estimation

The IDT capacitive value is estimated for matching and IDT variable design using a COMSOL model which is verified using equations. First the COMSOL model is described. Then the equations are explained. Finally, their results are compared in Table 5.2.

### 5.2.1. Static capacitance COMSOL model

For IDT static capacitance a model with just a single IDT pair is created. The geometry consists of a quartz block with a polymethyl methacrylate (PMMA) overlayer, with water on top and aluminium electrodes in an air filled sphere. The included model physics is the piezoelectric module, which is using the electrostatics and mechanical physics modules. Then a unity voltage is applied to one electrode, and the difference in charge is stored. This gives an estimation of the capacitance using  $C=Q/V$ .

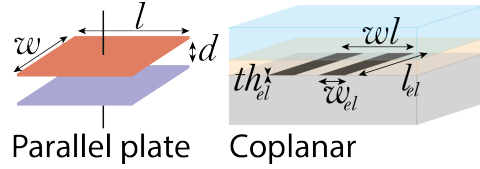


Figure 5.10: Dimensions for the capacitance conformal mapping based MATLAB calculation and COMSOL model calculation.

**5.2.2. Static capacitance calculation**

Using the derivation from [97] which are based on equations derived using conformal mapping for use in computer aided design software (CAD) [98], estimations are made for the capacitance of finger pairs. This still excludes the coupling between the piezoelectric substrate and the electrodes, which is included in the COMSOL model. This is expected to have limited impact but must be investigated. The full description of the equations that were implemented in MATLAB are included in Appendix D. The equations determine the capacitance between co-planar electrodes for each surrounding medium separately as illustrated in Figure 5.11.

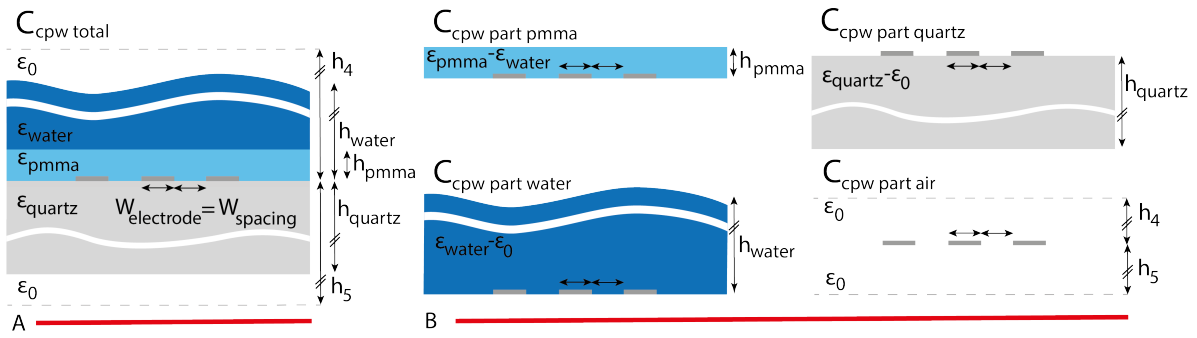


Figure 5.11: A) Geometry used to calculate the capacitance of a coplanar capacitance in multiple dielectric layers using conformal mapping. B) Decomposition of this geometry used to estimate the capacitance of a coplanar capacitor in multiple dielectric layers. Based on [98].

Table 5.2: Compare the derived capacitance from the CAD equations and from COMSOL. The dimensions are explained in Figure 5.10. For parallel plate, square area chosen to reduce fringing inaccuracy. Dimensions chosen close to single finger area to stay in the same order of magnitude. In COMSOL, 1 plate connected to ground, the other to 1V. Then using  $Q=C*V$ , follows  $C=Q/1$ , the charge on 1 plate is taken. The parallel plate contribution of the CPW capacitance is added at a 50nm electrode thickness to show its value is negligible compared to the total capacitance. This indicates most energy will be in the field lines travelling through the elliptic field lines, half of which perturbate the Quartz, exciting the piezoelectric effect.

Capacitor geometry	Dielectric	Dimensions (PP: $w, l, d$ ) (CP: $w_{el}, l_{el}, wl$ )	Capacitance Mathematical derivation	Capacitance COMSOL
Parallel plate (PP)	Vacuum	$20\mu\text{m}, 40\mu\text{m}, 0.8\mu\text{m}$	8.85fF	11.2fF
	PMMA	$20\mu\text{m}, 40\mu\text{m}, 0.8\mu\text{m}$	26.6fF	33.7fF
Coplanar (CP)	Vacuum	$2\mu\text{m}, 50\mu\text{m}, 8\mu\text{m}$	8.64fF	10.9fF
	PMMA	$2\mu\text{m}, 50\mu\text{m}, 8\mu\text{m}$	25.9fF	32.8fF
	Quartz-PMMA-water	$2\mu\text{m}, 50\mu\text{m}, 8\mu\text{m}$	135fF	45.4fF
	Piezoelectric coupling - Quartz-PMMA-water	$2\mu\text{m}, 50\mu\text{m}, 8\mu\text{m}$	-	46.4fF
Coplanar PP contr	PMMA	(CP, PP contr.: $th_{el}, w_{el}, l_{el}, wl$ ) $50\text{nm}, 50\mu\text{m}, 8\mu\text{m}, 2\mu\text{m}$	0.26fF	

The resulting calculated and simulated capacitance values are shown in Table 5.2. These are in reasonable agreement. This model and calculation is then extensively used for determining the impedance of an IDT structure as is treated in Section 6.6.

# 6 | Design

In the design, first the materials are chosen. This is done based on comparison of material properties, availability and microfabrication process compatibility. Then the IDTs are considered and choices are made based on simulations and calculations as discussed in Chapter 5 and state of art work as presented in Table 4.2. Finally, the over all PCB integration and sensor integration is considered.

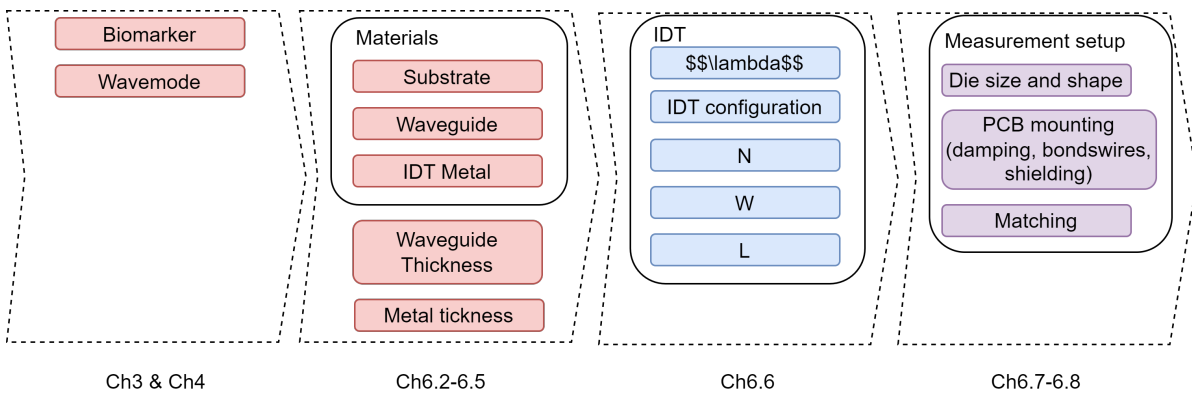


Figure 6.1: Design order sections

## 6.1. Requirements

The design must lead to a prototype adhering to the requirements stated in Section 1.6 of which are shortly repeated here. The two main requirements, design for sufficient sensitivity to qualitatively detect CD9 in liquid samples, while using the materials and processes as available at Else Kooi Lab at TU Delft. This largely affects Section 6.2.

For the secondary requirements, the designed devices should allow for rapid device characterisation. Then both the electrical properties as the PCB design in Section 6.6 and Section 6.8.1 should be such that the designed devices are easily measured by existing equipment. As second and third, the device should be able to cope with liquid samples and it must be a robust platform allowing for transport and repeated measurements. These are mainly a challenge for Section 6.8.

## 6.2. Substrate Materials

Materials that can be considered for the substrate will all have to be piezoelectric as explained in Section 4.3. Several piezoelectric materials are gathered and compared. The important performance determining variables, including crystal orientation, electromechanical coupling coefficient, shear horizontal wavespeed, TCF and  $\tan \delta$ , were discussed in Section 4.5. In Table 6.1, the relevant material parameters are listed for comparison. In the subsequent subsections, more details on the materials are described.

### ST Quartz

Stable temperature quartz (ST-Quartz) is named for its zero TCF for reighly waves. It is a robust material compared to other piezoelectric materials.

ST-Quartz has the very good property of having a wave propagation orientation with a SH mode that has only SH displacement, no displacement in the out of plane axis which indicates a pure SH-SAW mode [99]. This is of importance to reduce insertion loss by coupling of the SAW to the liquid sample in the sensor application.

ST-Quartz has a relatively low electromechanical coupling coefficient  $\kappa^2=0.14$  and propagation speed=5000m/s for ST-Quartz 90xX (with crystal orientation  $[0, 132.75^\circ, \Psi]$  with  $\Psi = 90^\circ$ ) [99].

Table 6.1: Substrate material options and summary of most relevant material properties. From top to bottom, density  $\rho$ , shear wave speed  $v_S$ , electromechanical coupling coefficient  $\kappa^2$ , temperature coefficient for frequency TCF, cost per wafer, if the substrate allows for pure or only leaky SH modes and finally if the material can be considered robust. The values are gained from COMSOL, granta Edupack and literature cited in the text.

		Substrate material		
		Quartz (ST or AT)	Lithium Niobate LiNbO3	Lithium Tantalate LiTaO3
$\rho$	(kg/m <sup>3</sup> )	2170	4647	7465
$v_S$	(m/s)	5050	4800	4200
$\kappa^2$	(%)	0,14	16	5
TCF	(ppm/K)	ST: 40, AT: 10	-80	-35
Cost/wafer	(€)	50	70	?
Pure SH mode		pure	leaky	leaky
Robustness		Very robust	Thermoshock	Thermoshock

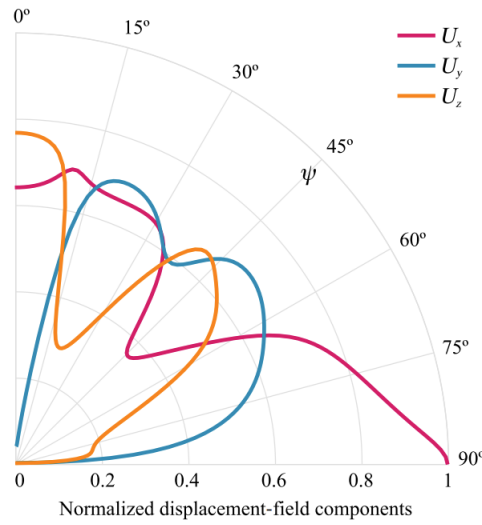


Figure 6.2: Surface displacement in ST-quartz for the same ST-Quartz surface but different propagation direction  $\Psi$ , from [99].

Although the TCF is zero for Rayleigh waves in AT and ST cut quartz [40], for SH mode operation, the substrate is rotated and for the SH polarised wave mode in ST-Quartz, a TCF around 40ppm/K is present (TCF=10ppm/K for AT-cut quartz) [40][56]. Still the WG introduces a WG-thickness dependent TCF [56][100] and a zero TCF design can be attempted by matching proper waveguide material that has balancing TCF at maximum sensitivity for some optimal waveguide thickness.

The pure SH wave mode in ST-Quartz is however a leaky SSBW [65], so, energy leaks into the bulk when the WG-layer does not properly trap the wave energy in Love mode operation.

### LiTaO3

Lithium tantalate (LiTaO3) is a much higher  $\kappa^2$  material with  $\kappa^2 \approx 5\%$ , it supports a leaky SH wave  $v_S = 4200\text{m/s}$  (no pure SH mode [101]) [102]. It has a TCF of around -35ppm/K [40][102]. Moreover, it has pyroelectric properties, creating a current wased on temperature changed, further complicating practical use [103]. Also, it is generally a fragile material as compared to quartz [40]. Careful handling required. It has a density  $\rho = 7465\text{ kg/m}^3$  and a refractive index of about 2.2 so a permittivity of  $\epsilon_r = 2.2^2 \approx 4.8$  [104].

### LiNbO3

Lithium niobate (LiNbO3) is another widely applied substrate material for SAW devices with a high electromechanical coupling coefficient  $\kappa$  compared to Stable Temperature cut quartz (ST-cut quartz) of  $\kappa^2 \approx 16\%$ . Its density  $\rho$  is  $4647\text{ kg/m}^3$  and its refractive index is 2.3 [105]. It also shows pyroelectric properties [106].

It has a TCF reported around -80ppm/°C and only a leaky SH-mode is supported with a velocity of  $v_S = 4800\text{m/s}$ . Lithium niobate is very sensitive for thermal shocks [40]. As the material is not robust in this sense,

careful handling is required making this material less suitable for a low cost application.

### 6.2.1. Substrate material conclusion

ST-cut Quartz is selected as substrate for its high mechanical stability to relax fabrication requirements and ability to support pure SH mode SAW to relax design requirements. Both contribute to lower sensor fabrication cost. Though LiNbO<sub>3</sub> and LiTaO<sub>3</sub> both have higher  $\kappa^2$ , this does not weigh up to the mechanical instability. Furthermore, the positive TCF of Quartz might be compensated for by the waveguide material as those might have negative a TCF.

## 6.3. Waveguide materials

For waveguide materials, materials which are reported to be suitable are collected. These can be roughly grouped in metals, ceramics and polymers. The investigated materials are summarised in Table 6.2. Metals are not suitable as they would need an additional passivation layer to prevent shorting the IDTs. Gold has very good biochemical coupling properties so it is included in the table for completeness. The included ceramics are aluminium nitride (AlN), zinc oxide (ZnO) and amorphous silicon dioxide (SiO<sub>2</sub>). Finally, several polymers were considered, these are polymethyl methacrylate (PMMA), polydimethylsiloxane (PDMS), polyimide (PI), polystyrene (PS) and the photoresist Novolac.

As more extensively discussed in Section 4.5.1, the most relevant material properties for the wave guide material are shear wave speed  $v_s$ , the damping  $\tan \delta$  and TCF. As explained in Section 4.3, the waveguide  $v_s$  should be lower than the  $v_s$  of the substrate. And Section 4.5.1, explains the waveguide  $v_s$  should be as low as possible. TCF should be low as possible or optimised in combination with the substrate material, see Section 4.5.1. Finally,  $\tan \delta$  should be low as possible, see Section 4.5.1.

Further, the cleanroom compatibility (CR-comp) and bio compatibility (bio comp) are considered. Material properties were extracted from literature, Ansys granta edupack and COMSOL material properties. Also some additional material properties are considered, such as, density  $\rho$ , Young's modulus E, Poisson's ratio  $\nu$ , to calculate the shear wave speed using equations 4.7 and 4.8 when it could not be reliably found in literature. The most relevant materials are discussed in the next subsections.

Table 6.2: The most relevant materials and their parameters for the SAW device waveguide design. From top to bottom: The reported in literature and calculated shear wave speed  $v_s$ , loss coefficient  $\tan \delta$ , relative permittivity  $\epsilon_r$ , density  $\rho$ , Young's modulus E, Poisson's ratio  $\nu$ , cleanroom (CR) compatible (comp) or contaminant (cont) and finally bio-compatibility (++ good, - bad). The values are gained from COMSOL, granta Edupack and literature cited in the text.

	Waveguide material								
	PMMA	PDMS	PI	PS	Novolac	SiO <sub>2</sub>	ZnO	AlN	gold
$v_s$ lit (m/s)	1100	100	-	-	-	3700	2558	5600	-
$v_s$ calc (m/s)	950	16	920	1050	1110	3690	3730	6440	1190
$\tan \delta$	0,0179	high	0,0193	0,0175	0,0823	-	-	30E-6	0,018
$\epsilon_r$	3	2,7	4	2,4	3,27	4,2	8,3	8,6	-
$\rho$ (kg/m <sup>3</sup> )	1180	1080	1330	1040	1050	2200	5670	3260	19300
E (GPa)	3	0,00075	3,1	3,2	3,5	70	210	338	78
$\nu$	0,4	0,49	0,4	0,4	0,35	0,17	0,33	0,25	0,42
TCF (ppm/°C)	-74/ $\mu$ m	-	-166/ $\mu$ m	-	-	-	-25/ $\mu$ m	-60/ $\mu$ m	-
CR-comp	comp	comp	comp	comp	comp	comp	cont	comp	cont
bio-comp	++	+	++	?	?	?	-	?	++

### 6.3.1. Metals

As already mentioned, metals are generally not suited due to the double function of the waveguide layer of protecting the IDTs from the liquid samples. So metals can only be used together with an additional passivation layer, which could be a polymer or ceramic. Gold is included due to its biocompatibility and superior biochemical coupling properties.

### 6.3.2. Ceramics

Many of these materials are standard cleanroom materials, making them very attractive for a low cost robust proces. Unfortunately, generally, the shear wave speed of ceramics is quite high, making them often

unsuitable as waveguide layer.

For these amorphous materials, it should be considered, poly crystalline materials have huge losses at frequencies with wavelengths comparable to their grain size. This occurs in the few MHz range [70].

#### SiO<sub>2</sub>

Silicon dioxide (SiO<sub>2</sub>), is a regularly used micro fabrication material. It is a good electrical insulator and chemically stable in contact with water [40]. It is a hard elastic material with low acoustic losses [48]. It is build up from the same molecules as quartz, but has a lower acoustic speed then crystalline quartz due to the amorphous structure of SiO<sub>2</sub> [107]. It should be noted the shear wave velocity is dependent on deposition parameters [108].

The TCF is about -3ppm/°C, at a SiO<sub>2</sub> layer thickness around 2.5μm and in the range between 25 to 40 °C [108].

#### ZnO

This material has a density of 5670 kg/m<sup>3</sup> and a phase velocity of 2558 m/s and a temperature coefficient of -25 ppm/°C [96]. Using nano-rod structures, it is possible to hugely increase surface area, possibly enabling higher sensitivity [96]. Unfortunately, it can dissolve in water and is considered a cleanroom contaminant [109] [40].

#### AlN

This sputtered or Chemical Vapour Deposited material has a phase velocity of 5600 m/s, a density of 3260 kg/m<sup>3</sup> and TCF of -60ppm/°C. It is an extremely hard material often used as etch stop or physical protection layer. Its robustness making it an interesting option.

### 6.3.3. Polymers

These often spincoated or molded materials have, generally speaking, lower shear wave speeds. The low  $v_s$  is very beneficial, but comes at the cost of generally higher losses (higher  $\tan \delta$ ). These relaxation losses of a polymer wave guide material can be very significant for soft materials such as PMMA with 200dB/cm attenuation [70].

As there are ample polymer variants available, Ansys Granta Edupack software material database was used to make a selection of the most suitable materials. A plot was made of polymers with the shear velocity set against the loss coefficient. Then materials of interest are the materials which are towards the lower left corner, low  $v_s$  and low loss. This plot is shown in Figure 6.3. Then materials that are cleanroom compatible are selected. These are discussed in the next sections.

#### PMMA

Polymethyl methacrylate (PMMA), a polymer which is spin coated on the wafer. The acoustic wave velocity is rather low at 1100 m/s, it has a density of 1.18 kg/m<sup>3</sup>. The material is cleanroom compatible. It is reported that PMMA has a large relaxation loss of 200dB/cm. This is however not problematic as long as the waveguide layer is not too thick, then the wave energy is captured at the surface of the substrate and is less affected by the waveguide losses [70]. TCF is negative. For any overlayer, the TCF is heavily thickness dependent. From the results from Harding et. al. 1997 [108], it can be deduced the TCF/(1μm PMMA thickness) is -73,9 ppm/°C/μm. Note that this value is only relevant if a PMMA layer of about 1.5μm thickness is used in a temperature range between 25 and 40°C. It can be concluded the negative TCF of PMMA has a beneficial effect if used together with a substrate with positive TCF.

Maarten Zijlmans reported issues in adherence between quartz and PMMA when dicing [81]. This is also considered in the material choice.

#### PDMS

Polydimethylsiloxane (PDMS) is currently a widely applied elastomer in organ-on-chip research and is therefore interesting to investigate as waveguide material. It is an easily processed, transparent, elastic, biocompatible material [110]. Few publications are available on the acoustic wave velocity this supposedly is due to the very high absorption losses in the material [83] making it not useful as waveguide material despite the low acoustic velocities mentioned of 1030m/s (longitudinal acoustic velocity) and 100m/s (shear wave velocity) [111]. The reported absorption losses are given by attenuation constants  $\alpha_L, \alpha_S$  and are 200/m and 10<sup>5</sup>/m for longitudinal and shear waves in PDMS respectively [112].



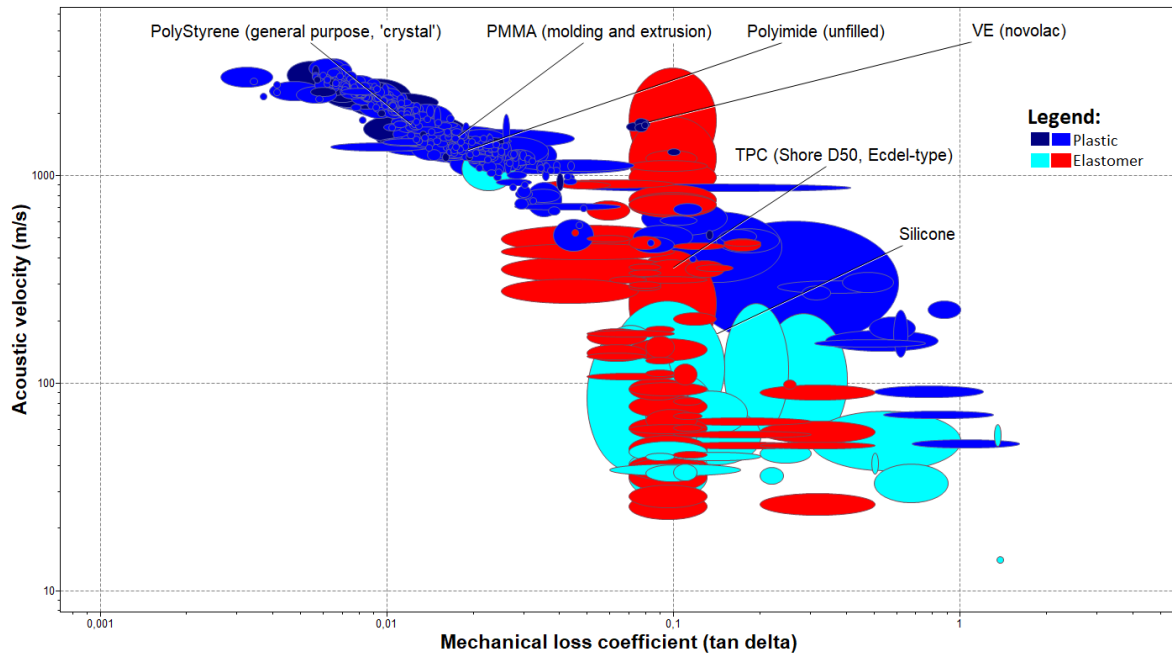


Figure 6.3: Selection of materials with potential use as waveguide material showing a clear trade-off between acoustic velocity (low as possible) and mechanical loss (also as low as possible). The figure is created with Granta Edupack materials database.

#### Photoresists

Novolac and SU-8 are photo resists. These polymers are very commonly used in the cleanroom. A big advantage is the material is directly patternable by means of UV-light exposure. For photo resists however, the long term stability is not important at all. So in this application, a very careful investigation on the long term stability of the material would be required.

#### Polyimide

Polyimide (PI) is a hard, translucent polymeric material. Several types of polyimide (PI) are commercially available. Of these types, multiple are reported to be a biocompatible material (low cytotoxicity and high stability in chemically harsh environments), even suitable for long term implants. There are special types of PI available that are photosensitive while other types are not. These photosensitive types are more prone to water absorption changing the material's mechanical properties (stretching and plasticising effects). These effects can be mediated with additives [113]. Also, work is published showing little difference in water absorption between photosensitive and non-photosensitive PI [114]. It can be concluded that if PI is to be applied, careful selection of a suitable type and manufacturer is required.

PI has a negative TCF, dependent on the applied thickness. Around a thickness of  $0,8\mu\text{m}$  and in a temperature range of 10 to  $80\text{ }^\circ\text{C}$ , a  $\text{TCF}/(1\mu\text{m PI thickness})$  of  $-166\text{ppm}/^\circ\text{C}/\mu\text{m}$  was calculated [115].

#### Polystyrene

As seen in Table 6.2, it is a material very comparable to PI. Its main differences are that there are no known photosensitive variants, so it requires additional processing steps for patterning. And it is arguably more expensive than PI (in conversation with EKL staff).

#### 6.3.4. Waveguide material conclusion

Finally, PI is opted as most suitable waveguide material as it has a suitable shear horizontal wave velocity, acceptable  $\tan \delta$ , a negative TCF which compensates for the ST-cut Quartz TCF, it is cleanroom compatible and is biocompatible. Most importantly, it is a UV sensitive material, so a lithography step can easily be performed if required. The possible water absorption should be accounted for when measuring and interpreting results.

#### 6.3.5. Interconnect and IDT metal materials

For the IDT material it was reasoned a figure of merit (FoM) can be devised based on the resistivity and density both of which should be as low as possible. This is to enable higher frequency application with thinner

electrodes, and reduce IDT mass loading effects respectively.

The considered metals are used in comparable work and are Aluminium, Tungsten, Copper and Gold. With a low resistivity and low density, Aluminium has the best FoM. Furthermore, Al is a standard cleanroom material and it is suited for wire bonding. It should be noted Al can diffuse into Si, so the application of Al on the Quartz (or SiO<sub>2</sub>) substrate should be treated with caution. But as no high temperature steps are taken, the risk of diffusion is minimal [116]. Al is selected as optimal IDT metal material from the compared metals.

Table 6.3: Relevant material parameters for the IDT material. A figure of merit (FoM) was calculated to compare the metals better. Ideally, the metal causes as little mass loading as possible for as much conductivity as possible. From this perspective Aluminium is clearly best. Data from [117].

IDT metal				
	Al	W	CU	Au
Conductivity $\sigma$ (MS/m)	36,9	8,9	58,7	44,2
Resistivity $\rho$ (n $\Omega$ m)	27	112	17	23
Density $\rho$ (g/cm <sup>3</sup> )	2,7	19,3	8,9	19,4
FoM (Conductivity/Density)	13,7	0,46	6,6	2,3

## 6.4. Materials selection conclusion

For the substrate, ST-quartz is selected for its mechanical stability and reported pure SH-BAW mode. This comes at the cost of lower electromechanical coupling.

For the waveguide, photosensitive PI is selected as it has very low  $v_s$  at a reasonable  $\tan \delta$ . And due to its photo sensitivity, the PI layer is patternable and can be removed from the contact pads in a simple expose and develop step. No additional photo-resist (PR) or etching would be required.

For the IDT and interconnect metal, Al is selected as it offers the best conductivity at low mass. Furthermore, it is an often used standard cleanroom metal, so it is easily available, well supported, well understood process. Which all helps to keep the process complexity limited.

## 6.5. Waveguide thickness

To determine the optimum waveguide thickness, first the literature was assessed. Using FEM models, the optimum thickness was determined.

In the literature, several experiments were done to determine the optimum waveguide thickness. For example the WGTH vs insertion loss from Gizeli et al. for novolac WG on quartz is shown in Figure 4.9, from [72]. These experiments are used as starting point for the geometry in the next fem models.

The WGTH changes both the centre frequency and the insertion loss. The influence of the WGTH on the centre frequency is hard to specify further than just an upper and lower band as given in equation 4.10. For the chosen materials for the substrate and waveguide in this work, ST-quartz and PI respectively, the expected centre frequencies are  $f_{0waveguide} = 920/8\mu \approx 115\text{MHz}$  and  $f_{0substrate} = 5050/8\mu \approx 631\text{MHz}$  this means the Love mode centre frequency  $f_{0Love}$  is expected to fall in the band:

$$115\text{MHz} < f_{0Love} < 631\text{MHz} \quad (6.1)$$

The 'time impulse' COMSOL model (Section 5.1.4) was used to determine the optimum waveguide thickness for PMMA and PI. The simulation leads to magnitude plots like in Figure 6.4 for PI.

The optimum PI thickness is then chosen at 510nm, as the DFT magnitude is highest. The magnitudes (only to be used as relative measure for the same simulation type, no indication of fabricated device IL), and centre frequencies are plotted in Figure 6.5.

The magnitude of the passband peak seems optimal when the apparent two passband peaks start to coincide. For example, the 800nm plot shows a 300MHz and 580MHz passband in Figure 6.4. In the 510nm plot, the 580MHz band has become much lower and the lower passband, now at 450MHz has increased. At thinner layers however, the DFT magnitude starts to decrease again. Then when the lower and higher frequency passbands couple, the best IL is attained. If the WGTH can be fabricated accordingly, the best IL devices are expected. As the IL in this simulation is a measure of the energy trapped at the surface, this is expected to be the WGTH with optimal sensitivity for surface mass loading.

It is hypothesised the two passbands arise from an eigenmode in the PI overlayer and a SSBW mode in the quartz substrate. Where the lower frequency passband of which the centre frequency is highly WGTH

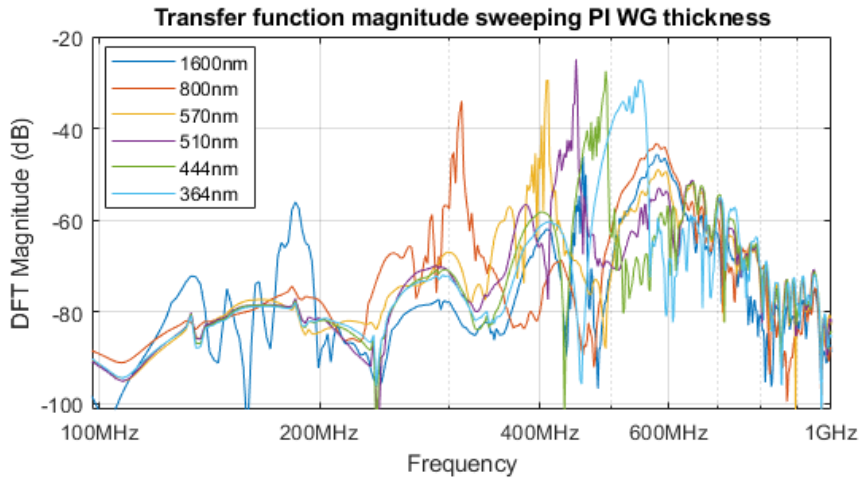


Figure 6.4: Slice time impulse model results for 6 PI thicknesses.

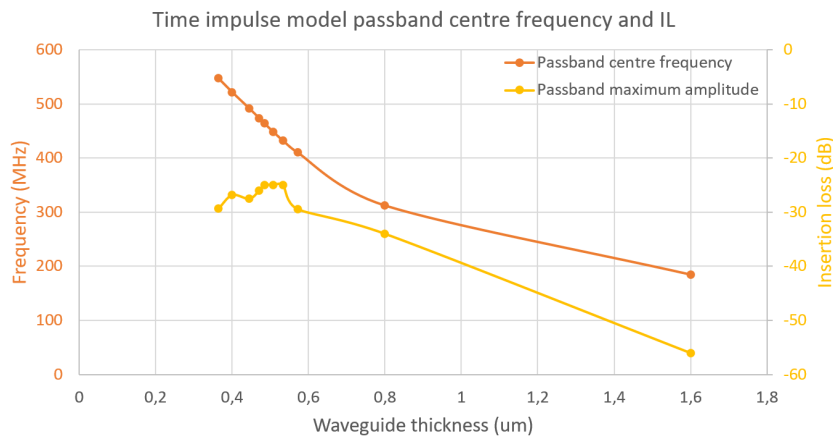


Figure 6.5: Slice time impulse model results PI.

dependent is the eigenmode in the PI WG layer. And the latter SSBW mode is the higher frequency passband, stable around 580MHz but differing in DFT magnitude.

Using Wang et al. (1994), see Section 4.5.3, the found optimum is double checked. Using equation 4.20,  $h_{wg-opt} = (1/4)(V/f)/\sqrt{(V^2/V_{swg}^2 - 1)} \approx (1/4)(V_{s-wg}/f)$  [55]. Then for this work,  $h_{wg-opt} \approx (1/4) * (920/500M) \approx 460nm$ . This in sufficient agreement with the result based on the COMSOL time impulse model.

Now the optimum thickness is known, experiments are required to determine the achievable thickness. This is done and extensively discussed in Appendix H. The used process is one of the topics of Chapter 7.

This work uses LTC9305 from Fujifilm as it is the most thin applied PI with achievable film thicknesses around 5um [118].

Unfortunately, this appendix concludes, 510nm PI thickness is not achievable with the available PI and equipment. Instead, using long spin times and high spin speeds (75 sec at 6000rpm), thinner thickness near 900nm can be achieved. Though both higher spin speeds and longer times are possible this is not advisable as small defects can cause big yield issues at these high spinspeeds and time. Non uniformities get stretched further out across the wafer with thinner films. This is all extensively discussed in Appendix H.

Film thicknesses around 800nm have lower power transfer from transducer to transducer and a clear separation between two passbands (around 300MHz and 580MHz) as was shown in Figure 6.4. Thinner thickness is unfortunately not achievable with the current equipment and material. Decreasing the thickness or altering the operation frequency remains a topic for future research.

## 6.6. IDT geometry

This section includes all aspects of the interdigitated transducer (IDT) geometry. Including finger thickness (or metal thickness), width, interconnect width, IDT shape and interconnect shape. After all materials are chosen and the waveguide thickness is determined, the IDT design is up next. The IDTs, being the transducers, have a huge impact on sensor performance. Hence the large amount of attention that is spend on their geometry in the coming section.

### 6.6.1. IDT Layout

As discussed in Section 4.5.2, reflectors can be added to reduce signal power loss by reflecting power back to the delay line. A SPUDT layout can increase efficiency by only transmitting the acoustic signal uni-directionally. These options come at the cost of design complexity. Furthermore, it was already mentioned, instead of reflectors, more finger pairs have a larger impact on IL. And the SPUDT comes at the cost of smaller feature size, with limited processing tools (specifically lithography resolution), this leads to higher centre frequencies.

Furthermore, power efficiency is for now not an important measure as in this experiment, the measurement equipment can deliver sufficient power. In future work where a sensor might be battery powered or even powered by energy harvesting, the reflectors and SPUDT should be reconsidered.

It is decided to use bi-directional, straight IDT layout without reflectors. The goal is to keep design complexity low to increase yield by relaxing fabrication constraints. Also, this reduces computational model complexity. Finally, the decision enables a high as achievable centre frequency.

### 6.6.2. IDT width

To obtain a operating frequency as high as possible, inspecting equation 4.9 indicates the wavelength  $\lambda$  should be as small as possible. This parameter is set with the spacing between the IDT electrodes. This spacing is limited by the minimum resolution of the EKL of  $1\mu\text{m}$ . Taking into account a safety factor of 2 for a more robust device and increasing the chances of a high yield the IDT width is set to  $2\mu\text{m}$ . Then the wavelength will be  $\lambda = 4 * 2\mu = 8\mu\text{m}$ . In a later iteration it might be among the options to reduce the width, reducing  $\lambda$  and increasing the operating frequency. As described in Section 4.4, the increased sensitivity due to the increased operation frequency comes at the cost of a higher noise floor. The limit of usable operation frequency is then determined by the readout method. Using equation 4.9 it can quickly be determined a  $2\mu\text{m}$  electrode width, corresponding to a  $8\mu\text{m}$  wavelength, will lead to a maximum operation frequency of  $f_r = 5050/8\mu = 631.3\text{MHz}$ . By inspecting the state of the art work from Table 4.2, it is decided around 600MHz is very high but still in the same order of magnitude as previous work en therefore the noise floor is not expected to be a limiting factor.

### 6.6.3. Metallisation ratio

Metallisation ratio is set to 0.5 as then no odd harmonics are excited [60], as shown in Figure 4.5 in Section 4.5.2. Furthermore, the smallest possible wavelength is only achievable with a 0.5 metallisation ratio.

### 6.6.4. IDT thickness

The IDT height (or thickness) is a trade-off between R-C constant, fabrication robustness, operating frequency and waveguide layer coverage [81]. Increasing the electrode thickness decreases the resistance but increases the capacitance. Increasing the thickness also improves the robustness against over-etch in fabrication. However, decreasing the electrode height reduces mass loading allowing a higher operating frequency. This also reduces the chances of shadowing effects of the waveguide layer in the fabrication process [115]. For Aluminium, thickness of  $0.1\mu\text{m}$  and  $0.2\mu\text{m}$  are reported [96].

An investigation using the COMSOL 'unite wavelength' model, shows the effect of the electrode thickness on the eigenmode frequency of interest and the maximum displacement of the waveguide layer. The simulation was run using pure Al as metal and PMMA as WG material, on a ST-quartz substrate. For more details on the model, the reader is referred to Section 5.1.3. The result in Figure 6.6 shows when the IDT thickness is increased, clearly the eigenfrequency, related to the desired eigen mode, increases as well. It is hypothesised, this is due to increased effective stiffness of the waveguide layer by the electrode material, allowing a faster propagating shear wave which, at a fixed wavelength, corresponds to a higher frequency. In COMSOL, aluminium has a Young's modulus of 70GPa where PMMA only is 3GPa. Aluminium and PMMA have a Poisson's ratio of 0.4 and 0.33 and a density of 2700 and 1190 kg/m<sup>3</sup> respectively. Based on equations 4.7 and 4.8, it is easily shown PMMA has a much lower shear wave velocity (al 3000m/s and pmma 31m/s). As

a higher frequency is desired, the IDT thickness is not limited by this. However, at increasing thickness, the maximum displacement of the waveguide, at the eigen mode frequency, decreases. This reduced displacement can lead to reduced sensitivity as any added mass on the surface is displaced less, resulting in a lower acceleration and thus less force. It must be considered every electrode thickness has had an own eigenmode study computation, this might make it less reliable to compare absolute values for displacement.

To try and maintain surface uniformity for spincoating later in the process, the metal is chosen as thin as possible keeping series resistance in mind. Another practical issue is wirebonding later in the process. When using aluminium, the absolute minimum advised thickness is 100nm, otherwise, the metal is at a high risk of serious damage due to the ultrasonic power used to connect the bond wire as was warned for by EKL personell. The 100nm thickness already requires an experienced technician to do the wirebonding.

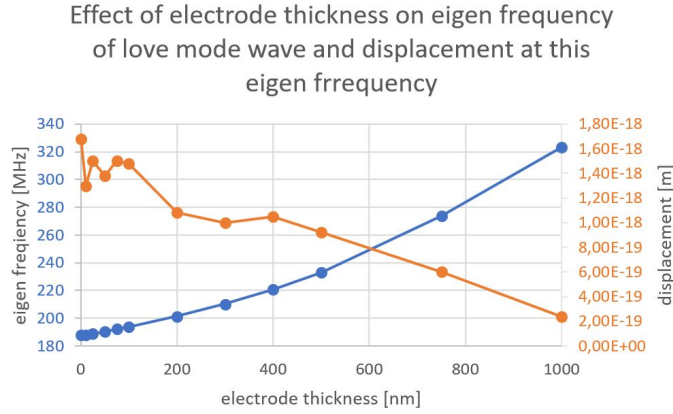


Figure 6.6: Eigen frequency and maximum WG displacement for the unit wavelength model using ST-quartz substrate, PMMA WG, pure-Al metal and a 8um wavelength for several electrode thicknesses. Increasing electrode thickness increases eigenfrequency at the cost of displacement.

### Skin Depth

For the IDT thickness, as an additional check, the skin depth is considered. When the electrode height exceeds twice the skin depth, part of the electrode does not participate in conduction. The skin depth  $\delta_{s,al}$  is determined below [119].

$$\delta_{s,al} = \frac{1}{\alpha_{al}} \quad (6.2)$$

$$\alpha_{al} = \omega_{target} \left[ \frac{\mu_{al}\epsilon_{al}}{2} \left[ \sqrt{1 + \left( \frac{\sigma_{al}/\omega_{target}}{\epsilon_{al}} \right)^2} - 1 \right] \right]^{1/2} \quad (6.3)$$

with  $\omega_{target} = 2\pi f_{target}$  and  $\sigma_{al} = 35.5E6$  S/m.

working with complex permittivity  $\epsilon = \epsilon' + j\epsilon''$ , with  $\epsilon' = \epsilon_0\epsilon_r$  and  $\epsilon'' = \sigma_{al}/\omega_{target}$

With in the following operating conditions:

$$f_{target} = 190.55E6\text{Hz}$$

$$\mu_{al} = \mu_0 = 4\pi E-7 \text{ H/m}$$

$$\epsilon_{al} = \epsilon_0 = 8.854E-12 \text{ F/m}$$

$$\sigma_{al} = 35.5E6 \text{ S/m}$$

This results in a skin depth  $\delta_{s,al} = 6.12\mu\text{m}$ . Then it can be concluded for any conductor thicknesses below  $2\delta_{s,al} = 12.24\mu\text{m}$ , skin effect will not increase the effective conductor resistance.

### IDT interconnect resistance and RC cutoff frequency

The effect of the metal interconnect on chip on the maximum operation frequency is checked. It is expected the metal interconnect behaves resistive and inductive. The IDT is expected to behave capacitively. For this quick analysis, only the resistive behaviour of the interconnect is considered using equation 6.4.

$$R_{ic} = \rho \frac{l}{A} = \rho \frac{l_{ic}}{w_{ic} t h_{el}} \quad (6.4)$$

with  $\rho$  the metal resistivity,  $l_{ic}$  the interconnect length,  $w_{ic}$  the interconnect width and  $t h_{el}$  the metal thickness which is equal for interconnect and IDT finger or electrode. For this estimation, the interconnect is estimated to be 2mm long, 400 $\mu$ m wide and the electrode thickness was set at 100nm. Then the estimated  $R_{ic} = 1.4\Omega$ .

The IDT capacitance is determined both through COMSOL and the conformal mapping based MATLAB calculation as described in Section 5.2.1. For this estimation, a mock up device based on state of the art work is used. Its parameters are:  $\lambda = 8\mu\text{m}$ ,  $N = 75$ ,  $W = 50\lambda$ ,  $W G_{th} = 700\text{nm}$ , Quartz substrate, polyimide waveguide. The resulting single finger pair capacitance per unit length is  $C_0 = 507\text{pF/m}$ . The total IDT capacitance is estimated at  $C_0 W N \approx 15\text{pF}$ .

The estimated cutoff frequency of this very crude RC estimation is then over 740MHz, which is sufficient but close to the designed centre frequency. This means the metal thickness is sufficient but not very conservative. Care must be taken not too much interconnect resistance is added later in the design process.

### 6.6.5. Transducer and delay line considerations

The number of finger pairs  $N$  and aperture  $W$ , together with the already set wavelength and materials, largely set the IDT capacitance (see Section 4.6). This capacitance determines the required matching as became apparent from the equivalent circuit model described in that same section. Then  $W$  and  $L$  together set the area that is sensitive for the analyte. First the main findings of this circuit model are described. Then the effect of the delay line area is discussed. Finally, a conclusion on  $N$ ,  $W$  and  $L$  can be drawn.

#### No matching network design

It is beneficial if the sensor already has good performance without implemented matching network for design ease and quick characterisation. If the sensor already has sufficient performance without matching, the matching network design is relaxed. Removing risk for errors. Moreover, as mentioned in Section 6.1, quick device characterisation should be enabled. An option for this is a probe station characterisation measurement. Then not all devices that are opted for characterisation have to be placed on an interfacing PCB. This hugely saves time and cost. However, in this probe station measurement, no matching network close to the IDT is present.

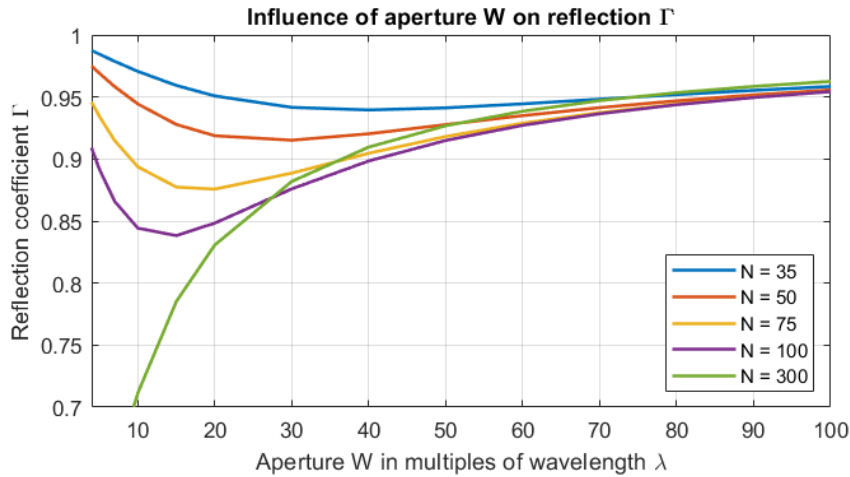


Figure 6.7: With the electrical equivalent model, the influence of  $W$  and  $N$  on the impedance can be determined. This can be used to determine the reflection coefficient for a 50 Ohm source impedance. For several IDT versions with increasing finger pairs the relation between the aperture  $W$  and the reflection coefficient is shown. It can be concluded that increasing the finger pairs  $N$  will have an increasingly low reflection coefficient optimum at a lower  $W$ . For a practical sensor,  $W$  can not be infinitely small. It can be seen at for example  $W=50$ , there exists an optimum  $N$  of about  $N=100$ .

The model described in Section 4.6, implemented in MATLAB, is used to calculate the reflection coefficient between the IDT and a source with 50 $\Omega$  source impedance. Sweeping  $W$  for several values of  $N$  shows

the optimum shifts to lower  $W$  for higher  $N$  (where a low as possible  $\Gamma$  means higher transmission improving acoustic power delivery to the sensitive area). As the system is completely reciprocal, this also improves acoustic power transfer to the  $50\Omega$  measurement load.

#### Single element matching network design

When the aperture is designed to match the real part to  $50\text{ Ohm}$ , only 1 inductor could suffice to create a device impedance with zero imaginary part.

The circuit model can also be used to try and design the IDT such that single element matching or even integrated matching becomes available. For this purpose, the IDT calculated impedance is plotted on the smith chart for three values of  $N$  (35, 75 and 100) and  $W$  is stepped from extremely small values ( $W < 0.1\lambda$ ) to extremely large values ( $W > 1500\lambda$ ) resulting in Figure 6.8. A more clear Smith chart with expanded explanation on how it should be interpreted can be found in Appendix G.

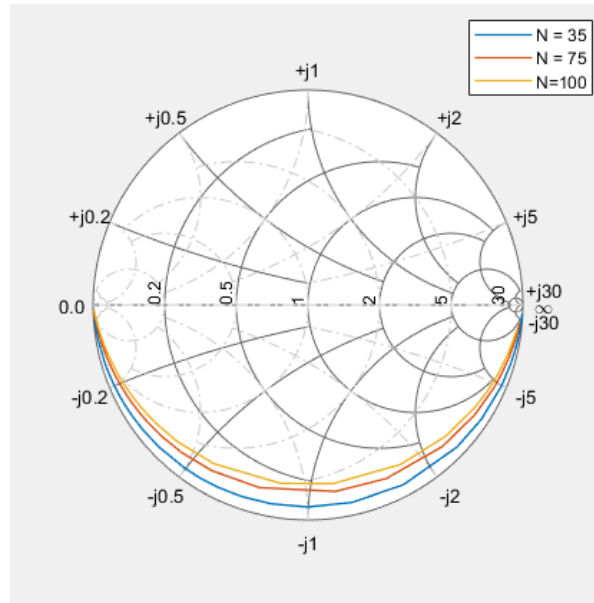


Figure 6.8: Smith chart based on electrical equivalent model. Sweeping  $W$  from extremely small to extremely big. Using three values for  $N$ : 35, 75, 100. The model shows increasing  $N$  brings the curves in the Smith chart closer to the centre.

Single element matching is achieved if the IDT impedance coincides with the black or grey circle going through the centre (labelled '1'). Then a series or shunt matching network needs to be chosen. A series solution is applicable when the IDT impedance coincides with the black circle, and a shunt solution for the grey circle. These matching solutions are depicted in Figure 6.9.

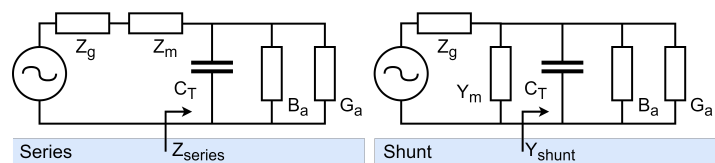


Figure 6.9: Series (left) and shunt (right) single element matching circuit schematic.

The found series solutions all are unrealistic devices, it is concluded single element matching is not possible for a series matching circuit. The shunt matching solutions become somewhat realistic in the area of  $N > 100$ . The validity of the equivalent circuit will have to be checked by measurements. Furthermore, there are hard to predict influences including, but not limited to, added inductances due to wirebonding, PCB tracing and connector parasitic. Therefore, even though single element matching seems a viable option, still multiple element impedance matching will be required.

Table 6.4: Solutions for single element matching

N	Series			Shunt		
	W	$C_T$	Match element	W	$C_T$	Match element
35	0.7 $\mu\text{m}$ (0.09 $\lambda$ )	12.7fF	9.9 $\mu\text{H}$	6400 $\mu\text{m}$ (800 $\lambda$ )	115pF	114pH
75	0.33 $\mu\text{m}$ (0.04 $\lambda$ )	12.7fF	9.8 $\mu\text{H}$	1400 $\mu\text{m}$ (175 $\lambda$ )	53pF	53pH
100	0.25 $\mu\text{m}$ (0.03 $\lambda$ )	12.7fF	9.6 $\mu\text{H}$	790 $\mu\text{m}$ (98 $\lambda$ )	40pF	40pH
300	0.08 $\mu\text{m}$ (0.01 $\lambda$ )	12.7fF	7.7 $\mu\text{H}$	87 $\mu\text{m}$ (11 $\lambda$ )	13pF	13pH

### Delay line length

In literature often referred to as delay line length (L). Increasing L increases the area that is functionalised, so more particles can be immobilised. This comes at the cost of increased IL due to various loss mechanisms described in Section 4.5.2.

The maximum length is determined by what is practically possible in terms of chip size and by the maximum allowable insertion loss (IL) of the readout system. For the latter, an estimation of the IL can be made. A COMSOL model for the estimation of the IL is left for future work due to challenges described in Section 11.1.2.

In Section 4.5.2, it was concluded it is hard to predict an optimum or maximum allowable L. Also, in that section it is concluded it is a conservative approach to compare the state of the art delay line lengths in terms of wavelengths.

Additionally to the state of the art work, a rough indication of the IL can be based on the power radiated by the IDT, the directionality of the radiated power, the loss of the delay line and efficiency of receiving the SAW and converting it back to an electrical signal. The radiated power efficiency will be roughly equal to the efficiency of receiving the SAW and converting it to an electrical signal as the IDTs are designed symmetrical and the system is completely reciprocal. The loss due to directionality is 3dB per IDT as the IDT is designed bi-directional (to obtain a smaller  $\lambda$ ). And a damping factor can be derived from the PI waveguide thickness, on ST-quartz, influence on damping results of Qian 1991 [69] as shown in Figure 4.8.

The damping factor is estimated at 0.02dB/ $\mu\text{m}/\lambda$ . Using Figure 4.8, the attenuation per wavelength can be determined for a 14  $\mu\text{m}$  WG thickness, 99MHz, device. This slope is then normalised for the WG thickness. Resulting in the empirical formula: attenuation/delayline length in  $\lambda$  / WG thickness = 5dB/18 $\lambda$ /14  $\mu\text{m}$  = 0.02dB/ $\mu\text{m}/\lambda$ .

A huge discrepancy of this derivation is the neglected relation between attenuation per wavelength and frequency. This steep linear dependency is not properly taken into account. A more thorough method would be to extrapolate the attenuation per wavelength linear relation to the used centre frequency. Then determine the expression for the quadratic influence of the WG thickness, and determine a factor based on that.

These observations lead to an indicative equation for the IL in dB

$$IL = 2 * 20 \log_{10}(1 - \Gamma) - 2 * 3 - 0.02WGTH_{\mu\text{m}}L_{\lambda} \quad (6.5)$$

with reflection coefficient  $\Gamma$ , waveguide thickness in  $\mu\text{m}$   $WGTH_{\mu\text{m}}$  and the delay line length in wavelengths  $L_{\lambda}$ . Leading to a plot like Figure 6.10.

Then equation 6.5 can be used to estimate the influence of both W and L on the IL and contour lines for constant IL can be made (Figure 6.11) to create a design space for W and L.

### Delay line area

Together, W and L determine the area that is sensitive for mass loading. A minimum delay line area can be derived from the sample sizes that are expected. Typical sample sizes are around 100  $\mu\text{L}$  [10]. A droplet contains approximately 50  $\mu\text{L}$ . Samples of tens of micro litres will be used. Hydrophilicity tests show PI has a contact angle of about 85° [120]. With this, the estimated area a  $\mu\text{L}$  volume droplet takes is calculated as shown as contour lines in Figure 6.12

Though specific numbers are challenging to obtain, it is estimated a 100  $\mu\text{L}$  sample contains in the order of magnitude  $10^8$  to  $10^{10}$  extracellular vesicles (EVs) per millilitre. Of these between 10% and 40% contain CD9. Meaningful measurements have been done with volumes of 100  $\mu\text{L}$  (this is a standard volume in lab equipment) [10]. It is to be expected that a smaller volume of 1  $\mu\text{L}$  or 0.1  $\mu\text{L}$  still contains a sufficient number of CD9 expressing EVs. Additionally, a 100  $\mu\text{L}$  sample can be divided over many delay lines and the individual results can be averaged to still examine larger volume samples if the need for improved sensitivity or accuracy becomes apparent.



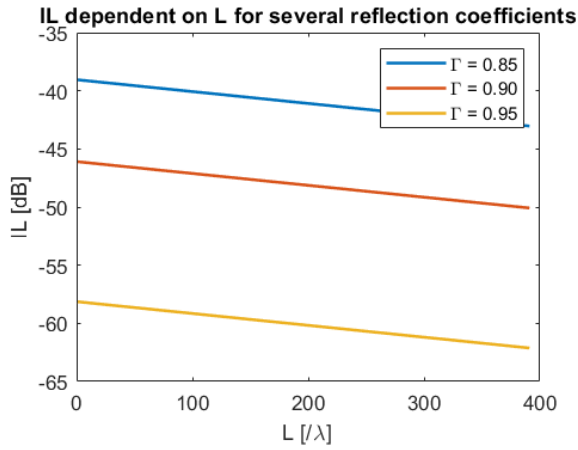


Figure 6.10: Influence L on IL for several  $\Gamma$ .

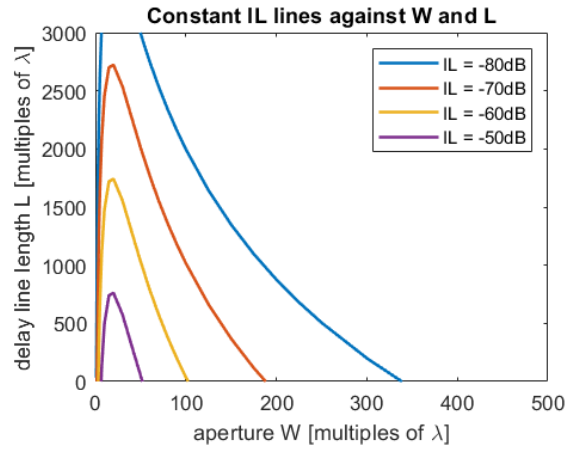


Figure 6.11: Constant IL contour lines for different W and L for  $N=75$

Another contour line is added for diffraction as explained in Section 4.5.2. Equation 4.12 is used for the 'maximum L at W' diffraction contour line in Figure 6.12. The chosen W and L should lead to a point below this line.

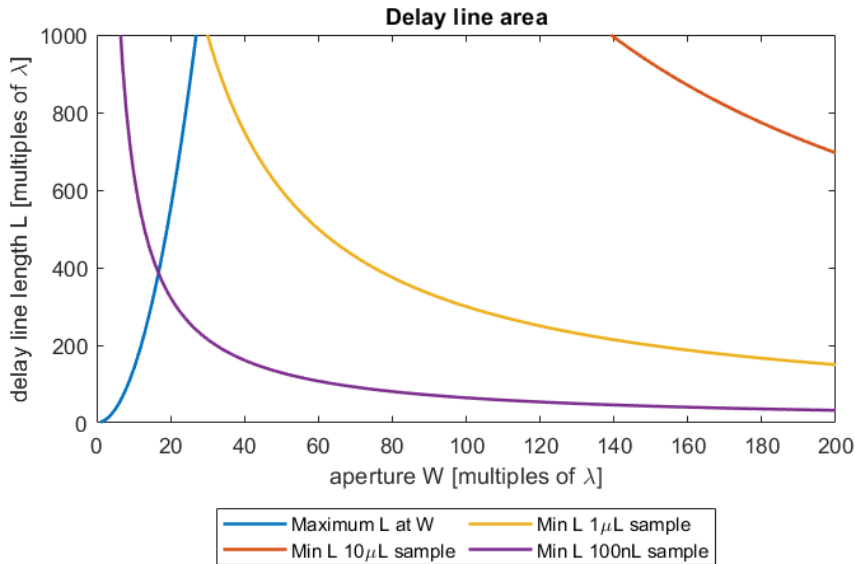


Figure 6.12: Using diffraction equation 4.12, a maximum delayline length is found for any aperture. The diffraction is clearly no limiting factor in the directionally constant (or isotropic along the wave plane of propagation) ST-cut quartz. Also constant area lines are shown corresponding to the area required for a droplet with a volume as shown in the legend. It shows that for even very small volumes, quite a large area is required.

### 6.6.6. Final device versions

To conclude, straight bi-directional IDT layout is chosen for design simplicity, computational model predictability and highest possible frequency reachable with the EKL equipment.

The number of finger pairs ( $N$ ) is set to  $N=75$  to keep the designed devices versatile in application. As then  $N$  is already quite high but the BW is kept quite large. A large BW is preserved as then the sensors can also be used in an open-loop, fixed frequency based measurement setup as described in Section 4.7.

Figure 6.7 shows a high  $N$  improves transmission up to a certain point ( $N=300$  is already detrimental for realistic  $W$  values). In the previous analysis (Table 6.4), it is concluded a high  $N$  might enable single element matching. This is for now out of the scope and  $N=75$  is expected to have sufficient performance without

matching.

For the aperture, a trade off is chosen at  $W=40\lambda$  based on the reflection coefficient and the area. At an  $N=75$ , the reflection coefficient plot (Figure 6.7 shows the reflection is still quite low at  $W=40\lambda$ , though the optimum is a lower  $W$ . And the area contour lines (Figure 6.12) are used to demonstrate at this  $W$ , sufficient sample sizes can be obtained for feasible  $L$ .

Finally  $L$  is set to  $100\lambda$ , based of the state of the art literature. Also, at this value, combined with the set  $W$ , sufficient sample size is enabled. At the chosen values, the device is also within the  $-50\text{dB}$  IL contour lines of Figure 6.11.

The hypothetically optimum device is then:  $N=75$ ,  $W=40\lambda$ ,  $L=100\lambda$ , but many more versions are fabricated to verify the optimum device through measurements. The main parameters,  $N$ ,  $W$  and  $L$  are varied. Also some extra large devices, rotated devices and lower centre frequency devices are included for specific tests. The versions are listed below. A complete list of fabricated devices can be found on the final page of the flowchart in Appendix J.

- N sweep: Confirm  $N$  and bandwidth relation. Confirm added power delivery with increased  $N$ .
- W sweep: Test multiple sensitive area sizes to verify if optimum was found.
- L sweep: Find if the  $IL/L$  can be verified.
- Large area devices: Test influence of surface area on sensitivity.
- Rotated devices (Rot90deg): A selection of versions is rotated on the substrate so now a Rayleigh mode is expected. This is for trouble shooting purposes.
- Lower  $f_0$  devices (WL): Some other centre frequency devices are included to relax required lithography resolution and to stay closer to state of the art work.

For all planned device versions, their locations in the contour plots is shown in Figure 6.13.

With the planned fabricated devices: Figure 6.13.

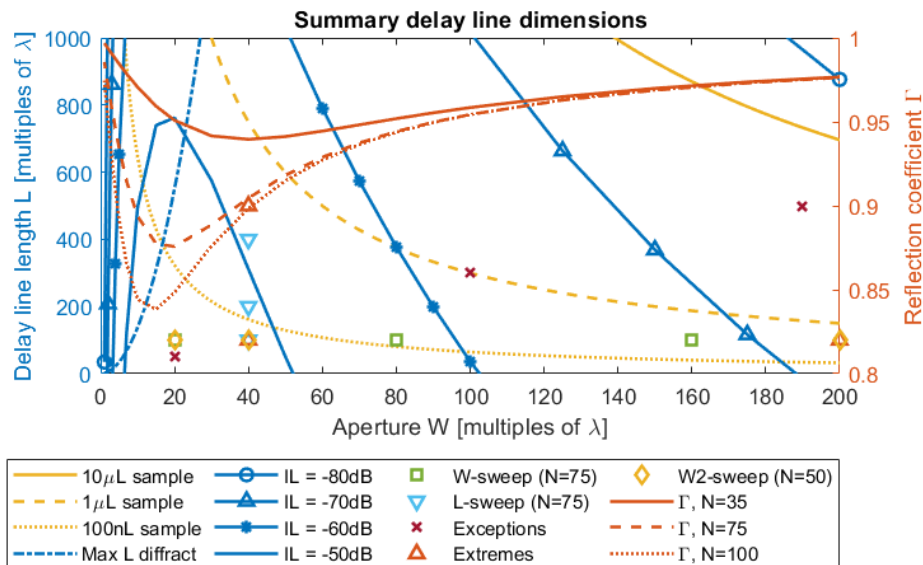


Figure 6.13: Summary of previous plots combined to show trade-off between area and IL together with the maximum  $L$  before diffraction and the reflection coefficient with the SAW devices that are planned to be fabricated pointed out.

## 6.7. Mask design considerations

The mask is drawn in L-edit. This dedicated mask drawing CAD tool can straightforwardly be used to export in .gds files, the standard for mask fabrication. A template for the contact aligner (MA/BA8 SUSS MicroTech Contact Aligner) in the micro fabrication cleanroom lab (EKL) was supplied by the lab database (FWAM mask file). Here the mask borders are already set out and the compatible alignment markers are already correctly placed in the template. L-edit then works well with actively connected cells, so repeated structures are easily created and updated when a correction is needed. The snap grid is set to the critical dimension.

When designing the die and wafer layout considerations for fabrication and device performance are taken into account. First the considerations relating to fabrication are discussed. Then the considerations for device performance are explained.

### 6.7.1. Wafer orientation and Euler angles

As discussed in Section 4.5.1, the crystal orientation is crucial for the proper functioning of the sensor. The flat of the wafer is aligned with the Y axis and the X axis is perpendicular to the flat. The SH-wave then is expected to prefer propagation parallel to the flat of the wafer. This was relayed by the wafer producer, Microchemicals.

### 6.7.2. Free dicing lines

Free dicing lines to avoid damage to the polymer layer due to the dicing saw blade. The largest risks are the polymer being peeled off or washed off. The first can happen when it is gripped instead of cut by the blade. The latter is due to the high pressure cooling and flushing jets. The saw blade can be 50um up to 200um wide. Also, chipping of quartz is expected up to several hundreds of um, approximately 300um. The polymer dice line clearance immediately gives access to the contact pads.

The minimal clearing for dicing per die is then decided as  $200\text{um}/2 \text{ blade} + 300\text{um chipping} + 100\text{um margin} = 500\text{um}$ . Then a dicing line between two chips has at least 1mm free of PI.

Other damage due to dicing is the particles that come free in the dicing process. When very fine mechanically moving structures are present or when the particles are conductive this is problematic. The adverse effects can be avoided by adding a sacrificial layer that is removed after dicing. However, in this case the particles can not cause shorts or prevent mechanical movement as in a MEMS device. Therefore no protective sacrificial layer is required.

Also, the removal of the WG layer from the dicing lines helps reducing the full wafer measurements interference from neighbouring devices. The Love mode wave can not cross to another die and be reflected by the IDT there. Only a smaller SSBW might travel on. And due to acoustic impedance changes, reflections occur, causing less energy to be available for reflection by the neighbouring device IDT.

### 6.7.3. Dice under angle

To help reduce the interference of a reflected wavefront from the die edges, and on wafer level measurements reduce neighbouring die device interference, the dies can be diced under an angle. Then the wavefront travelling to the substrate edge is reflected in alternative direction, not back to the IDT.

Another implication of this angle is when performing full wafer measurements, the end of WG layer reflections (described above in Section 6.7.2) are directed away from the originating IDT. Furthermore, the SSBW energy transmitted across the WG gap gets an offset as illustrated by Figure 6.14.

An angle of  $12^\circ$  is decided on based on 'angle of incidence = angle of reflection'. The distance between the IDT and substrate and the aperture of the IDT determine this angle.

### 6.7.4. Bond wire reach

In conversation with a technician, wirebonding limits were discussed. The maximum bond wire reach is 7000um. However, 3500um is a more realistic scope. Then the bond connection on the PCB needs some distance from the die as well, approximated at 1000um. The bondpad to die edge separation will have to stay below the 2500um. All values are empirical and determined in conversation with F. Simjanoski, technician in the ECTM group at TU Delft.

### 6.7.5. The final wafer and die layout

All above mask design considerations are summed in Table 6.5.

For this 2 mask design, defining the wafer lithography features is done in L-Edit. The first mask defining the metal layer (IDT and interconnect definition). The second mask defines the places where the polymer is

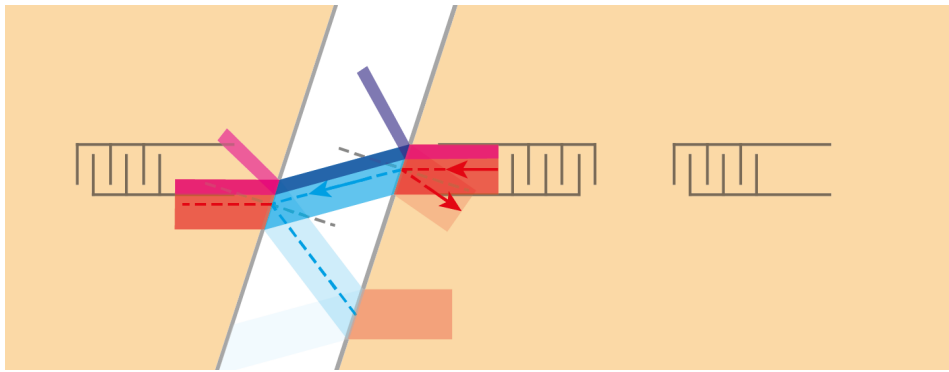


Figure 6.14: On wafer example of effect removing PI from dicing line. Both attenuation (SSBW instead of Love wave) and shift of wave propagation so part of energy misses next IDT. However, part of energy is reflected by next IDT and has a return path to original IDT, finally arriving at receiving IDT.

not cured, to remove it between dies.

The masks are ordered at MicroCreate. The mask fabrication there offers standard resolution down to  $2\mu\text{m}$  for quartz mask with chromium. All mask details can be found in the mask order files as added in Appendix I.

Table 6.5: Summary of mask design considerations.

Dicing blade width	max 100um
Chipping due to dicing	max 300um
Dicing damage to polymer	free dicing lines, at least 500um per chip, 1mm clearance
Achievable bondwire length	max 7000um, better 3500um
End of device reflections	dice under $12^\circ$ angle
Other device interference	remove wg under angle
Removal of polymer from bondpads for electrical contact	
Bondpad size	150x400um

## 6.8. Peripherals

After the design of the SAW devices has been discussed, in this section the integration of the device in a measurement platform is described. First the designed die is interfaced through a PCB which is described first. Second, the fluid samples have to be contained which is the topic of the following subsection.

### 6.8.1. PCB considerations

Finally, the SAW devices are placed on a PCB for quick interface to a measurement system. The PCB design in Altium is described here. It is ordered at Eurocircuits. The design is guided adhering to the extensive guidelines provided by the company. The resulting design is shown in Figure 6.16. The most relevant considerations are discussed here.

To keep the PCB affordable and increase chances of quick delivery, the design is kept in the simplest class possible. This means, the biggest drill class. The most coarse PCB features class. And finally, only two metal layers. All according to the Eurocircuits guidelines.

One inevitable deviation from the standard PCB is the surface finish which needs to be gold. An Au/Ni finish is required for wire bonding the aluminium contact pads to the PCB. To ensure a proper fit when wire bonding, a custom footprint and 3d model of the SAW devices was made in Altium.

#### High frequency design considerations

As the centre frequency is designed in the hundreds of MHz order of magnitude, precautions against radiation and reflections are taken. Though the electrons reside in the conductors, the propagating electromagnetic field travels through the media surrounding the conductor. On the PCB, the wavelength of the electromagnetic wave is then approximately  $\lambda = v/f = c/\sqrt{\epsilon_r}f$ . With  $v = c/\sqrt{\epsilon_r}$ . Then  $\lambda = 3 * 10^8 / (\sqrt{4} * 500 * 10^6) = 0.3$  meter. Then a quarter wavelength is only  $\lambda/4 = 7,5\text{cm}$ . So the PCB size features are comparable to a quarter

wavelength and so the PCB and other interconnections should be designed with high frequency design rules in mind.

To avoid reflections and radiation on the PCB, all traces are designed to avoid tight corners. Furthermore, to reduce reflections, the traces width is altered gradually, again avoiding corners. For proper ground plane connection, the ground planes are stitched around the signal traces with vias on an interval smaller than  $1/20$ th of the wavelength on the PCB. Finally, the traces are matched to  $50\Omega$  as described in next section.

#### Matched copper traces

For matched transmission lines on the PCB the automated function in Altium is used. This leads to a  $1150\mu\text{m}$  copper width when using  $250\mu\text{m}$  spacing between the signal trace and ground plane. This dimension was checked with the model described by Simons [97] as described in Section 5.2.2. The result is shown in Figure 6.15, confirming the traces characteristic impedance is near the designed  $50\Omega$ .

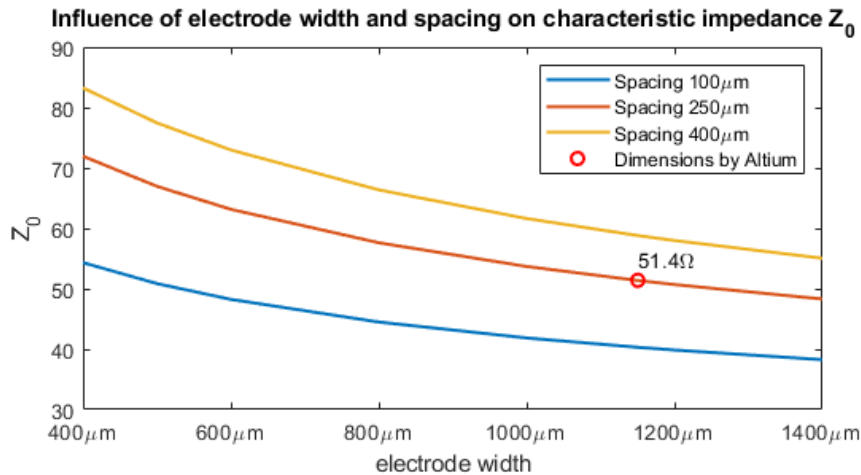


Figure 6.15: The model by Simons used to check the dimensions of the copper trace on the PCB as calculated by Altium.

#### Matching network

Though an attempt for single element matching was done, this was not feasible for all SAW versions. Furthermore, due to parasitics and model shortcomings, a deviation from the calculated impedance is to be expected. Therefore, the PCB leaves room for a  $\pi$  matching network. The pad size and spacing is left for 0805 elements as these are still hand solderable and it was checked likely matching components are available in this size. Initially, the network is shorted with 0805 zero ohm resistors or jumpers for initial characterisation. Then the required matching network is calculated and soldered.

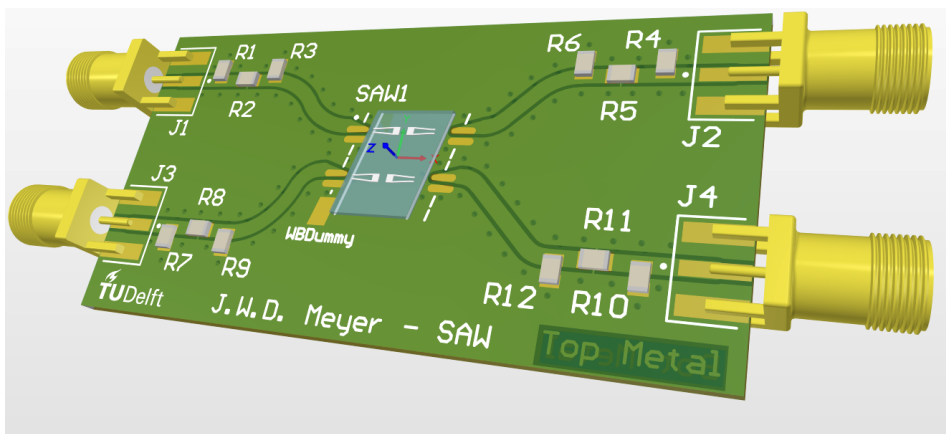


Figure 6.16: Render of designed PCB in Altium

### 6.8.2. Fluid well

To isolate the bond pads and bond wires from the liquid sample and protect the extremely fragile bonds from mechanical perturbations, some medical grade epoxy will be used (epoxy that will not have fleeting toxic components that might cause denaturation of protein). This Loctite Hysol M-31CL Medical Epoxy glue has as advantage it cures at room temperature and has low shrinkage. Here the latter is important to not damage the bonds while curing.

To guarantee the epoxy will not cover the IDT or delay lines, wells are experimented with as shown in Figure 6.17. PMMA is expected to be compatible with bioconjugation techniques and is readily available as Acrylate plates. Wells with 500um wall thickness were successfully lasercut from a 4mm thick acrylic plate. Thinner walls or a thicker plate (for increased well volume) leads to buckling of the walls and melting against the bulk, preventing release.

Unfortunately, as is more extensively explained in Appendix L, the wells have unexpected reactions with the functionalisation process making them unsuitable. A chemical reaction is suspected to take place and particles release and find their way to the delay line area.

For this reason the well will be made from just epoxy. It has sufficiently low viscosity that it can be slowly deposited around the SAW device. It will however be impossible to separate two devices on one die with this method.

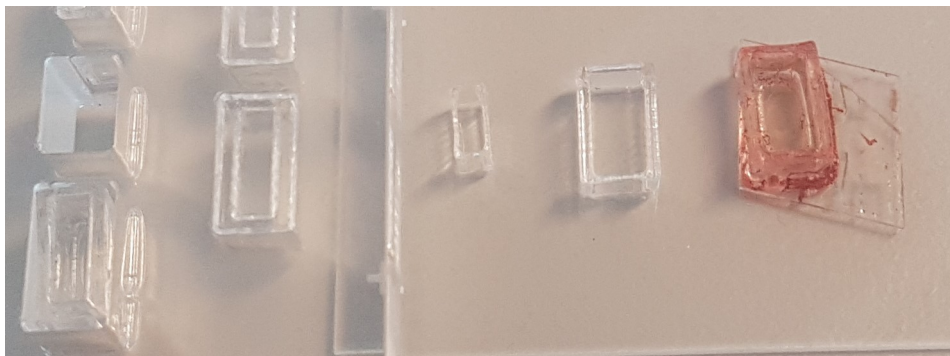


Figure 6.17: Wells lasercut from acrylic plate from left to right: wells melted stuck in 8mm thickness acrylic, 500nm wall thickness 4mm high well, 1mm wall thickness 4mm high well, well on SAW device after functionalisation process showing red discolouring and particles.

## 6.9. Design conclusion

To conclude the entire design phase, here, the major choices are summed. The materials have been selected to be ST-quartz, polyimide and aluminium. The wavelength is designed at  $8\mu\text{m}$ . Then the centre frequency is in the 600MHz order of magnitude. The waveguide thickness is designed 510nm, unfortunately, fabrication only allows 900nm.

The IDT is designed bi-directional and straight. Using an electrical equivalent model, it is predicted the optimal device has  $N=75$ ,  $W=40\lambda$ ,  $L=100\lambda$ . Many more device versions are fabricated for validation purposes.

For peripherals, a PCB is designed with impedance matched traces. Room is left to implement a  $\pi$  matching network after on PCB device impedance characterisation. A laser cut well from acrylic plate was proposed but failed. Instead an epoxy well will be fabricated.

The next step is to fabricate the device. This is discussed in the next chapter.

# 7 | Fabrication

In this chapter, the fabrication process is briefly touched upon. A discussion of some crucial steps in the fabrication process is given. For a complete list of steps with all details, henceforth referred to as the flowchart, the reader is referred to Appendix J. The fabrication is done in house at TU Delft at the cleanroom facility, Else Kooi Lab (EKL).

## 7.1. Process flowchart

The process is based on the flowchart build in the work of Maarten Zijlmans [81] and the process integration training (PIT) and specific tool module training supplied by EKL.

This fairly straightforward, 2 mask, process is shortly described here. All significant steps are visualised in Figure 7.1. For fabrication details, the reader is referred to the flowchart, completely included in Appendix J.

The process starts with 5 double side polished (DSP) stable temperature (ST)-cut quartz wafers from MicroChemicals. Before processing, and after every processing break over 4 hours, the wafers are to be cleaned. This, and other factors, limits the moments where processing can be paused. These moments are also highlighted in the flowchart in the appendix. A standard cleaning step consists of a high power oxygen etch using a Tepla plasma 300, HNO<sub>3</sub> 99% wet etch to dissolve organics and a HNO<sub>3</sub> 69.5% at 110° to dissolve metals (omitted after Aluminium deposition).

Physical vapour deposition or sputtering is used to deposit 100nm pure aluminium (Al) at 350°C for the interconnect and IDT electrodes using a Trikon Sigma 204 PVD tool. This tool uses infrared laser tracking to avoid alignment errors. This laser can not identify a quartz wafer. This can be solved by having a tool owner turn off the laser or have the tool owner place the quartz wafer on a silicon customised carrier wafer (slots are diced in the carrier wafer and pump down time is dramatically increased to avoid floating of the quartz wafer). The first comes at the risk of alignment errors. The latter requires the deposition temperature to go

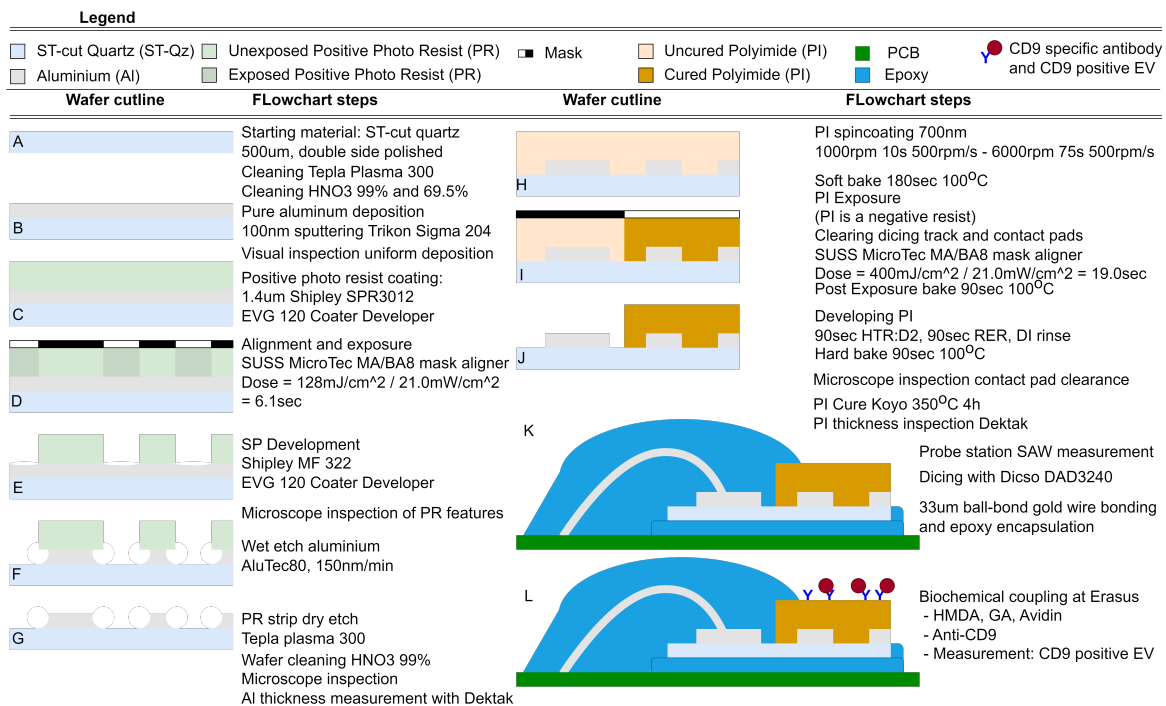


Figure 7.1: Complete fabrication flowchart schematic with processing details. Stylised figure, not drawn to scale.

down to 50°C, increasing Al grain size. Both strategies are experimented with and discussed in Section 9.1.1.

Then, 1.4µm Shipley 3012 photo resist (PR) is spincoated and soft baked by a EVG 120 Coater-Developer using a recipe specialised for glass wafers (more careful wafer handling). With a SUSS MicroTech MA/BA8 mask aligner, the wafers are hard contact exposed with the 'JWD M IDT METAL' mask (Appendix I). The dose is based on the EKL documentation on the required energy and most recent power intensity measurement. For Shipley 3012 1.4µm on Al (Al introduces a 80% correction factor due to reflection),  $E = 160\text{mJ}/\text{cm}^2 \cdot 0.8 = 128\text{mJ}/\text{cm}^2$ . Then the dose =  $128\text{mJ}/\text{cm}^2 / 21.0\text{mW}/\text{cm}^2 = 6.09$  seconds. Development is then finalised by the EVG 120 Coater-Developer, standard 57s single puddle (SP) recipe for the used resist, Shipley MF322 developer with 115°C post exposure bake and 100°hard bake, both 90 seconds.

A microscope visual inspection is done to verify proper feature definition. If not sufficient, the PR can be stripped and the coating, exposure, development step re-attempted.

With a 35°C wet etch, the Al is etched. First, to improve etchant surface contact, the wafers are treated in a  $\text{H}_2\text{O}$ /Triton bath for 60 seconds. Then the wet etch time is calculated based on the most recent reported etch rate (170nm/minute). This gives an indicative etch time, Al thickness / etch rate =  $100\text{nm} / (170\text{nm}/60\text{s}) = 35\text{s}$ . The actual etch time is determined visually by inspecting if the Al is removed from the large open planes. This happens after 62seconds (the etch rate has deviated since the last measurement). A bit over etch (several nm) is acceptable. After a DI rinse (use manual spin dryer to reduce risk of fragile quartz wafer loss), the PR is removed with a Tepla plasma 300 high power oxygen plasma or an acetone 40°C wet etch.

Using a microscope visual inspection the features are inspected. Then with a Dektak 8, the Al thickness is measured. If the layer is not acceptable, the metal can be etched and the process started over.

Polyimide (PI), Fujifilm LTC 9305, photosensitive, is spin coated with a spreading step of 1000rpm for 10 seconds and a spinning step of 8000rpm for 75 seconds. Both ramped up to with 500rpm/s. Four hours before processing, the PI is removed from the cooled storage. First, to avoid condensation in the stock, the whole batch and after 30 minutes the required volume is stored in a separate container, so the stock can be returned to the cooled storage. Approximately 2mL PI is dispensed in the centre of the wafer. After the spin process is finished, the wafer backside is manually cleaned with isopropanol (IPA). This process is described in much more detail in Appendix H.

A soft bake of 180 seconds at 100°C is followed by a visual inspection. Then soft contact exposure in the contact aligner with the 'JWD M WGUIDE CLEAR' mask (Appendix I) to clear the PI from the dicing lines and contact pads and cure it on the SAW devices area is done. The required energy determined from the LTC9305 datasheet is  $400\text{mJ}/\text{cm}^2$ . Leading to a dose of  $400/21.0 = 19\text{s}$ . Then a post exposure bake (PEB) of 90 seconds at 100°C is done.

Then, the PI is developed using the process suggested by the manufacturer using a 90 second HTR:D2 submersion, followed by a 90 second RER submersion development stop. Then a manual DI water rinse, intense enough to flush away the development product but not damage the PI film. Then after a manual spin dry step, a 90 second, 100°C hard bake closes the development process. A visual microscopic inspection is done to verify exposure and development is successful. If not, development can be done again or the uncured PI can be stripped and new spin coating done.

Finally the PI is cured in a Koyo inert gas oven following the cycle: 1 hour to 300°C heat up, continuing 1.30 hour to 350°C, stay for 1 hour at 350°C, then start the cool down in 1.3 hour to 280 deg and finally cool down in 3 hours to 20°C. The temperature rise time is much faster then the set rise time, so the samples are at 350 deg for 4 hours. Now the PI is chemically very stable and can only be removed with a high power oxygen plasma.

Now the wafer can be measured in a probe station to quickly determine device performance. This measurement setup is discussed in Section 8.1.1. The results are the topic of Section 9.3.

After this, the wafer is diced with a DISCO DAD 3240 using R07 BB101 resin bond blade for glass wafers. The wafer is immobilised on a UV release tape so easily, only devices selected for PCB measurements are released. The selected versions are wire bonded using gold ball bonds, 33µm diameter gold wire by a wire



bonding expert.

The PCBs already have their surface mount components soldered on before wire bonding. Now the wire bonds and contact pads are protected by pouring epoxy, doubling as well for the fluid sample. IPA on cloths is used to remove superfluous uncured epoxy from the device delay line area. An extremely tedious process prone to error.

After PCB device characterisation, the matching network is calculated and soldered on. Finally the devices are ready for the functionalisation, the topic of the next section. The last step before mass loading tests.

## 7.2. Functionalisation Protocol

At the Erasmus MC urology lab, in the fume hood, the PCB with SAW device is functionalised for CD9 positive EVs as in Figure 7.2. The complete protocol is included in Appendix M.

Functionalisation protocol  
for PCB sensitivity measurement

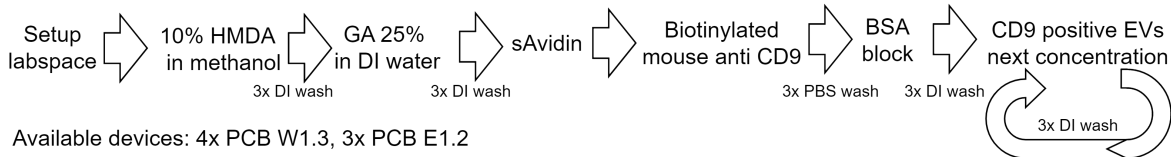


Figure 7.2: Functionalisation protocol.

First, using 10% hexamethyldiamine (HMDA) in methanol, amine groups (-NH<sub>2</sub>) are added to the PI surface carboxyl groups (-COOH). Then 25% glutaraldehyde (GA) in DI water enables the covalent binding of a protein with amine group [121]. Streptavidin (sAvidin) is then covalently bond to the PI surface. Biotinylated mouse-anti-CD9 is immobilised by the biotin-sAvidin interaction. Bovum serum albumin (BSA) buffered in PBS is used to block any vacancies in the sAvidin binding areas. The surface can now selectively immobilise CD9 protein.

The sensor fabrication and functionalisation have been concisely described. In the next chapter, measurement setups using the devices fabricated according to above description are explained.

## 8 | Experimental Methods

Probe station device characterisation and mass loading sensitivity are the two main experiments in this thesis. In this chapter, the measurement setup, protocol, data processing and used equipment is explained. Also, room is given to shortly describe the performed data processing. Results from visual inspections during fabrication are given in the next chapter, their protocol is not relevant here.

### 8.1. Measurement protocols

The device characterisation is about comparing devices and mass sensitivity experiment is a much more individualistic measurement. Their protocols and setup are described separately here.

#### 8.1.1. Probe station wafer level device characterisation protocol and setup

To quickly evaluate the fabricated device performance and possibly determine the yield, all device versions, still together as a full wafer, are measured in a probe station. To limit measurement time for the lab technician, every device version is measured once. By only measuring every version only once, the experiment is blind to process variation or yield issues.

The designed centre frequency around 600MHz imposes the use of RF-probes as the long DC-needle-probes (several cm long) would likely introduce a too big self inductance avoiding the signal to reach the wafer. RF-probes are matched to  $50\Omega$  up to the probe tip. The RF-probes have several contact needles spaced with 150 or 200 $\mu\text{m}$  pitch interfaced with coax cables (SMA or 3.5mm), where the DC probe is interfaced with triax and only supports the contact of 1 trace (so 2 probes are required for a signal and a ground connection, so 4 probes for 1 device). The RF-probe is available in many ground (G) and signal (S) needle configurations. The wafer was designed for GSG probes with 150 or 200 $\mu\text{m}$  pitch. As a device only needs a GS, a dummy G pad is added to avoid tilting of the probe upon landing. Eventually, measurements were done with a GS and SG probe (mirrored configuration). Using RF-probes imposes the use of specialised micro-manipulators. These can in turn only interface with an RF probe station.

The probes were connected with 1.5m long SMA cables to a Keysight P9370A USB Vector Network Analyser. Maximum frequency up to 4.5GHz, 2-port measurements, 115dB dynamic range and up to 7dBm output power. This VNA is connected to a desktop where the Keysight proprietary software is used to interpret and store the S-parameter data and store it in .csv files for later reference. The software is set up to instruct a 1MHz-1001MHz frequency range in 4000 points (250kHz frequency resolution).

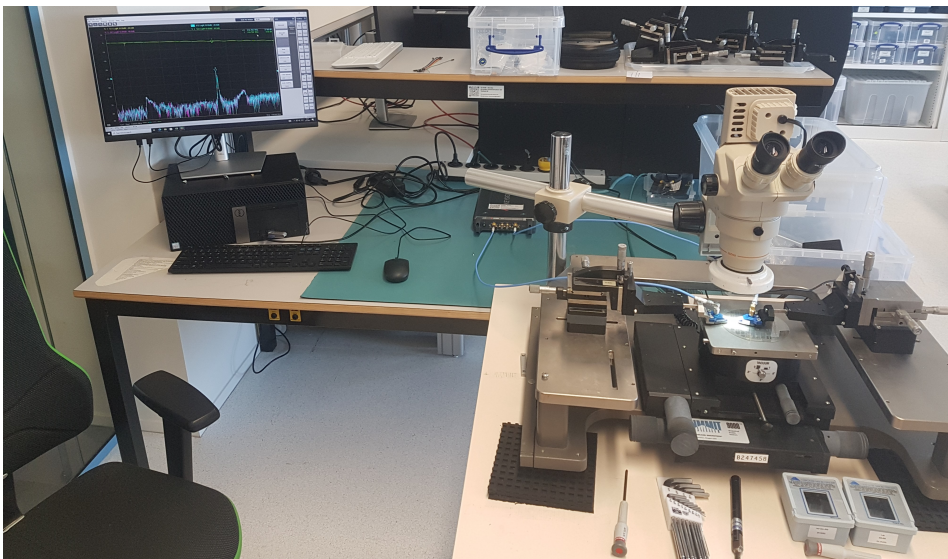


Figure 8.1: Setup used for the probe station wafer level device characterisation.

### 8.1.2. PCB mass loading protocol and setup

After final step of the functionalisation process, the binding of biotinylated-anti-CD9 to strept-Avidin, on the same day the mass loading experiments are conducted. A PCB is first washed 3 times in PBS. Then, 15 $\mu$ L PBS is applied to the sensitive area. Next, the surface is washed three times with PBS and carefully all PBS is pipetted away from the surface. Care must be taken the surface is not dry for too long as it can damage the anti-CD9. Then, 15 $\mu$ L of the lowest concentration to be tested EV containing sample is applied. Then again a 3 times wash with PBS is done before the next concentration is applied. The delay line is protected from air flow with a plastic cap to reduce evaporation of the small liquid samples.

The samples to be tested are PBS, and four concentrations of CD9 positive EV containing fluid, VCaP. These concentrations are a 10000, 1000, 100 and 10 times dilution from the same VCaP stock. These dilutions will be referred to in the results with C1, C2, C3, C4 respectively. EV Quantification method EV Quant [122] is used to determine the particles per mL in the used VCaP stock (measurement results by the lab technician are shown in Appendix M). A concentration of  $3.5 \times 10^{12}$  is determined in the stock. Of these EVs, for VCaP, approximately 10%-20% is CD9 positive as determined previously by the Erasmus MC staff (see Appendix M).

Upon dripping the sample on the delay line, the first measurement is started. The S parameter files have to be named and stored manually. In the first two minutes, the measurements are performed as fast as possible. After two minutes, the measurement frequency is somewhat relaxed to every 30 seconds. Finally, after 10 minutes the frequency is in some cases further reduced until the final measurement at 25 minutes.

To extract data on mass loading from the PCB mounted chip, the S11 and S21 parameters are measured and saved. The NanoVNA has memory for 101 data points. Using the free, open licence, interfacing software 'nanovna-saver', a frequency span from 616MHz up to 625MHz with only the resonance band for the measured W1.3 devices is set up. This band is subdivided in 20 parts, each measured with 101 points, leading to a 2020 point measurement with a frequency resolution of 4.46kHz. As mentioned in the NanoVNA documentation, the 101 point sweep takes approximately 1.5 seconds. It was measured the 2020 point measurement takes about 20 seconds. Then the nanoVNA with Amphenol RF 609.6mm SMA coaxial cables is calibrated by disconnecting the PCB and using the calibration kit included with the nanoVNA (short, open, load, isolation, through).

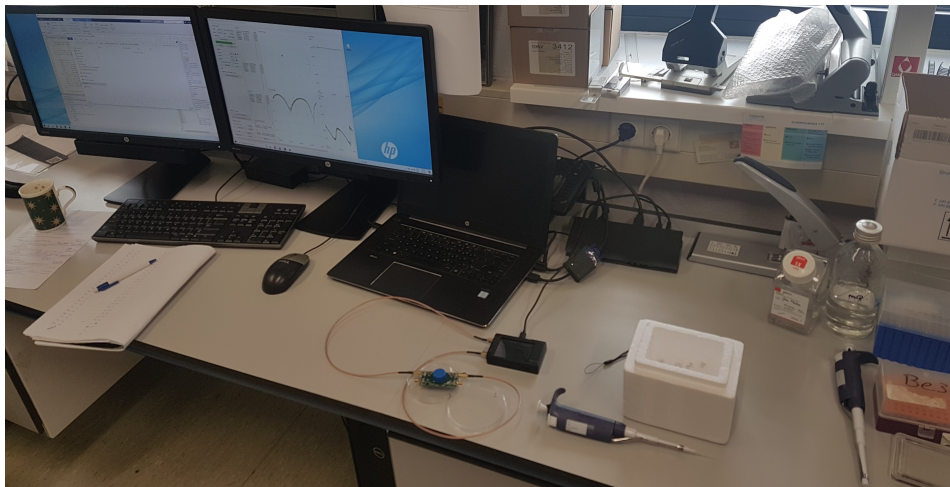


Figure 8.2: Setup used for the mass loading experiments.

## 8.2. Data processing

After raw S-parameter data over a frequency range is obtained, the applicable information is extracted and normalised with the following techniques. To enable comparison of probe station data of different device versions, the measurements are normalised according to Section 8.2.1. Probe station data is used to compare devices as described in Section 8.2.2. PCB measurements are focussed on determining the sensitivity for surface mass loading (or gravimetric sensing), Section 8.2.3.

### 8.2.1. MATLAB artificial matching

To enable comparison between measured device performance in terms of S21 insertion loss, a computational matching normalisation method is used. As different IDT-geometries have different impedance, their reflection coefficient differs and in terms of insertion loss (IL) of the S21 parameters, their comparison is not 'fair'. It is solved by designing an optimum achievable matching network for every measured device. The effect of the designed matching network is then calculated as in Figure 8.3.

As every PCB has space for a  $\pi$  matching network, the optimum matching is also calculated using the method described in Figure 8.3. Using a Smith chart, the suitable component values are determined, then the effect is validated and optimised iteratively with the MATLAB code.

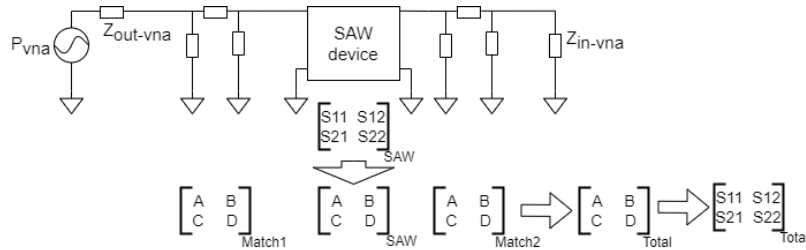


Figure 8.3: Matching artificially using MATLAB. First calculate the ABCD-matrix for the  $\pi$  matching network. Rewrite the measured S parameters to ABCD-matrix. Determine the total ABCD-matrix and convert it back to S-matrix. Then the effect of the matching network is computationally (artificially) determined.

### 8.2.2. Full wafer device characterisation measurements IL data

Data processing (e.g. artificial matching as discussed in Section 8.2.1) and visualising data is done using a MATLAB script reading the .csv files. To compare device version performance the lowest IL magnitude and frequency (before and after artificial matching) is manually stored in Excel. Then the influence of IDT variables is envisioned. As every version has only one measurement, no possibilities for averaging are available and inter/extrapolating is not reliable.

### 8.2.3. PCB measurements phase shift

The data, obtained as S21 and S11 parameters, is used to extract the S11 Smith chart, the S21 insertion loss (IL) and the S21 phase. Using the Smith chart, it is checked if the calibration is still correct. Based on the S21 IL and S21 phase, a frequency band is chosen where the received signal is sufficiently strong and the phase is dropping linearly as illustrated in Figure 8.4. This band is for all devices 1.6MHz around 621.8MHz. In this frequency band, using the Matlab function 'polyfit()', a linear regression estimation of the phase is made. Then the mean and standard deviation from this estimation are calculated. This gives per data set a mean phase. Then, for timed data sets, this information can be visualised in an absolute phase plot and in a normalised phase plot where the first measurement (at t=0s) is considered  $\Delta\phi = 0^\circ$ . Alternatively, information in the slope of the linear regression estimate  $\frac{\Delta\phi}{\Delta f}$  and the normalised version of this data is visualised.

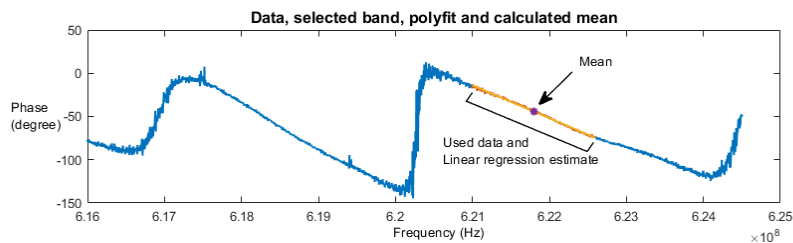


Figure 8.4: Example of data selection and processing to extract less noisy phase at some selected frequency.

## 9 | Results and Discussion

First the fabrication and functionalisation protocol results are discussed. Then the results of the probe station and PCB measurements are given and discussed. It will be shown the fabrication process is satisfactory robust and the yield is high. The probe station measurements prove valuable in quick device characterisation. The mass sensitivity measurements are not conclusive on the sensitivity for gravimetric sensing for CD9 positive EVs.

### 9.1. Fabrication

Challenges and observations during the fabrication are discussed. First, a successful fabricated PCB with SAW device is presented in Figure 9.1. SMA connectors are soldered, matching network is soldered, the SAW die is wire bonded and a dual purpose protective and fluid well epoxy well is placed around the delay line. This particular version can be used differentially with the right measurement equipment. The wirebonded device on this picture is the 3rd one from the top and the bottom one.

This was not achieved without several steps requiring re-consideration. These are presented next. According to the fabrication order, starting with challenges in the aluminium deposition. Then a note on the achieved feature size and a remark on flat alignment, both related to exposure. Rounding off the fabrication with notes on the dicing process.

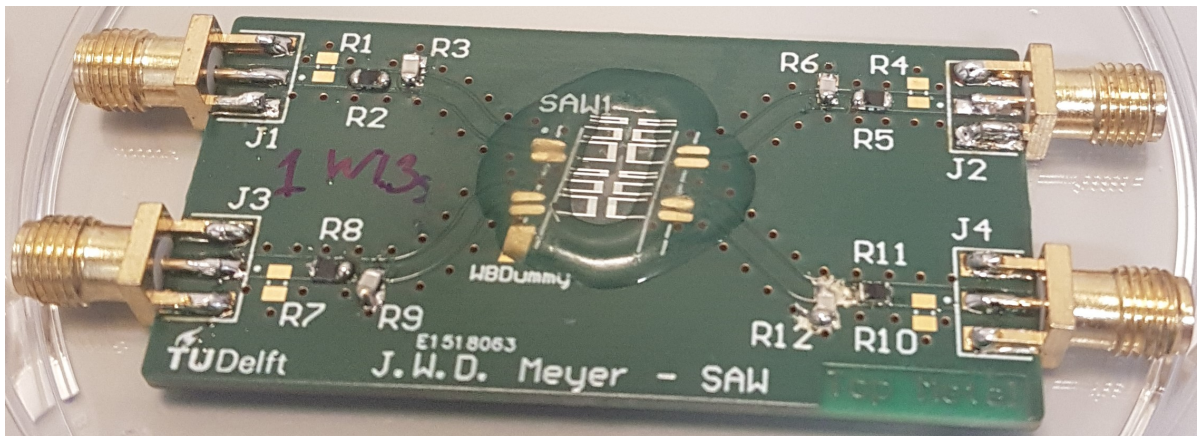


Figure 9.1: Finalised PCB #1, with W1.3 str Love mode SAW device version in place. 100uL capacity epoxy well placed around the delay lines. Matching network soldered on.

#### 9.1.1. Floating in sputter coater

In two separate runs, a total of 5 quartz wafers were processed of which 3 did not survive, of which two (near miss for a third) broke during the aluminium deposition procedure. When coating the quartz wafers with pure aluminium, the laser tracking system can not detect the quartz. There are two possible solutions, turn off the laser tracking or use of a specialised carrier Si wafer (with grooves to allow air to escape between the process and carrier wafer).

In the first solution, upon returning the quartz wafer to the wafer carrier, the wafer is broken. Debris is found in the loading chamber, not the deposition chamber. It is suspected the quartz wafers start floating in the Trikon Sigma deposition chamber causing misalignment. As the laser system is turned off, this is not detected and upon return to the wafer cassette, the wafer breaks.

It should be remarked for every run a SSP Si wafer is used as first wafer for debugging purposes, which has no trouble at all in the Sigma. The prior processing (only plasma and wet cleaning) are exactly equal.

The Using Si carrier wafers (requiring an experienced user to adjust pumpdown speed to avoid the quartz wafer floating off of the carrier wafer), solves this breakage, but the maximum processing temperature is reduced to 50°C. This deteriorates Al grain size, maybe causing trouble in the Al wet etch later.

The latter had issues after Al wet-etch (Figure 9.2). This is likely caused by poor adhesion of the Al to the quartz. Further investigation is required to determine the cause of this. It could be related to the lower deposition temperature, but also, a wet cleaning step was omitted before low temperature deposition. Then particles might have caused poor adhesion.

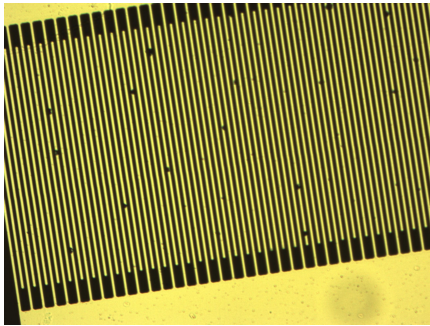


Figure 9.2: Metal showing many holes after Al wet etch. Picture taken after PI develop.

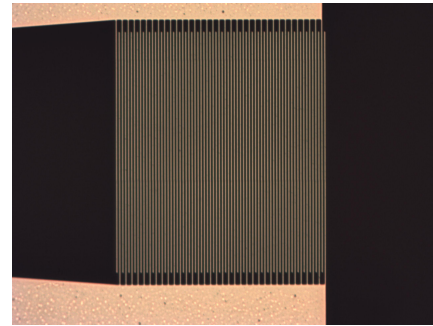


Figure 9.3: Example of very well defined metal without defects after PI cure step.

### 9.1.2. Feature size

With the exposure settings described in Chapter 7, structures down to 1 $\mu$ m critical dimension (CD) were fabricated (Figure 9.4). This is below the CD expected from both the mask and contact aligner. The yield of these 1 $\mu$ m CD structures however, is only 50%.

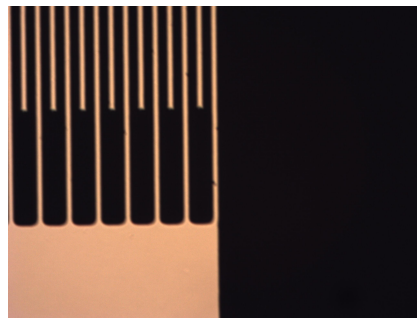


Figure 9.4: Microscope photo of a 1 $\mu$ m CD structure.

### 9.1.3. Flat alignment

The stepper has automatic flat alignment. In the contact aligner, this is not the case, so there is some deviation from the optimal SH-direction alignment. By Mazzamurro et al. [99], it is shown the coupling coefficient for SH waves suffers little from a slight propagation direction error. However, the displacement in z-direction is increasing rapidly when the orientation is not exactly 90°. This z-displacement will be dampened by both the waveguide and sample liquid. This leads to increased insertion loss. So the wafer must be very carefully placed in the contact aligner, or, an additional layer with alignment markers has to be added using the stepper.

### 9.1.4. Dice blade

Dicing, done in a DISCO DAD 3240 using R07 BB101 resin bond blade for glass wafers leads to a large loss of blades. The crystalline quartz is even harder than glass, requiring blades designed for quartz (R07 BB200) with a longer blade life at the cost of feed speed and cut quality according to the Disco R07 series documentation.

### 9.1.5. Dice markers

Using any metal as dice markers causes a risk for short circuits as the dicing debris is conductive. This is an easily avoided risk by just using a polymer as dice marker. In this design, both PI and Al are used to indicate dicing lines. The risk in this specific design is however limited as all small feature size conductive elements in this design are protected by a polymer layer.

## 9.2. Functionalisation

After the timed measurements using CD9 positive EVs, the efficacy of the functionalisation process was verified. By attaching antibodies against mouse antibodies, linked to horseradish peroxidase, it is possible to colour the delay line if indeed mouse based antibodies are attached to the delay line. The anti-CD9 used in the functionalisation process is mouse based (MaCD9). This makes the goat-anti-mouse-horseradish peroxidase (GaM-HRP) test a solid check on the functionalisation process. In Figure 9.5, it is shown the GaM-HRP is sticking to PCB 1 on the right by the brown colour after adding horseradish. PCB 2 on the left did not receive the GaM-HRP, but also got horseradish dripped on the delay line. It shows no brown colour making it a clear reference, and proving the colour on PCB 1 can only be from the GaM-HRP attaching to MaCD9. It can be concluded the functionalisation protocol was successful and anti-CD9 is immobilised on the delay lines of the functionalised delay lines. For further details on this test refer to Appendix M.

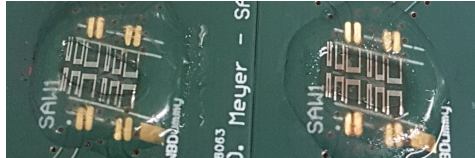


Figure 9.5: HRP staining of PCB 1 and PCB 2 where goat-anti-mouse antibodies conjugated with horse radish peroxidase (GaM-HRP) are added to PCB 1. Both PCBs are functionalised and used for EV capture in timed measurements. After adding horse radish in buffer solution to both samples, only PCB 1 shows a clear brown colour. This indicates the colour is due to GaM-HRP, binding to mouse derived anti-CD9. It is then proved the anti-CD9 is successfully immobilised on PCB1. Here PCB 2 serves as a negative control. It is assumed the capture of CD9 by anti-CD9 is a highly reliable process.

## 9.3. Full wafer device characterisation measurements interpretation

Before dicing, full wafer measurements are done to check if the fabricated devices show activity associated with Love mode SAWs and the best device version is selected to be used on the PCB. First the general output of a probe station measurement is discussed. Next the effect of stepping the IDT variables is shown. Then the optimum device is selected. Following this, the different wavelength designs are discussed. Finally, a probe station artefact is discussed and the simulation and probe station measurement is qualitatively compared.

### 9.3.1. Typical full wafer device characterisation measurement result

This is discussed to indicate where the data is derived from that is used to determine what device performs best. A typical probe station device characterisation measurement S21 parameter magnitude looks like a single trace in Figure 9.6. Zoomed in on the passband in Figure 9.7, a clear bandwidth (BW) of about 9MHz, a fractional BW of about  $9/618=1.5\%$  for the W1.2 and W1.3 versions. The magnitudes range from -31dB, to versions showing no passband at all, just a noise floor at -50dB or -60dB.

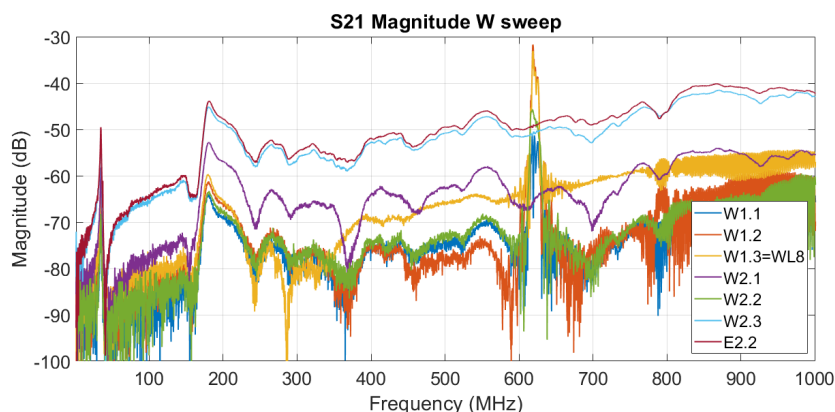


Figure 9.6: Full wafer probe station measurement of devices with different aperture, S21 magnitude.

Most measurements without clear passband, such as W2.1 in Figure 9.7, showed at least one contact pad to not be scratched, indicating bad probe contact. Another cause for a missing passband can be due to fab-

rication error. But all measured devices were also microscopically inspected for fabrication failures. On the measured devices, non were discovered.

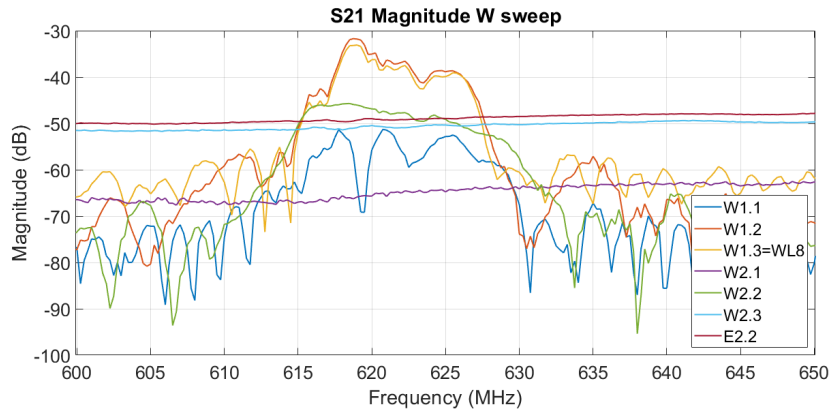


Figure 9.7: Full wafer probe station measurement of devices with different aperture, S21 magnitude zoomed in around resonance band.

For the W1.3 version, the S21 parameter phase is shown in Figure 9.8 demonstrating a big phase drop in the passband. This is ideally sought for as the phase sensitivity for surface mass loading then is large (small  $\Delta f$  causes big  $\Delta\phi$ ).

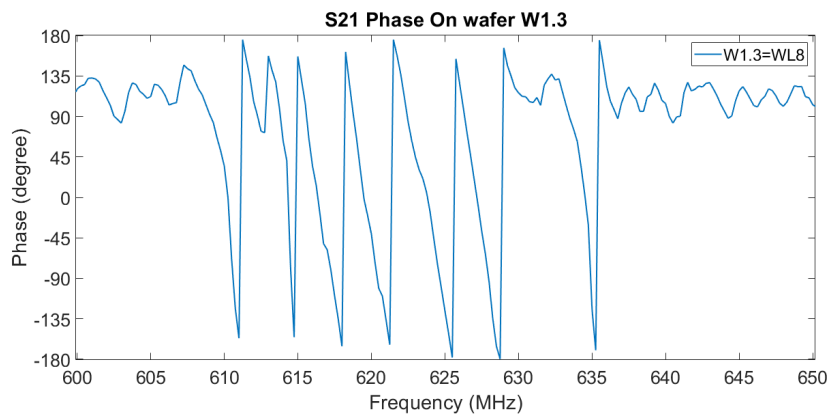


Figure 9.8: Full wafer probe station measurement of device W1.3, S21 phase.

Different IDT variable values change the device version impedance and thus reflection coefficient as becomes clear in the Smithchart for the S11 parameter shown in Figure 9.9. It shows the same device versions shown in the S21 magnitude and phase plots in figures 9.6 and 9.8 respectively. This change of reflection coefficient stresses the need for matching before a fair comparison in performance can be made.



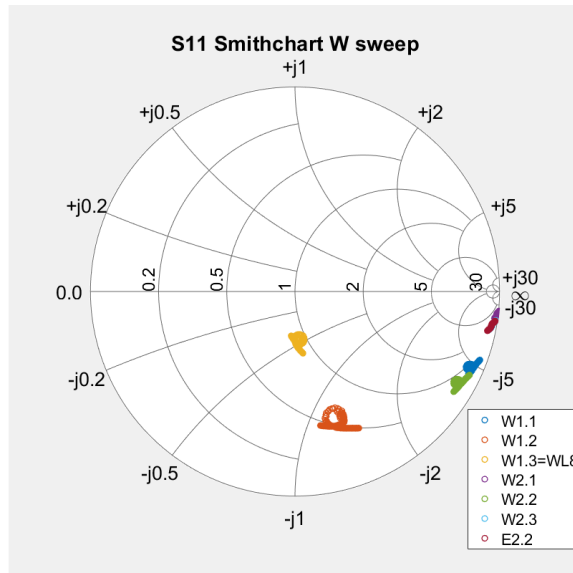


Figure 9.9: Full wafer probe station measurement of devices with different aperture, S11 Smith chart for the frequency band around the resonance band.

9.3.2. Wavelength and measured frequency

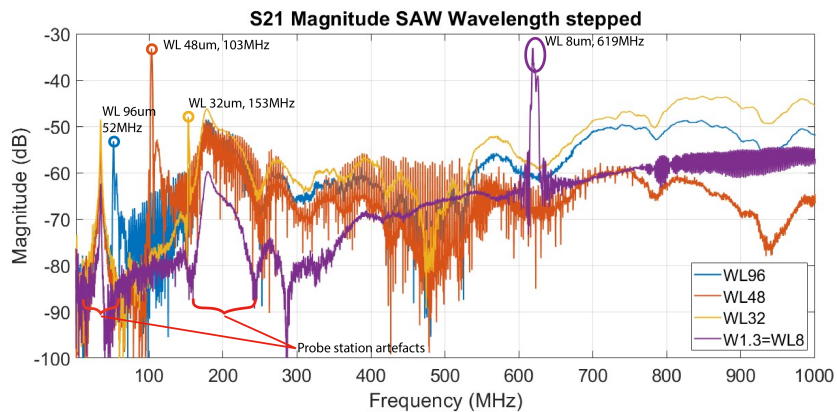


Figure 9.10: Full wafer probe station measurement of decreasing wavelength devices showing decreasing the wavelength increases the resonant band to higher frequencies.

Figure 9.10 clearly shows the resonance band changes when the wavelength is changed. Using the relation given in equation 4.9, the propagation speed of the acoustic wave in the delayline is calculated. All speeds are adhering to the condition given in Section 4.5.1 that the Love mode wave speed is between the SH wave speeds supported by the substrate and waveguide.

Table 9.1: Fabricated wavelengths and measured resonance band centre frequencies and calculated wave speed

WL	f0	according waves peed
96um	52MHz	4968m/s
48um	103MHz	4958m/s
32um	153MHz	4896m/s
8um	619MHz	4952m/s

9.3.3. Spurious pass bands

Spurious passbands are demonstrated in Figure 9.6 and Figure 9.10 as these show IL peaks near 34MHz and 180MHz of which the origin is not yet understood. They are present in all probe station measurements where

a SAW is detected (even if the devices are oriented along a different crystal axis as in Figure 9.11). They are however not measured in any PCB measurement (Figure 9.16). Some hypotheses were considered regarding the origin of these bands.

The peaks might originate from spurious SH or L waves. Again using the relation from equation 4.9, it is determined that the 180MHz wave corresponds to wavelengths around 30um and the 34MHz wave around 155um. Then several wavelengths fit in the thickness dimension of the wafer and maybe a QCM mode is excited, though unlikely as it should be filtered out by the IDT.

Another hypothesis is that the waves are somehow modes supported on the wafer due to the surrounding SAW devices. This is also unlikely as the peaks are very constant even though the measured devices locations change a lot and the surroundings are also very inconsistent.

Then finally, a third hypothesis is that the frequency bands arise due to calibration errors or artefacts of the measurement setup and equipment. It would best explain why the peaks arise as soon as a good SAW device is measured, but are then consistent, almost completely device independent. Also, in PCB measurements such as Figure 9.16 the spurious passbands are not present.

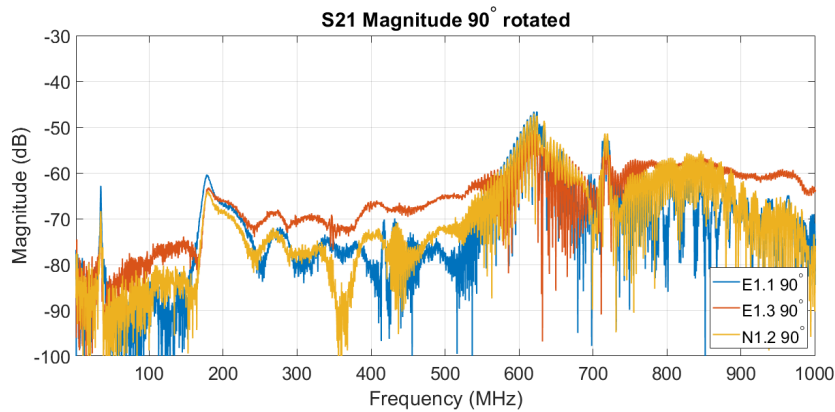


Figure 9.11: Full wafer probe station measurement of several device versions placed 90°rotated on the wafer so the quartz crystal orientation should now support Rayleigh-mode. Included to check if other measurements are indeed likely to be Love-mode and as backup if an error is made in wafer orientation.

### 9.3.4. Full wafer device characterisation measurement result deviation from simulation

The passband centre frequency and bandwidth and insertion loss of the simulation and measured devices are not in perfect agreement. The time impulse simulations, as explained in Section 5.1.4, are only suited to predict the device optimal centre frequency for different waveguide thicknesses. The simulation insertion loss can only be used relatively to similar simulations (for example to determine the optimum waveguide thickness).

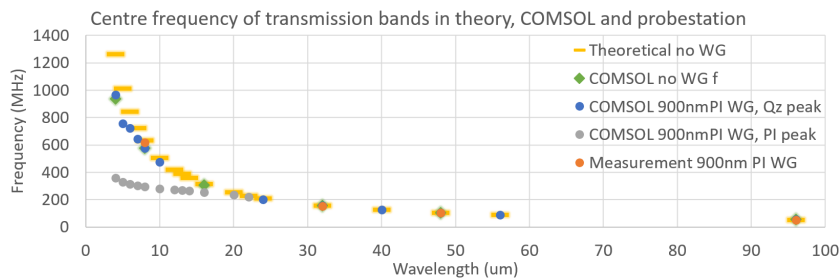


Figure 9.12: Passband centre frequencies calculated without waveguide, modeled in COMSOL with and without 900nm PI WG and measured in the probestation with 900nm PI WG. For big wavelengths and low frequency, measurement and simulation are in good agreement. At thinner WG thickness, deviation starts.

The measurements show a centre frequency deviating from the simulation prediction, which might be explained by further inspection of the simulation results. For thicker waveguide thicknesses, two passbands seem to appear. A consistent passband near 600MHz, and a much lower passband that was assumed to be due to the Love mode SAW as it corresponds to the eigenfrequency of the unit wavelength simulation. It is

well possible, this mode is dampened too much due to the relatively high losses in the WG as compared to the substrate. Then the near 600MHz passband is expected to be coupled to the SH-mode in the quartz substrate.

Alternatively, for a constant waveguide thickness (900nm PI as fabricated), at big wavelengths (low frequency) a single passband is simulated. Whereas at high frequencies, two passbands show up in the simulation. These are shown in Figure 9.12. The high frequency passband is close to the measurement result, whereas the low frequency passband, hypothesised to be the WG eigenmode, is not distinguishable in the measurement.

This hypothesis is ideally tested by also measuring samples without PI waveguide. Unfortunately, due constrained equipment availability, this remains a recommendation.

As already hypothesised in Section 6.5, the ideal WGTH is expected when it is such that it causes the lower and higher passbands to coincide. Unfortunately, this thickness for a ST-quartz substrate with PI waveguide is expected to be 444nm, which could not be achieved in processing.

## 9.4. Full wafer device characterisation measurement optimal devices

After the interpretation and validation of the probe station measurements, optimum SAW device versions can be decided on for the PCB tests. This is the topic of the next two sections where first an 8 $\mu$ m design is selected. Then a lower frequency version is selected as backup.

### 9.4.1. Best performing fabricated device

The W1.3 device is chosen as it is one of the best performing devices and it has a large aperture, leading to a delay line with a larger area for biochemical coupling. If concentration of the analyte to detect becomes really low, the chance of interfering with the delay line surface area should be made as large as possible by creating a large sensitive area.

All S21 magnitude measurements, excluding measurements without clear passband and phase shift, are summarised in Figure 9.13. From these, only the stepped L can be fairly compared as all IDT impedances are equal, only a differing distance between them. And indeed a relation between length and insertion loss is discovered. The figure also shows without any matching, W1.2 and W1.3 have the best IL at the centre frequency.

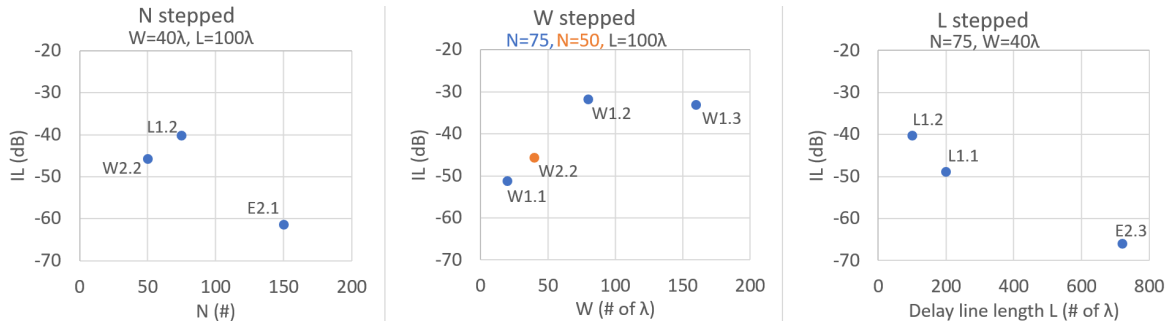


Figure 9.13: Full wafer probe station measurement of all devices, excluding different design wavelength and not responsive devices.

Using a normalisation method based on matching computationally using Matlab, the insertion loss can be improved even more. This is also enabling a more fair comparison between different IDT geometries. The best improvement was attained for the W1.2 device. Still, due to the larger aperture, and thus area, W1.3 is expected to function optimally for mass sensitivity measurements on the PCB.

### 9.4.2. Best performing lower frequency device

Also, different wavelength devices were fabricated to verify if the measured signals are behaving as a Love mode SAW. Moreover, the state of the art literature often uses lower centre frequency designs. These are included here as backup if the higher frequency designs are not satisfactory, for this purpose, the WL 48 version is selected.

The wavelength centre frequency relation is highlighted in the left part of Figure 9.15. On the right hand side of this figure, the matching normalised IL is shown. Due to the vastly different IDT geometries, even after matching as well as possible, comparing directly should be treated with care. It can be concluded, WL 48 has

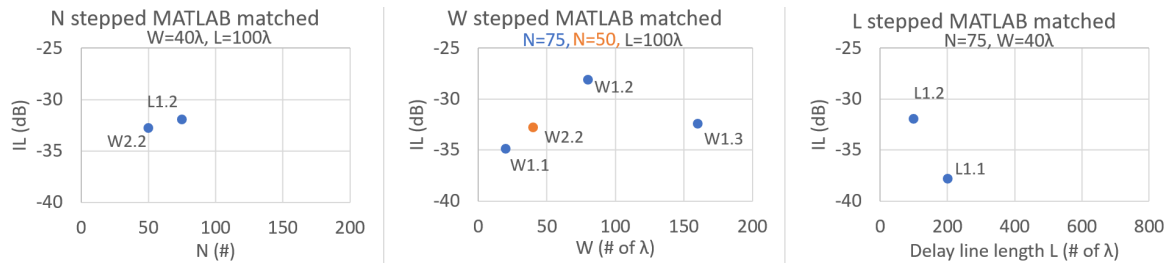


Figure 9.14: Full wafer probe station measurement of all devices, artificially matched using MATLAB data processing, excluding different design wavelength and not responsive devices.

the best potency to be a well functioning device due to its highest IL. To the reason of this, no conclusion can be drawn due to the many changing variables.

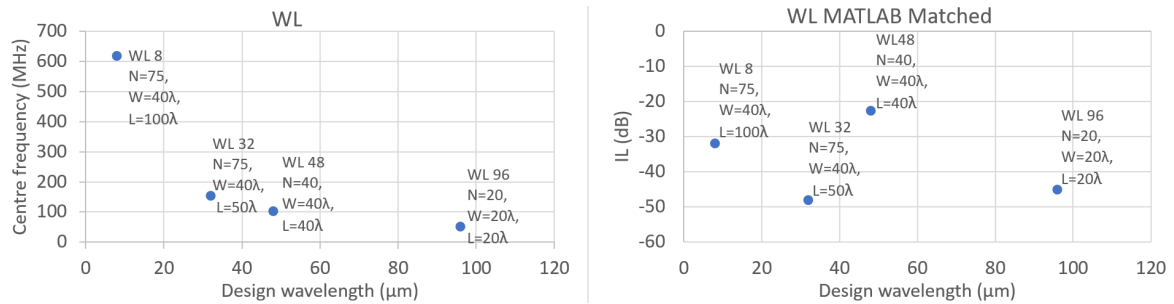


Figure 9.15: Full wafer probe station measurement of all WL devices. Left measured centre frequency. Right, insertion loss, artificially matched using MATLAB data processing. Both excluding not responsive devices.

## 9.5. PCB characterisation

The devices measured with a NanoVNA on the PCB show a drop in S21 IL when liquid is used, resulting in noisy measurements and the devices show big sensitivity to fluid composition and fluid sample volume. To find limitations of the used NanoVNA setup and protocol these next measurements were done.

The NanoVNA and full wafer setup show very consistent performance when dry (Figure 9.16). The NanoVNA shows a 10dB deteriorated noise floor compared to the probe station measurement. This is likely due to the much more sensitive VNA used in the latter experiment. The PCB measurement does not show the two pass bands at lower frequencies as was discussed before. Importantly, the passband is not deteriorated, an equal IL, centre frequency and bandwidth are observed. Concluding, the device was not deteriorated by PCB placement, wirebonding and adding an epoxy well.

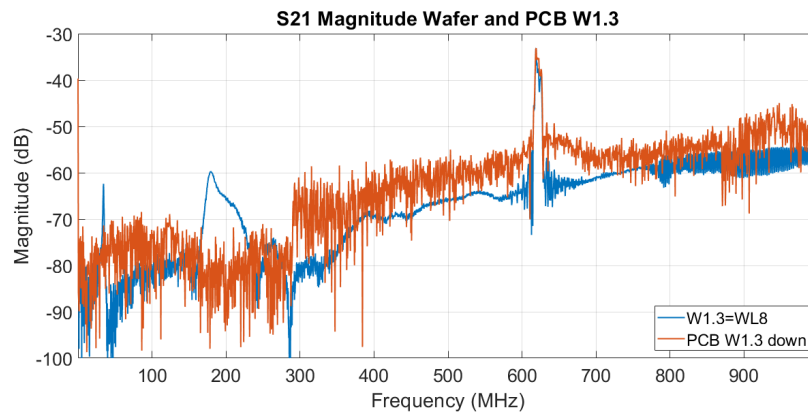


Figure 9.16: On wafer probe station measurement and PCB placed measurement of the S21 IL of the W1.3 version showing great resemblance. Additionally, the spurious passband from the probe station measurement has disappeared.

### 9.5.1. DI, 50/50 DI/PBS, PBS loading PCB1

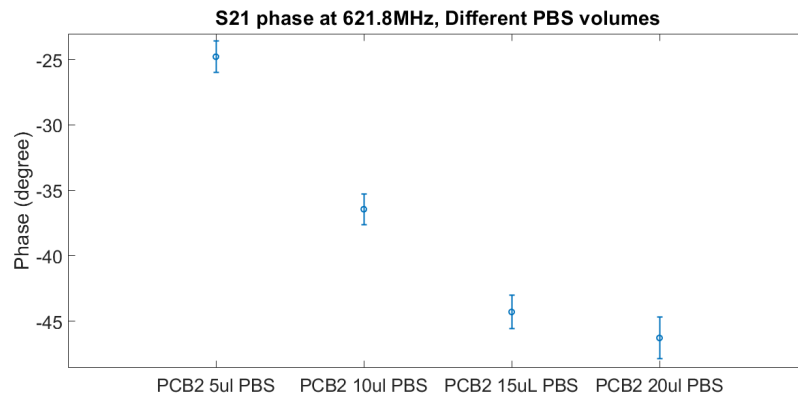


Figure 9.17: By loading several PBS volumes with in between wash steps on the delay line the influence of sample volume on the phase is determined. The measurements are taken at  $t=30s$  after deposition of the test volume PBS sample.

The devices have a cross sensitivity for liquid composition as it is shown DI water, and PBS can be differentiated by the measurement setup in Figure 9.18. This measurement is done before the functionalisation protocol was executed. Unfortunately, from only this measurement, it can not be derived if the phase shift arises due to the difference in density or difference in conductivity or any other difference between the two liquids.

### 9.5.2. PCB2 volumes

The sample volume on the device has a profound impact on the phase shift (Figure 9.17). Several volumes were tested as it is expected in the mass loading tests, the sample volume can differ some micro litres.

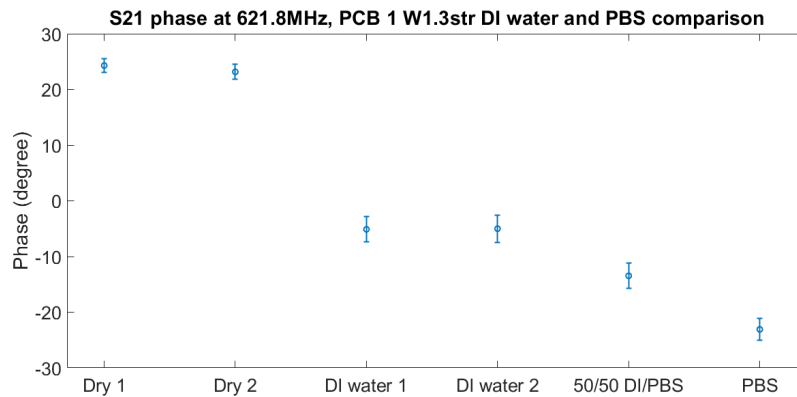


Figure 9.18: Subsequently, the device is measured dry (Dry 1), with DI water (DI water 1), then 50/50 PBS and DI water, then only PBS, then again DI water after a DI wash (DI water 2) and finally the dried device (Dry 2).

Higher volume measurements would be of interest to determine if this behaviour stabilises after a certain volume. The necessity for a well controlled sample volume becomes clear. As it is damaging to the antibodies to completely dry the functionalised surface, this control poses a challenge due to the left volume on the surface between samples.

### 9.5.3. PCB3 PBS 15uL repeatability

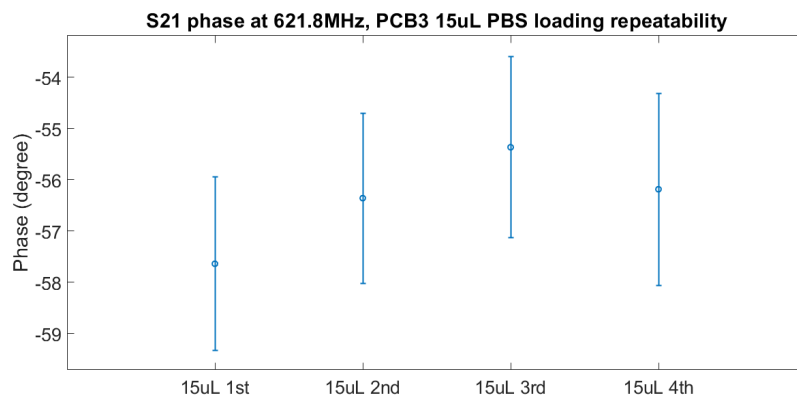


Figure 9.19: The consistency between measurements is tested by loading the delay line with 15uL of PBS for 4 times with wash steps in between. Every measurement is taken at  $t=30s$  after the next PBS 15uL volume is pipetted on the delay line.

Inter concentration consistency is tested by repeating the loading and pipetting away, washing and re-loading with PBS on the delay line and it is found the loading and washing process causes a phase shift. In Figure 9.19, a variation of 3 degrees is found as the error bars show, and between the measurements, up to two degrees phase shift is observed. This might be due to inaccuracies in the applied volumes as is tested in Figure 9.17.

### 9.5.4. On PCB Matching

This shows DI water loading significantly changes the required matching compared to the dry delay line and the implemented matching circuit effect deviates from the calculated effect. The digital and physical match is both using a single 5pf shunt capacitor and a completely symmetrical matching network and in and output. Figure 9.20 shows how well the circuit impedance matching to 50 ohm is achieved. Also, it becomes apparent adding a fluid changes the start impedance and will change the required matching network. Finally, this figure shows the calculated effect (referred to with 'digitally matched') of matching is different from the achieved effect by implementing the matching network.

In Figure 9.21, the IL shows applying a fluid decreases the signal strength at the output. It is predicted matching will improve the received signal strength and this is confirmed with a physical measurement, though

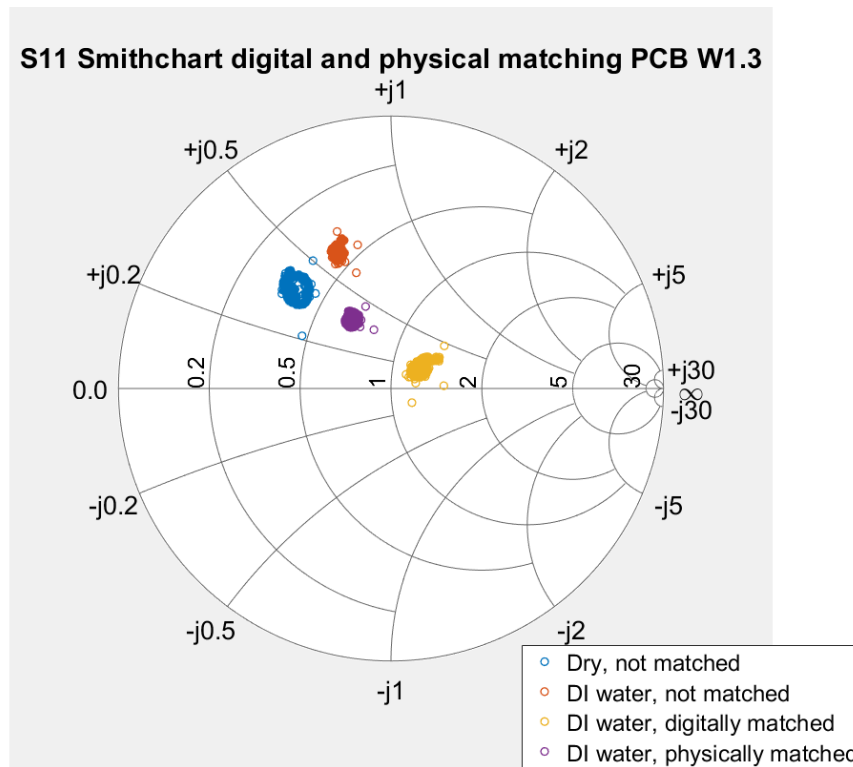


Figure 9.20: S11 Smith chart for the W1.3 str device on a PCB in dry and DI loaded conditions.

be it to a lesser extent. The phase is shown in Figure 9.22. Fluid dampens the phase jumps but in all cases the phase jumps stay distinguishable.

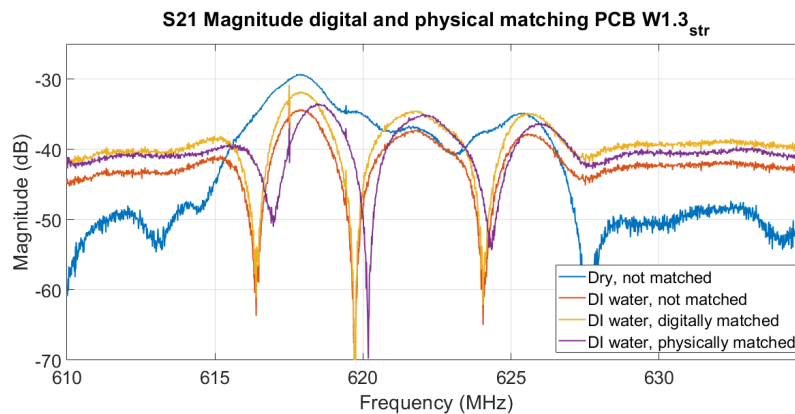


Figure 9.21: S21 insertion loss for the W1.3 str device on a PCB in dry and DI loaded conditions showing decreased received signal when the SAW device is loaded with a fluid and matching improves the received signal.

Comparing figures 9.9 and 9.20, it becomes apparent the impedance is changed much by placing the sensor on the PCB. Matching is first computationally applied to the probe station measurements to more fairly compare performance. Then after placement on the PCB, the same Matlab script is used to determine the required matching components on the PCB.

Furthermore, in Figure 9.20, it stands out the impedance of the device is significantly changed upon adding a liquid sample. Eventually, for the liquid sample loaded, PCB mounted device, the matching is computationally determined using Matlab. In the same figure, the actual effect of the implemented matching circuit is shown. The effect is much lower than was expected from the computation. This might be due to non-idealities in the real component that were not taken into account in the calculation. Furthermore, the real component is subject to spread, that was not measured. To get a better physically implemented match-

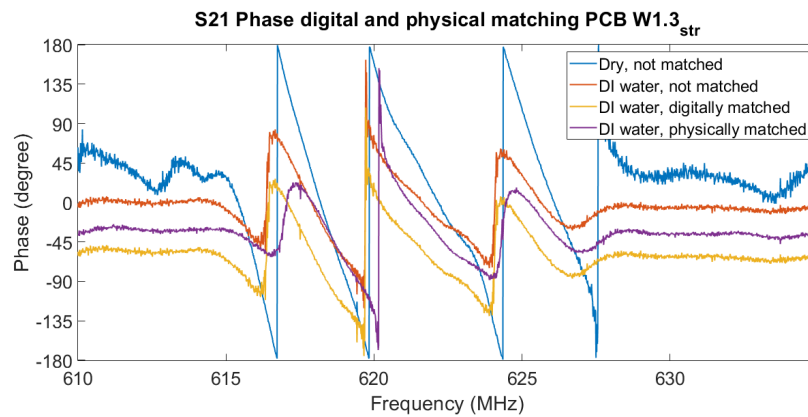


Figure 9.22: S21 phase for the W1.3 str device on a PCB in dry and DI loaded conditions.

ing network, several component values should be experimented with, using the calculation mostly to find the order of magnitude.

It should be noted, as the insertion loss of the S21 parameter in the transmission band is over the noise floor of the measurement equipment, the matching is not very stringent. In Figure 9.21, it is shown in all cases the insertion loss indeed stays above the noise floor. In Figure 9.22 the detrimental influence of a fluid sample on the slope of the phase shift becomes clear. This is expected to harm the sensitivity for mass loading, as a small frequency shift will result in a smaller phase shift.

### 9.5.5. Love mode wave

The measured S21 IL passband is hypothesised to be supported by Love mode SAW energy transmission. Though an input signal results in a received signal at the output, it is not automatically proven this is due to energy transmission by a Love mode SAW. However, the good relation between the wavelength, centre frequency and according wave speed in Table 9.1 resulting in a wave speed (around 4950m/s) just below the SH speed of bare quartz (5050m/s as in Table 6.1) is a good indication of a Love-mode energy transmission. Furthermore, Figure 9.11 shows a expectedly heavily dampened transmission band, indicating Rayleigh mode in the rotated devices, affirming the hypothesis a Love-mode is excited in the other devices.

Another indication was found when HMDA is dried in as one of the steps in the functionalisation protocol, killing the passband, proving the transmitted and received signals of the IDT's is not of electromagnetic, but of acoustic nature. When the HMDA is crystallised on the surface as shown in microscope picture 9.23 an input signal is not leading to a signal on the output anymore. The signal transmission is restored upon dissolving the HMDA crystals in methanol again. The added solid crystal on the delay line is hypothesised to impede surface movement and kill the SAW. The dried in material is not expected to affect any electromagnetic properties.



Figure 9.23: Microscope image of PCB 9 after 16 hours pass since the HMDA step (during the day long dry period) showing some crystallised material (expected to be HMDA) on the IDT.



### 9.5.6. PCB characterisation conclusion

It can be concluded the PCB setup with NanoVNA experimental setup has serious cross sensitivity for sample contents (not mass specific), is sample volume sensitive and has large variance in general. The implemented matching circuit effect was not as accurate as the calculations predicted reducing transmitted energy to the delay line. It is expected the excited SAW mode is a Love-mode as designed.

This all results that the next experiments with EVs and functionalised delay line area should be treated with care. It is concluded, the mass loading measurements are most reliable if the active capturing of the antigen over time is monitored and the phase shift can be normalised to the first measurement. Directly comparing measurements after a new sample was added is not feasible due to the found shift between equal samples.

## 9.6. Mass loading experiments

First, relevant plots of the S parameters are shown in figures 9.24, 9.25 and 9.26 for a single mass loading measurement to give an idea of the obtained and available data. Then the extracted information after data processing is shown and discussed.

### 9.6.1. S parameter plots of timed data

The IL is not distinguishably changed after introduction of EV containing samples. In the measurement setup shown in Figure 8.2, and following the protocol as described in Section 8.1.2, data is obtained as shown in figures 9.24 and 9.25. In the first, it is confirmed the measured signal is in the transmission band of the SAW device. The latter figure shows the phase shift. The reflection coefficient is very stable as in Figure 9.26, so the measurements on the same device with the same sample over time are well comparable without normalisation. It becomes apparent that there is no large, easily detectable phase shift. Data processing is required.

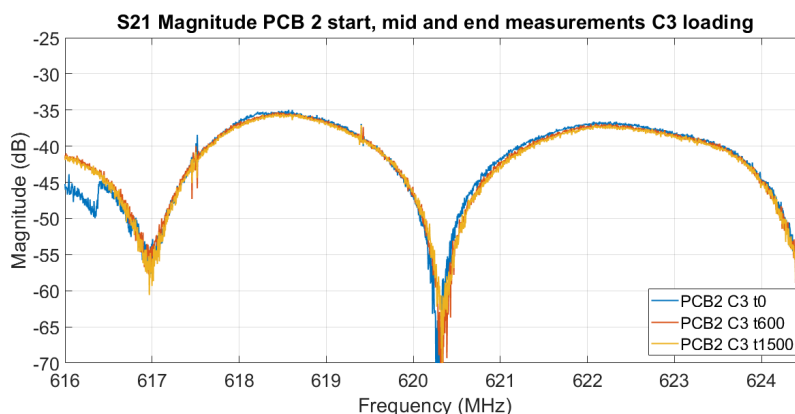


Figure 9.24: S21 magnitude data for three time points showing very little visible change.

### 9.6.2. Timed mass loading measurements PCB 2

The absolute phase in Figure 9.27, contains little information as there is no clear relation between between the absolute phase and the different concentrations. The samples are tested in order of appearance in the legend. First, PBS, then C3 (EV containing sample diluted 100 times), then C4 (EV containing sample diluted 10 times) and finally a larger sample volume of C4. The only clear information is that the phase is noisy, the phase variance, shown with the error bars, is much larger then any total phase shift over time.

The phase normalised to  $0^\circ$  for  $t=0$  for PCB 2 in Figure 9.28 seems to show that the 2 volumes with highest concentration C4 have a similar phase shift over time while the C3 has a smaller phase shift. It can be hypothesised C4 causes a slight shift and C3 is a too low concentration and behaves similar to the null condition, PBS. However, the variance is relative to the detected phase shift very significant and no strong conclusions can be drawn.

Then the slope of the phase is shown in Figure 9.29 with phase variance divided by the chosen bandwidth shown in the error bars. When this measure is normalised by setting the first measurement moment,  $t=0$ s, to  $\Delta\phi/\Delta f = 0^\circ/Hz$ , again, the two C4 concentrations behave comparable, C3 and PBS both have a decreasing

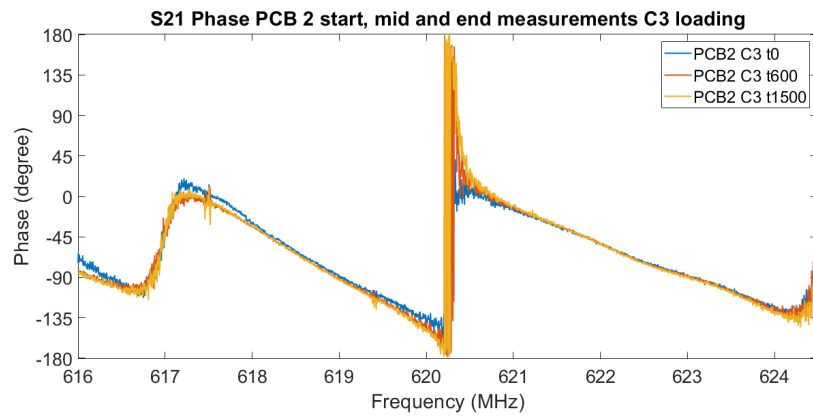


Figure 9.25: S21 phase data for three time points showing very little visible change.

**S11 Smithchart PCB 2 start, mid and end measurements C3 loading**

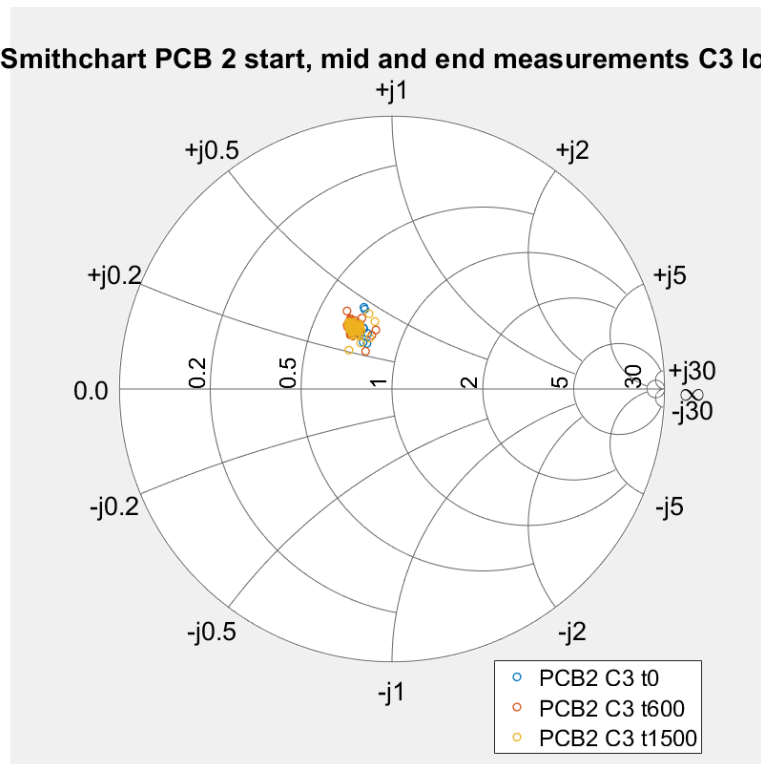


Figure 9.26: S11 of three time points plotted in a Smithchart to indicate the seen impedance by the transmitter is constant through the measurement.

slope over time. Here, from  $t=300s$  onward, the concentrations are ordered according to EV concentration. It can be hypothesised the change in slope is due to drift, and mass loading has an opposite effect than the drift that PBS experiences. However, again the phase variance, though omitted from this figure, is still large. Moreover, more measurements would be required to sustain the previous claim.

### 9.6.3. Timed mass loading measurements PCB 1

The results from PCB 1 are presented secondly as this SAW device has a worse S21 IL, so less signal power is received by the detector causing more noisy measurements. Furthermore, it should be noted the 'PBS Noise test' sample was applied before functionalisation was executed making it a less comparable data set. Also, when recording the 'PBS null test' data, the cap against evaporation was not used and the evaporation of the PBS shows a huge impact on the data.

Where in Figure 9.28, PCB 2 shows a negative phase shift after normalisation with higher EV concentra-

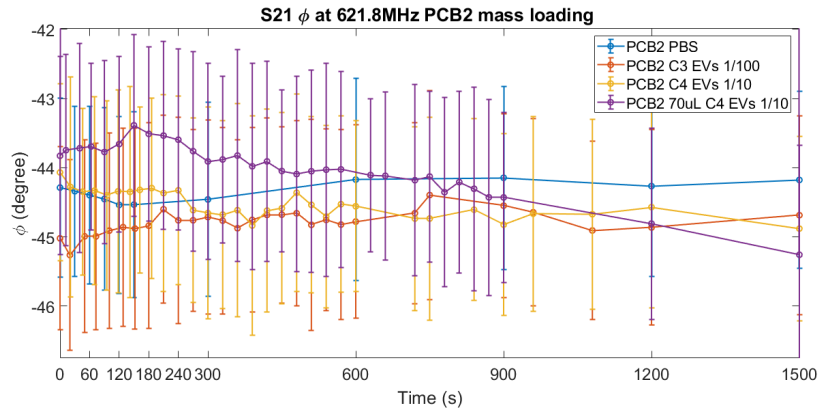


Figure 9.27: S21 phase with error bars showing the consecutive loading of the delay line with PBS and two concentrations of EVs containing sample applied in 15uL and again a sample of 70uL.

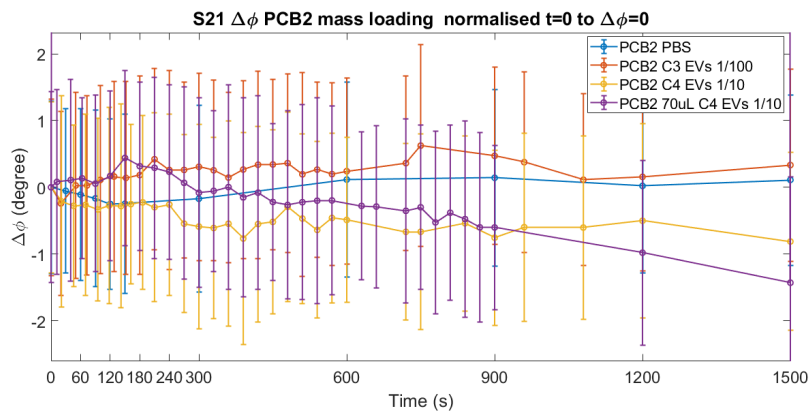


Figure 9.28: S21 phase, normalised with the initial measurement to zero degrees to observe the relative phase shift during the time the EVs can bind to the sensor surface with error bars. Indicating the consecutive loading of the delay line with PBS and two concentrations of EVs containing sample applied in 15uL and finally a sample of 70uL.

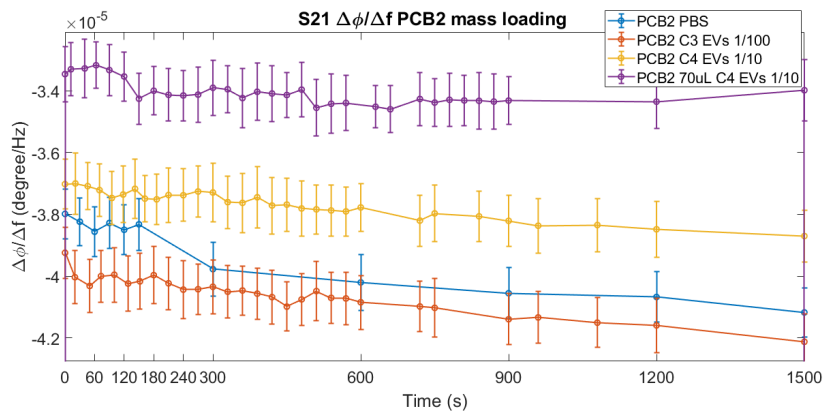


Figure 9.29: S21 phase vs frequency slope with error bars showing the consecutive loading of the delay line with PBS and two concentrations of EVs containing sample applied in 15uL and finally a sample of 70uL.

tion, this trend can not be found in the normalised phase shift for PCB 1 in Figure 9.31.

The normalised phase slope of PCB 1 in Figure 9.32 does seem to follow the same trend as PCB 2, so higher EV concentrations seem to cause less change in slope over time. Here the 'PBS Noise test' data set collected before functionalisation does not follow this trend however. As the explanation for this phenomenon given before is weak and the data has such high variance, more and less noisy measurements should be done to draw strong conclusions.

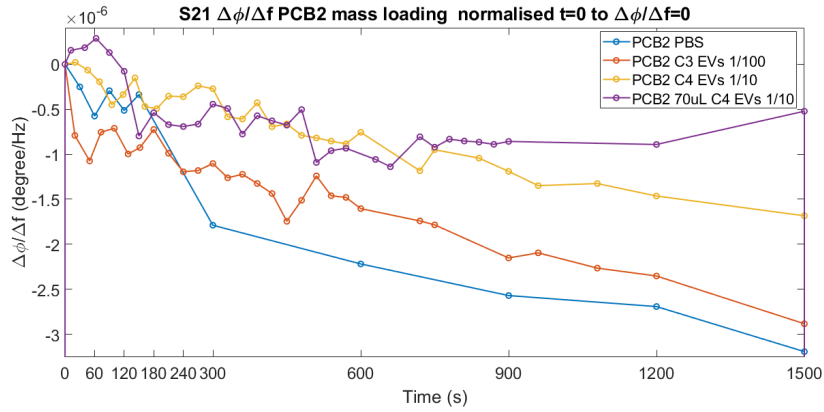


Figure 9.30: S21 phase vs frequency slope, normalised with the initial measurement to zero degrees/Hz to observe the relative change of slope during the time the EVs can bind to the sensor surface. Indicating the loading of the delay line with PBS and two consecutive concentrations of EVs containing sample applied in 15uL and finally a sample of 70uL.

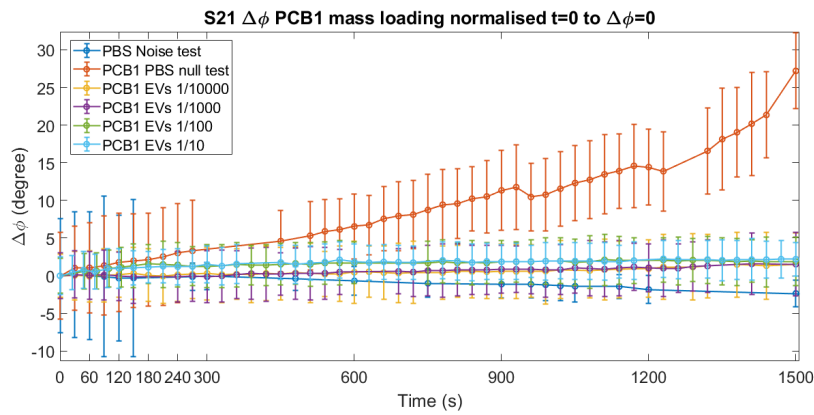


Figure 9.31: S21 phase, normalised with the initial measurement to zero degrees to observe the relative phase shift during the time the EVs can bind to the sensor surface with error bars. Indicating the consecutive loading of the delay line with PBS before functionalisation in 'PBS Noise test' and loading with PBS and 4 concentrations of EVs containing sample applied in 15uL volumes.

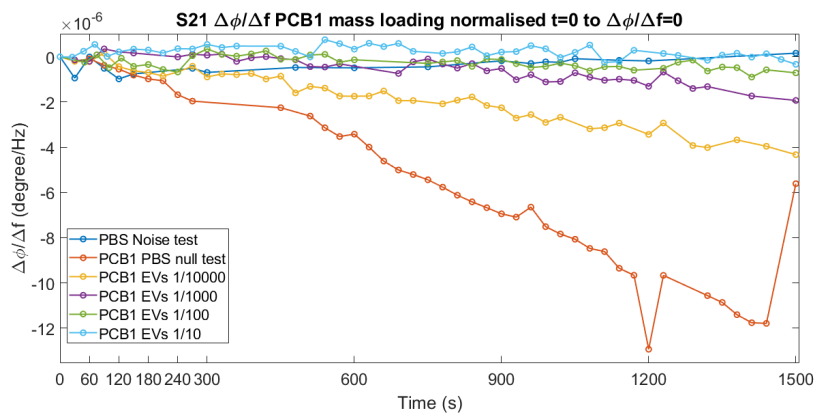


Figure 9.32: S21 phase vs frequency slope, normalised with the initial measurement to zero degrees/Hz to observe the relative change of slope during the time the EVs can bind to the sensor surface. Indicating the loading of the delay line with PBS before functionalisation in 'PBS Noise test' and loading with PBS and 4 consecutive concentrations of EVs containing sample applied in 15uL volumes.

# 10 | Conclusions

First the research question is answered based on the previously presented results. Then it can be presented what requirements were met and if the thesis aim was achieved.

## 10.1. Research question

The thesis answered the research question: What properties can be achieved by a Love-mode SAW sensor, for gravimetric sensing for CD9, fabricated at EKL?

A Love-mode SAW sensor was successfully fabricated. It uses an epoxy well to contain liquid samples on the delay line up to 100 $\mu$ L. The fabrication process is sensitive for particles due to the small feature size interdigitated transducer (IDT) used. However, very well developed IDTs were fabricated and feature sizes down to 1 $\mu$ m were achieved. It was demonstrated, anti-CD9 can be successfully immobilised on the polyimide sensor surface.

Using on wafer device characterisation, the yield can be determined. Poorly functioning devices can be ruled out from further processing. The devices operating frequency band can be characterised. The optimal device version can be determined. And the design variables influence on the output parameters can be investigated of a large population of devices. This includes the effect of finger pairs  $N$ , aperture  $W$  and delay line length  $L$  on the power send over the delay line. An optimum for  $N$  is between 50 and 150 finger pairs. An optimum aperture is found around  $W=80\lambda$ . Increasing  $L$  reduces the received power as is expected due to losses in acoustic wave transmission. A clear relation between the wavelength and operating frequency is established and a constant wave speed around 4900m/s is found.

Love-mode SAW signal transmission is achieved as rotating the crystal orientation causes a loss of a clear passband and adding a solid on the delay line kills signal transmission. The rotated crystal orientation confirms the literature that the required SH-mode SAW propagates ideally along the [0;42,5;90] direction of propagation and it does not propagate perpendicular to that. The added solid shows, impeding the surface movement inhibits signal transmission, so signal transmission must have been SAW mediated and not capacitive feed-through or any other signal path.

It is found COMSOL can be used to predict passband center frequency for Love-mode SAW based designs with wave guide thicknesses that are thin compared to the SAW wavelength. For relatively thick wave guide thickness (thickness/wavelength  $> 0.06$ ), the model shows two passband peaks were a SH-mode for the substrate and waveguide decouple. In that case, the passband due to the substrate SH-mode is best predictive of the properties of the fabricated devices.

The fabricated devices can be placed on a PCB and successfully read out by a NanoVNA for measurements without liquid samples showing a clear passband with big phase shift in the passband. Adding liquid reduces power transmission through the delay line causing received signal power to come closer to the equipment noise floor. The phase shift becomes less steep and noisy. Noise analysis is required to determine if more sensitive equipment or data processing tools can improve measurement setup sensitivity.

The devices show sensitivity for liquid sample consistency and volume. This impedes absolute comparison between measurements after changing the sample, giving rise for the need of time altering response based detection. Liquid loading changes the device impedance causing the need for matching circuit design after liquid loading characterisation.

The devices are not sufficiently sensitive for CD9 mass loading in liquid samples in the current measurement setup. Phase shift normalised to 0° at  $t=0s$  and phase shift angle ( $\Delta\phi/\Delta f$ ) normalised to 0°/Hz at  $t=0s$  both show responses to CD9 far below the noise induced response.

## 10.2. Aim and requirements

This thesis set out to design, fabricate and test a SAW based sensor with an as high as possible sensitivity for surface mass loading with low cost production in mind and with the material and equipment available at TU Delft.

This aim was divided in main and secondary requirements. The main requirements in short are firstly, to fabricate a device, sufficiently sensitive for CD9 in liquid samples. And secondly, to create this design and do this fabrication within the facilities available at the Else Kooi Lab at TU Delft.

The secondary requirements included, first, the option for rapid prototyping. Secondly, create a measurement setup coping with liquid samples. And thirdly, make the setup robust, meaning, portable and capable of multiple subsequent measurements.

For the main requirements, the first is not met while the second is successfully achieved. In the results, it becomes apparent there is no clear unambiguous relation between any of the extracted measures and mass loading due to EVs. By means of HRP colour staining, the presence of anti-CD9 on the chip was proven. It has to be concluded, the designed SAW device in this measurement setup is insufficiently sensitive to the small mass loading of CD9 positive EVs.

However, a device transmitting and receiving surface acoustic waves through a delay line are demonstrated. It is believed the wave mode is Love-mode as designed. The SAW device fabrication was possible within the available materials and facilities at TU Delft. An elaborate and robust process flow was established.

For the secondary requirements were all achieved. Firstly, rapid prototyping was partly achieved by allowing for wafer level characterisation of the designed devices using an RF probestation. It was not realised to allow for functionalisation of many SAW devices as for functionalisation the device had to be wirebonded to a PCB. This introduces high cost as every tested chip requires a new PCB. Also, it introduces high time constraints as wirebonding many chips is a fragile and time consuming process. Secondly, the designed PCB with chip was well suitable for coping with liquid samples. Finally, the measurement platform in finalised state was very robust, allowing for transport and repeated measurements.

This summarises to a thesis were a Love-mode SAW device on a platform capable of measuring in liquid samples was realised. The process allowed for selecting optimum devices. Determining the exact achieved sensitivity and improving the sensitivity for CD9 positive EVs remain the major topics for future research.

# 11 | Future research and recommendations

A Love mode SAW was demonstrated and sensitivity for different liquids shown but no sufficient sensitivity for CD9 positive EVs is demonstrated leaving room for future improvements. Here, recommendations required to achieve the goal of this work are given. More general recommendations on the design and fabrication process are also included. First the design is discussed. Then the fabrication. Afterwards, more general discussions on the stability and durability on the functionalisation method are discussed. Finally, recommendations to increase systematically move on wards to the next generation are presented.

## 11.1. Design

For the design, the simulations and used materials are commented on. Also, a recommendation on the designed system in the form of micro-fluidics is done.

### 11.1.1. 2d sim

To speed up simulation times and enable more parametric sweeps, it is very interesting to step to a 2d-simulation. The 3d-simplified model is symmetric along one axis. Therefore this axis does not add information and can be omitted, heavily reducing the degrees of freedom. This could result in much faster simulations. However, it is very difficult to check if the piezoelectric material crystal orientation is as desired.

Furthermore, on several discussion platforms it is suggested it is impossible to use a rotated system that has other rotations than  $90^\circ$ , nor does the COMSOL documentation supply any information on this use-case [123]. It would then be impossible to simulate ST-cut quartz in a 2d-model with its  $(0;42,75^\circ+90^\circ;0)$  Euler angles (where the  $=90^\circ$  is only for the COMSOL Z-X-Z Euler angles rotated system conversion).

A suggested solution in the COMSOL Discussion Forum is to extract the material matrices and rotate these as desired externally and then enter a new material with these rotated matrices [124].

### 11.1.2. Include damping in model

Though the losses in the substrate tend to be low as usually a low  $\tan \delta$  material is applied, this is not the case for all WG options. Here,  $\tan \delta$  is often interpreted as a measure of how well a material can dissipate energy, or similarly, a loss factor [57]. Some stiff over layers like SiO<sub>2</sub> still have a low  $\tan \delta$ , however, for most polymers the  $\tan \delta$  becomes orders of magnitude larger [57]. To find an upper bound on the delay line length, it is of interest to find for a certain device the damping per wavelength or damping per unit distance. The upper bound is then found at the maximum tolerable insertion loss, which is defined by the noise floor of the measurement system.

### 11.1.3. Automated time impulse model simulations

Now, simulations of the time impulse model are run per geometry. Time data is read in Matlab and the fast Fourier transform (FFT) is calculated as is all described in Section 5.1.4. To construct a plot as Figure 6.5 requires starting and updating the model many times and save each data file for Matlab processing and data extraction. These repetitive tasks are difficult to automate in COMSOL.

However, it is possible to call a COMSOL model from Matlab, update model parameters and execute it. This could speed up simulation speed very much. It would enable the gathering of more data and verification studies. And it reduces the operator time allowing the operator to focus on additional subjects.

The two options are 'LiveLink for MATLAB' or 'COMSOL with MATLAB'. The first is the most popularly supported by COMSOL and MATLAB documentation. With LiveLink for MATLAB, Matlab is connected to a (local) COMSOL server. It is possible to automatically generate the Matlab code for a build COMSOL model and from there on integrate the Matlab code in a Matlab model. For more details, the reader is referred to the LiveLink for MATLAB user guide [125].

### 11.1.4. Operation frequency and noise floor

As described in Section 6.6.2, the IDT width is chosen as small as possible to maximise the operation frequency to get the highest achievable sensitivity as explained in Section 4.4. In Section 6.6.2, the maximum

operation frequency was quickly estimated and decided achievable as state of art work uses operation frequencies in the same order of magnitude. Because of the complexity, no further noise estimation was made. This noise estimation is however extremely relevant. A noise estimation of all noise contributors is expected to be a big challenge but very much worthwhile.

### 11.1.5. Operation frequency and WG thickness

As discussed in Section 6.5, at the fabricated WG thickness, the transferred energy plot shows two passbands. As discussed in Section 9.3.4, these might be to a much dampened WG eigenmode and a SSWB substrate eigenmode. It is concluded, the combination of operation frequency and waveguide thickness is not optimal.

A next step should be to investigate if the sensor performance (combination of sensitivity for mass loading and IL) can be improved by switching to a WG material that can be fabricated nearer its optimum thickness. This comes likely at the cost of additional processing steps to remove the WG material from the interconnects and dicing lines.

Alternatively, the frequency can be reduced (wavelength increased), so the designed centre frequency is closer to the achievable WG thickness. According to equation 4.4, this comes at a cost of achievable sensitivity for mass loading. It is however expected that by better energy capture at the WG-substrate interface, the sensitivity is improved and the lower frequency implies lower noise as explained in Section 4.4.

### 11.1.6. Matching

Now matching was done by surface mount components on a PCB. This leads to distance between the matching circuit and the capacitively behaving IDT. Using planar technology, it is possible to integrate the matching network on the chip itself. Capacitors are commonly used in integrated IC design and micro Henry inductances in planar technology have been demonstrated [126]. Then on chip matching can be achieved. There are large challenges as wire bonding introduces a significant inductance and predicting the optimal matching network before fabrication is not trivial. Therefore, on chip matching is expected to be an iterative process where first, fabricated devices are characterised and a next generation can be matched on chip. Moreover, the need for on chip matching is not stringent as in the mega hertz range, the electrical wavelength is sufficiently long (in the order of tens of centimetres) so some distance between the matching circuit and the sensor is not heavily detrimental. If a future generation moves to higher frequencies for more sensitivity, on chip matching might play a larger role.

### 11.1.7. PCB design

Split the sensor PCB from the SMA connector PCB to test several device versions (more robust against wire-bond errors and enable the wire-bonded device to be placed in an O<sub>2</sub> plasma and be more easily transported in DI water. For this, a connection between the SAW PCB and SMA connector PCB is required.

Moreover, for comparing the sensitivity of different SAW device geometry versions, many devices must be characterised. This becomes better achievable if the SAW chip is easily replaced on the PCB to reduce the number of required PCBs. This mostly enlightens the desirability to avoid wire-bonding.

An option is PDOT:PSS, a high conductivity conductive polymer [127]. Other options are silver containing paint or grease as summarised in Table 11.1.

Table 11.1: Materials to be considered to make, low-ohmic, re-configurable connections between a small PCB with wire bonded SAW sample and another PCB with matching and connectors for interfacing with the measurement equipment.

PDOT:PSS [128]	200 S/cm	500 Ohm/sq	Hardens out.
Conductive lacquer [129]		0.03 Ohm/sq	Hardens out.
Silver conductive grease [130]	0.006 S/cm		Stays viscous.

### 11.1.8. Process dependencies

In the design phase, the dependencies of the process required for the design should be charted and minimised where possible. Though using equipment from various departments and using labs with differing specialities, the experiments can become extremely tailored to the project aim, this implies the project becomes dependent on many factors. More importantly, dependent on many equipment owners and lab supervisors. Though extremely interesting and they all try to help as much as they can within their busy schedule,



every new dependency causes time in the project where the project core is delayed. Of course, this means time for intermediate re-considerations and documenting are created. It is key to find a feasible balance.

For this thesis, the dependencies are listed in Table 11.2. For clarity, I want to express my gratitude to all professionals in the referred table, the cooperation was always pleasant and very educational. To be realistic, every dependency will take at least a week per occurrence in the Thesis flow. This should be taken into account when planning the project.

Table 11.2: Thesis dependencies

EKL lab use	EKL training staff
Pure Al on Qz sputtering	EKL staff and target availability
Dicing	EKL or Bioelectronics staff
Probe station measurements	Earl McCune lab equipment and technician
Wire bonding	Senior wire bonding expert (due to thin Al)
Ordering materials	Group technician
Biological lab Erasmus MC	Lab owner and technician

In this project, the possibly reduced dependencies are shortly discussed here.

Pure Al on Qz sputtering might be reduced by using Si carrier wafers, maybe avoiding the need to run the tool with tool owner supervision. And if Al 1% Si can be used, the material is always available as it is a standard cleanroom material as opposed to Pure Al.

Probe station measurements give the possibility for selecting the optimum device at the cost of waiting time before tool and technician availability.

Wire-bonding is needed when designing for the small RF-probes from the probestation. Larger pads might avoid the wire-bonding dependency. Also, thicker Al layer makes the wire bonding more easy, enabling less senior technicians to perform the handling, possibly speeding up the process.

When ordering materials, always enquire to the availability and choose the process with materials with realistic delivery times.

Try and reduce the number of used labs (three in this thesis), as they all require new introductions and have their own written and unwritten policies. If one lab is very busy, but inevitable however, an additional lab might instead cause a speedup.

### 11.1.9. Integrate automated microfluidics

Figures 9.19 and 9.17 show the necessity for accurately controlled sample fluids as discussed in Section 9.5.2. Furthermore, the higher analyte concentration samples can be used, the better. As higher analyte concentrations are more expensive to obtain, only small volumes are available. To accurately work with small volumes, a next interesting step would be to integrate microfluidics with the sensor. Examples of this already exist as shown by Raimbault et al. [131] in Figure 11.1.

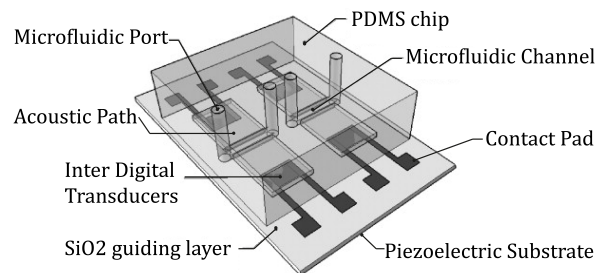


Figure 11.1: Example of method to integrate microfluidics automatisation and standardisation on SAW device. Figure taken from [131].

## 11.2. Fabrication

### 11.2.1. Metal

To improve process standardisation, it should be considered to use Al 1% Si, at the cost of having to do a dry etch of Al, reducing the surface smoothness of the Qz. Pure aluminium is not the conventional metal to use as aluminium can diffuse into silicon with high temperature processing steps (say 600°C). This can

cause conductive spikes into the silicon, possibly shorting active layers [116]. To reduce this diffusion, 1% Si is added to aluminium. This Al 1% Si is the standard cleanroom material [116]. For the SAW device, no high temperature steps are done after Al deposition (curing PI is not considered high temperature). Diffusion is thus not expected, so pure Al can be used. This has an advantage when etching the Al, no residues are left with a wet etch. Al 1% Si will leave precipitates. These are removed with a dry etch and any over etch will have a detrimental affect on the quartz surface uniformity.

### 11.2.2. Standardisation of substrate

To improve process standardisation it would be beneficial if silicon substrates can be used. In piezoelectric applications, the crystal orientation is of huge impact on the functioning of the device, so growing or depositing Qz on Si is not trivial. Examples where Qz is bonded to Si have been shown, even opening the possibility to have the electronics for readout integrated in the same Qz-on-Si chip [132].

### 11.2.3. Well for fluid containment

The epoxy well proved difficult to manufacture as the high viscosity curing epoxy can flow out for a long period. It is not possible to achieve high aspect ratio well walls without moulding. A laser cut polymer well was experimented with but showed defects after the GA functionalisation step. It was assumed the material for the well is PMMA, but this can not be confirmed as it was a leftover material from the workshop. It is recommended to find a well material that is compatible with the functionalisation process of investigate techniques of moulding the epoxy.

## 11.3. Surface functionalisation

In this proof of concept phase, a more time and resources consuming surface functionalisation protocol was opted to increase chances of success. Many more protocols and methods exist and depending on available lab materials and equipment, a critical review of methods would be of value for this research.

### 11.3.1. Storage

Also, it is worthwhile to make an assessment on the proper stage to store the devices between experiments. Antigens should be stored in liquid and at low temperature (around 4°C), and even then have a limited duration before deterioration. In conversation with the Erasmus MC lab technician specialising in EVs, it was discussed antibodies can not be stored in dry phase as the antibodies will be damaged upon dry in [133]. Storage before any step of the biochemical immobilisation protocol is executed ensures it won't deteriorate, but makes the time before an experiment can start impractically long. Depending on the optimum functionalisation process, a convenient storage moment should be decided on.

After Avidin immobilisation is expected to be the optimum stage for storage as Avidin is well resistant against dry-in and re-hydration. Moreover, 96-well plates prepped with immobilised Avidin are commercially available like the SigmaScreen<sup>TM</sup> Streptavidin High Capacity Coated Plates S6940 Plates. And the steps after Avidin immobilisation can be performed within two hours which is a very acceptable startup time for a proof of concept experiment. Storage at an earlier stage would result in much longer startup time as even Avidin immobilisation now includes a 12h dry-in time.

### 11.3.2. Sensor re-usability

In conversation with Erasmus MC staff G. Jenster, it was discussed CD9 and anti-CD9 are well separable. Proven protocols exist for this [134] [135]. With a covalent bond, avidin immobilised on the PI and is difficult to remove. Avidin-biotin is nearly at covalent bonding strength with a dissociation constant or  $K_D$  value in the order of magnitude of  $10^{-15}$  [136]. However, anti-CD9 and CD9 have a dissociation constant  $K_D \approx 10^{-11}$  [137] which is okay to break with a suitable washing buffer. Care must be taken however to not deal lasting damage to the antibodies.

Another option is soft release Avidin, where the Avidin-Biotin bond is made less strong with a  $K_D$  of  $10^{-7}$ , making it possible to remove the biotinylated antigen. Commercially available is the SoftLink<sup>TM</sup> Soft Release Avidin Resin available at Promega V2011.

Using the proper elution protocol, the sensor becomes reusable several cycles, depending on the protocol. A review on the possible protocols and experiments to verify this are relevant topics for future work.

### 11.4. Sensor stability and durability

Stability over short term, up to several hours) is already limited due to evaporation of the sample. This can be limited if properly designed micro fluidics is utilised. The effect of evaporation can be experimented using PBS or DI volumes, not in any other way interacting with the sensor. Other factors possibly limiting stability are fluid diffusion into the polymer wave guide or epoxy well and settling of the sample fluid. The first two matters can be alleviated with proper material choice as was aimed to do in this work. The latter matter should have limited effect due to the SH nature of the used wave mode. However, for both situations, the effect should be experimentally verified. The fluid settling effect can be tested using DI solution and beads. The beads should not be immobilised by any antibodies, and they will settle with a speed dependent on the chosen beads mass. Then the phase shift can be monitored and settling effects can be visualised after compensating for evaporation.

Durability, meaning long term usability, is very dependent on the moment of storage and elution protocol as discussed before. It is expected the sensor can be stored for several weeks after Avidin immobilisation. It can be used for several cycles if the proper protocol is used, but then antibodies are already immobilised, so the storage is expected to become limited to several days. Experimental verification needs to be executed.

### 11.5. Cross sensitivity

Once a proof of concept has been demonstrated, the cross sensitivity becomes important. The antibody-antigen reaction is considered very specific. And using the proper blocking agent once the antibodies have been introduced, will fairly certainly avoid capture of protein after immobilisation of the antibodies. Then still, as became clear in figures 9.19 and 9.17, the system is sensitive for much more than antigen immobilisation. The factors responsible for a phase shift can be grouped in sample related and device related.

The influence of sample volume was already discussed. But also, the influence of environment and sample temperature, sample settling behaviour, sample ionic contents (or conductivity) will have to be addressed.

As treated in Section 4.5.1, the temperature coefficient of frequency of the substrate introduces a temperature dependency. As opted by Jakoby et al. [56][100], it is possible to design for reduced temperature dependence. And other compensation techniques as a temperature controlled environment can be contemplated. Further device related factors include, but are not limited to, electromagnetic interference and waveguide polymer water penetration. For this last factor, the frequency drift due to water absorption can be minimised by exposing surface to water for several hours before test [108].

Spurious response can also lead to apparent mass loading by creating sensitivity to unexpected variables. Electromagnetic feed through might increase sensitivity to ion distribution in the settling sample. Bulk waves might increase sensitivity to temperature change and create a sensitivity for conditions changing on the bottom of the substrate surface. Triple transit error can cause sensitivity for water penetrating the epoxy well.

By far most of the sample, device and spurious response related factors might be compensated using differential readout, utilising a reference sample. To reduce the effect of process variation, these two sensors should be as close as possible, ideally on the same substrate. The currently designed wafer and PCB allows for differential readout on most device versions. It is strongly suggested the upcoming experimental setups make use of this possibility. Now the well has to be redesigned to reliably separate the fluid coming in contact with the delay lines. The currently used epoxy wells have too wide walls. It is hypothesised the optimal experiment is to keep the fabrication process and functionalisation protocol equal for both active and reference delay line except for immobilising antibodies, leaving the reference delayline empty of antibodies. Having all protein bonding sites blocked by BSA (as is the standard next step in the functionalisation protocol). Then the same sample liquid can be used on active and reference delayline.

Then still the sensor will have sensitivity for mismatch between the reference and active sensor. This can be further reduced by, as advised previously, measuring the immobilisation of the analyte real time and find a time dependent interaction behaviour. Effectively being a time based filter looking only at changes at the speed of change associated with immobilising antigens by antibodies. Filtering too fast and too slow effects, reducing noise and drift effects. For this situation, an estimation of the speed of antibody-antigen reaction speed is of great interest.

### 11.6. Sensitivity for surface mass loading characterisation

Very likely, the SAW devices do function and a Love wave is produced and sensed. The sensor does show sensitivity for evaporation as in Figure 9.31 where the 'PBS null test' sample evaporated during the measurement.

It is also sensitive for different fluids like DI water and PBS. Now the task remains to prove the sensitivity is due to the Love wave transduction and not any electromagnetic relation.

### 11.6.1. Initial sensitivity estimation

More specifically, it is desired to show the sensitivity for mass loading in liquid samples. To be detectable by the Love wave, the analyte should be immobilised on the surface. A method for this would be to attach more or bigger particles to the delay line. More CD9 containing EVs is little useful as the used concentration C4 was already an extremely high concentration. Moreover, a higher concentration would be extremely expensive as these high concentrations are very costly and time consuming to produce.

Bigger particles that can be bio-conjugated might pose a solution like labelling particles as magnetic beads or even bigger particles. More research would need to be conducted to the available particles to immobilise. Labelling particles are already a widely applied method to detect smaller analytes. Therefore, several options are expected to be available but research is required. A drawback is that these labelling particles are all already quite small and might prove already too small for a first design with limited sensitivity.

A slightly different waveguide material or a slightly different layer thickness would result in a surface mass change that could be relevant for determining the achieved sensitivity. Unfortunately, these methods would change too many parameters, like the waveguide shear horizontal wave speed in the first case, or the supported surface wave mode in the latter case. Making a different material or altered waveguide thickness a bad model for mass loading. The altered thickness might be useful if the change is only little.

Depositing another material on the delay line gives even more freedom but also imposes the need for more investigations on another material on the sensor functioning.

Another method might be to dry in particles, however, as happened during the functionalisation process, crystallised salts on the delay line kill the output power of the sensor. This reinforces the idea the measured signal is due to a Love mode SAW. It however implicates, drying in materials on the delay line might easily impede sensor operation, making it a poor method of sensitivity calibration.

### 11.6.2. Data acquirement equipment

In this setup, the very flexibly usable nanoVNA seemed a usable measurement system to find the S parameters. However, upon liquid loading of the delay line, the noise floor was increased much, and more sensitive equipment might improve the measurement data quality.

Furthermore, now the entire passband was monitored while only a part of it is used to determine the phase. Therefore, the measured range can be reduced so the frequency resolution can be increased or the measurement speed can be increased.

Now the measurements were all manually started and saved, severely impeding measurement speed. This should definitely be automated to improve measurement speed. Now, in the first 30 seconds, interesting reactions might have gone by unseen as the time base of the CD9 capture by anti-CD9 is not well known and was only estimated to be in the order of magnitude of several minutes. Even if the reaction is indeed slow, faster measurements allow for multi-sample averaging, still improving information quality. So an automated data acquisition platform is a must for further experiments.

### 11.6.3. Noise analysis

NanoVNA measurements become noisy when fluid is added to delay line what might be mitigated by more sensitive equipment. It might prove worthwhile to test if more sensitive equipment reduces the problem as with fluid loading, the insertion loss gets closer to the noise floor of the nanoVNA. This might add noise to the phase as well.

A careful analysis of the noise is also relevant as Figure 9.21 indicates both the insertion loss deteriorates and the noise floor increases. The underlying reason of the increasing noise floor is of interest as there might be factors in play that can be alleviated. For example, if the liquid sample increases sensitivity to electromagnetic interference, shielding can reduce part of the noise (strictly speaking, interference). Furthermore, if the added noise is due to thermal energy in the liquid samples and resulting random ionic movement, lowering the measurement environment temperature can reduce some of the noise. The temperature is also expected to have an influence on the antigen-antibody immobilisation speed and might influence the reaction itself. This should be further investigated but it is certain the temperature can not drop below 0°C as the liquid sample would go to a solid phase. Concluding, a noise analysis can be of great benefit to the measurement setup design.

### 11.7. Conclusion

On simulation, design, fabrication, functionalisation and measurement setup level, interesting research opportunities and necessary improvements were identified. This also leads to new topics for inclusion in the background information. It was attempted to imply the difference between essential further developments and interesting additional research paths. It can be concluded, though currently the envisioned results were not attained and the achieved sensitivity was not determined due to time constraints, the project still has an interesting future.

# Bibliography

- [1] Nederlandse kankerregistratie (nkr), integraal kankercentrum nederland (iknl). [accessed: 21-03-2022]. [Online]. Available: <https://iknl.nl/nkr-cijfers>
- [2] Antoni van leeuwenhoek, prostaatanker. [accessed: 21-03-2022]. [Online]. Available: <https://www.avl.nl/alles-over-kanker/kankersoorten/prostaatanker>
- [3] Erasmus mc prostaatanker. [accessed: 10-04-2022]. [Online]. Available: <https://www.erasmusmc.nl/nl-nl/kankerinstituut/patientenzorg/aandoeningen/prostaatacarcinoom-prostaatanker>
- [4] Umc utrecht prostaatanker. [accessed: 10-04-2022]. [Online]. Available: <https://www.umcutrecht.nl/ziekenhuis/ziekte/prostaatanker>
- [5] C. Stephan, B. Ralla, and K. Jung, "Prostate-specific antigen and other serum and urine markers in prostate cancer," *Biochimica et Biophysica Acta (BBA) - Reviews on Cancer*, vol. 1846, no. 1, pp. 99–112, 2014. [Online]. Available: <https://www.sciencedirect.com/science/article/pii/S0304419X14000377>
- [6] H. K. Walker, W. D. Hall, and J. W. Hurst, *Clinical methods: the history, physical, and laboratory examinations*. Butterworths, 1990.
- [7] Biopt through perineum illustration. [accessed: 21-03-2022]. [Online]. Available: <https://www.avl.nl/alles-over-kanker/diagnostisch-onderzoek/biopsie-prostaat/>
- [8] H. U. Ahmed, A. E.-S. Bosaily, L. C. Brown, R. Gabe, R. Kaplan, M. K. Parmar, Y. Collaco-Moraes, K. Ward, R. G. Hindley, A. Freeman et al., "Diagnostic accuracy of multi-parametric mri and trus biopsy in prostate cancer (promis): a paired validating confirmatory study," *The Lancet*, vol. 389, no. 10071, pp. 815–822, 2017.
- [9] H. G. Welch and W. C. Black, "Overdiagnosis in cancer," *Journal of the National Cancer Institute*, vol. 102, no. 9, pp. 605–613, 2010.
- [10] D. Duijvesz, C. Y. L. Versluis, C. A. Van Der Fels, M. S. Vredenbregt-van den Berg, J. Leivo, M. T. Peltola, C. H. Bangma, K. S. Pettersson, and G. Jenster, "Immuno-based detection of extracellular vesicles in urine as diagnostic marker for prostate cancer," *International Journal of cancer*, vol. 137, no. 12, pp. 2869–2878, 2015.
- [11] M. Alhajj and A. Farhana, "Enzyme linked immunosorbent assay," *StatPearls* [Internet], 2022.
- [12] E. N. Marieb and K. Hoehn, *Human Anatomy and Physiology*, tenth edition, global edition. Pearson, 2016.
- [13] L. Xin, "Cells of origin for cancer: an updated view from prostate cancer," *Oncogene*, vol. 32, no. 32, pp. 3655–3663, 2013.
- [14] G. D. Steinberg, B. S. Carter, T. H. Beaty, B. Childs, and P. C. Walsh, "Family history and the risk of prostate cancer," *The prostate*, vol. 17, no. 4, pp. 337–347, 1990.
- [15] I. Mordukhovich, P. L. Reiter, D. M. Backes, L. Family, L. E. McCullough, K. M. O'Brien, H. Razzaghi, and A. F. Olshan, "A review of african american-white differences in risk factors for cancer: prostate cancer," *Cancer Causes & Control*, vol. 22, no. 3, pp. 341–357, 2011.
- [16] Meetinstrumenten in de zorg, international proostate symptom score, ipss. [accessed: 25-04-2022]. [Online]. Available: <https://meetinstrumentenzorg.nl/instrumenten/international-prostate-symptom-score/>
- [17] Federatie medisch specialisten richtlijndatabase. [accessed: 10-04-2022]. [Online]. Available: [https://richtlijndatabase.nl/richtlijn/prostaatacarcinoom/pathologisch\\_onderzoek/gleason\\_score.html](https://richtlijndatabase.nl/richtlijn/prostaatacarcinoom/pathologisch_onderzoek/gleason_score.html)

- [18] J. Barentz and I. Schoots. (2020) New guidelines for the detection of prostate cancer, mri instead of tissue samples. [accessed: 25-04-2022]. [Online]. Available: <https://www.radboudumc.nl/en/news/2020/new-guidelines-for-the-detection-of-prostate-cancer>
- [19] H. Lilja, J. Oldbring, G. Rannevik, C. Laurell et al., "Seminal vesicle-secreted proteins and their reactions during gelation and liquefaction of human semen." *The Journal of clinical investigation*, vol. 80, no. 2, pp. 281–285, 1987.
- [20] Prostate-specific antigen (psa) test, is the psa test recommended for prostate cancer screening? [accessed: 22-03-2022]. [Online]. Available: <https://www.cancer.gov/types/prostate/psa-fact-sheet>
- [21] M. J. Duffy, "Biomarkers for prostate cancer: prostate-specific antigen and beyond," *Clinical Chemistry and Laboratory Medicine (CCLM)*, vol. 58, no. 3, pp. 326–339, 2020.
- [22] A. Usman, "Nanoparticle enhanced optical biosensing technologies for prostate specific antigen biomarker detection," *IEEE Reviews in Biomedical Engineering*, 2020.
- [23] C. Horlock. Enzyme-linked immunosorbent assay (elisa). [accessed: 06-05-2022]. [Online]. Available: <https://www.immunology.org/public-information/bitesized-immunology/experimental-techniques/enzyme-linked-immunosorbent-assay>
- [24] Prostaarkanker diagnose, gleason-score. [accessed: 10-05-2022]. [Online]. Available: <https://www.kanker.nl/kankersoorten/prostaatkanker/diagnose/gleason-score>
- [25] R. M. Hoffman, "Screening for prostate cancer," *New England Journal of Medicine*, vol. 365, no. 21, pp. 2013–2019, 2011.
- [26] D. Ilic, M. Djulbegovic, J. H. Jung, E. C. Hwang, Q. Zhou, A. Cleves, T. Agoritsas, and P. Dahm, "Prostate cancer screening with prostate-specific antigen (psa) test: a systematic review and meta-analysis," *bmj*, vol. 362, 2018.
- [27] C. E. Barbieri, C. H. Bangma, A. Bjartell, J. W. Catto, Z. Culig, H. Grönberg, J. Luo, T. Visakorpi, and M. A. Rubin, "The mutational landscape of prostate cancer," *European urology*, vol. 64, no. 4, pp. 567–576, 2013.
- [28] J. Groskopf, J. Siddiqui, L. Sefton-Miller, S. M. j. Aubin, A. Blase, S. Varambally, K. Sakamoto, Y. Fradet, J. Schalken, H. Rittenhouse et al., "Feasibility and clinical utility of a tmprss2: Erg gene fusion urine test," *The Journal of Urology*, vol. 181, no. 4S, pp. 814–814, 2009.
- [29] J.-N. Cornu, G. Cancel-Tassin, C. Egrot, C. Gaffory, F. Haab, and O. Cussenot, "Urine tmprss2: Erg fusion transcript integrated with pca3 score, genotyping, and biological features are correlated to the results of prostatic biopsies in men at risk of prostate cancer," *The Prostate*, vol. 73, no. 3, pp. 242–249, 2013.
- [30] D. Duijvesz, T. Luider, C. H. Bangma, and G. Jenster, "Exosomes as biomarker treasure chests for prostate cancer," *European urology*, vol. 59, no. 5, pp. 823–831, 2011.
- [31] J. S. Brzozowski, D. R. Bond, H. Jankowski, B. J. Goldie, R. Burchell, C. Naudin, N. D. Smith, C. J. Scarlett, M. R. Larsen, M. D. Dun et al., "Extracellular vesicles with altered tetraspanin cd9 and cd151 levels confer increased prostate cell motility and invasion," *Scientific reports*, vol. 8, no. 1, pp. 1–13, 2018.
- [32] M. Salih, R. A. Fenton, J. Knipscheer, J. W. Janssen, M. S. Vredenburg-van den Berg, G. Jenster, R. Zietse, and E. J. Hoorn, "An immunoassay for urinary extracellular vesicles," *American Journal of Physiology-Renal Physiology*, vol. 310, no. 8, pp. F796–F801, 2016.
- [33] G. Köhler and C. Milstein, "Continuous cultures of fused cells secreting antibody of predefined specificity," *nature*, vol. 256, no. 5517, pp. 495–497, 1975.
- [34] G. T. Hermanson, *Bioconjugate techniques*, third edition. Academic press, 2013.
- [35] J. W. Grate, "Acoustic wave microsensors for vapor sensing," *Chemical Reviews*, vol. 100, no. 7, pp. 2627–2648, 2000.
- [36] S. Middelhoek, S. Audet, and P. French, *Silicon Sensors and Actuators*. Delft Academic Press, 2020.

- [37] L. Rayleigh, "On waves propagated along the plane surface of an elastic solid," *Proceedings of the London mathematical Society*, vol. 1, no. 1, pp. 4–11, 1885.
- [38] R. M. White and F. W. Voltmer, "Direct piezoelectric coupling to surface elastic waves," *Applied physics letters*, vol. 7, no. 12, pp. 314–316, 1965.
- [39] G. Gugliandolo, Z. Marinković, G. Crupi, G. Campobello, and N. Donato, "Equivalent circuit model extraction for a saw resonator: Below and above room temperature," *Sensors*, vol. 22, no. 7, p. 2546, 2022.
- [40] M. I. G. Rocha, Y. Jiménez, F. A. Laurent, and A. Arnau, "Love wave biosensors: a review," *State of the Art in Biosensors-General Aspects*, 2013.
- [41] K.-y. Hashimoto and K.-Y. Hashimoto, *Surface acoustic wave devices in telecommunications, Chapter 1: Bulk Acoustic and Surface Acoustic Waves*. Springer, 2000, vol. 116.
- [42] V. Krylov, "Resonant properties of finite cracks and their acoustic emission spectra," *arXiv preprint*, 2018.
- [43] O. Y. Andreykiv, M. V. Lysak, M. Serhiyenko, and V. R. Skalsky, "Analysis of acoustic emission caused by internal cracks," *Engineering Fracture Mechanics*, vol. 68, no. 11, pp. 1317–1333, 2001.
- [44] A. Love, *Some Problems of Geodynamics*, Cambridge, 1911. Cambridge University Press, 1911.
- [45] H. Altenbach, "Love, augustus edward hough," *Encyclopedia of Continuum Mechanics*, pp. 1492–1493, 2020.
- [46] K. Yen, K. Lau, and R. Kagiwada, "Recent advances in shallow bulk acoustic wave devices," in *1979 Ultrasonics Symposium*. IEEE, 1979, pp. 776–785.
- [47] Y. Q. Fu, J. Luo, N.-T. Nguyen, A. Walton, A. J. Flewitt, X.-T. Zu, Y. Li, G. McHale, A. Matthews, E. Iborra et al., "Advances in piezoelectric thin films for acoustic biosensors, acoustofluidics and lab-on-chip applications," *Progress in Materials Science*, vol. 89, pp. 31–91, 2017.
- [48] E. Gizeli, A. Stevenson, N. Goddard, and C. Lowe, "A novel love-plate acoustic sensor utilizing polymer overlayers," *IEEE Transactions on Ultrasonics, Ferroelectrics, and Frequency Control*, vol. 39, no. 5, pp. 657–659, 1992.
- [49] D. Ballantine Jr, R. M. White, S. J. Martin, A. J. Ricco, E. Zellers, G. Frye, and H. Wohltjen, *Acoustic wave sensors: theory, design and physico-chemical applications Chapter 6 - Practical Aspects of Acoustic-Wave Sensors*. Elsevier, 1997.
- [50] T. M. Gronewold, "Surface acoustic wave sensors in the bioanalytical field: Recent trends and challenges," *analytica chimica acta*, vol. 603, no. 2, pp. 119–128, 2007.
- [51] J. J. Campbell and W. R. Jones, "A method for estimating optimal crystal cuts and propagation directions for excitation of piezoelectric surface waves," *IEEE Transactions on Sonics and Ultrasonics*, vol. 15, no. 4, pp. 209–217, 1968.
- [52] D. Morgan, "Surface acoustic wave devices and applications: 1. introductory review," *Ultrasonics*, vol. 11, no. 3, pp. 121–131, 1973.
- [53] R. Hooke, "Lecture de potentia restititiva, or of spring, explaining the power of springing bodies to which are added some collections," L. Martin, 1678.
- [54] B. Auld, *Acoustic Fields and Waves in Solids, ser. Acoustic Fields and Waves in Solids*. Wiley, 1973, no. v. 1.
- [55] Z. Wang, J. Cheeke, and C. Jen, "Sensitivity analysis for love mode acoustic gravimetric sensors," *Applied physics letters*, vol. 64, no. 22, pp. 2940–2942, 1994.
- [56] B. Jakoby, J. Bastemeijer, and M. J. Vellekoop, "Temperature-compensated love-wave sensors on quartz substrates," *Sensors and Actuators A: Physical*, vol. 82, no. 1-3, pp. 83–88, 2000.



- [57] Ansys, Granta EduPack. Ansys, 2022.
- [58] V. Chvets, P. Ivanov, V. Makarov, and V. Orlov, "Low-loss saw filters using new spudt structures," in 1997 IEEE Ultrasonics Symposium Proceedings. An International Symposium (Cat. No. 97CH36118), vol. 1. IEEE, 1997, pp. 69–72.
- [59] A. Tran, "Aln piezoelectric films for sensing and actuation," Master's thesis, TU Delft, the Netherlands, 2014.
- [60] C. Campbell, "Obtaining the fundamental and harmonic radiation conductances of a reflective saw interdigital transducer," in 1998 IEEE Ultrasonics Symposium. Proceedings (Cat. No. 98CH36102), vol. 1. IEEE, 1998, pp. 169–173.
- [61] J. Weber, M. Link, R. Primig, D. Pitzer, W. Wersing, and M. Schreiter, "Investigation of the scaling rules determining the performance of film bulk acoustic resonators operating as mass sensors," IEEE transactions on ultrasonics, ferroelectrics, and frequency control, vol. 54, no. 2, pp. 405–412, 2007.
- [62] T. Manzanegue, R. Lu, Y. Yang, and S. Gong, "Low-loss and wideband acoustic delay lines," IEEE Transactions on Microwave Theory and Techniques, vol. 67, no. 4, pp. 1379–1391, 2019.
- [63] C. Campbell, Surface Acoustic Wave Devices and Their Signal Processing Applications, Chapter 3 Principles of Linear Phase SAW Filter Design. Academic Press, 1989.
- [64] J. Haartsen, "Programmable surface acoustic wave detection in silicon: Design of programmable filters," Master's thesis, TU Delft, the Netherlands, 1990.
- [65] C. Campbell, Surface Acoustic Wave Devices and Their Signal Processing Applications, Chapter 2 Basics of Acoustic Waves and Piezoelectricity. Academic Press, 1989.
- [66] J. Visser, "Surface acoustic wave filters in zno-si02-si layered structures; design, technology, and monolithic integration with electronic circuitry," Master's thesis, TU Delft, the Netherlands, 1989.
- [67] G. S. Kino, Acoustic waves: devices, imaging, and analog signal processing. Prentice-hall Englewood Cliffs, NJ, 1987, vol. 107.
- [68] J. Krautkrämer and H. Krautkrämer, "Attenuation of ultrasonic waves in solids," in Ultrasonic Testing of Materials. Springer, 1983, pp. 107–118.
- [69] W. Qian, A. Venema, and M. Vellekoop, "An acoustic absorption film for saw devices," Sensors and Actuators A: Physical, vol. 26, no. 1-3, pp. 535–539, 1991.
- [70] A. C. Stevenson, E. Gizeli, N. J. Goddard, and C. R. Lowe, "Acoustic love plate sensors: a theoretical model for the optimization of the surface mass sensitivity," Sensors and Actuators B: Chemical, vol. 14, no. 1, pp. 635–637, 1993.
- [71] B. Auld, Acoustic Fields and Waves in Solids, ser. Acoustic Fields and Waves in Solids. Wiley, 1973, no. v. 2.
- [72] E. Gizeli, F. Bender, A. Rasmusson, K. Saha, F. Josse, and R. Cernosek, "Sensitivity of the acoustic waveguide biosensor to protein binding as a function of the waveguide properties," Biosensors and Bioelectronics, vol. 18, no. 11, pp. 1399–1406, 2003.
- [73] F. Bender, R. W. Cernosek, and F. Josse, "Love-wave biosensors using cross-linked polymer waveguides on litao3 substrates," Electronics letters, vol. 36, no. 19, pp. 1672–1673, 2000.
- [74] D. W. Branch and S. M. Brozik, "Low-level detection of a bacillus anthracis simulant using love-wave biosensors on 36 yx litao3," Biosensors and Bioelectronics, vol. 19, no. 8, pp. 849–859, 2004.
- [75] L. Liljeholm, "Electroacoustic evaluation of thin film piezoelectric resonators for frequency control and sensing applications," 2005.
- [76] C. Campbell, Surface Acoustic Wave Devices and Their Signal Processing Applications, Chapter 4 Equivalent Circuit Models for a SAW Filter. Academic Press, 1989.

- [77] W. R. Smith, H. M. Gerard, J. H. Collins, T. M. Reeder, and H. J. Shaw, "Analysis of interdigital surface wave transducers by use of an equivalent circuit model," *IEEE transactions on microwave theory and techniques*, vol. 17, no. 11, pp. 856–864, 1969.
- [78] O. Onen, A. Sisman, N. D. Gallant, P. Kruk, and R. Guldiken, "A urinary bcl-2 surface acoustic wave biosensor for early ovarian cancer detection," *Sensors*, vol. 12, no. 6, pp. 7423–7437, 2012. [Online]. Available: <https://www.mdpi.com/1424-8220/12/6/7423>
- [79] Y. Montagut, J. V. García, Y. Jiménez, C. March, Á. Montoya, and A. Arnau, "Validation of a phase-mass characterization concept and interface for acoustic biosensors," *Sensors*, vol. 11, pp. 4702–4720, 2011.
- [80] A. Sisman, E. Gur, S. Ozturk, B. Enez, B. Okur, and O. Toker, "A low-cost biomarker-based saw-biosensor design for early detection of prostate cancer," *Procedia Technology*, vol. 27, pp. 248–249, 2017, biosensors 2016. [Online]. Available: <https://www.sciencedirect.com/science/article/pii/S221201731730107X>
- [81] M. Zijlmans, "Design of a surface acoustic wave sensor for the detection of urinary prostate cancer biomarkers," Master's thesis, TU Delft, the Netherlands, 2021.
- [82] V. Raimbault, D. Rebière, C. Dejous, M. Guirardel, V. Conedera, and J. Pistré, "High viscosity sensing using a love wave acoustic platform combined with a pdms microfluidic chip," *ECS Transactions*, vol. 4, no. 1, p. 73, 2007.
- [83] L. Johansson, J. Enlund, S. Johansson, I. Katardjiev, and V. Yantchev, "Surface acoustic wave induced particle manipulation in a pdms channel—principle concepts for continuous flow applications," *Biomedical microdevices*, vol. 14, no. 2, pp. 279–289, 2012.
- [84] A. Ozcelik, R. Becker, T. J. Huang, A. Sisman, P. French, A. Ogan, E. Korkmaz, A. Husseini, A. Yazdani, and J. Meyer, *Acoustic Technologies in Biology and Medicine, Chapter Acoustic Biosensors*. John Wiley & Sons, 2023.
- [85] L. Euler, "Novi commentarii aedemiae scientiarum imperialis petropolitanae," vol. XX, p. 189, 1776.
- [86] E. T. Whittaker, *A treatise on the analytical dynamics of particles and rigid bodies*. CUP Archive, 1964.
- [87] R. Pio, "Euler angle transformations," *IEEE Transactions on automatic control*, vol. 11, no. 4, pp. 707–715, 1966.
- [88] W. Bond, "Chapter ii: Methods for specifying quartz crystal orientation and their determination by optical means," *The Bell System Technical Journal*, vol. 22, no. 2, pp. 224–262, 1943.
- [89] C. Lam, C. Y. Wang, and S. Wang, "A review of the recent development of temperature stable cuts of quartz for saw applications," in *Proceedings of the Fourth International Symposium on Acoustic Wave Devices for Future Mobile Communication Systems*, Chiba, Japan, 2010, pp. 3–5.
- [90] W. L. Bragg and R. E. Gibbs, "The structure of  $\alpha$  and  $\beta$  quartz," *Proceedings of the Royal Society of London. Series A, Containing Papers of a Mathematical and Physical Character*, vol. 109, no. 751, pp. 405–427, 1925.
- [91] M. L. Huggins, "The crystal structure of quartz," *Physical Review*, vol. 19, no. 4, p. 363, 1922.
- [92] W. H. Bragg and W. L. Bragg, *X rays and crystal structure*. G. Bell and sons, Limited, 1915.
- [93] IRE-Standards-Committee, "Standards on piezoelectric crystals," *Proceedings of the I.R.E.*, pp. 1378–1395, 1949.
- [94] ANSI, "Ieee standard on piezoelectricity (ansi/ieee std 176-1978)," 1978.
- [95] R. Weis and T. Gaylord, "Lithium niobate: Summary of physical properties and crystal structure," *Applied Physics A*, vol. 37, no. 4, pp. 191–203, 1985.
- [96] Z. Xu and Y. J. Yuan, "Implementation of guiding layers of surface acoustic wave devices: A review," *Biosensors and Bioelectronics*, vol. 99, pp. 500–512, 2018.

- [97] R. N. Simons, Coplanar waveguide circuits, components, and systems, Chapter 2: Conventional Coplanar Waveguide. John Wiley & Sons, 2001.
- [98] S. Gevorgian, L. P. Linner, and E. L. Kollberg, "Cad models for shielded multilayered cpw," IEEE transactions on microwave theory and techniques, vol. 43, no. 4, pp. 772–779, 1995.
- [99] A. Mazzamurro, Y. Dusch, P. Pernod, O. B. Matar, A. Addad, A. Talbi, and N. Tiercelin, "Giant magnetoelastic coupling in a love acoustic waveguide based on tb co  $2/fe$  co nanostructured film on st-cut quartz," Physical Review Applied, vol. 13, no. 4, p. 044001, 2020.
- [100] B. Jakoby and M. Vellekoop, "Reducing the temperature sensitivity of love-wave sensors," in 1998 IEEE Ultrasonics Symposium. Proceedings (Cat. No. 98CH36102), vol. 1. IEEE, 1998, pp. 447–450.
- [101] S.-Y. Chu, W. Water, and J.-T. Liaw, "An investigation of the dependence of zno film on the sensitivity of love mode sensor in zno/quartz structure," Ultrasonics, vol. 41, no. 2, pp. 133–139, 2003.
- [102] F. Herrmann, M. Weihnacht, and S. Buttgenbach, "Properties of sensors based on shear-horizontal surface acoustic waves in litao/sub  $3/sio/sub 2$  and quartz/sio/sub  $2$  structures," IEEE transactions on ultrasonics, ferroelectrics, and frequency control, vol. 48, no. 1, pp. 268–273, 2001.
- [103] A. Hossain and M. H. Rashid, "Pyroelectric detectors and their applications," IEEE Transactions on industry applications, vol. 27, no. 5, pp. 824–829, 1991.
- [104] Roditi, litao3 properties. [accessed: 02-10-2022]. [Online]. Available: <http://www.roditi.com/SingleCrystal/Lithium-Tantalate/LiTaO3-Properties.html>
- [105] Roditi, linbo3 properties. [accessed: 02-10-2022]. [Online]. Available: <http://www.roditi.com/SingleCrystal/LiNbO3/liNBO3-Properties.html>
- [106] M. R. H. Sarker, H. Karim, R. Martinez, D. Delfin, R. Enriquez, M. A. I. Shuvo, N. Love, and Y. Lin, "Temperature measurements using a lithium niobate (linbo3) pyroelectric ceramic," Measurement, vol. 75, pp. 104–110, 2015.
- [107] E. Nazaretski, R. Merithew, R. Pohl, and J. Parpia, "Measurement of the acoustic properties of amorphous silica above 4.5 mk," Physical Review B, vol. 71, no. 14, p. 144201, 2005.
- [108] G. L. Harding and J. Du, "Design and properties of quartz-based love wave acoustic sensors incorporating silicon dioxide and pmma guiding layers," Smart materials and structures, vol. 6, no. 6, p. 716, 1997.
- [109] M. Gaso, Y. Jiménez, L. Francis, and A. Arnau, "Love wave biosensors: a review," State of the Art Biosensors - General Aspects, pp. 277–310, 2013.
- [110] J. Schoonhoven, "Characterization and processing of elastomers for organ-on-chip applications," Master's thesis, TU Delft, the Netherlands, 2022.
- [111] E. L. Madsen, H. J. Sathoff, and J. A. Zagzebski, "Ultrasonic shear wave properties of soft tissues and tissuelike materials," The Journal of the Acoustical Society of America, vol. 74, no. 5, pp. 1346–1355, 1983.
- [112] G. Xu, Z. Ni, X. Chen, J. Tu, X. Guo, H. Bruus, and D. Zhang, "Acoustic characterization of polydimethylsiloxane for microscale acoustofluidics," Physical Review Applied, vol. 13, no. 5, p. 054069, 2020.
- [113] C. P. Constantin, M. Aflori, R. F. Damian, and R. D. Rusu, "Biocompatibility of polyimides: A mini-review," Materials, vol. 12, no. 19, p. 3166, 2019.
- [114] Y. Sun, S. Lacour, R. Brooks, N. Rushton, J. Fawcett, and R. Cameron, "Assessment of the biocompatibility of photosensitive polyimide for implantable medical device use," Journal of Biomedical Materials Research Part A: An Official Journal of The Society for Biomaterials, The Japanese Society for Biomaterials, and The Australian Society for Biomaterials and the Korean Society for Biomaterials, vol. 90, no. 3, pp. 648–655, 2009.

- [115] A. Turton, D. Battacharyya, and D. Wood, "Love-mode surface acoustic wave liquid sensors using a polyimide waveguide layer," in Proceedings of the 2004 IEEE International Frequency Control Symposium and Exposition, 2004. IEEE, 2004, pp. 250–256.
- [116] A. Šakic, V. Jovanović, P. Maleki, T. L. Scholtes, S. Milosavljević, and L. K. Nanver, "Characterization of amorphous boron layers as diffusion barrier for pure aluminium," in The 33rd International Convention MIPRO. IEEE, 2010, pp. 26–29.
- [117] Metal material properties. [accessed: 02-10-2022]. [Online]. Available: <https://www.tibtech.com/metal-conductivity>
- [118] Fujifilm Electronic Materials, Technical product information low temperature cure ltc 9300 photosensitive polyimide precursor, EU-FCD-00005 Rev 1, 2023.
- [119] F. T. Ulaby and U. Ravaioli, Fundamentals of Applied Electromagnetics 7th Edition Global Edition. Pearson, 2015.
- [120] X. Huang, B. Chen, M. Mei, H. Li, C. Liu, and C. Wei, "Synthesis and characterization of organosoluble, thermal stable and hydrophobic polyimides derived from 4-(4-(1-pyrrolidinyl) phenyl)-2, 6-bis (4-(4-aminophenoxy) phenyl) pyridine," Polymers, vol. 9, no. 10, p. 484, 2017.
- [121] S. Hosseini, F. Ibrahim, I. Djordjevic, H. A. Rothan, R. Yusof, C. van der Marel, and L. H. Koole, "Synthesis and processing of elisa polymer substitute: the influence of surface chemistry and morphology on detection sensitivity," Applied surface science, vol. 317, pp. 630–638, 2014.
- [122] T. Hartjes, J. Slotman, M. Vredenburg, N. Dits, R. Van der Meel, D. Duijvesz, J. A. Kulkarni, P. French, W. Van Cappellen, R. M. Schiffelers et al., "Evquant; high-throughput quantification and characterization of extracellular vesicle (sub) populations," bioRxiv, pp. 2020–10, 2020.
- [123] C. documentation. Comsol ref definitions, rotated system. [accessed: 25-09-2023]. [Online]. Available: [https://doc.comsol.com/5.5/doc/com.comsol.help.comsol/comsol\\_ref\\_definitions.12.092.html](https://doc.comsol.com/5.5/doc/com.comsol.help.comsol/comsol_ref_definitions.12.092.html)
- [124] R. Klochin and I. Kjelberg. Coordinates in mapped system, expressions (x,y,z). [accessed: 25-09-2023]. [Online]. Available: <https://www.comsol.com/forum/thread/29540/Coordinates-in-mapped-system-expressions-XYZ>
- [125] COMSOL 5.4, LiveLink for MATLAB User's Guide, 2018.
- [126] J. Poliakine, F. Copt, D. M. Araujo, Y. Civet, and Y. Perriard, "Modeling, design, and manufacturing of microfabricated coils with high inductance density," Journal of Microelectromechanical Systems, vol. 26, no. 6, pp. 1248–1258, 2017.
- [127] L. Manjakkal, A. Pullanchiyodan, N. Yogeswaran, E. S. Hosseini, and R. Dahiya, "A wearable supercapacitor based on conductive pedot: Pss-coated cloth and a sweat electrolyte," Advanced Materials, vol. 32, no. 24, p. 1907254, 2020.
- [128] Sigma-Aldrich, Data Sheet Poly(3,4-ethylenedioxythiophene)-poly(styrenesulfonate) - 3.0-4.0% in H<sub>2</sub>, high-conductivity grade, 655201, 2023.
- [129] Electrolube Conductive Lacquer, Technical Data Sheet Silver Conductive Paint, SCP26G, 2015.
- [130] MG Chemicals, Technical Data Sheet Silver Conductive Grease, 8463, 2018.
- [131] V. Raimbault, D. Rebière, and C. Dejous, "A microfluidic surface acoustic wave sensor platform: Application to high viscosity measurements," Materials Science and Engineering: C, vol. 28, no. 5-6, pp. 759–764, 2008.
- [132] Y. Eo, S. Hyun, P. Choi, K. Lee, G. Oh, and J.-W. Lee, "Reference saw oscillator on quartz-on-silicon (qos) wafer for polyolithic integration of true single chip radio," in International Electron Devices Meeting 1999. Technical Digest (Cat. No. 99CH36318). IEEE, 1999, pp. 761–764.

- [133] Sigma aldrich, antibodies in practise: General information. [accessed: 27-09-2023]. [Online]. Available: <https://www.sigmaaldrich.com/NL/en/technical-documents/technical-article/protein-biology/immunohistochemistry/antibodies-in-practice-general-information>
- [134] P. Howard, "Principles of antibody elution," *Transfusion*, vol. 21, no. 5, pp. 477–482, 1981.
- [135] V. Shpacovitch and R. Hergenroeder, "Optical and surface plasmonic approaches to characterize extracellular vesicles. a review," *Analytica Chimica Acta*, vol. 1005, pp. 1–15, 2018.
- [136] E. A. Bayer and M. Wilchek, "Application of avidin—biotin technology to affinity-based separations," *Journal of Chromatography A*, vol. 510, pp. 3–11, 1990.
- [137] A. Kowalczyk, A. Gajda-Walczak, M. Ruzicka-Ayoush, A. Targonska, G. Mosieniak, M. Glogowski, A. Szumera-Cieckiewicz, M. Prochorec-Sobieszek, M. Bamburowicz-Klimkowska, A. M. Nowicka et al., "Parallel spr and qcm-d quantitative analysis of cd9, cd63, and cd81 tetraspanins: A simple and sensitive way to determine the concentration of extracellular vesicles isolated from human lung cancer cells," *Analytical Chemistry*, 2023.
- [138] E. P. Meulenberg, L. Eyer, and M. Franek, *Antibodies Applications and New Developments*, chapter 2. Bentham eBooks, 2012.
- [139] J.-C. Wang, L. R. Bégin, N. G. Bérubé, S. Chevalier, A. G. Aprikian, H. Gourdeau, and M. Chevette, "Down-regulation of cd9 expression during prostate carcinoma progression is associated with cd9 mrna modifications," *Clinical cancer research*, vol. 13, no. 8, pp. 2354–2361, 2007.
- [140] S. Ikeyama, M. Koyama, M. Yamaoko, R. Sasada, and M. Miyake, "Suppression of cell motility and metastasis by transfection with human motility-related protein (mrp-1/cd9) dna." *The Journal of experimental medicine*, vol. 177, no. 5, pp. 1231–1237, 1993.
- [141] M. Higashiyama, T. Taki, Y. Ieki, M. Adachi, C.-l. Huang, T. Koh, K. Kodama, O. Doi, and M. Miyake, "Reduced motility related protein-1 (mrp-1/cd9) gene expression as a factor of poor prognosis in non-small cell lung cancer," *Cancer research*, vol. 55, no. 24, pp. 6040–6044, 1995.
- [142] J.-F. Cojot, I. Sordat, T. Silvestre, and B. Sordat, "Differential display cloning identifies motility-related protein (mrp1/cd9) as highly expressed in primary compared to metastatic human colon carcinoma cells," *Cancer Research*, vol. 57, no. 13, pp. 2593–2597, 1997.
- [143] M. Miyake, K. Nakano, Y. Ieki, M. Adachi, C.-L. Huang, S.-i. Itoi, T. Koh, and T. Taki, "Motility related protein 1 (mrp-1/cd9) expression: inverse correlation with metastases in breast cancer," *Cancer research*, vol. 55, no. 18, pp. 4127–4131, 1995.
- [144] T. Pisitkun, R. Johnstone, and M. A. Knepper, "Discovery of urinary biomarkers," *Molecular & Cellular Proteomics*, vol. 5, no. 10, pp. 1760–1771, 2006.
- [145] H. Shin, Y. H. Park, Y.-G. Kim, J. Y. Lee, and J. Park, "Aqueous two-phase system to isolate extracellular vesicles from urine for prostate cancer diagnosis," *PLoS One*, vol. 13, no. 3, p. e0194818, 2018.
- [146] National human genome research institute. [accessed: 06-05-2022]. [Online]. Available: <https://www.genome.gov/genetics-glossary/Antibody>

# A | (Strept)avidin-Biotin

Streptavidin is a protein with four identical subunits, each containing a biotin binding site. It is similar to the glycoprotein Avidin originating from egg-whites, but Streptavidin originates from bacteria, *Streptomyces avidinii*. Streptavidin has improved specific binding compared to Avidin the latter has a higher isoelectric point (pH10 vs pH5), the overall charge of the second causes more ionic interactions and being a glycoprotein, avidin can bind additional carbohydrate receptors. This biospecificity compares to antibody-antigen binding. Streptavidin has a total atomic weight of 60,000 Daltons. For comparison, an IgG antibody has an approximate atomic weight of 160,000 [34].

The exceptionally strong biotin-avidin interaction, with a dissociation constant of  $1.3 \times 10^{-15} \text{M}$  is one of the strongest noncovalent affinities known. Tryptophan and lysine residues are involved in forming binding pockets, also causing the biotin to get mechanically trapped causing the immense binding force. This mechanically very stable protein is also very hard to dissociate, a pH of 1.5 is required to denature it.

Biotin, a vitamin, also known as vitamin H, has a bicyclic ring structure. By biotinylating (attaching biotin to molecules, process described later) antibodies specific for the antigen desired to detect and biotinylating markers (like fluorescent enzymes), the biotin-streptavidin conjugate can be very useful for biosensing applications. The presence of four binding sites on streptavidin allows the binding of multiple markers to one antigen. This highly improves the sensitivity of this method over using antibodies directly tagged with a marker.

If the biotin-streptavidin complex do not block all binding sites on the streptavidin, it is even possible to have multiple streptavidin molecules bridging to the antibody, allowing more marker molecules, causing even more enhanced sensitivity.

Biotinylation is the covalent bonding of one or more biotin groups to a molecule of interest. The relatively small biotin components cause little change in physical or chemical properties to the molecule they bind to. A range of commercially available biotin derivatives enables the tagging to many different molecules making the streptavidin-biotin detection a widely applicable method. For biotinylation, a spacer and a reactive group is bound to the bicyclic biotin. Biotin is hydrophobic and the spacer can be used to make the entire structure even more hydrophobic or hydrophilic to avoid aggregation in an aqueous environment [34].

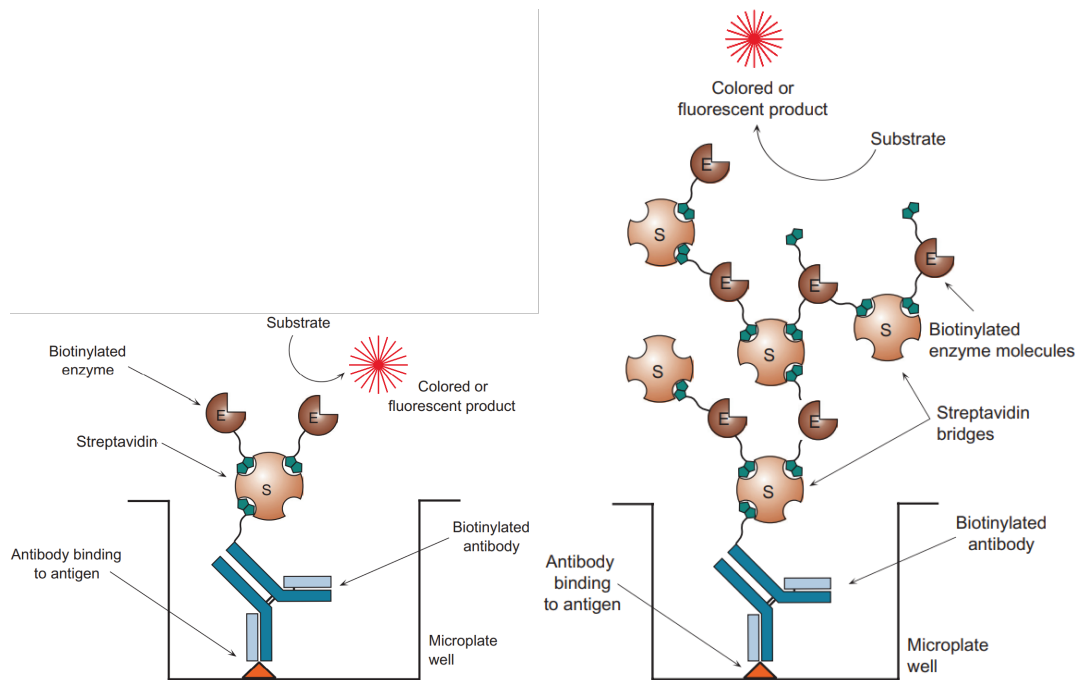


Figure A.1: Streptavidin-biotin binding used to detect the binding of antibodies to antigen in analyte. Left using a single streptavidin molecule. Right using streptavidin bridges for improved signal strength. Figure adapted from [34].

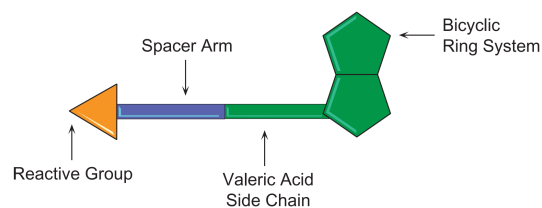


Figure A.2: Biotin bicyclic structure with spacer arm which can be made hydrophobic or hydrophilic and a reactive group to biotinylate a molecule of interest to later be detected using streptavidin. Figure taken from [34].

## B | Obtaining antibodies

Antibodies, the Y shaped protein as in Figure C.4, are made by B-lymfocytes. There are multiple methods of obtaining these antibodies. The oldest is to inject an organism with an antigen of interest. The organism immune system will produce antibodies against the antigen. After sufficient time and one or several injections with the antigen, blood is taken from this organism. Then by separating the antibodies from the blood, antiserum is obtained containing many relevant antibodies. However, with this method, not only antibodies against the desired antigen are obtained. Furthermore, one antigen has multiple binding sites or epitopes. Different antibodies are now obtained for different epitopes on the same antigen, these are called polyclonal antibodies. This is causes bad repeatability of experiments as every batch of antibodies would be unique [138].

A better method is, when the organism immune system is actively producing the antibodies, to euthanise the organism and retrieve the spleen for cell fusion (dissolving the spleen to separate all cells). Then the B-lymphocytes making the antibody of interest are selected. To enable the survival of these B-lymphocytes, Köhler and Milstein [33] thought of merging the B-lymphocyte of interest with a myeloma cell as they divide fast and are thus easy to grow. The merged cell has good survival and still produces the antibody of interest. This enabled the antibody production for a specific epitope on a specific antigen. The obtained antibodies are then all identical or, monoclonal [138].

It is ofcourse also possible to use different B-lymphocytes, then antibodies for the same antigen but different epitopes can be obtained. These are then polyclonal antibodies, all specific for the same antigen, but different epitopes. This can improve sensitivity for the antigen, but comes at the cost of lower inter experiment consistency as every batch would be unique again [138].

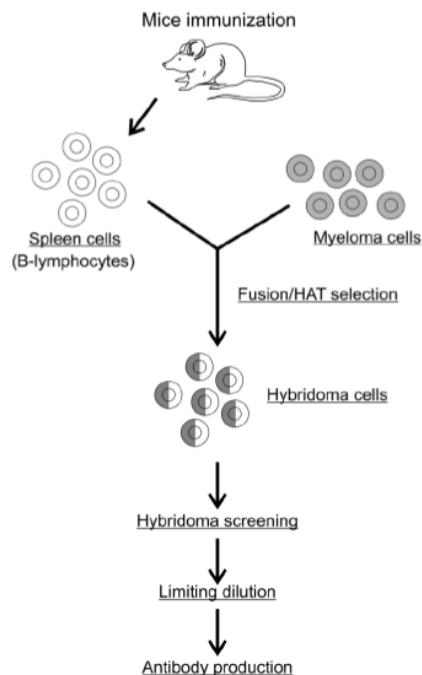


Figure B.1: Monoclonal antibodies can be produced by injecting an organism (usually a mouse) with the antigen of interest. Its immune system (B-lymphocytes) will start making antibodies. After giving the immune system sufficient time and after one or several resubmissions of the antigen, the organism is euthanised and the spleen is removed for cell fusion (dissolving it to separate the cells). The spleen B-lymphocytes are selected for the desired antibody and merged with myeloma cells to improve their survival [33]. These merged cells then keep producing the desired antibodies. If all antibodies are obtained from a single B-lymphocyte, the antibodies are monoclonal, all binding to the exact same epitope on the antigen of interest. The advantage of this is high continuity in different experiments. Figure from [138].



After the desired antibodies are obtained, they can be conjugated with a marker enzyme or with biotin to later detect the antibody or immobilise it in a sensing application. Along the antibody, many sites are available for bioconjugation as the antibody has both amine and carboxylate groups available uniformly along the entire antibody. This causes random conjugation on random locations which can cause blocking of the antigen binding site. Therefore, conjugation techniques are used to bind on more specific groups, for example the disulfides in the hinge region (after cleavage, thiols are exposed suitable for conjugation) or the glycan carbohydrate chains between the heavy chains [34].

## C | CD9 and immobilisation

First the biomarker of interest CD9 is investigated. Then a short discussion on the use of antibodies for immobilisation is included.

### C.1. CD9 background information

The cluster-of-differentiation antigen 9 (CD9) gene has been identified as a gene with altered expression between tumorigenic and non-tumorigenic hybrids from human fibroblasts [139]. The CD9 protein is a member of the tetraspanin family, which counts at least 33 members [31]. It is also known as the mobility related protein 1 (MRP-1) [140]. It is a transmembrane glycoprotein involved in associations with each other, with other transmembrane molecules and with adhesion molecules. In this way, the tetraspanin family is believed to be involved in, among others, tissue differentiation, cell motility and cell adhesion through a dynamic tetraspanin web, organising molecular structures on the cell surface influencing cellular functions. It has been shown that transfection of CD9 suppresses motility and metastasis in-vivo [140].

Throughout the body, CD9 is present and it is expressed on EV. These EV are nano-sized containers originating from a cell membrane and contain the molecular contents of the cell of origin, see Figure C.1, hence the interest in EV for potential cancer biomarkers. They play a role in short and long distance intercellular communication and they can spread freely through the human body, including to the urine. This enables the use of CD9 as a urinary biomarker. Multiple types of EV exist, for example, exosomes (where CD9 is found, 50 to 100nm size), protasomes, oncosomes, microvesicles, ectosomes [31] [30].

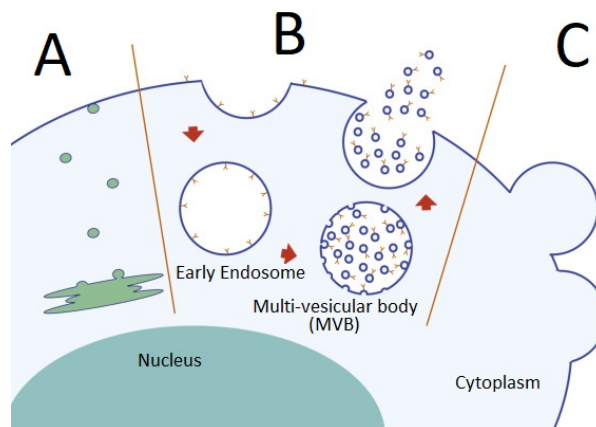


Figure C.1: The origin of EV involving the transmembrane glycoprotein availability on the cell membrane, the forming of an endosome, the formation of an endosome with vesicles (a multi-vesicular body) and the excretion of these vesicles (containing the glycoprotein) so the EV can move through the body [30].

Wang et.al. found reduced CD9 expression in advanced (metastatic) PCa cases while CD9 expression stays high in localised PCa and BHP as is shown in Figure C.2. And, CD9 has been correlated with poor prognosis of several more cancers like non-small cell lung [141], colon [142] and breast [143] cancer. The deprived expression of CD9 is thought to allow for increased motility and promotes progression and metastasis.

A study on the CD9 expression on EV by Brzozowski et.al. concludes low CD9 expression causes increased absorption of these EV by other cells (still healthy cells). This research also concluded high CD151, another tetraspanin, then actually causes increased motility. Then the low CD9 and high CD151 expression combination has negative influence on the metastatic behaviour of a cancerous tissue [31].

Another challenge is the volume of analyte. In urine, approximately 97% consists of proteins like albumin, immunoglobulins, transferrin, fibrinogen and more. These are not useful as biomarker. The actual useful proteins are present in only small quantities, diluted by the other contents [30] [144].

To use CD9 as a urinary biomarker, a normalisation is required to compensate for differing urine volume. An option would be to measure for a biomarker that is not significantly influenced by PCa (for example uri-

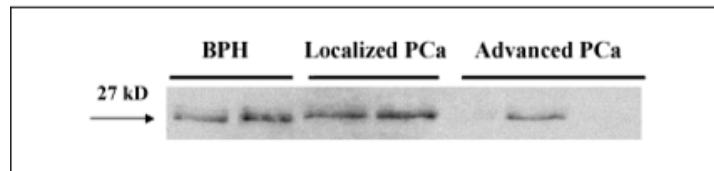


Figure C.2: Low CD9 expression (indicated with the 27kD arrow) in advanced PCa while levels are normal for BHP and localised PCa in western blot analysis by [139].

nary prostate-specific membrane antigen) and normalise it to CD9. A relative high urinary prostate-specific membrane antigen now indicates malignant PCa [145].

### C.2. Capturing CD9

Guido Jenster about capturing CD9 in an immunoassay [32]. It clearly shows CD9 is stuck at an EV, so it is also only captured while attached to an EV.

Urine PSA not PCa dependent [10]. Therefore useful as reference when detecting CD9. Same article underlines the need for DRE before taking a urine sample: the DRE increases CD9 levels. Also claiming increased CD9 expression while often downreguation is mentioned.

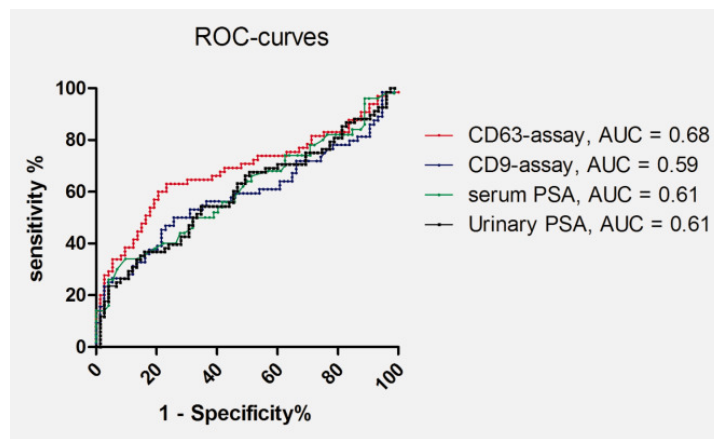


Figure C.3: Comparing sensitivity and specificity for CD9, CD63, Urinary PSA and serum PSA. Not the expected result. This paper is from Jenster in 2015. Expected better from CD9. [10].

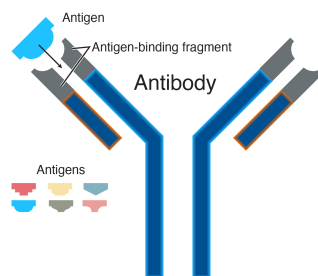


Figure C.4: Antibodies, also called immunoglobins (Igs), are proteins secreted in response to an antigen by effector B, or plasma cells. Five types of antibodies exist, IgM (secreted first during primary response), IgA, IgD, IgG (75% to 80% of all circulating antibodies accounting for the late primary and secondary response) and IgE. They are all constructed from one or more Y or T shaped monomers and can contain up to five monomers in case of the IgM type. The types have different functions and are made and can be found in different locations in the body. Antibodies can neutralise (by blocking binding sites) and mark antigens for destruction by innate defences. Monoclonal antibodies are prepared commercially for research, used to detect very specific antigens. Antigens are antibody generating proteins. Virtually all foreign molecules can act as antigens. Information from [12]. An IgG antibody has an approximate total weight around 160,000 [34]. Figure taken from [146].

increased CD9 expression correlated with circulating tumor cells (CTC). High CTC is bad prognosis for cancer. CD9 expression much more correlated then CD63. 2017  
state lower CD9 with PCa but when normalised for uPSA the CD9 levels where higher with PCa.  
Beautiful PSA vs CD9 diagnostic performance comparison. Also stating increased CD9

# D | Conformal mapping based calculation of a coplanar capacitor capacitance

Using the derivation from [97] which are based on equations derived using conformal mapping for use in computer aided design software (CAD) [98], estimations are made for the capacitance of finger pairs. This still excludes the coupling between the piezoelectric substrate and the electrodes. This is expected to have limited impact but must be investigated.

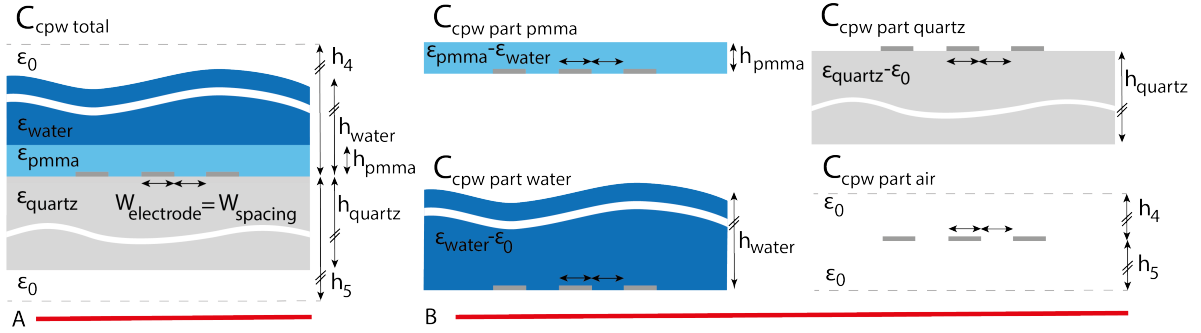


Figure D.1: Decomposition of the geometry used to estimate the capacitance of a coplanar capacitor in multiple dielectric layers. Based on [98].

The equations from [97] and [98] are given below.

$$w_{electrode} = 2\mu\text{m}; w_{spacing} = w_{electrode}; h_{quartz} = 500\mu\text{m}; h_{pmma} = \lambda/5; h_{water} = 1\text{mm}; \quad (\text{D.1})$$

$$k_1 = \frac{\sinh(\pi w_{electrode}/4h_{quartz})}{\sinh((\pi(w_{electrode} + 2w_{spacing}))/4h_{quartz})} \quad (\text{D.2})$$

$$k'_1 = \sqrt{1 - k_1^2} \quad (\text{D.3})$$

$$K_{k_1} = \text{ellipke}(k_1); K'_{k_1} = \text{ellipke}(k'_1) \quad (\text{D.4})$$

'ellipke' is the elliptic integral of the first kind.

$$k_2 = \frac{\sinh(\pi * w_{electrode}/(4 * h_{pmma}))}{\sinh((\pi(w_{electrode} + 2w_{spacing}))/4h_{pmma})} \quad (\text{D.5})$$

$$k'_2 = \sqrt{1 - k_2^2} \quad (\text{D.6})$$

$$K_{k_2} = \text{ellipke}(k_2); K'_{k_2} = \text{ellipke}(k'_2); \quad (\text{D.7})$$

$$k_3 = \frac{\sinh(\pi * w_{electrode}/4h_{water})}{\sinh((\pi(w_{electrode} + 2w_{spacing}))/4h_{water})} \quad (\text{D.8})$$

$$k'_3 = \sqrt{1 - k_3^2} \quad (\text{D.9})$$

$$K_{k_3} = \text{ellipke}(k_3); K'_{k_3} = \text{ellipke}(k'_3) \quad (\text{D.10})$$

$$Ccpw_{quartz} = W2\epsilon_0(\epsilon_{quartz} - 1) \frac{K_{k1}}{K_{k1'}} \quad (D.11)$$

with  $W$  the aperture,

$$Ccpw_{pmma} = W2\epsilon_0(\epsilon_{pmma} - \epsilon_{water}) \frac{K_{k2}}{K_{k2'}} \quad (D.12)$$

Notice that  $\epsilon_{pmma} < \epsilon_{water}$ , so the resulting capacitance from equation D.12 is negative, compensating from the overestimation due to the  $Ccpw_{water}$  calculation in equation D.13.

$$Ccpw_{water} = W2\epsilon_0 * (\epsilon_{water} - 1) \frac{K_{k3}}{K_{k3'}} \quad (D.13)$$

$$h_5 = 1; h_4 = 1 \quad (D.14)$$

In meters to move shielding electrodes far away to remove any influence.

$$k_4 = \frac{\tanh(\pi w_{electrode}/4h_4)}{\tanh(\pi(w_{electrode} + 2w_{spacing})/4h_4)} \quad (D.15)$$

$$k_4' = \sqrt{1 - k_4^2} \quad (D.16)$$

$$k_5 = \frac{\tanh(\pi w_{electrode}/(4h_5))}{\tanh(\pi(w_{electrode} + 2w_{spacing})/(4h_5))} \quad (D.17)$$

$$k_5' = \sqrt{1 - k_5^2} \quad (D.18)$$

$$K_{k4} = \text{ellipke}(k_4); K_{k4'} = \text{ellipke}(k_4'); \quad (D.19)$$

$$K_{k5} = \text{ellipke}(k_5); K_{k5'} = \text{ellipke}(k_5'); \quad (D.20)$$

$$Ccpw_{air} = W2\epsilon_0 \left( \frac{K_{k5}}{K_{k5'}} + \frac{K_{k4}}{K_{k4'}} \right); \quad (D.21)$$

$$Ccpw_{tot} = Ccpw_{air} + Ccpw_{pmma} + Ccpw_{quartz} + Ccpw_{water} \quad (D.22)$$

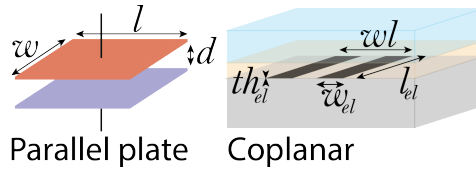


Figure D.2: Dimensions for the capacitance conformal mapping based MATLAB calculation and COMSOL model calculation.

Table D.1: Compare the derived capacitance from the CAD equations and from COMSOL. The dimensions are explained in Figure D.2. For parallel plate, square area chosen to reduce fringing inaccuracy. Dimensions chosen close to single finger area to stay in the same order of magnitude. In COMSOL, 1 plate connected to ground, the other to 1V. Then using  $Q = C V$ , follows  $C = Q/1$ , the charge on 1 plate is taken. The parallel plate contribution of the CPW capacitance is added at a 50nm electrode thickness to show its value is negligible compared to the total capacitance. This indicates most energy will be in the field lines travelling through the elliptic field lines, half of which perturbate the Quartz, exciting the piezoelectric effect.

Capacitor geometry	Dielectric	Dimensions (PP: $w, l, d$ ) (CP: $w_{el}, l_{el}, wl$ )	Capacitance Mathematical derivation	Capacitance COMSOL
Parallel plate (PP)	Vacuum	$20\mu\text{m}, 40\mu\text{m}, 0.8\mu\text{m}$	8.85fF	11.2fF
	PMMA	$20\mu\text{m}, 40\mu\text{m}, 0.8\mu\text{m}$	26.6fF	33.7fF
Coplanar (CP)	Vacuum	$2\mu\text{m}, 50\mu\text{m}, 8\mu\text{m}$	8.64fF	10.9fF
	PMMA	$2\mu\text{m}, 50\mu\text{m}, 8\mu\text{m}$	25.9fF	32.8fF
	Quartz-PMMA-water	$2\mu\text{m}, 50\mu\text{m}, 8\mu\text{m}$	135fF	45.4fF
	Piezoelectric coupling - Quartz-PMMA-water	$2\mu\text{m}, 50\mu\text{m}, 8\mu\text{m}$	-	46.4fF
Coplanar PP contr	PMMA	(CP, PP contr.: $th_{el}, w_{el}, l_{el}, wl$ ) $50\text{nm}, 50\mu\text{m}, 8\mu\text{m}, 2\mu\text{m}$	0.26fF	

## E | Crossed-Field Model

The crossed-field model, derived from the Mason equivalent circuit treats each IDT as a three port network. Two ports are acoustic (to accommodate for the bidirectional function) and one port electric. The following derivation is based on and explained more elaborately in [76]. This derivation was originally described by Smith (et. al) 1969 [77].

To express the three port in electric terms, the mechanical ports or acoustic ports need to be converted to electric equivalent ports. Here the acoustic forces  $F$  can be expressed as voltage  $V$  and the acoustic velocities  $v$  can be expressed as currents  $I$  using a proportionality constant  $\phi$ :

$$V = F/\phi \quad (\text{E.1})$$

and

$$I = v\phi. \quad (\text{E.2})$$

Here  $\phi$  can be interpreted as the turns ratio of an acoustic-to-electric converter.

Using these definitions, an acoustic or mechanical impedance can be defined as  $Z_m = F/v$ . Then for a uniform acoustic wave travelling through a material with density  $\rho$  (kg/m<sup>3</sup>) and cross-sectional area  $A$  (m<sup>2</sup>), this mechanical impedance can also be written as  $Z_m = \rho v A$  (kg/sec), and the equivalent electrical impedance is  $Z_0 = Z_m/\phi^2$ .

From these definitions, the electrical characteristic admittance can be derived as:

$$G_0 = \kappa^2 C_s f_0, \quad (\text{E.3})$$

in  $\mathcal{U}$ , with  $G_0 = 1/Z_0$ ,  $C_s$  being the static capacitance of a single electrode pair and  $f_0$  the IDT centre frequency. Notice that  $C_s$  can be expressed in terms of the unit length capacitance of an electrode pair  $C_0$  and the aperture  $W$  as  $C_s = C_0 W$ .

Now a three port admittance matrix can be derived for a single IDT. This can be simplified due to symmetry in the IDT and SAW propagation. When this matrix is expanded near the centre frequency  $f_0$ , the input admittance for the electric port can be found as:

$$Y_e(f_0) = \left. \frac{I_e}{V_e} \right|_{f_0} = G_a(f_0) + j2\pi f_0 C_T, \quad (\text{E.4})$$

with the radiation conductance,

$$G_a(f_0) = 8\kappa^2 f_0 C_s N^2 \quad (\text{E.5})$$

in  $\mathcal{U}$ . So near the centre frequency,  $B_a = 0$ . For the matrix expansion steps the reader is referred to [77].

Now for frequencies near the centre frequency, the radiation conductance can be generalised by,

$$G_a(f) \approx G_a(f_0) \left| \frac{\sin x}{x} \right|^2 \quad (\text{E.6})$$

with  $x = N\pi(f - f_0)/f_0$  and a sinc function can be recognised.

Finally, the input admittance can also be generalised as:

$$Y_e(f) \approx G_a(f) + j\omega C_T. \quad (\text{E.7})$$

The resulting equivalent circuit is then depicted in Figure E.1, A. When the input and output IDTs are symmetrical, the equivalent circuit can be represented as shown in Figure E.1, B, where the output IDT excitation source represents the arriving acoustic waves and is modelled with a current source causing a voltage over the output IDT and load.

The crossed-field model is actually a simplification, as is shown in Figure E.2. For the crossed-field model, the transducer electrical input immittance is best described by a shunt equivalent circuit representation, whereas the in-line model is best represented with a series equivalent circuit. These are however very comparable as long as  $[(4/\pi)\kappa^2 N]^2 \ll 1$  [77].



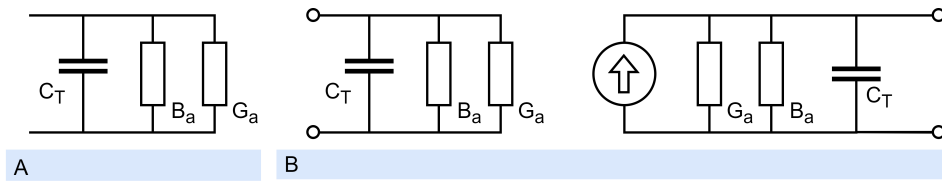


Figure E.1: Equivalent circuit for a SAW sensor based on the crossed-field model [77].

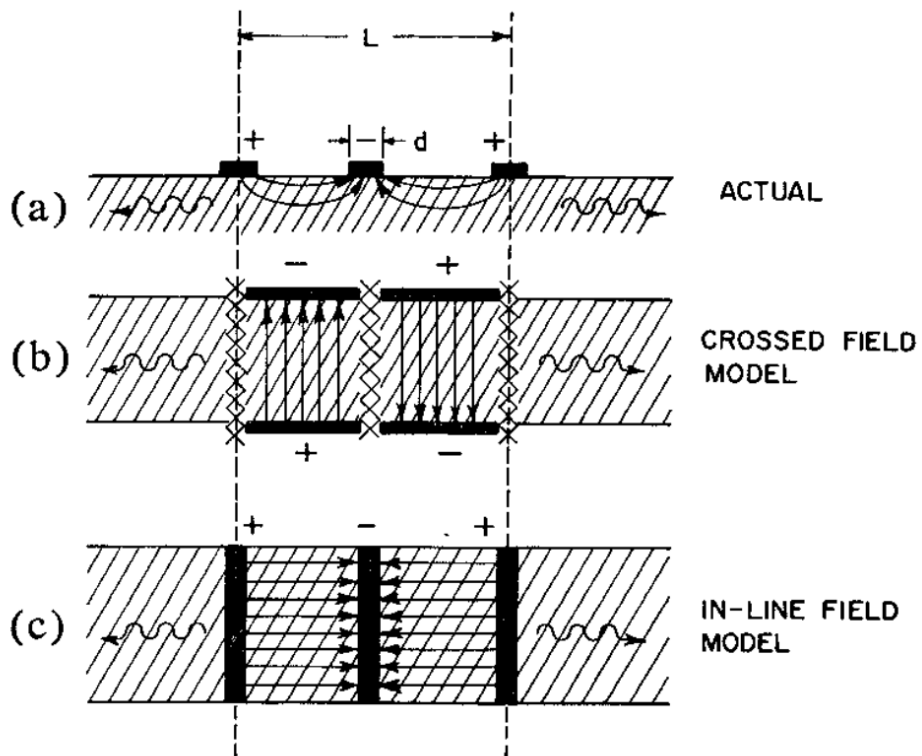


Figure E.2: Field lines between IDT fingers and the crossed field and in-line model assumptions, figure from [77].

# F | Parameter and Variable relation

In Chapter 4, relevant design variables were discussed and how they influence performance variables. In Figures F.1 and F.2, the dependencies are visualised. This can then be used to construct a design order that avoids design loops and unnecessary iterations.

Notice these are only the most relevant parameters and the most significant interactions. For example temperature is not included while it affects many parameters. It would be impossible to include all parameter interactions in a readable 2D figure. Moreover, the relevancy would eventually be lost.

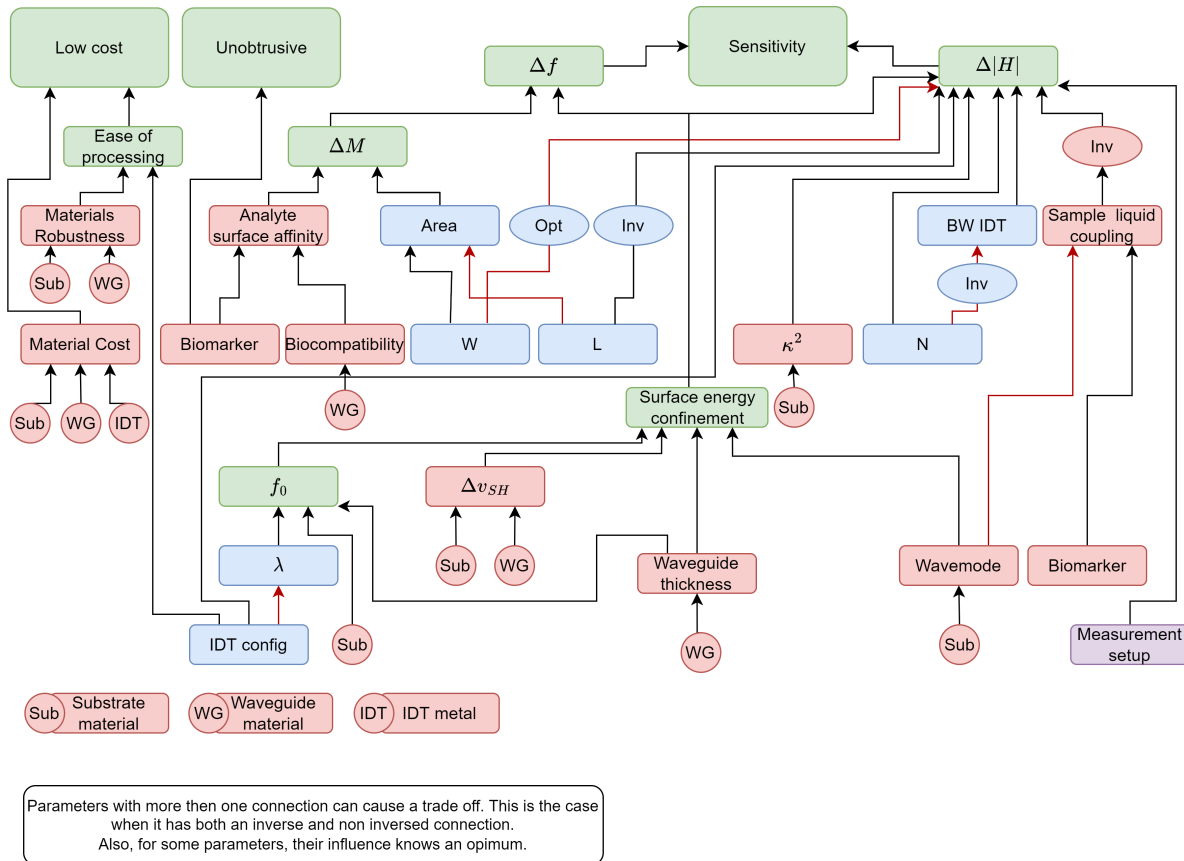


Figure F.1: All parameters and materials that can be chosen independently have no arrow into them. From bottom up, the influence of each material of parameter on eventually the sensitivity is represented. Notice this is a simplified diagram where several blocks can be further subdivided. All red blocks are dependent on material choices. All blue blocks are determined by IDT design. Finally, all green blocks are defined by both material and IDT design. As the material choices influence many variables, they have been represented with circles to avoid an unreadable amount of interconnections.

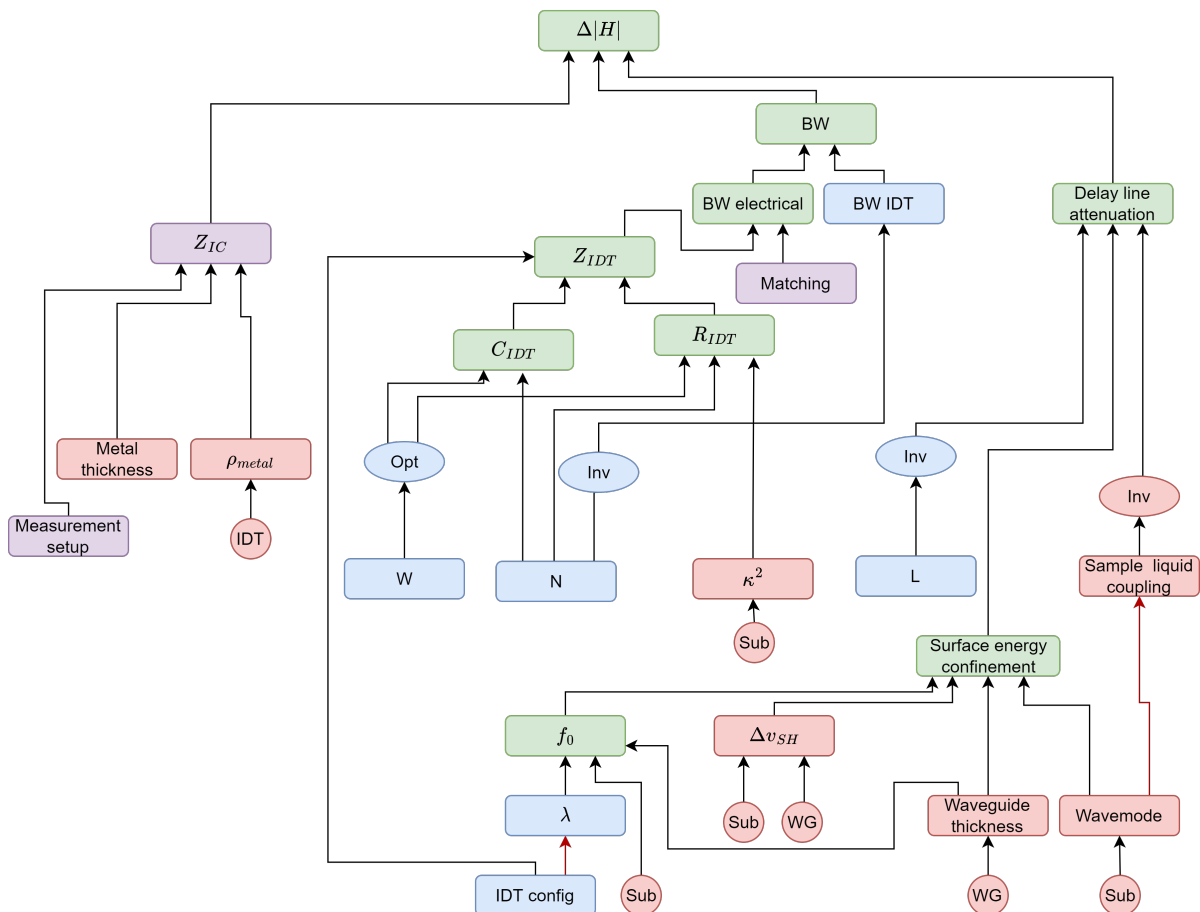


Figure E2: All parameters and materials that can be chosen independently have no arrow into them. From bottom up, the influence of each material of parameter on eventually the sensitivity is represented. Notice this is a sub-block for the IL or magnitude of the transfer  $H$ . It is still a simplified diagram where several blocks can be further subdivided. All red blocks are dependent on material choices. All blue blocks are determined by IDT design. Finally, all green blocks are defined by both material and IDT design. As the material choices influence many variables, they have been represented with circles to avoid an unreadable amount of interconnections.

## G | Smith chart

The Smith chart based on the crossed field electrical equivalent model described by Campbell et al. 1989 [76], originally derived by Smith et al. [77]. In this Smith chart, SAW device parameters aperture ( $W$ ) and finger pairs ( $N$ ) are stepped to find single element matching solutions.

The coloured dots correspond to the  $W$  values mentioned in the coloured text at the bottom of the page, all for  $N=35$ ; ([green:  $N=35, W=100\lambda$ ], [lightblue:  $N=35, W=50\lambda$ ], [darkblue:  $N=35, W=20\lambda$ ], [lightblue/black:  $N=35, W=0.7\lambda$ ], [green/black:  $N=35, W=630\lambda$ ]). Where the last two are single element matching solutions.

The yellow line is then interpolated based on the above described dots for  $N=35$ .

The yellow dots correspond to  $N=100$  and the values of  $W$  given at the bottom of the page ( $W=1500, 125, 40, 20, 15, 10, 5, 1$ ) $\cdot\lambda$ . They appear from left to right in the plot corresponding from high  $W$  to low  $W$ .

The purple line is interpolated based on these above calculated points for  $N=100$ .

The pink dashed line is based on  $N=35$ , when calculated without water in the capacitance calculation. It shows a shift with respect to the yellow line.

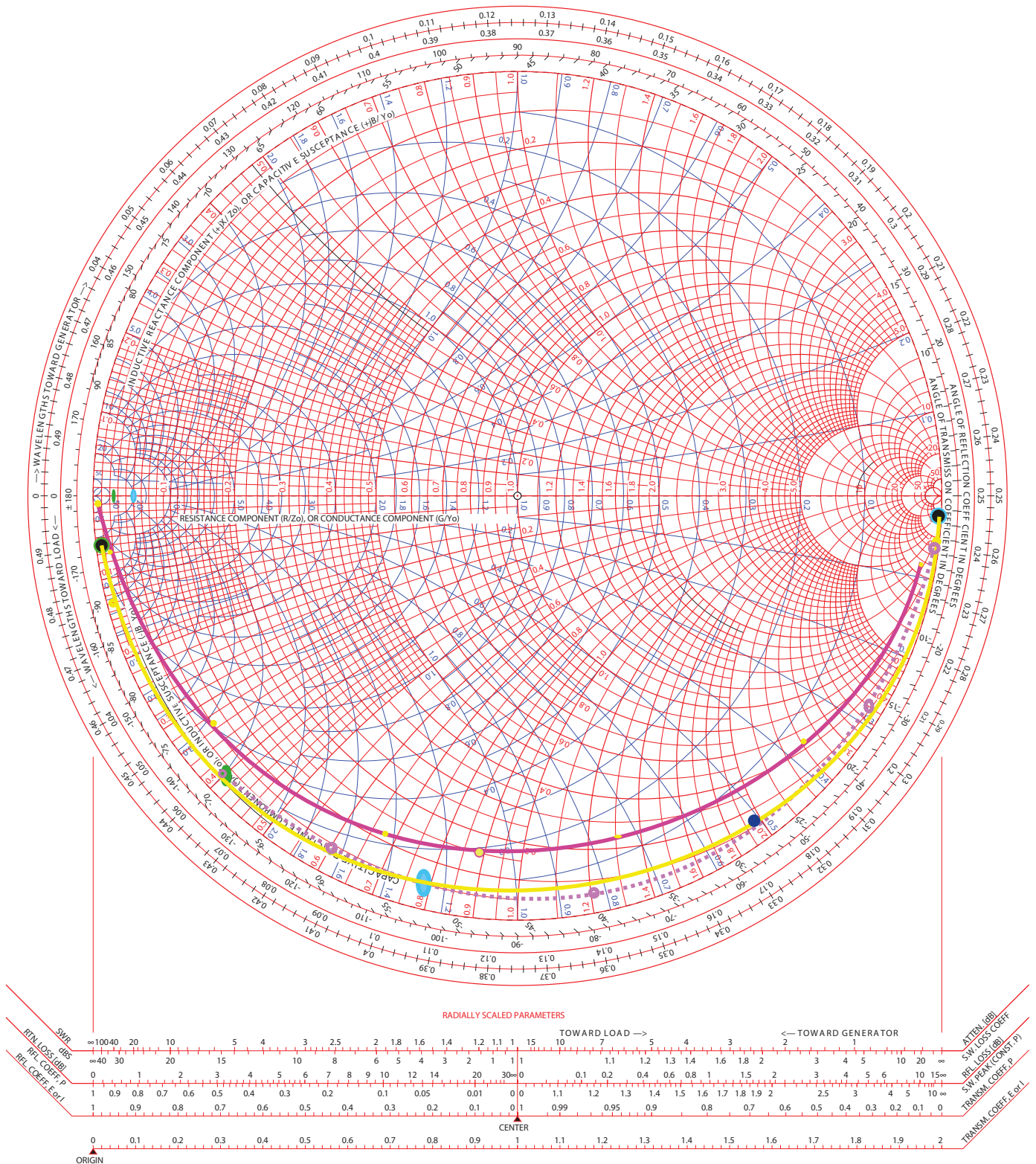
From this Smith chart, it is concluded, single element matching is possible but not practical. When the IDT is matched, in the normalised Smith chart, the IDT impedance needs to appear at the centre. Using purely reactive elements, the impedance can be shifted over the blue and red circles. With single element matching, the original IDT impedance needs to be exactly on the blue or red circle going through the origin (labeled '1'). For this device, this only happens for extreme values of  $W$  as described next.

In the current design, only by using extreme values for  $W$  near  $0.7\cdot\lambda$  or  $630\cdot\lambda$  for  $N=35$ , the IDT impedance coincides with the red circle or blue circle going through the origin respectively. The value of  $W$  can become a bit less extreme when choosing a higher  $N$ . For example, using  $N=100$ , it is interpolated  $W=80$  or  $W=2$  is required.

The found values of  $W$  are impractical, so single element matching is not possible. Extremely small  $W$  means a very narrow sensitive area, reducing sensitivity. Extremely big  $W$  leads to impractically big devices and higher risk for yield loss. Also internal RC value might start to play a role.

NAME	TITLE	DWG. NO.
SMITH CHART FORM ZY-01-N	COLOR BY J. COLVIN, UNIVERSITY OF FLORIDA, 1997	DATE

### NORMALIZED IMPEDANCE AND ADMITTANCE COORDINATES



$Z_{saw}(W=100\lambda)$

$C_u$  without water line

$Z_{saw}(W=50\lambda)$

$N=35$

$Z_{saw}(W=20\lambda)$

$N=100$

$W = [1500, 125, 40, 20, 15, 10, 5, 1] * w_l$

$Z_{series}(W=0.7\lambda)$

$Z_{shunt}(W=630\lambda)$

# H | PI spin test

To determine the required process to reach the required PI thickness, the spin curve of the used PI (LTC 9305) is determined. This spin curve is not known near the required thickness by the supplier as the PI is used far below its typical application thickness of 5µm as seen in H.1. The goal is to find the process parameters to reach around 500nm PI thickness after curing.

It is assumed, even though the material is used for thicknesses far below its typical application, the spin curve still has inverse square root dependency on speed. Then the curve has a dependency as in equation H.1.

$$th = \frac{c}{\sqrt{\omega_{spin}}} \tag{H.1}$$

with  $th$ , the obtained PI thickness,  $c$  some process dependent coefficient that is to be determined based on previous work or new spin tests and  $V_{spin}$  the rotational speed used in the spinning process.

Also, it is expected, due to the thin layer thickness, high spinning speeds are to be used, causing no equilibrium is achieved in a reasonable spinning time. In other words, the achieved thickness is expected to be time dependent.

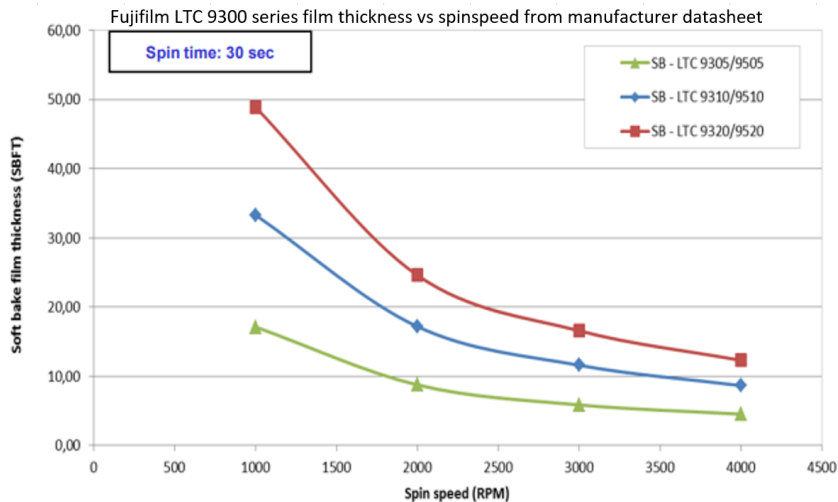


Figure H.1: Soft bake spin curves from datasheet by manufacturer, Fujifilm [118].

Prior results by H. Aydogmus, N. Gaio and W. Quiros Solano, see Table H.1, indicate PI thicknesses near 500nm could be feasible, though the calculated required spinning speeds already are very inconsistent and some already quite high. From their process parameters, start values for the spin test are derived and determined to be 1000rpm spreading for 10 seconds, ramped to with 500rpm/s. And a 5700rpm spin step, also ramped up to with 500rpm/s.

## H.1. Flowchart

The process is run at the Else Kooi Lab in Delft (EKL). The process is designed to the capabilities and constraints of EKL.

First, five silicon (Si) wafers with silicon dioxide layer (SiO<sub>2</sub>) are used to determine the required spin speed. The SiO<sub>2</sub> layer is included as it is expected the SiO<sub>2</sub> will closer resemble Qz than a Si surface, making the tests more relevant for Qz wafers as used later in the process. The tests are not done on Qz wafers as they are only limited available and cured PI is not easily removed. Furthermore, Si wafers are more robust for testing purposes. Quartz (Qz) and Si dummy wafers used in the following process runs are also included in these results for completeness.

All substrates are cleaned in a high power oxygen plasma, HNO<sub>3</sub> 99% and HNO<sub>3</sub> 69%. Then for the Si test wafer batch, plasma enhanced chemical vapour deposition (PECVD) SiO<sub>2</sub> xxum layer is deposited with an Omega 204 plasma enhanced chemical vapour deposition tool. The process wafers are first given a metal layer, patterned and then cleaned before spin coating.

For adhesion promotion of PI to the substrate, wafers with O<sub>2</sub> low power plasma treatment, HMDS treatment and no surface enhancement treatment are fabricated.

The spincoater allows to enter a spin speed up to 12000rpm, but it is seldom used at this speed. Therefore, lower speeds are attempted. A volume of approximately 4mL is placed on the wafer, covering about 30% of the wafer area before the spreading step. It is visually confirmed, after the spreading step, the wafer is completely covered. Then the high speed spin step is done. After spin coating, based on previous work, a 90 second soft bake is done.

All substrates are exposed using a SUSS MicroTech Contact Aligner. The exposure time is determined from the dose given in the LTC9305 datasheet and the recent measured exposure intensity of the Contact Aligner.

Then the PI is developed with a 100°C 90 second post exposure bake, 90 seconds HTD:R2 submersion, subsequent a 90 second RER submersion to stop the development process. After this the wafers are cleaned with a DI water jet, care must be taken to not apply too much force with the water jet to damage the soft PI, but sufficient water pressure and water flow is required to remove the development products.

Now the wafer can be inspected microscopically. Another develop step can be done if development was not complete or develop remains show during this inspection. Then another 90 second bake at 100°C is done.

The samples are cured at 350deg for 4 hours in a Koyo inert gas oven. More precisely following the cycle, heating up for 1h to 300deg, heating further in 1.30h to 350 deg, staying for 1h at 350deg, then start the cool down in 1.3h to 280 deg and finally cool down in 3h to 20deg. The actual temperature rise time is much faster, so the samples are indeed at 350 deg for 4h.

Then the acquired PI thickness after curing is determined with profilometry with a Dektak 8 profilometer as on Qz, optical techniques are exceedingly challenging. All samples are patterned to create profiles to measure. By microscopic visual inspection, measurement locations free of particles are selected. Locations all over the waver area are measured to also check if the layer thickness is dependent on the distance to the wafer centre.

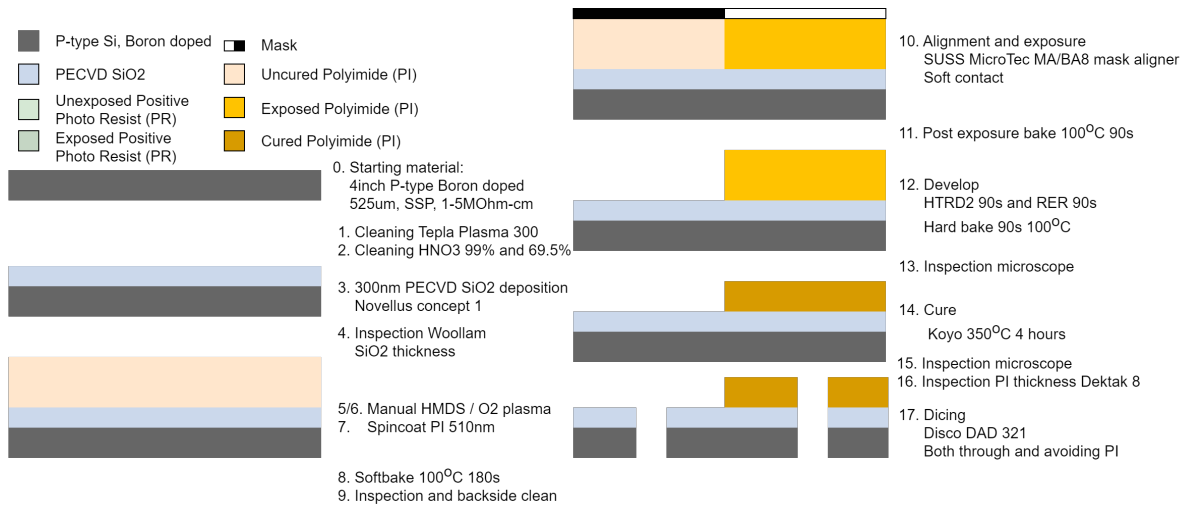


Figure H.2: Flowchart for PI spinning thickness tests with indicated process steps.

## H.2. Profilometry Results

The determined average thickness per wafer for a 75 second spun wafer against several speeds is plotted in Figure H.3 A. The obtained average thickness per wafer for a 6000rpm spin speed for several spin times is plotted in Figure H.3 B.

The spread in all measurements per wafer is shown in Figure H.4 A. The uniformity per wafer apparently differs from wafer to wafer. And all thickness measurements ordered with respect to distance to the wafer

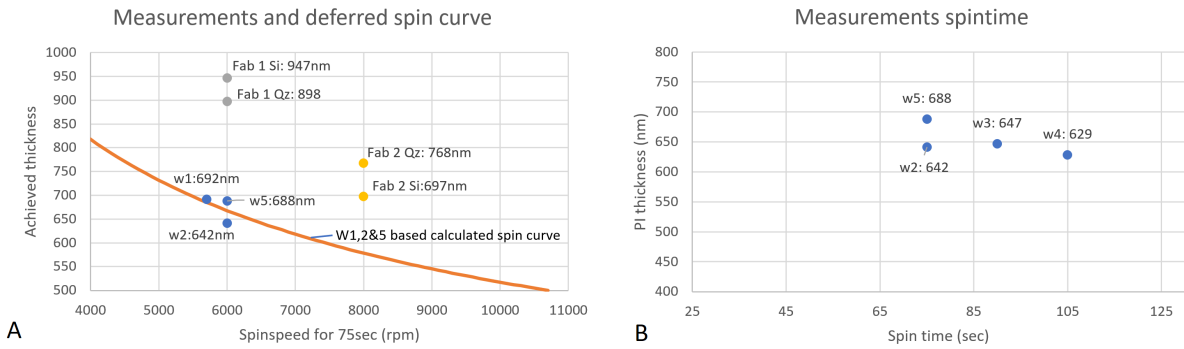


Figure H.3: Measured points on spin curve. A) Measurements with a 75 second spin time and the calculated corresponding spin curve. B) Measurements at 6000rpm for several spin times to determine time related thickness dependency.

centre normalised from 0 (center) to 1 (outer edge) are shown in Figure H.4 B. Consistently, all wafers show on average a slight decrease in thickness towards the wafer edge.

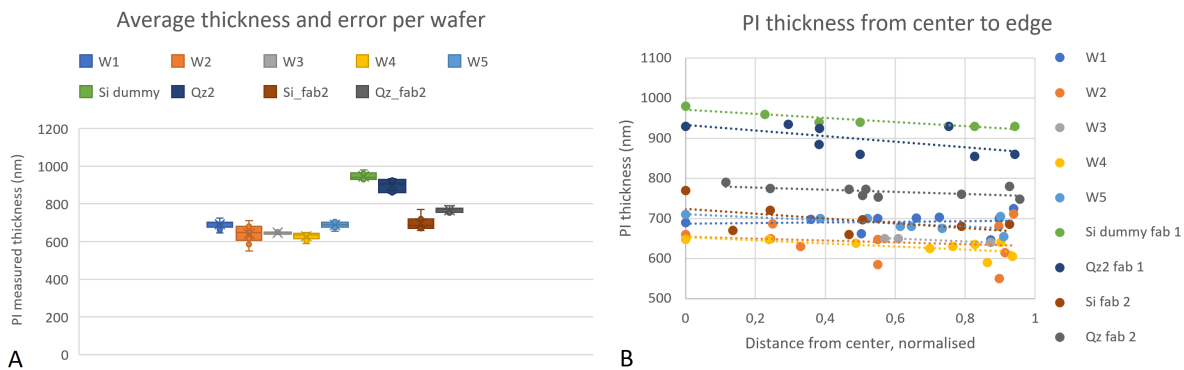


Figure H.4: A) Spread in measured points per wafer. B) Dependency of thickness on distance to centre showing a slight dependency for most wafers.

For completeness, the measurement locations of all profilometry measurements are shown in Figure H.5. The locations were chosen along the x or y axis for convenient distance to centre reference. It was assumed, the wafer is circularly symmetrical as a result from the spinning process.

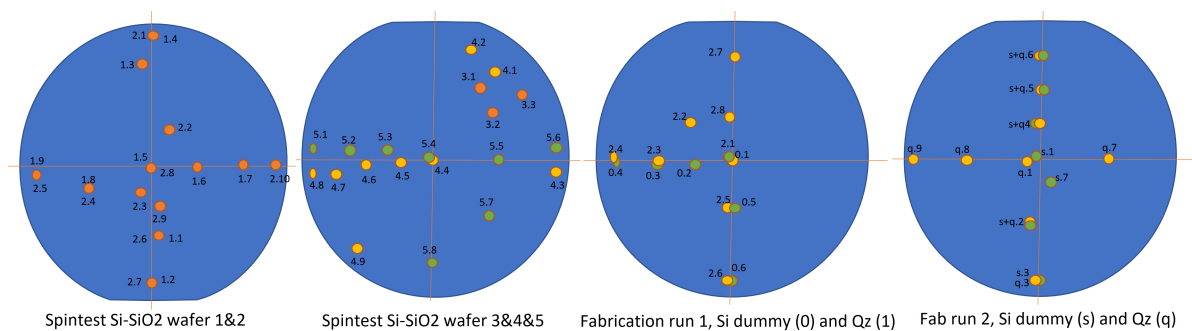


Figure H.5: Locations of Dektak measurements.

### H.3. Discussion

The most important findings from the processing and measurements are discussed next. First processing related topics are expound. Then the measurement findings, limits and shortcomings are listed. Finally, the last processing step, dicing, is discussed.



### Tool limits

As the required speeds are close to the limit of the tool after the data was extrapolated, it is chosen to accept a thicker layer thickness. This comes at the cost of signal strength in the final sensor application as higher losses in the WG layer will occur. In the future, different materials can be considered that can be diluted to influence the viscosity when spincoating to reach the desired thickness at reasonable spin speed at the cost of a more complicated process flow. For the photosensitive LTC9305, this was not considered as the photosensitivity is likely influenced by diluting. When a non-photosensitive polymer is used, the freedom of diluting becomes available but additional steps must be included to remove the polymer from the contact pads, complicating the process.

### Surface chemistry

No clear relation between surface chemistry and acquired thickness was observed. Qz, Si, SiO<sub>2</sub>, and SiO<sub>2</sub> O<sub>2</sub> plasma treated surfaces all had similar thickness results. Though this is based on only few samples, both the on wafer variation and inter wafer variation seem to have larger influence than surface chemistry.

HMDS is a PI contaminant as was found in the develop process of the HMDS treated test wafer (W3) and as is mentioned in the data sheet. Wafer W3 showed poor adhesion, causing the PI to wrinkle off in the develop step, only keeping a small area in the upper right corner measurable with profilometry.

### PI batch

The reached thickness is very LTC9305 batch dependent. The difference in obtained thickness for the same process for two batches (expiry date 2022 and 2023) was around 200nm. This might be caused by different manufacturing dates, but also storage and previous use (read temperature cycles) might have significant influence on the material. Therefore always calibration tests must be run when switching to a new batch.

### Variance

The variation between wafers for the same process parameters is around 50nm. This is below 10% of the achieved thickness which is an acceptable variation.

In nearly all processed wafers, the PI layer tends to become thinner away from the centre of the wafer indicating no uniformly distributed equilibrium between the centrifugal force and the material viscosity is reached. The maximum on wafer variation in thickness from centre to edge ranges from 50nm to 150nm. No clear relations between spinspeed, spintime or surface chemistry are indicated. This poses a challenge for process repeatability in later stages.

Both the inter wafer and on wafer uniformity might very well be influenced by the dispensed PI volume before spinning. Now, every volume was not exactly measured and therefore subject to variance. Furthermore, the volume was never sufficient to cover the entire wafer before the spreading step to restrict PI consumption. After the spreading step however, the wafer was always fully covered with PI for the actual high rpm spinning step.

### Uniformity

When the process wafers are well cleaned, very uniform layers are obtained. Several wafers proved a small particle can cause a large difference in thickness over several centimetre long lines straight from the centre to the edge. A particle was measured to cause over 800nm error in the thickness (hill and valley). This can hugely influence the yield indicating the importance of a cleaning step before spincoating.

### Dektak accuracy

The Dektak accuracy was not calibrated. Depending on the needle size, needle movement speed and other factors, the accuracy can be influenced. This might cause unseen measurement error. Other Dektak related challenges are overshoot near a rising edge, so no thickness data right on the rising edge should be used. And drift, which is zeroed in the data processing by selecting two reference locations.

### Spinspeed and spintime

The spinspeed shows a quadratic relation with the obtained PI thickness. And it is observed increasing the spin time results in thinner layers. The combination of these parameters can be used to obtain a thin as possible layer against the boundaries of the equipment.

The spinspeed is then limited by the used equipment. The combination of spin time and speed is limited by a trade-off between layer thickness and yield where the cleanness of the wafer shifts the optimum.

### Dicing

Dicing did not show any damage to the PI when dicing through PI cleared substrates and when dicing straight through PI coated surfaces. Surface O<sub>2</sub> activation did not demonstrate clear adhesion improvement. Dicing tests show already sufficiently strong adhesion without O<sub>2</sub> plasma.

### Previous work and measurements summary

Table H.1 shows the collected previous work and the results of all spinning steps done in the test runs and processing runs. It serves as reference for future processing plans.

Table H.1: Summary of found processing parameters with results from previous works and own conducted process.

		Information and Measurements					Calculated	
	material	thickness measured (nm)	spin recipe				calculated constant (-)	for 510nm required spin speed (rpm)
			spin 1 (rpm)	time 1 (sec)	spin 2 (rpm)	time 2 (sec)		
Previous work								
Hande 1	LT9305	700	600	10	6000	75	54000	11000
Hande 2	LT9305	500	1000	10	6000	75	39000	5800
Wiliam	N.A.	600	300	5	2000	30	27000	2800
Nikolas	LT9305	800	N.A.	N.A.	N.A.	N.A.	N.A.	N.A.
Own results, PI from EKL storage								
W1	LTC9305	692	1000	10	5700	75	52000	10500
W2&5	LTC9305	986	1000	10	6000	75	76000	22000
W3	LTC9305	647	1000	10	6000	90	50000	9700
W4	LTC9305	629	1000	10	6000	105	49000	9000
Own results, other PI batch from EKL storage								
Si1	LTC9305	947	1000	10	6000	75	73000	21000
Qz1	LTC9305	898	1000	10	6000	75	70000	19000
Si2	LTC9305	697	1000	10	8000	75	62000	15000
Qz2	LTC9305	768	1000	10	8000	75	69000	18000

## H.4. Conclusion

To reach 500nm, the spincoater has to be used at speeds near its limit depending on the PI batch. Due to batch variation, test runs are always required if accurate thicknesses are required.

Finally, the actual flowchart used for these spin tests is included.

# Flow Chart PI fabrication

Batch Information - Version 14-11-2022			
Name of owner:	Johan Meyer	Mask set:	
Name of mentor:	Paddy French	Mask Box:	
Run number:	eg. JWDM2022PI1	Die size:	10mm
Wafer amount:	6	Sart date:	
Subject to PCC:		PCC approved:	

Starting material	
Type	P-type / Boron Si SSP
Orientation	[100]
Resistivity	1-5 MOhm-cm
Thickness	525 $\pm$ 15 $\mu$ m
Diameter	100mm $\pm$ 0.5mm (4 inch)

## GENERAL RULES

### CLEANROOM BEHAVIOUR

Always follow the "Security and Behaviour" rules when working in the EKL laboratories.

Always handle wafers with care during processing. Use cleanroom gloves and work as clean as possible!!

Use cleanroom gloves when working with vacuum equipment. Do not touch the inside or carriers with bare hands.

Always check equipment and process conditions before starting a process. Do **NOT** make unauthorized changes!

Directly notify the responsible staff member(s) when there are problems with equipment (like malfunction or contamination). Put the system down in the Phoenix reservation system, and turn the equipment status sign from **UP** or **Usable** to **DOWN**.

**DO NOT TRY TO REPAIR OR CLEAN EQUIPMENT YOURSELF**, and **NEVER** try to refresh a contaminated etch or cleaning bath! Only authorized staff members are allowed to do this.

### PCC RULES

All substrates, layers and chemicals which are not CMOS compatible are considered to be "NON-STANDARD" materials, and may be contaminating.

The use of "non-standard" materials for processing in the class 100 and SAL cleanroom must **ALWAYS BE EVALUATED AND APPROVED** by your mentor and in agreement with the PCC document.

Wafers that are contaminated may **NEVER** be processed in any of the equipment without permission of the Equipment owner. Special precautions may have to be taken, like the use of a special substrate holder or container.

Check the PCC "Rules & Instructions" - available on the "[EKL intranet webpage](#)" - for more details.

## CLASS 100 RULES

### CLEANING OF WAFERS

After several hours (4 hours max) of storage wafers must always be cleaned before performing a **COATING, FURNACE, EPITAXY** or **DEPOSITION** step.

Use the correct cleaning procedure:

- Tepla stripper ⇒ for removal of implanted or plasma etched photoresist
- Acetone ⇒ for removal of photoresist that is not implanted or plasma etched
- HNO<sub>3</sub> 99% (Si) ⇒ for IC compatible wafers which do not need a HNO<sub>3</sub> 69.5% step
- HNO<sub>3</sub> 99% (Al) ⇒ for wafers which are or have been in contact with one of the following metals: like Al, Al(1% Si), Ge, Ti, Zr
- HNO<sub>3</sub> 99% (Si) + HNO<sub>3</sub> 69.5% (Si) ⇒ for all other IC compatible wafers

**Note:**

- The above described cleaning procedures are only valid for IC compatible wafers with "standard" materials on them. **In all other situations follow the PCC rules (Previously to be discussed with the mentor).**
- Wafers do not have to be cleaned **after** a furnace, epitaxy or deposition step if the next process step will be performed immediately, unless the wafers are covered with particles.

### FURNACE RESTRICTIONS

Wafers that are covered with photoresist or a metal layer may **NEVER** be processed in any of the furnaces. This also applies for wafers from which a metal layer has been removed by etching. Only alloying in tube C4 is allowed for wafers with an aluminium layer.

### MEASUREMENTS

Always perform all the measurement and inspection steps, and **write down the results in your journal and in the result tables that can be found at some of the equipment!!** The results are used to check the condition of the processes and/or equipment.

It is possible to use the following Class 100 equipment to measure directly onto your (IC compatible) process wafers:

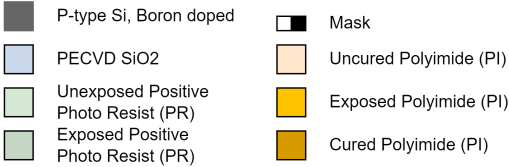







- The Leitz MPV-SP, the WOOLLAM and the SAGAX. These systems are used for thickness measurements of transparent layers. The measurements are non-destructive and without contact to the wafer surface.
- The Dektak 8 surface profilometer. This system is used for step height measurements. In this case a needle will physically scan over the wafer surface (contact measurement), which can be destructive for structures.
- The XL50 SEM. It can be used for inspection of your wafers and for width, depth or thickness measurements.

**Note:** After certain measurements cleaning of your wafers may be required for further processing.

An extra wafer must be processed when other measurement methods will be used (like sheet resistance and junction depth measurements). These wafers cannot be used for further processing.

## Process Steps

1	Wafer Cleaning - CR100 T5 - Tepla plasma 300	5
2	Wafer Cleaning - CR100 T5 Wet Cleaning - HNO3 99% (Si) and 69.5%	5
3	PECVD 300nm SiO2 deposition - CR100 T3 (Plasma) - Novellus Concept 1	5
4	Inspection SiO2 thickness - CR100 T2 (Metrology) - Woollam Ellipsometer	6
5	Surface activation - CR100 T1A - Manual HMDS	6
6	PI deposition 510nm - CR100 T1 (Polymerlab) - Spinner polymers (Poly 2 fume-hood)	6
7	Soft bake - CR100 T1 (Polymerlab)- Fumehood poly 2	6
8	Inspection and clean - CR100 T1 (Polymer lab) - Fumehood poly 2	7
9	Alignment and Exposure - CR100 T1B (Litho) - SUSS MicroTec MA/BA8 mask aligner	7
10	Post exposure hard bake - CR100 T1 (Polymerlab) - Fumehood poly 2	7
11	Development PI - CR100 T1 (PolymerLab) - Fumehood poly 3	7
12	Inspection uncured PI - CR100 T1 (Polymerlab) - Olympus or Axiotron microscope	8
13	Cure PI - CR100 T1 (Polymerlab) - Koyo oven	8
14	Inspection PI clearance - CR100 T1 - Olympus or Axiotron microscope	8
15	Inspection PI thickness - CR100 T2 (Metrology) - Dektak 8	8
16	Dicing - MEMS-Travee3 (Bonding) - Disco DAD321	9
17	Inspection - MEMS-Travee3 (Bonding) - Microscope Leitz	9

Wafer cutline	Flowchart steps	Remarks
		
	Starting material: 4inch P-type Boron doped 525um, SSP, 1-5M0hm-cm	
	Cleaning Tepla Plasma 300 Cleaning HNO3 99% and 69.5%	
	300nm PECVD SiO2 deposition Novellus concept 1	
	Inspection Woollam SiO2 thickness	
	Manual HMDS Spincoat PI 510nm	
	(Degassing) Softbake 100°C 180s Inspection and backside clean	
	Alignment and exposure SUSS MicroTec MA/BA8 mask aligner Soft contact	
	Post exposure bake 100°C 90s	
	Develop HTRD2 90s and RER 90s Hard bake 90s 100°C	
	Inspection microscope	
	Cure Koyo 350°C 4 hours	
	Inspection microscope Inspection PI thickness Dektak 8	
	Dicing Disco DAD 321 Both through and avoiding PI	

# Flowchart

## 1 Wafer Cleaning - CR100 T5 - Tepla plasma 300

1. use program from PIT: **Program 1:** 1000 watts of power, automatic endpoint detection + 2 minutes overetching.

## 2 Wafer Cleaning - CR100 T5 Wet Cleaning - HNO3 99% (Si) and 69.5%

1. Clean - Submerge wafer for 10 minutes in HNO3 99% (Si) at ambient temperature, red dot. Done to dissolve organic materials.
2. Rinse - Submerge wafer in quick dump rinser DI-water for 15 minutes or until 5M  $\Omega$  resistivity is reached.
3. Clean - 10 minutes in concentrated nitric acid at 110C to dissolve metals. "HNO3 69.5% 110C (Si)" and carrier with red dot. Done to remove any metals.
4. Rinse - Submerge wafer in quick dump rinser DI-water for 15 minutes or until 5M $\Omega$  resistivity is reached.
5. Dry - Dry wafer with "Avenger Ultra-Pure 6" rinser/dryer. Standard program, white carrier, red dot.

## 3 PECVD 300nm SiO2 deposition - CR100 T3 (Plasma) - Novellus Concept 1

1. Check if box at back is off to deposit SiO2
2. Set temperature to 350°C
3. Fill wafers from slot 1 (automatic wafer detection)
4. Select recipe ".xxx\_siostd"

Process conditions from .xxx_siostd recipe					
Gasses and flows	Pressure	HF Power	LF Power	Temperature	Time
N <sub>2</sub> /SiH <sub>4</sub> /N <sub>2</sub> O 3150/205/6000 sccm	2.2 Torr	1000W	0W	400 °C	calculate with logbook

Station deposition time (SDT)	
average deposited thickness [nm]	goal deposit thickness [nm]
	300nm
average time	required time

**Fabrication break possibility**

## 4 Inspection SiO<sub>2</sub> thickness - CR100 T2 (Metrology) - Wool-lam Ellipsometer

1. Place wafer on chuck
2. Turn on vacuum
3. Select project: "Dimes general"
4. Select recipe: "Dimes\_oxide(0-1 $\mu$ m)"
5. Give measurement a name: "JWDM2022PI1"

Wafer #	thicknesses measured	avg	std
1			
2			
3			
4			
5			
6			

## 5 Surface activation - CR100 T1A - Manual HMDS

1. Place wafers in manual HMDS carrier.
2. Place carrier in manual HMDS box and close the box.
3. Open the HMDS flow until flow indicator is in specified region (little metal ball in tube).
4. Leave wafers in for 10 minutes.
5. Close HMDS flow.
6. Remove wafers from HMDS box and place back in transport box.
7. Close HMDS box and place carrier back.

## 6 PI deposition 510nm - CR100 T1 (Polymerlab) - Spinner polymers (Poly 2 fumehood)

Perform 'PI deposition' and 'Soft bake' together per wafer.

1. Get PI from fridge and let acclimate to room temp at appropriate cupboard for several hours.
2. Dispense approx 10mL of PI LT9305 precursor and crosslinker solution in a clean beaker.
3. Start up the spinner and log in.
4. Load recipe: "hande\_test".
5. Rename recipe and alter according to the table below.
6. Place wafer on the chuck and center the wafer.
7. Do a test spin without PI to verify the setup is correct.
8. Dispense PI solution on the wafer and start spinning process.
9. Clean the wafer backside using a swap and acetone.

## 7 Soft bake - CR100 T1 (Polymerlab)- Fumehood poly 2

1. Place the tabletop clean hotplate (Hotplate 1 Cl100) in fumehood poly 2 (polymers).
2. Place dummy wafer on hotplate (to ensure hotplate stays clean).
3. Soft bake 180 sec at 100°C



Wafer #	goal PI th	recipe spreading - ramp - spinning - ramp	measured PI th [nm]
1	500nm	1000rpm 10s - 500rpm/s - 6000rpm 75s - 500rpm/s	
2	510nm	1000rpm 10s - 500rpm/s - 5700rpm 75s - 500rpm/s	
3			
4			
5			
6			

## 8 Inspection and clean - CR100 T1 (Polymer lab) - Fumehood poly 2

1. Clean backside of wafer with acetone
2. Visually inspect for any backside PI residues, none are allowed.

## 9 Alignment and Exposure - CR100 T1B (Litho) - SUSS MicroTec MA/BA8 mask aligner

PS-PI is a negative resist. Use any mask that has some large open spaces.

1. Load (MaskID) mask in machine. Use frontside exposure with soft contact.
2. Perform calculation in lab with 'contact aligner exposure energy data log'.
  - Energy required: 400mJ/cm<sup>2</sup>
  - Wavelength
  - Intensity
  - Time

Exposure time calculation:  
Dose(time) = (energy required)/(intensity lamp)

## 10 Post exposure hard bake - CR100 T1 (Polymerlab) - Fumehood poly 2

1. Use the still ready tabletop clean hotplate (Hotplate 1 Cl100) in fumehood poly 2 (polymers).
2. PEB for 90 sec at 100°C

## 11 Development PI - CR100 T1 (PolymerLab) - Fumehood poly 3

1. Prepare a HTRD2 beaker and a RER beaker in fumehood poly 3.
2. Submerge wafer in HTRD2 beaker for 90 sec. (Developer)
3. Submerge wafer in RER for 90 sec. (Develop stop)
4. Rinse with DI water
5. If all wafers are processed, dispose of HTRD2 and RER in organics container (cabinet fumehood poly 3).
6. Hard bake at 100°C for 90 sec using the tabletop hotplate in fumehood poly 2.
7. If all wafers are processed, place hotplate back on shelf.

## 12 Inspection uncured PI - CR100 T1 (Polymerlab) - Olympus or Axiotron microscope

1. After curing, PI can not be removed, so inspect dice track clearance now.
2. If any intolerable errors are spotted, Tepla high power oxygen plasma etch and HNO3 99% cleaning to totally remove PI. Improve process where necessary and retry.

## 13 Cure PI - CR100 T1 (Polymerlab) - Koyo oven

1. Turn on oven and wait for it to start up and self calibrate.
2. Select Program #6 and check if the time and temperatures are correct.
3. Place wafers in oven.
4. Something about Al carrier plate for clean wafers.??
5. Start "Program #6": Cure 350 °C for 4 hours.
6. Once the oven has cooled down, remove wafers and turn off the tool with the main switch.

### Fabrication break possibility

## 14 Inspection PI clearance - CR100 T1 - Olympus or Axiotron microscope

1. Check if PI is neatly removed from dicing track.

## 15 Inspection PI thickness - CR100 T2 (Metrology) - Dektak 8

1. Make sure to use a long measurement track as the relatively soft PI might deform a little by the needle, resulting in a distorted measurement.

Sample location W# Die code #	PI thickness	Sample location W# Die code #	PI thickness	Sample location W# Die code #	PI thickness

Wafer #	recipe: RPM ramp time	average PI thickness	Remarks
1			
2			
3			
4			
5			

## **16 Dicing - MEMS-Travee3 (Bonding) - Disco DAD321**

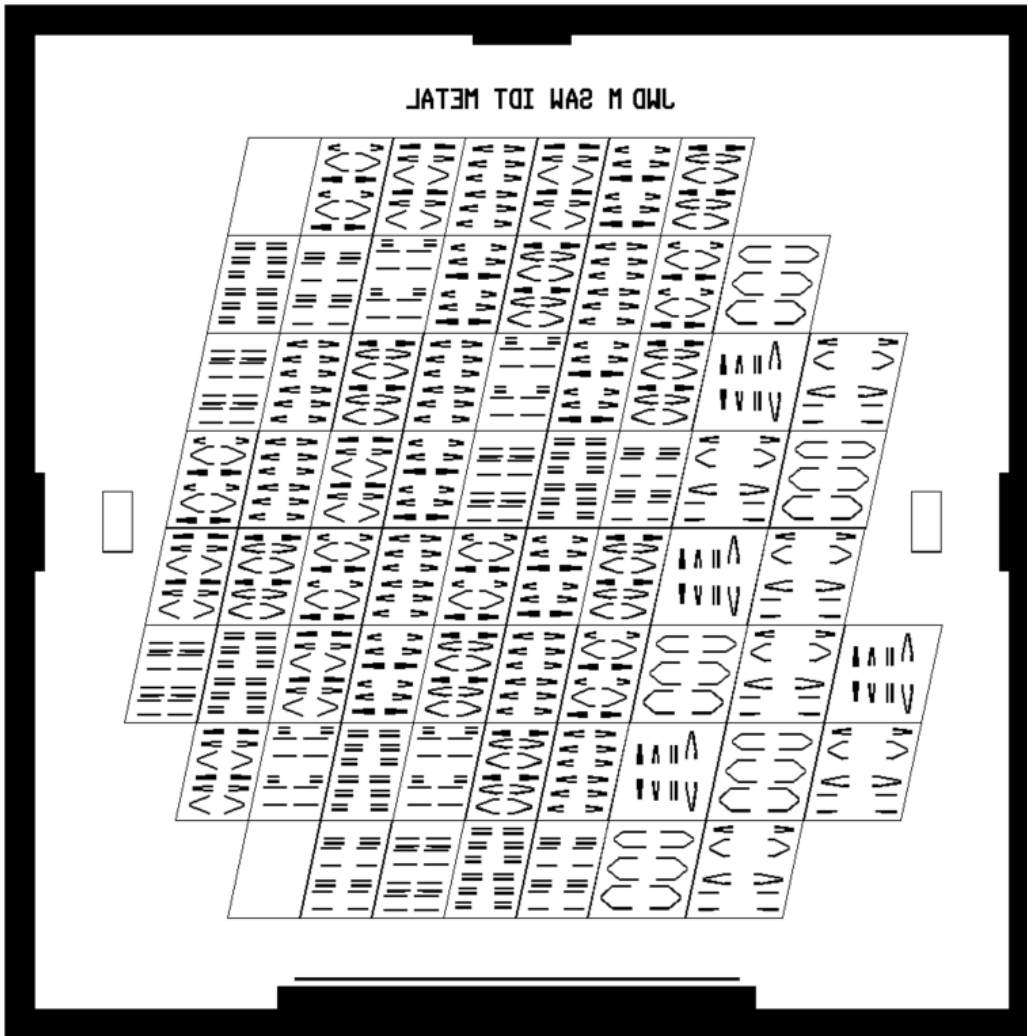
1. Dice wafer in 10x10mm chips in the wafer dicer
2. Dice both over dice lines and over PI to check for destructive effect
3. Rinse chips with DI-water and dry with nitrogen gun.
4. Use feedrate:.....
5. Use cooling water volume: .....

## **17 Inspection - MEMS-Travee3 (Bonding) - Microscope Leitz**

Inspect cleanness dicing tracks and possible PI damage

## I | Mask

In this appendix, the files to order the mask are included. Here all details including material, minimum resolution, inverse or not and other details can all be found. These files are based on the 'ECTM Lithography mask ordering guide'. This guide is based on the information required by Compugraphics. It is adjusted to the information as required by MicroCreate.

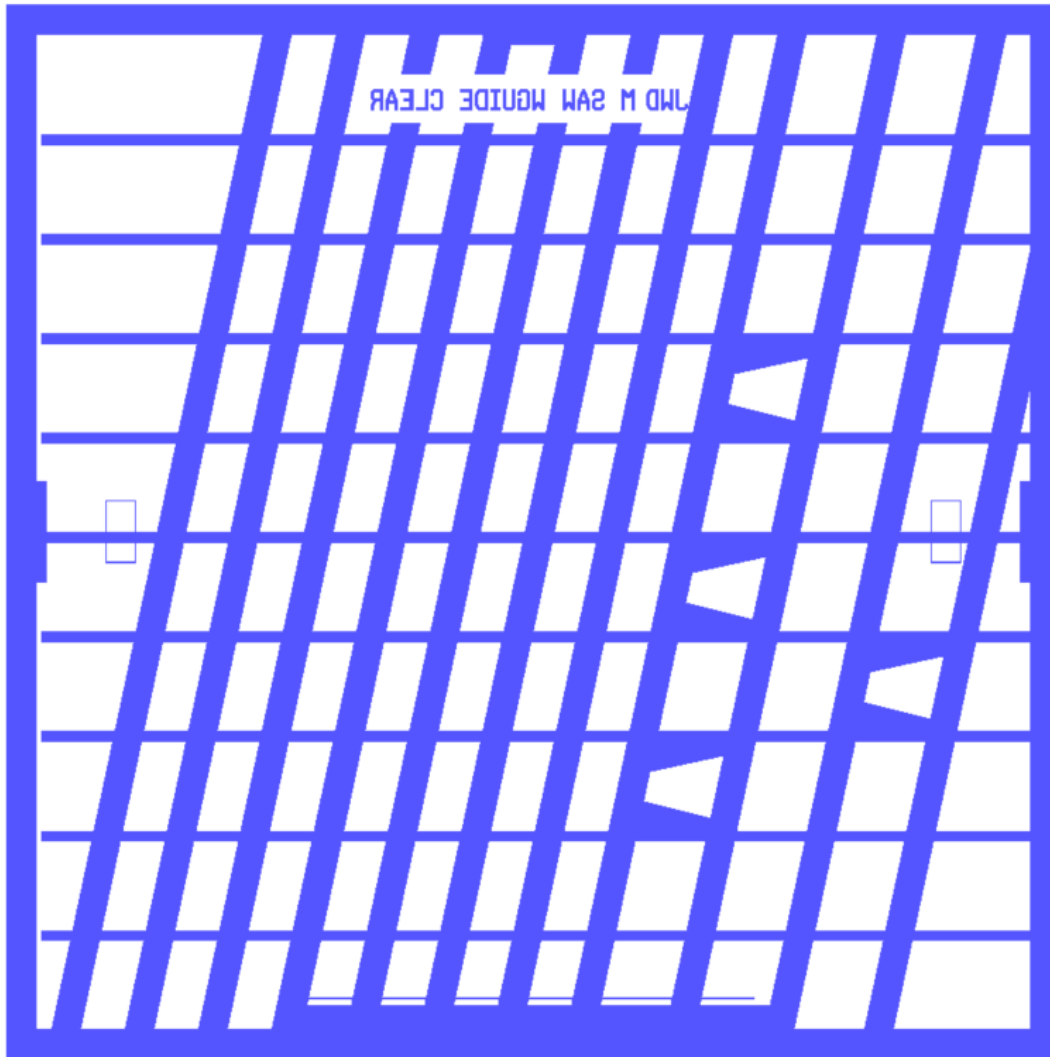


**Description:**

A mask to define aluminium electrodes. After sputtering of 100nm Al, positive resist will be applied and exposed so the excess Al can be removed with a wet etch process. Smallest dimension is 1µm.  
The electrodes are used to transfer an electric signal to an acoustic signal in a piezoelectric substrate (Quartz) and to receive the acoustic signal and transfer it back to the electric domain (SAW delay line).

**Technical data:**

1. Data filename: FWAMv351\_free\_masks\_JWDM\_SAW.gds
2. Data top cell: topcell
3. Data format: GDSII (.gds)
4. Device name: SAW Love mode
5. Mask title: JWD.M SAW IDT METAL
6. Layer name: Zero Layer (GDS\_80\_DT\_00)
7. Product code: ?? (CD: 1µm)
8. Digitalised data: DARK (Chrome)
9. Data parity: Wrong  
Title parity: Right
10. Project code:
11. Comments: Use GDS layer number 80
  - Labels near the devices on the chips are made such that they are readable on the wafer, so they are readable when the chrome is down. The title has been mirrored so it is readable when the chrome is up (in the mask box).



### Description:

Mask to clear the waveguide layer from the contact pads.

The waveguide layer is a photosensitive polymer (polyimide). It behaves as a negative resist, so it is only developed where exposed. By shielding the contact pads from exposure, the contact pads will be reachable. The waveguide layer is also removed from the dice lines to prevent damage to this layer in the dicing process.

### Technical data:

1. Data filename: FWAMv351\_free\_masks\_JWDM\_SAW.gds
2. Data top cell: topcell
3. Data format: GDSII (.gds)
4. Device name: SAW Love mode
5. Mask title: JWD.M SAW WGUIDE CLEAR
6. Layer name: 1inverse Layer (GDS\_82\_DT\_00)
7. Product code: ?? (CD: 10um)
8. Digitalised data: DARK (Chrome)
9. Data parity: Wrong  
Title parity: Right
10. Project code:
11. Comments: Use GDS layer number 82
  - The title has been mirrored so it is readable when the chrome is up (in the mask box).

## J | Flowchart

# Flow Chart SAW based sensor

Batch Information - Version 16-05-2023			
Name of owner:	Johan Meyer	Mask set:	JWD M SAW
Name of mentor:	Paddy French	Mask Box:	
Run number:		Die size:	7.4mmx10mm
Wafer amount:	5	Sart date:	
Subject to PCC:		PCC approved:	

Starting material	
Type	ST-cut Quartz DSP
Orientation	[0°;42,75°;0°]
Resistivity	
Thickness	500 ± 25 μm
Diameter	100mm (4 inch)



## GENERAL RULES

### CLEANROOM BEHAVIOUR

Always follow the "Security and Behaviour" rules when working in the EKL laboratories.

Always handle wafers with care during processing. Use cleanroom gloves and work as clean as possible!!

Use cleanroom gloves when working with vacuum equipment. Do not touch the inside or carriers with bare hands.

Always check equipment and process conditions before starting a process. Do **NOT** make unauthorized changes!

Directly notify the responsible staff member(s) when there are problems with equipment (like malfunction or contamination). Put the system down in the Phoenix reservation system, and turn the equipment status sign from **UP** or **Usable** to **DOWN**.

**DO NOT TRY TO REPAIR OR CLEAN EQUIPMENT YOURSELF**, and **NEVER** try to refresh a contaminated etch or cleaning bath! Only authorized staff members are allowed to do this.

### PCC RULES

All substrates, layers and chemicals which are not CMOS compatible are considered to be "NON-STANDARD" materials, and may be contaminating.

The use of "non-standard" materials for processing in the class 100 and SAL cleanroom must **ALWAYS BE EVALUATED AND APPROVED** by your mentor and in agreement with the PCC document.

Wafers that are contaminated may **NEVER** be processed in any of the equipment without permission of the Equipment owner. Special precautions may have to be taken, like the use of a special substrate holder or container.

Check the PCC "Rules & Instructions" - available on the "[EKL intranet webpage](#)" - for more details.

## CLASS 100 RULES

### CLEANING OF WAFERS

After several hours (4 hours max) of storage wafers must always be cleaned before performing a **COATING, FURNACE, EPITAXY** or **DEPOSITION** step.

Use the correct cleaning procedure:

- Tepla stripper ⇒ for removal of implanted or plasma etched photoresist
- Acetone ⇒ for removal of photoresist that is not implanted or plasma etched
- HNO<sub>3</sub> 99% (Si) ⇒ for IC compatible wafers which do not need a HNO<sub>3</sub> 69.5% step
- HNO<sub>3</sub> 99% (Al) ⇒ for wafers which are or have been in contact with one of the following metals: like Al, Al(1% Si), Ge, Ti, Zr
- HNO<sub>3</sub> 99% (Si) + HNO<sub>3</sub> 69.5% (Si) ⇒ for all other IC compatible wafers

**Note:**

- The above described cleaning procedures are only valid for IC compatible wafers with "standard" materials on them. **In all other situations follow the PCC rules (Previously to be discussed with the mentor).**
- Wafers do not have to be cleaned **after** a furnace, epitaxy or deposition step if the next process step will be performed immediately, unless the wafers are covered with particles.

### FURNACE RESTRICTIONS

Wafers that are covered with photoresist or a metal layer may **NEVER** be processed in any of the furnaces. This also applies for wafers from which a metal layer has been removed by etching. Only alloying in tube C4 is allowed for wafers with an aluminium layer.

### MEASUREMENTS

Always perform all the measurement and inspection steps, and **write down the results in your journal and in the result tables that can be found at some of the equipment!!** The results are used to check the condition of the processes and/or equipment.

It is possible to use the following Class 100 equipment to measure directly onto your (IC compatible) process wafers:

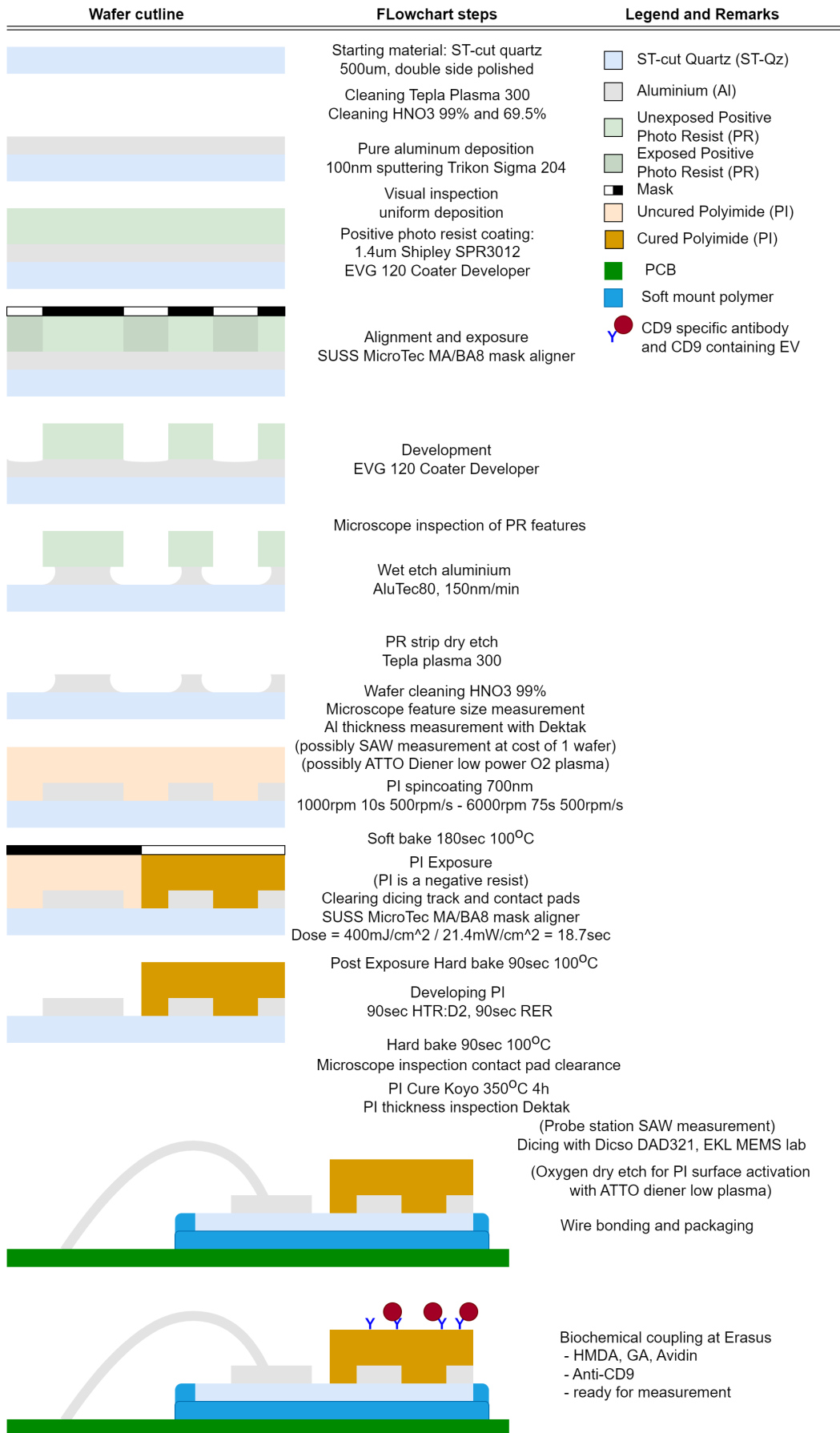
- The Leitz MPV-SP, the WOOLLAM and the SAGAX. These systems are used for thickness measurements of transparent layers. The measurements are non-destructive and without contact to the wafer surface.
- The Dektak 8 surface profilometer. This system is used for step height measurements. In this case a needle will physically scan over the wafer surface (contact measurement), which can be destructive for structures.
- The XL50 SEM. It can be used for inspection of your wafers and for width, depth or thickness measurements.

**Note:** After certain measurements cleaning of your wafers may be required for further processing.

An extra wafer must be processed when other measurement methods will be used (like sheet resistance and junction depth measurements). These wafers cannot be used for further processing.

## Process Steps

1	Wafer Cleaning - CR100 tunnel 5 - Tepla plasma 300	6
2	Wafer Cleaning - CR100 tunnel 5 Wet Cleaning - HNO3 99% (Si)	6
3	Metalization Aluminium pure - CR100 tunnel 3 - Trikon Sigma 204	6
4	Inspection metal deposition- CR100 tunnel 3 - x	6
5	Photo resist coating - CR100 tunnel 1B - EVG 120 Coater Developer	7
6	Alignment and Exposure - CR100 tunnel 1B (Litho) - SUSS MicroTec MA/BA8 mask aligner	7
7	Development - CR100 tunnel 1B - EVG 120 Coater Developer	7
8	Inspection - CR100 tunnel 1B (Litho) - Microscope Axiotron	8
9	Wet etch aluminium - CR100 tunnel 4 - Al ets. 35°C	8
10	Photoresist removal - CR100 tunnel 4 - Acetone 40°C	8
11	Wafer Cleaning - CR100 tunnel 5 Wet Cleaning - HNO3 99% (green metals)	9
12	Dimension measurement - CR100 tunnel 1 (PolymerLab) - Microscope Olympus	9
13	Inspection Aluminium thickness - CR100 tunnel 2 (Metrology) - Dektak 8	9
14	Surface activation optional - CR100 T1A - ATTO Diener low plasma	9
15	PI deposition 510nm - CR100 T1 (Polymerlab) - Spinner polymers (Poly 2 fume-hood)	10
16	Soft bake - CR100 T1 (Polymerlab)- Fumehood poly 2	10
17	Inspection and clean - CR100 T1 (Polymer lab) - Fumehood poly 2	10
18	Alignment and Exposure - CR100 T1B (Litho) - SUSS MicroTec MA/BA8 mask aligner	11
19	Post exposure hard bake - CR100 T1 (Polymerlab) - Fumehood poly 2	11
20	Development PI - CR100 T1 (PolymerLab) - Fumehood poly 3	11
21	Inspection uncured PI - CR100 T1 (Polymerlab) - Olympus or Axiotron microscope	11
22	Cure PI - CR100 T1 (Polymerlab) - Koyo oven	11
23	Inspection PI clearance - CR100 T1 - Olympus or Axiotron microscope	12
24	Inspection PI thickness -CR100 T2 (Metrology)- Dektak 8	12
25	SAW VNA probe station measurement - Earl McCune Lab 21st floor EWI	12
26	Dicing - MEMS-Travee3 (Bonding) - Disco DAD321	12
27	Wire bonding and packaging - by Brian	12
28	Biochemical coupling, surface activation - Erasmus	12



## Contamination:

Probe station  
Dicing  
Wire bonding

# Flowchart

Remember, always backside wafer to H bar of box carrier. Especially important with transparent wafers.

## 1 Wafer Cleaning - CR100 tunnel 5 - Tepla plasma 300

1. use program from PIT: **Program 1:** 1000 watts of power, automatic endpoint detection + 2 minutes overetching.

## 2 Wafer Cleaning - CR100 tunnel 5 Wet Cleaning - HNO3 99% (Si)

1. Clean - Submerge wafer for 10 minutes in HNO3 99% (Si) at ambient temperature, red dot. Done to dissolve organic materials.
2. Rinse - Submerge wafer in quick dump rinser DI-water for 15 minutes or until 5M  $\Omega$  resistivity is reached.
3. Dry - Dry wafer with "Avenger Ultra-Pure 6" rinser/dryer. Standard program, white carrier, red dot.

## 3 Metalization Aluminium pure - CR100 tunnel 3 - Trikon Sigma 204

Qz wafers demonstrate floating in the Trikon Sigma. As the laser system is turned off, this is not detected and leads to extremely high chances of Qz wafer breakage. Using Si carrier wafers (requiring an experienced user to adjust pumpdown speed to avoid Qz wafer floating off carrier wafer), solves this breakage, but the maximum processing temperature is reduced to 50°C. This deteriorates Al grain size, maybe causing trouble in the Al wet etch later. The 350°C recipe includes a 45s hot sputter etch (HSE) step at 400°C, whereas the 50°C recipe does not use this.

1. Check that cassette is free ----, chamber at atmospheric pressure ----. Open door so arm can come out of chamber.
2. Check if machine has been used in past 2 hours \_Yes\_/\_No\_. If No, place dummy wafer in first slot.
3. Non standard wafer is used so manually select wafer to be used. As Sigma can't see the wafer with its laser. An EXPERIENCED USER (Johannes) will have to do this beforehand.
4. Take cassette of shelf and load wafers in slots with backsides to the H-tube.
5. Use wafer aligner to have all primary flats face downwards.
6. Put cassette back onto the shelf and make sure its placement is correct.
7. On the screen, load the cassette and close the door.
8. If a dummy wafer is included, select for the first wafer: \_Alp\_TargetClean\_350°C.
9. Deposit 100 nm pure Al at 350°C.
10. Once all wafers are done, eject and wait for 'okay to open door' message.
11. Move wafers back to their wafer box. Do a visual inspection.
12. Put cassette back onto shelf. Once placed correctly, load cassette on the screen.
13. Close door manually.
14. Abort all used blocks.
15. Once message "Abort" is shown, click on the control block and set all used blocks to idle.
16. Log off.

## 4 Inspection metal deposition- CR100 tunnel 3 - x

1. Check visually for uniform shiny metal layer.

## 5 Photo resist coating - CR100 tunnel 1B - EVG 120 Coater Developer

1. Check if relative humidity is [48+-2%??]
2. Put wafers in the carrier labeled 'coater'. Work from back to forward to avoid scratches (polished side wafer faces frontside and add other wafers working backwards).
3. Align wafers primary flats facing upwards with the aligner.
4. Place the carrier in the machine.
5. On the computer, load the coater and select the slot which is loaded with the wafers.
6. Select the 1\_Co - 3012 - 1.4 $\mu$ m recipe.
7. Press OK to start the coating process.
8. Once done, take the carrier and put the wafers back in own carrier.

### Fabrication break possibility

## 6 Alignment and Exposure - CR100 tunnel 1B (Litho) - SUSS MicroTec MA/BA8 mask aligner

1. Load (**JWD M IDT METAL**) mask in tool.
2. Use frontside exposure with hard contact.
3. Expose 1.4 $\mu$ m SPR3012. Calculate in lab with 'contact aligner exposure energy data log'.

Exposure time calculation:

Energy required = _____mJ/cm <sup>2</sup>	Wavelength lamp = _____	Intensity in logbook = _____mW/cm <sup>2</sup>
Dose(time) = (energy required)/(intensity lamp)		
Dose =		
23/05/2023: E = 140mJ/cm <sup>2</sup> *0.8 (Outdated Contact Aligner manual and 80% for Al background compensation)		Dose = 112/26.1 = 4.29 sec
08/08/2023: E = 160mJ/cm <sup>2</sup> *0.8 (Up to date stepper manual increased with 1.3 correction factor)		Dose = 128/21.0 = 6.09 sec

## 7 Development - CR100 tunnel 1B - EVG 120 Coater Developer

Follow photo resist coating step 5, but now use the developer cassette.

1. Check relative humidity is 48 $\pm$ 2%.
2. Put wafers in carrier labeled 'developer'. Use load technique from step 5 technique to avoid scratches.
3. Align all primary flats facing upwards with wafer aligner.
4. Place the carrier in the machine.
5. On computer, load [what program??] and select the slot loaded with wafers.
6. Select the ["1-Dev - SP"] program and press OK to start. [No EBR, No HMDS (due to tool malfunction)]
7. Once finished, take the carrier and move wafers back to own carrier.

post exposure bake	115°C	90 sec
developing with single puddle process	Shibley MF322	
hard bake	100°C	90 sec

## 8 Inspection - CR100 tunnel 1B (Litho) - Microscope Axiotron

1. Check critical structures feature width to validate exposure dose.
2. Check for resist residues.
3. If non acceptable defaults (critical defaults) are found, etch resist (Tepla+HNO3 or Acetone) and redo steps. (Change flow where necessary.)

Sample location Die code # N-W-L	Critical linewidth	Residues? and remarks
1		
2		
3		
4		
5		
6		
7		
8		

## 9 Wet etch aluminium - CR100 tunnel 4 - Al ets. 35°C

1. Moisten - Rinse for 1 minute in "H2O/Triton X-100 tbv Al Ets". Use yellow dot carrier. Step to reduce surface tension improving etchant coverage.
2. Etch - "Aluminium 35°C etch" bath. (1L of Al ets fluid contains 770ml H3PO4 85%, 19ml HNO3 65%, 140ml CH3OOH 100% and 71ml DI water)
3. Load wafers in yellow dot carrier
4. Dip wafers for [calculated time]. Then [measured thickness] Al will be removed.
5. Continue etching until Al visually totally etched. Few seconds = few nano meter over etch is acceptable.
6. Rinse - in DI-water until 5MΩ resistivity is reached.
7. Drying - Dry wafer with "Avenger Ultra-Pure 6" rinser/dryer. Standard program, white carrier, black dot.

Reported etch rate:	24/05/'23	08/08/'23
Required etch time =	100nm/(170nm/60s) = 35,3s	110/(170/60) = 38s
Etch time = (Metal thickness)/(reported etch rate)	Actual: 62s	Actual: 59s

## 10 Photoresist removal - CR100 tunnel 4 - Acetone 40°C

1. Place wafers carrier.
2. Place carrier acetone bath for 1 minute
3. Visually check if PR is gone.
4. Rinse.

**Fabrication break possibility**

## 11 Wafer Cleaning - CR100 tunnel 5 Wet Cleaning - HNO3 99% (green metals)

1. Clean - Submerge wafer for 10 minutes in HNO3 99% (metal) at ambient temperature, red and yellow dot. Done to dissolve organic materials.
2. Rinse - Submerge wafer in DI-water for 15 minutes
3. Dry - Dry wafer with "Avenger Ultra-Pure 6" rinser/dryer. Standard program, white carrier, black dot.

## 12 Dimension measurement - CR100 tunnel 1 (PolymerLab) - Microscope Olympus

1. Place wafer in the Olympus microscope
2. Sample different IDT to validate fabrication procedure.
3. Examine feature width to validate (exposure dose and) over etch.

#	Site name	Al th (nm)	w (nm)	corners, overetch, uniformity and other comments
Fab 1	Si	110	OK	One device version has mask drawing error
Fab 1	Qz 2	110	OK	WL4 (1um) versions defective
Fab 2	Si	80	OK	Even several 1um sizes well etched
Fab 2	Qz 2	80	OK	Pinholes random in Al
...				

## 13 Inspection Aluminium thickness - CR100 tunnel 2 (Metrology) - Dektak 8

1. Place wafer in tool
2. Check metal thickness, keep into account measured structure might be lost.
3. Setup: red tip needle (12.5um), software set to 5um. Hills and valleys, 400um path length, 3ng tip force, 8s duration, 6500nm thickness range.

Wafer #	Deposition time	Measured thickness
1		See previous table
2		
3		
4		
5		

## 14 Surface activation optional - CR100 T1A - ATTO Diener low plasma

Step can be omitted without significant influence on PI adhesion to substrate.

1. Turn tool on with switch at back
2. Place wafers on horizontal (for e.g. chips with dummy wafer) or vertical boat.
3. Oversight of current settings in 'main picture'
4. Choose program, typical: 1min pumpdown, 1min O2 plasma duration, power 40% (100%=200W).
5. Start program.



## 15 PI deposition 510nm - CR100 T1 (Polymerlab) - Spinner polymers (Poly 2 fumehood)

Perform 'PI deposition' and 'Soft bake' together per wafer.

1. Get PI stock from fridge and let acclimate to room temp at appropriate cupboard for 30 minutes to avoid condensation in stock.
2. Dispense approx 10mL of PI LT9305 precursor and crosslinker solution in a clean beaker.
3. Let this volume acclimate further for 3.5 hours (total 4 hours of acclimatising).
4. Prepare hotplate with dummy wafer.
5. Cover spinner inlay in aluminium.
6. Use black spinner chuck (aluminium chuck has vacuum problems).
7. Prepare Acetone or isopropanol, wipes, pipette and swap.
8. Start up the spinner and log in.
9. Load recipe: "hande.test".
10. Rename recipe and alter according to the table below.
11. Place wafer on the chuck and center the wafer, test vacuum.
12. Do a test spin without PI to verify the setup is correct.
13. Dispense PI solution on the wafer and start spinning process.
14. Clean the wafer backside using a swap and acetone.
15. After last wafer clean up area. Clean all surfaces with Acetone wipe.

Wafer #	goal PI th	recipe spreading - ramp - spinning - ramp	measured PI th [nm]
Fab1 Si	700nm	1000rpm 10s - 500rpm/s - 6000rpm 75s - 500rpm/s	947nm
Fab1 Qz2	700nm	1000rpm 10s - 500rpm/s - 6000rpm 75s - 500rpm/s	898nm
Fab2 Si	700nm	1000rpm 10s - 500rpm/s - 8000rpm 75s - 500rpm/s	697nm
Fab2 Qz2	700nm	1000rpm 10s - 500rpm/s - 8000rpm 75s - 500rpm/s	768nm
5			
6			

## 16 Soft bake - CR100 T1 (Polymerlab)- Fumehood poly 2

1. Place the tabletop clean hotplate (Hotplate 1 C1100) in fumehood poly 2 (polymers).
2. Place dummy wafer on hotplate (to ensure hotplate stays clean).
3. Soft bake 180 sec at 100°C

## 17 Inspection and clean - CR100 T1 (Polymer lab) - Fumehood poly 2

1. Clean backside of wafer with acetone
2. Visually inspect for any backside PI residues, none are allowed.

## 18 Alignment and Exposure - CR100 T1B (Litho) - SUSS MicroTec MA/BA8 mask aligner

PS-PI is a negative resist. Use any mask that has some large open spaces.

1. Load (**JWD M WGUIDE CLEAR**) mask in tool. Use frontside exposure with soft contact.
2. Perform calculation in lab with 'contact aligner exposure energy data log'.

Exposure time calculation:

Energy required = 400 mJ/cm<sup>2</sup> Wavelength lamp = \_\_\_\_\_ Intensity in logbook = \_\_\_\_\_mW/cm<sup>2</sup>

Dose(time) = (energy required)/(intensity lamp)

Dose(time) = 400 mJ/cm<sup>2</sup> /

## 19 Post exposure hard bake - CR100 T1 (Polymerlab) - Fume-hood poly 2

1. Use the still ready tabletop clean hotplate (Hotplate 1 C1100) in fumehood poly 2 (polymers).
2. PEB for 90 sec at 100°C

## 20 Development PI - CR100 T1 (PolymerLab) - Fumehood poly 3

1. Prepare a HTRD2 beaker and a RER beaker in fumehood poly 3.
2. Submerge wafer in HTRD2 beaker for 90 sec. (Developer)
3. Submerge wafer in RER for 90 sec. (Develop stop)
4. Rinse with DI water
5. If all wafers are processed, dispose of HTRD2 and RER in organics container (cabinet fumehood poly 3).
6. Hard bake at 100°C for 90 sec using the tabletop hotplate in fumehood poly 2.
7. If all wafers are processed, place hotplate back on shelf.

## 21 Inspection uncured PI - CR100 T1 (Polymerlab) - Olympus or Axiotron microscope

1. After curing, PI can not be removed, so inspect dice track clearance now.
2. If any intolerable errors are spotted, Tepla high power oxygen plasma etch and HNO<sub>3</sub> 99% cleaning to totally remove PI. Improve process where necessary and retry.

## 22 Cure PI - CR100 T1 (Polymerlab) - Koyo oven

1. Turn on oven and wait for it to start up and self calibrate (oxygen calibration takes at least 30min).
2. Select Program #6
3. Check if the time and temperatures are correct: press 'func' and 'program' simultaneously.
4. Place wafers in oven.
5. Something about Al carrier plate for clean wafers.??
6. if O<sub>2</sub> below 20%, use 'run/hold' button to start.
7. Start "Program #6": Cure 350 °C for 4 hours.
8. Once the oven has cooled down, remove wafers and turn off the tool with the main switch.

**Fabrication break possibility**

## 23 Inspection PI clearance - CR100 T1 - Olympus or Axiotron microscope

1. Check if PI is neatly removed from dicing track.
2. Check if PI is removed from bond pads

## 24 Inspection PI thickness -CR100 T2 (Metrology)- Dektak 8

1. Make sure to use a long measurement track as the relatively soft PI might deform a little by the needle, resulting in a distorted measurement.
2. place flat of wafer against single pin on chuck (flat away from user).

Sample location W# Die code #	PI thickness	Sample location W# Die code #	PI thickness	Sample location W# Die code #	PI thickness
Etc.					

Wafer #	recipe: RPM ramp time	average PI thickness	Remarks
1			
2			
...			

## 25 SAW VNA probe station measurement - Earl McCune Lab 21st floor EWI

Description in separate measurement plan.

## 26 Dicing - MEMS-Travee3 (Bonding) - Disco DAD321

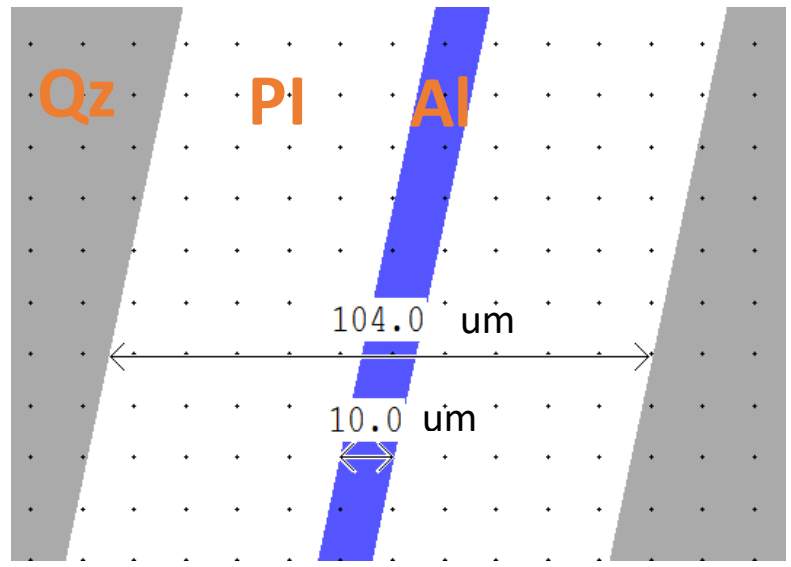
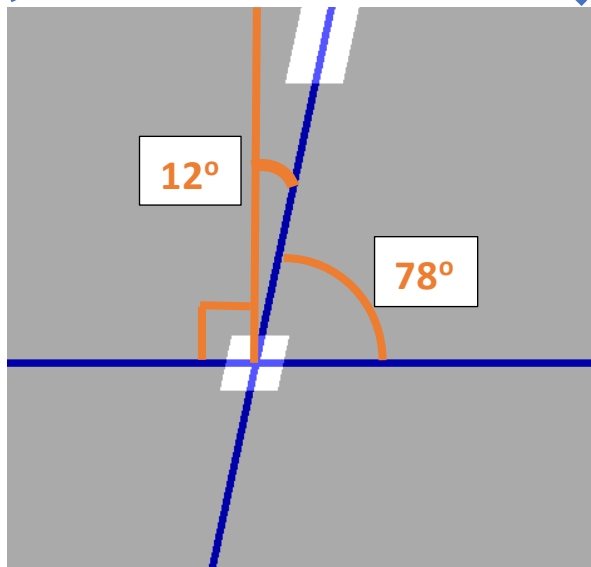
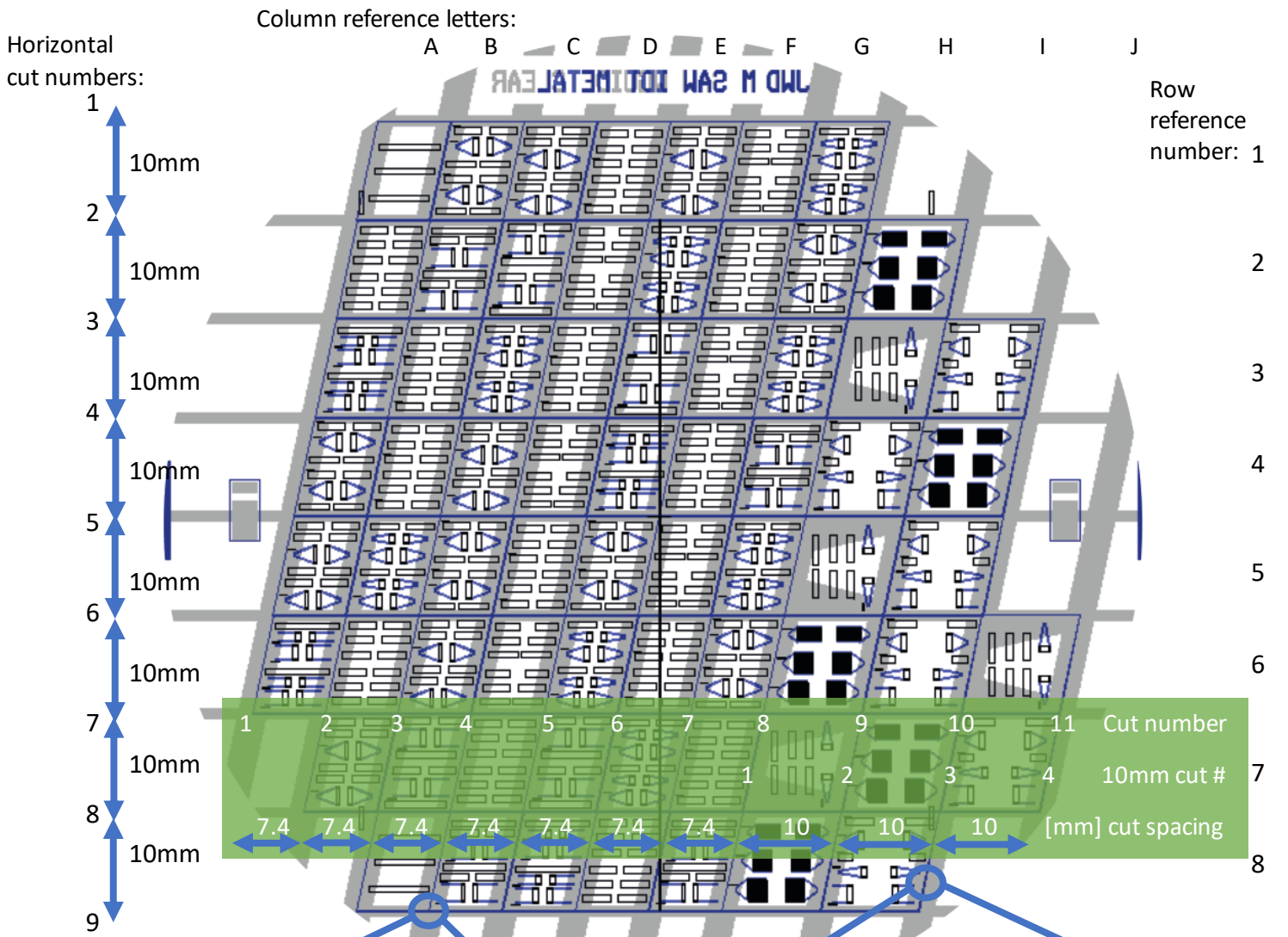
1. Dice wafer in 7.4x10mm chips and 10x10mm chips.
2. Vertical spacing (horizontal cut) is always 10mm.
3. Horizontal spacing (vertical cut), first 8 cuts are spaced 7.4mm and last 4 cuts spaced 10mm.
4. Vertical cuts are 12 degree away from normal or rotated 78 degree from horizontal cut direction.
5. Alignment tracks are 10um wide Aluminium and 104um wide PI to allow the angled alignment.
6. Feed speed low as possible to minimise damage to Qz and PI (test used 10m/s).
7. Rinse chips with DI-water and dry with nitrogen gun.

## 27 Wire bonding and packaging - by Brian

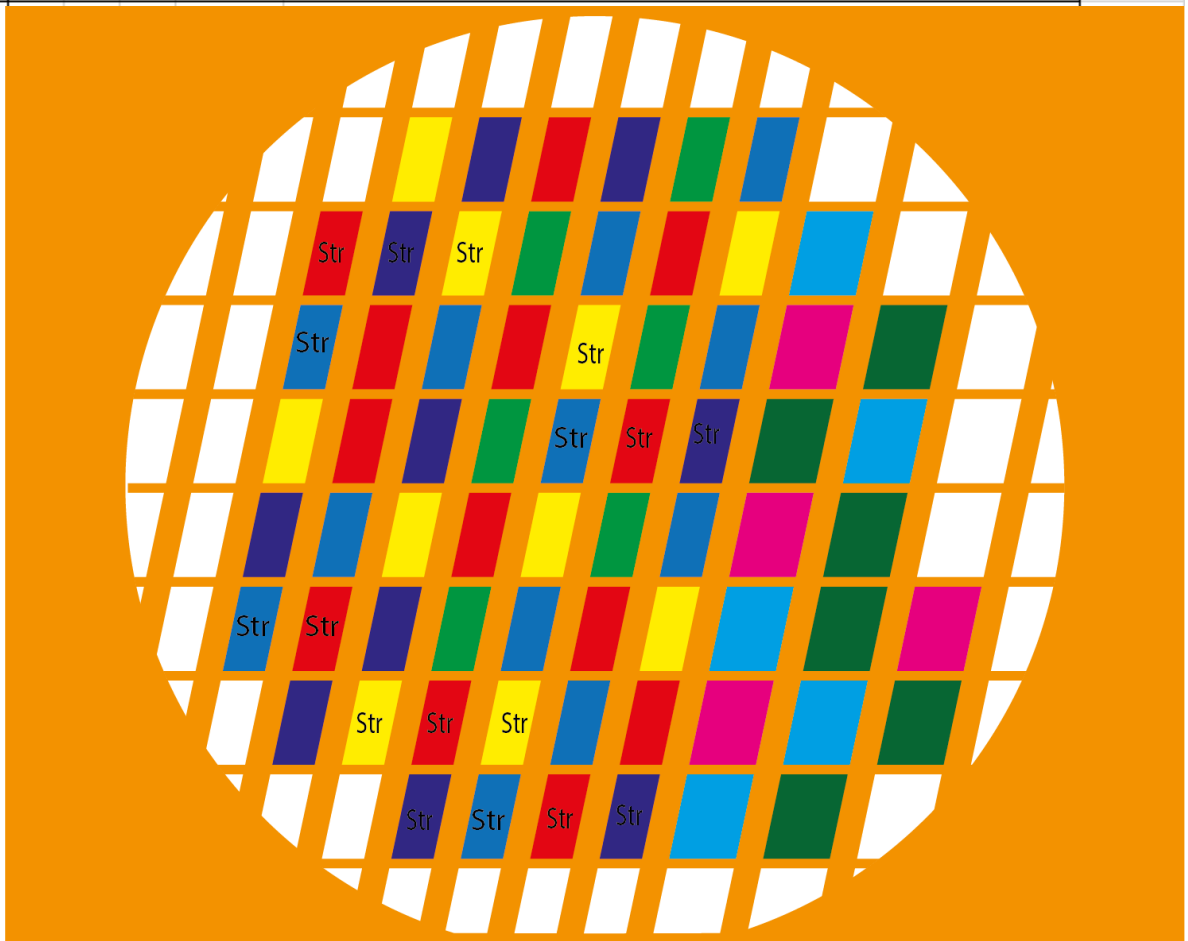
Separate file for wire bonding instructions.

## 28 Biochemical coupling, surface activation - Erasmus

Separate file for surface activation process.



	N	W	L	dies	remark	Die size
Sweep N					8 check IL due to reflection, find best power delivery, check BW relation	7,4x10mm
	N1.1	35	40	100		
	N1.2	75	40	100	expected optimal device	
	N1.3	100	40	100		
Sweep W					8 find best power delivery	7,4mm
	W1.1	75	20	100		
	W1.2	75	80	100		
	W1.3	75	160	100		
Sweep L					6 find loss per length	7,4mm
	L1.1	75	40	200	switched to have optimal device in middle	
	L1.2=N1.2	75	40	100	expected optimal device	
	WL4	75	40	100	4um wl (1um electr) For CD test and for backup SAW presence test.	
Exceptions die					6	7,4mm
	E2.1	150	40	100	N	
	E2.2	75	200	100	W	
	E1.3	75	20	50	SAW precense struct:	
90 degree rotated version					4	10mm
	90d1=E1.3	75	20	50	SAW pres	
	90d2=N1.2	75	40	100	Expected optimal	
	N1.2str	75	40	100	Expected optimal, straight	
90d3=E1.1	75	100	300	1ul		
Sweep W2					6	7,4mm
	W2.1	50	20	100		
	W2.2	50	40	100	also N sweep	
	W2.3	50	200	100		
Wavelength					5	10x10mm
	WL32	75	40	50	30um	
	WL48	40	40	40	50um	
	WL96	20	20	20	100um just calculate, check if feasible.	
					include 50 Ohm track for calibration purposes	
L2 long device chip					6	10mm
	L1.3	75	40	400		
	E1.2	75	190	500	5ul area	
	E2.3	75	40	720	L	
	E1.2str	75	190	500	5ul area, str	
	E1.1	75	100	300	1ul area	



# K | Bonding Diagram





The bonding diagram as it is delivered to the technician to wirebond the SAW device to the PCB.

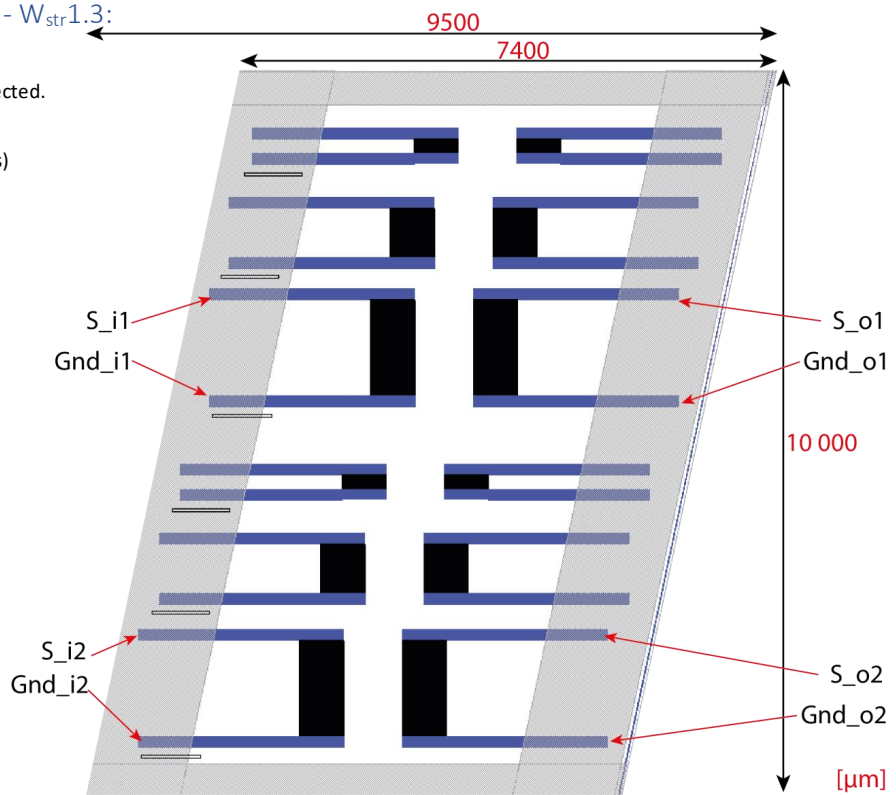
Your Name and group :	Johan Meyer, Bioelectronics
Chip Process Technology:	- (500µm Quartz DSP substrate, 100nm thick Aluminium pads, 2µm Critical Dimension)
Chip pad material:	Aluminium 100nm thickness
Pad size chip:	150 µm × 400 µm
Pad pitch chip:	200 µm
Package type (DIL/PCB/other):	PCB
PCB pad NiAu finish (yes/no):	NiAu finish
PCB pad size:	500 µm × 2200 µm
Type of glue (electrical conductive/non-conductive):	non-conductive
Number of samples to be wire bonded:	6 chips, per version stated

Layout of the chip version 1 -  $W_{str}1.3$ :  
1 sample to wirebond

Only the indicated pads are to be connected.

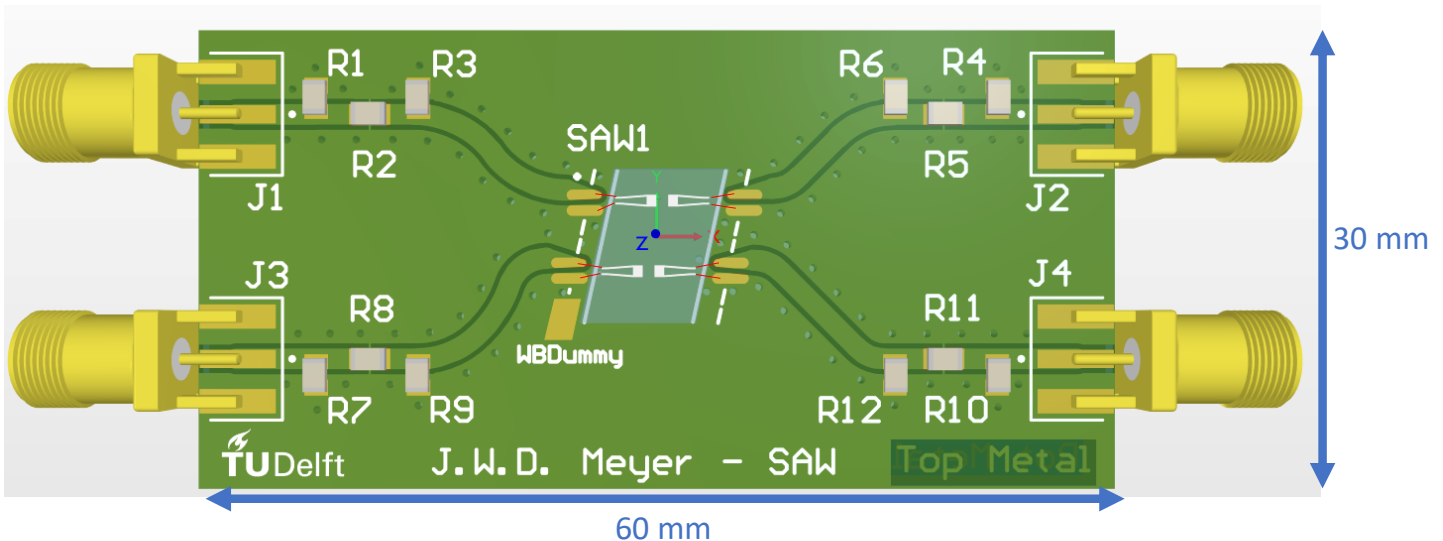
Legend is from bottom to top.  
(Qz-Al-PI, then PI is removed from pads)

-  Quartz 500µm (Qz)
-  Aluminium (Al) 100nm on Qz
-  Transducer (Al structure)
-  Polyimide (PI) 700nm on Qz



PCB:

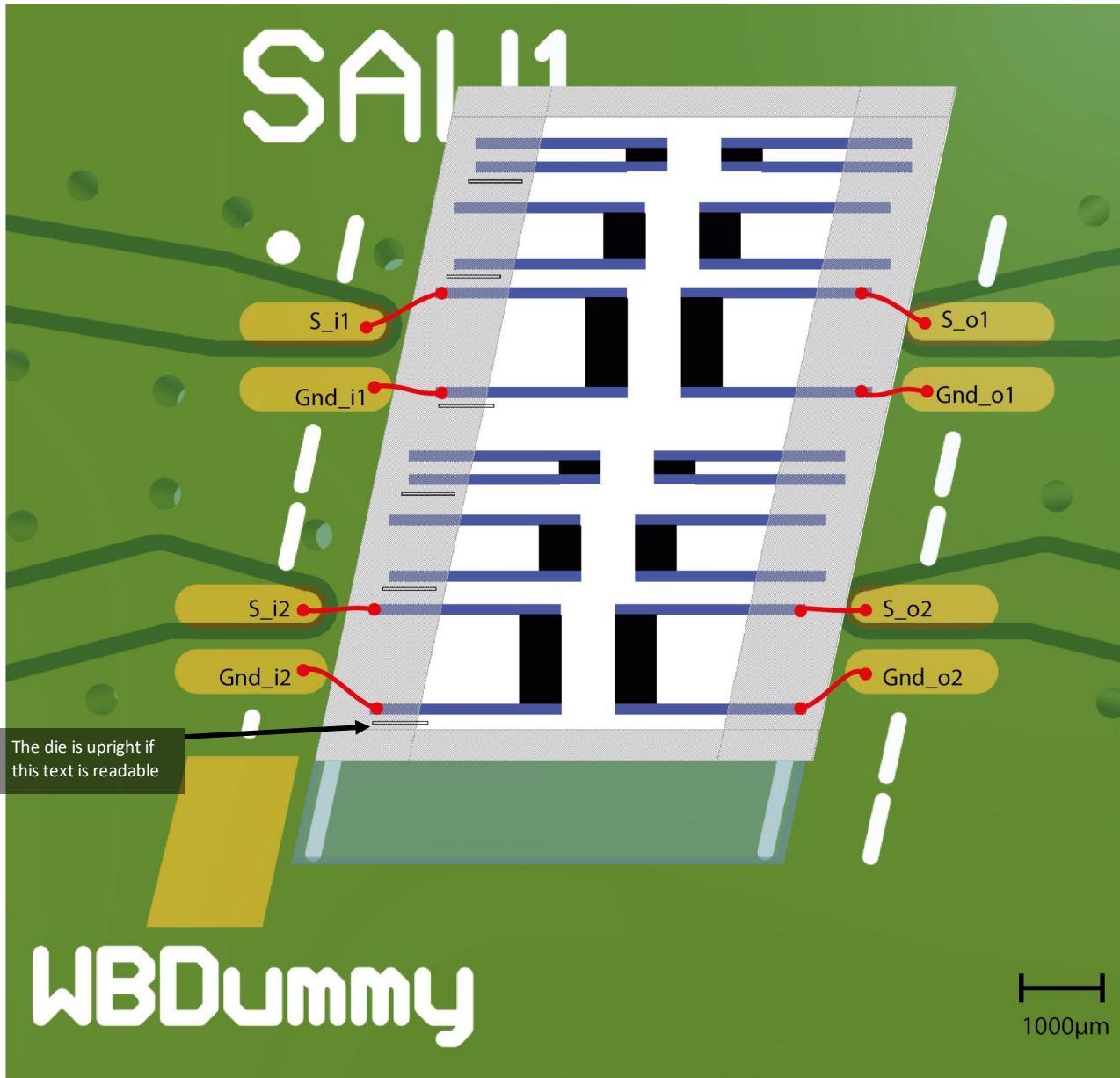
Only the devices to be connected are shown in this render. The chip is to be shifted so as to align the desired devices to the pads.



Wire bonding diagram scale 1:1 version 1– Wstr1.3

WBDummy pad on PCB added to setup/test/practice bonding setup. In most configurations usable, though when bottom SAW device is to be used, the dummy pad cannot be bonded to the chip.

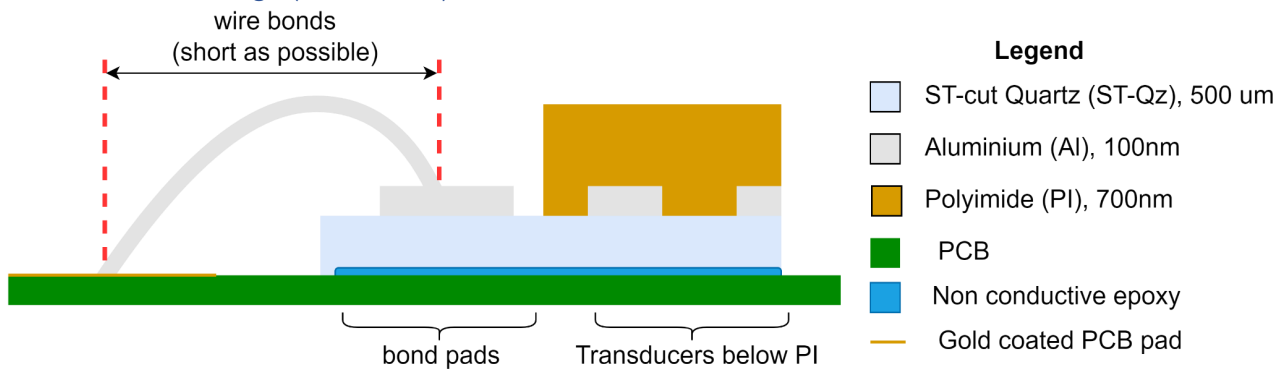
Also, 10mm wide chips are available. Then the chip partly overlaps the PCB pads (up to the white dashed lines).



Wire bonding diagram zoomed:

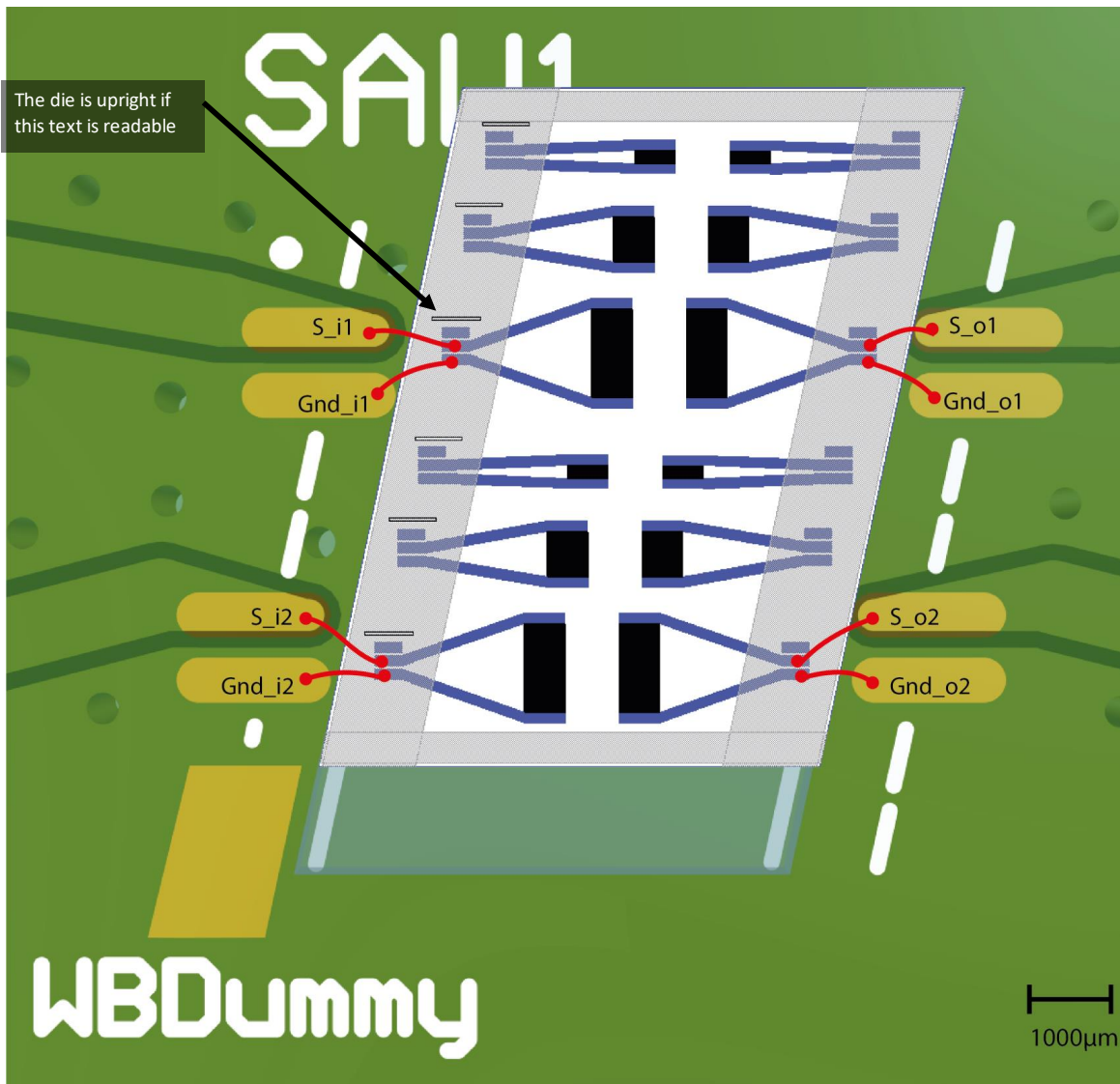
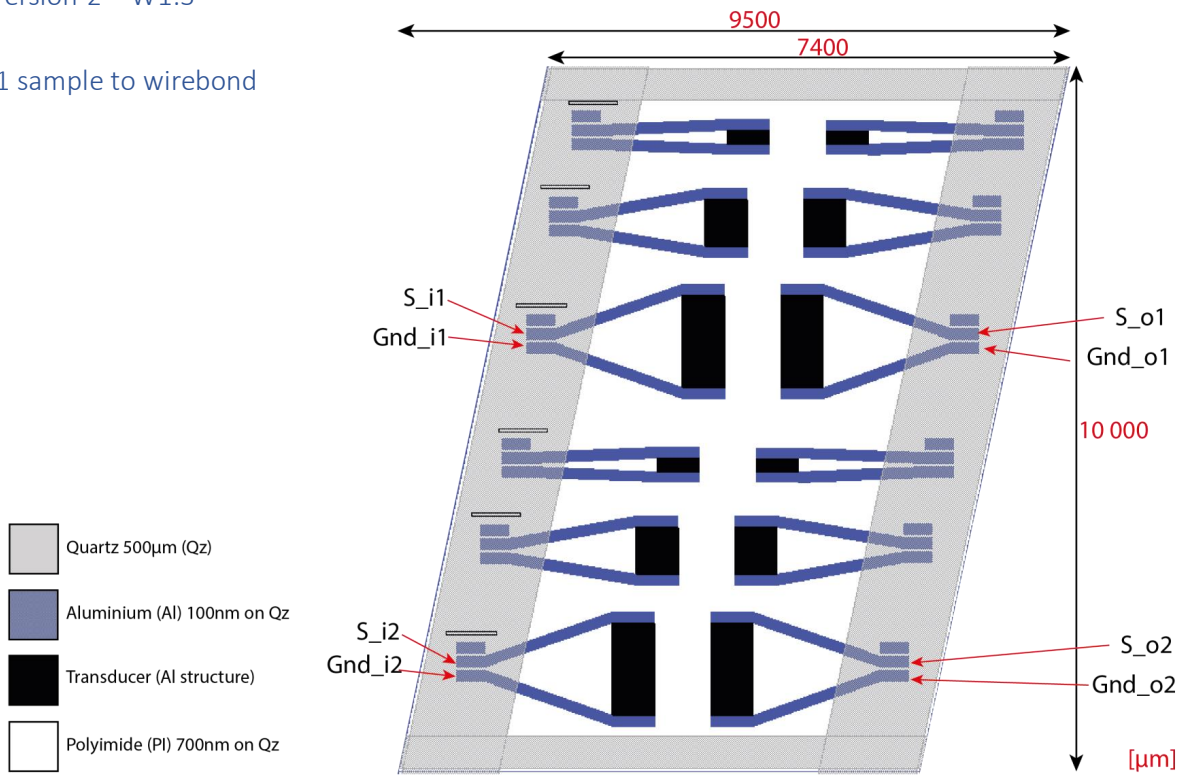
Omitted.

Wire bond cut through (not to scale)

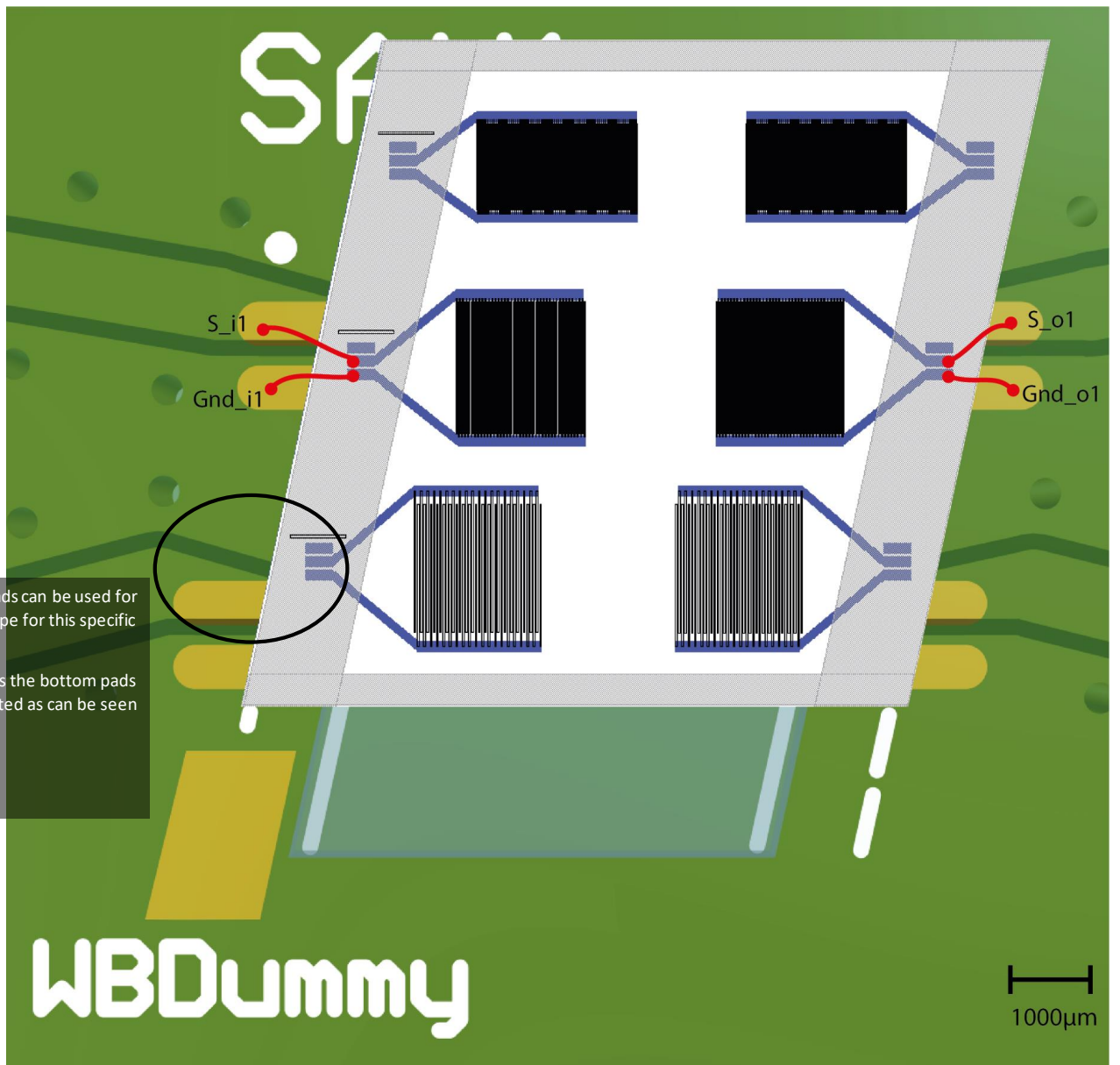
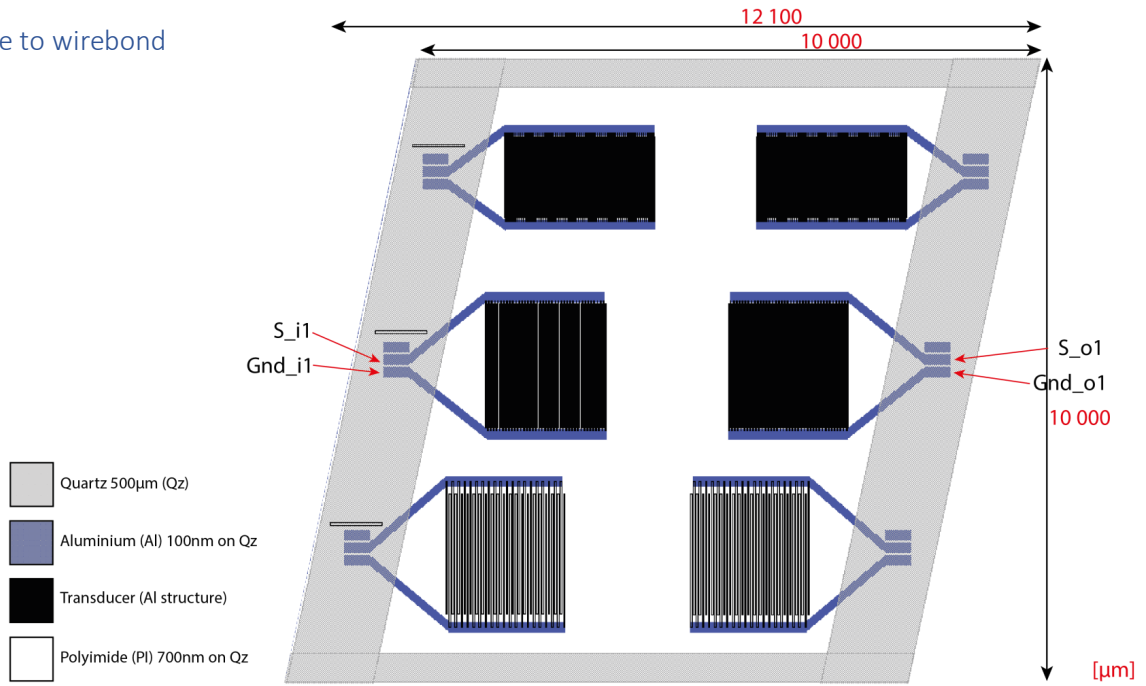




1 sample to wirebond



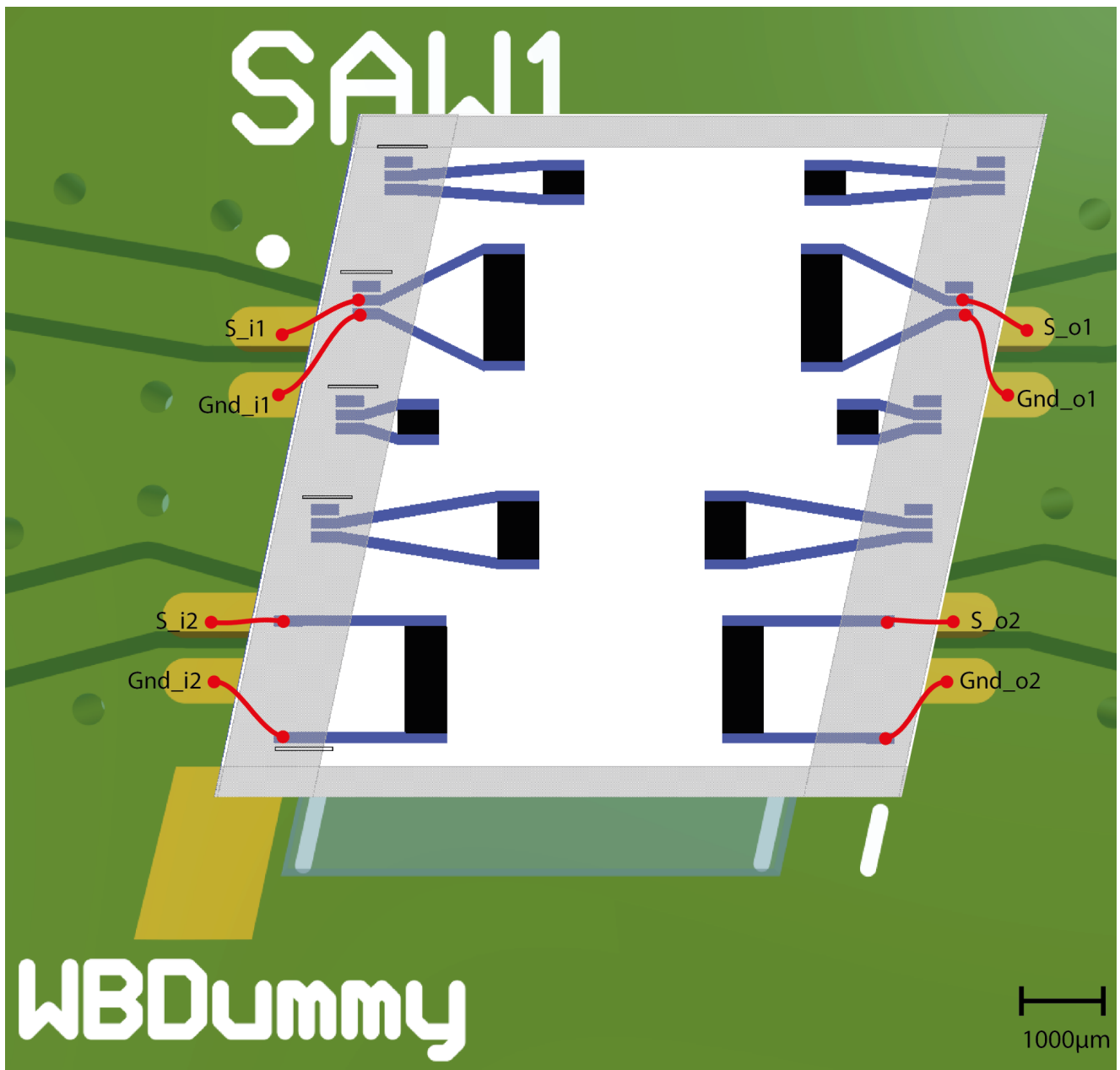
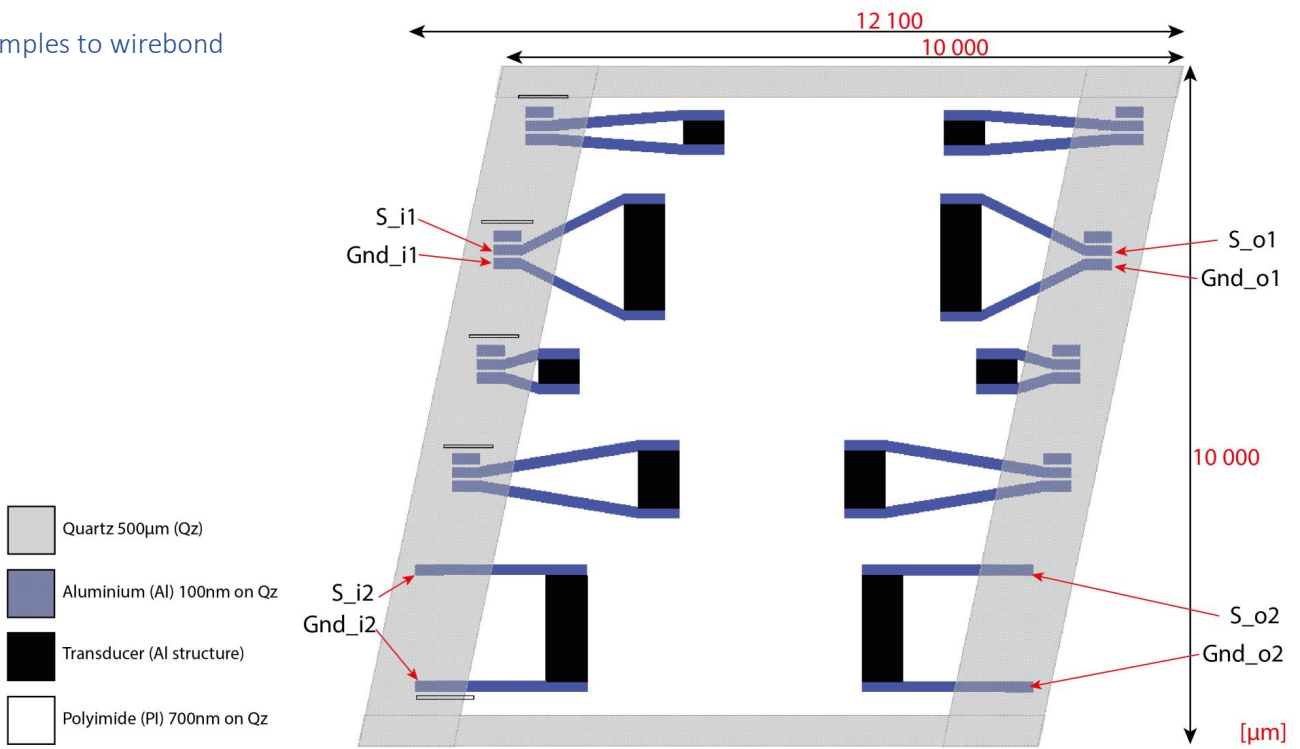
1 sample to wirebond



Bottom device and pads can be used for testing wirebond recipe for this specific SAW device version.

In the other versions the bottom pads are also to be connected as can be seen on the drawings.

3 samples to wirebond



# L | Functionalisation Test

In this appendix the functionalisation protocol is tested. Included are a short background information, the used materials and chemicals, the setup, the results, a short discussion and a conclusion.

## Functionalisation test on polyimide (PI)

### Short description

The goal of this test is to validate the adhesion of a specific protein binding layer to polyimide (PI), specifically, Fujifilm LTC9305 polyimide. Eventually, proteins like CD9 have to be immobilised on the PI using anti-CD9 biotinylated-antibody. The antibodies are immobilised using the strong biotin-streptavidin (sAvidin) binding.

For this purpose, samples on a 10mm x 10mm silicon (Si) substrate with 700nm thick spin coated PI and Quartz (Qz) samples with 900nm PI, will first be treated to add amine groups to the PI surface using HMDA in methanol. Secondly, Glutaraldehyde (GA) in water is applied so the surface can now easily bind to an amine group on a protein like sAvidin. Then sAvidin can be immobilised on the substrate.

Now the biotinylated-antibody can be immobilised. For the purpose of this test, any biotinylated-antibody that can proof the efficacy of an sAvidin-biotin binding of an antibody to a surface of PI is sufficient. If necessary, some colour-stained antigen can be used to bind to an antibody to show the proper immobilisation of an avidin-biotin-antibody complex on PI.

To exclude a false positive result, a control group of samples without biotinylated antigen is included. These samples should not show any colouration or fluorescence.

The sensor is made of Qz, hence the Qz samples. Ideally the sensor has wells to contain the fluid, though these PMMA wells attached with epoxy might disturb the SAW functioning (to be investigated), but might also interfere with the functionalisation process. Therefore, Qz samples with and without wells are tested. For redundancy, the Si samples with and without well are added.

### Recipe

The recipe has 3 main steps, each with several sub-steps.

- Amine functionalisation (Thursday)
  - o Submerge substrate in 10ml 10% HMDA in methanol (1gr in 10ml) for 30 minutes
  - o Wash with methanol to remove excess HMDA
  - o Dry for 1 day
- Glutaraldehyde activation (Friday)
  - o Immerse substrate in 10mL GA 25% for 1 hour
  - o Wash with distilled water to remove excess GA
  - o Dry for 1 day
- Covalent immobilization (Sunday)
  - o Prepare 50uL, 0.1mg/mL sAvidin in PBS solution. Drip on to substrate
  - o Dry for 12h at 25°C, finish drying in dry stove if still wet.

Now the surface can bind any antibody.

- Antibody immobilisation and detection (Monday)
  - o Phosphate buffered saline (PBS) rinse
  - o Prepare 50uL, 10ng/uL = 0.01mg/mL Biotinylated antibody (anything would be fine) (normal is 1ng/uL), Drip on samples, soak for 1hour, make sure it does not dry out.  
SKIP FOR NEGATIVE TEST
  - o PBS rinse
  - o 0.5% BSA in PBS block, submerge samples in 2mL

- Prepare 150uL Fluorescent goat anti mouse 1/50 for Si samples and 500uL HRP-goat-anti-mouse 1/500 for Qz samples.
- Drip on samples, soak for 1 hour, make sure does not dry out.
- DI water rinse
- For HRP samples, apply xxuL Chromogen for xx minutes
- DI water rinse

### Disposal

- HMDA collected in blue container with yellow lid. This container is destroyed.
- GA in black container
- sAvidin, Biotinylated-mouse-anti-CD9, goat-anti-mouse-HRP/fluorescence washed through drain
- Tools/glassware/materials, washed with plenty of water and soap.

### List of chemicals

- Methanol
- Hexamethyldiame (HMDA)  
(Sigma-Aldrich H11696, HMDS)  
[Hexamethylenediamine 98 124-09-4 \(sigmaaldrich.com\)](https://www.sigmaaldrich.com/NL/en/product/sial/g6257)
- GA  
(Sigma-Aldrich G6257, GA, grade II, 25% in H2O)  
<https://www.sigmaaldrich.com/NL/en/product/sial/g6257>
- DI water
- Stepto-Avidin  
(Sigma-Aldrich 189725 Avidin, Egg White)  
<https://www.sigmaaldrich.com/NL/en/product/mm/189725>
- PBS
- Biotinylated antigen  
Biotinylated Mouse-anti-CD9  
UPDATE supplier
- BSA
- Detection:  
Goat-Anti-Mouse-Peroxidase
  - Dako Polyclonal Goat-Anti-Mouse Immunoglobins HRP P0447, 1.0g/L
  - OR Dako Substrate buffer and Dako chromogen K3468
  - OR Dako DAB+ substrate buffer and Dako DAB+ Chromogen (X50)
- Goat-Anti-Mouse-Fluorescence
  - Dako Polyclonal Goat-Anti-Mouse Immunoglobins FITC F0479, 1.0g/L

### List of materials

- Gloves
- Safety glasses
- Lab coat
- Fumehood

- Petridish 20ml, 2 per step variant (1 for biochemical material, 1 for wash)
- ~~— 7x Beaker (HMDA, Methanol, GA, DI water, Avidin, antibody, detection agent)~~
- Organic waste container
- ~~— Magnetic stirring~~
- ~~— Hotplate~~
- Scales
- Tweezers
- ~~— Nitrogen gun~~
- ~~— Vacuum~~
- Micro pipetting 1uL, 5uL and 10uL (Avidin, biotinylated antibody and antigen)
- Pipettes 10mL, (HMDA and GA solutions)
- Optical tool / microscope to check result
- 3 PI coated Si samples (10mm x 10mm)
- 1 PI coated Si with well sample
- 2 Qz samples
- 3 Qz+well samples
- Cloth / wipes
- Dry stove

### Substrates

The test is to be performed on several substrates simultaneously. A blank PI substrate as baseline , with actual submersion steps. An actual SAW device, not PCB mounted, with only droplets applied to the surface. A PCB mounted SAW device with fixated well, only droplets can be applied to the surface.

This is done to troubleshoot if the process is not working for one of the fluid application methods. Every substrate increases the risk as it is further from the original process.

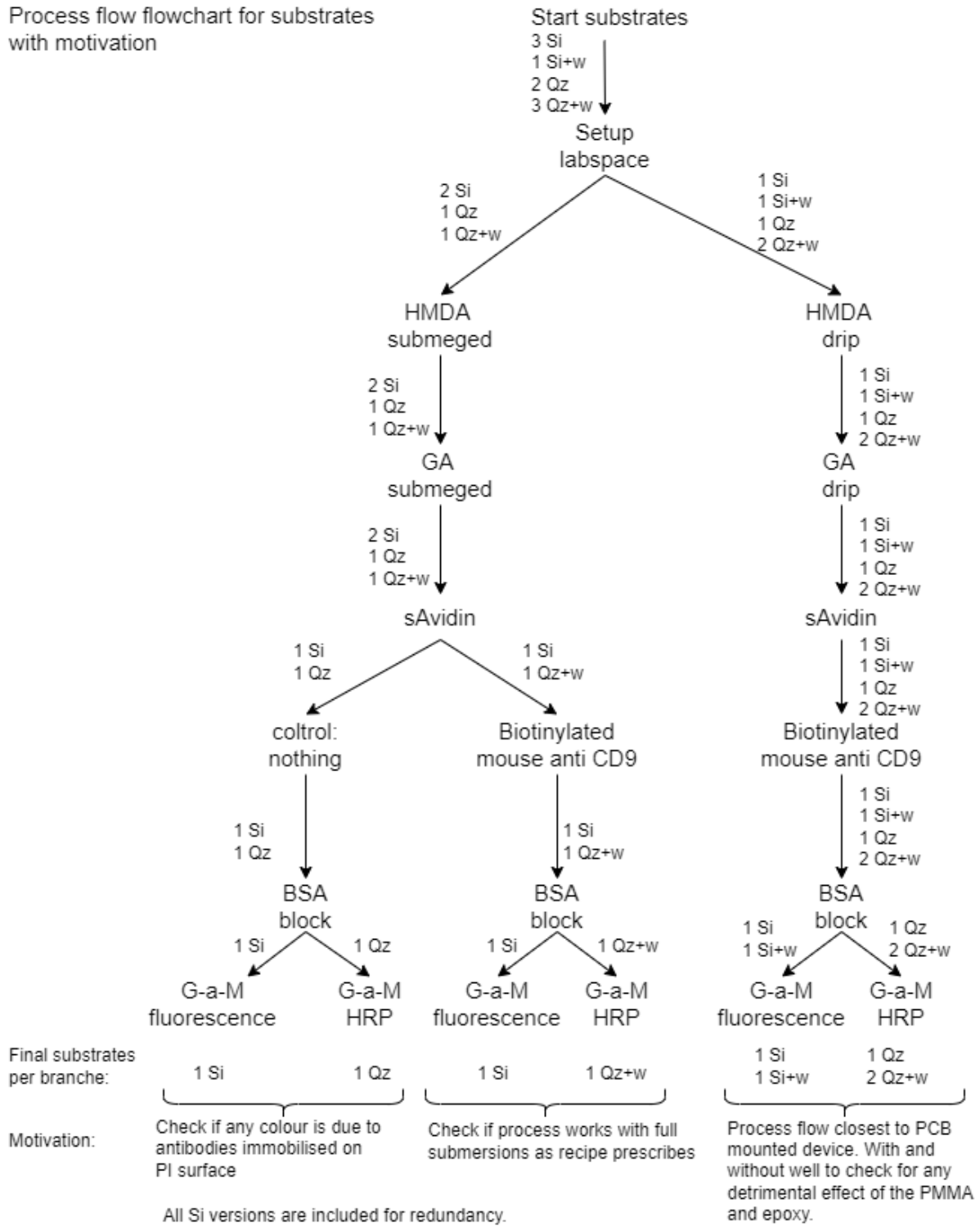
Claims to support with proof:

- HMDA + GA can be used to immobilise sAvidin on PI.
  - Proof: use recipe on any PI coated sample and add any colour stain or fluorescence to detect immobilised Avidin.
- PMMA well not problematic
  - Do test on any sample with well attached
- Dripping and submersion both work
  - Do tests with submersed samples and only drip on samples

Substrates:

- ~~• Standard (ELISA?) substrate for baseline check~~
- Si with PI substrate, submerged
- Si with PI, dripping
- SAW device bare, submerged
- SAW device with well, submerged
- SAW device OR Si and PI, with well, dripping (depend on microscope and Qz visibility)
- SAW device with well on PCB, dripping

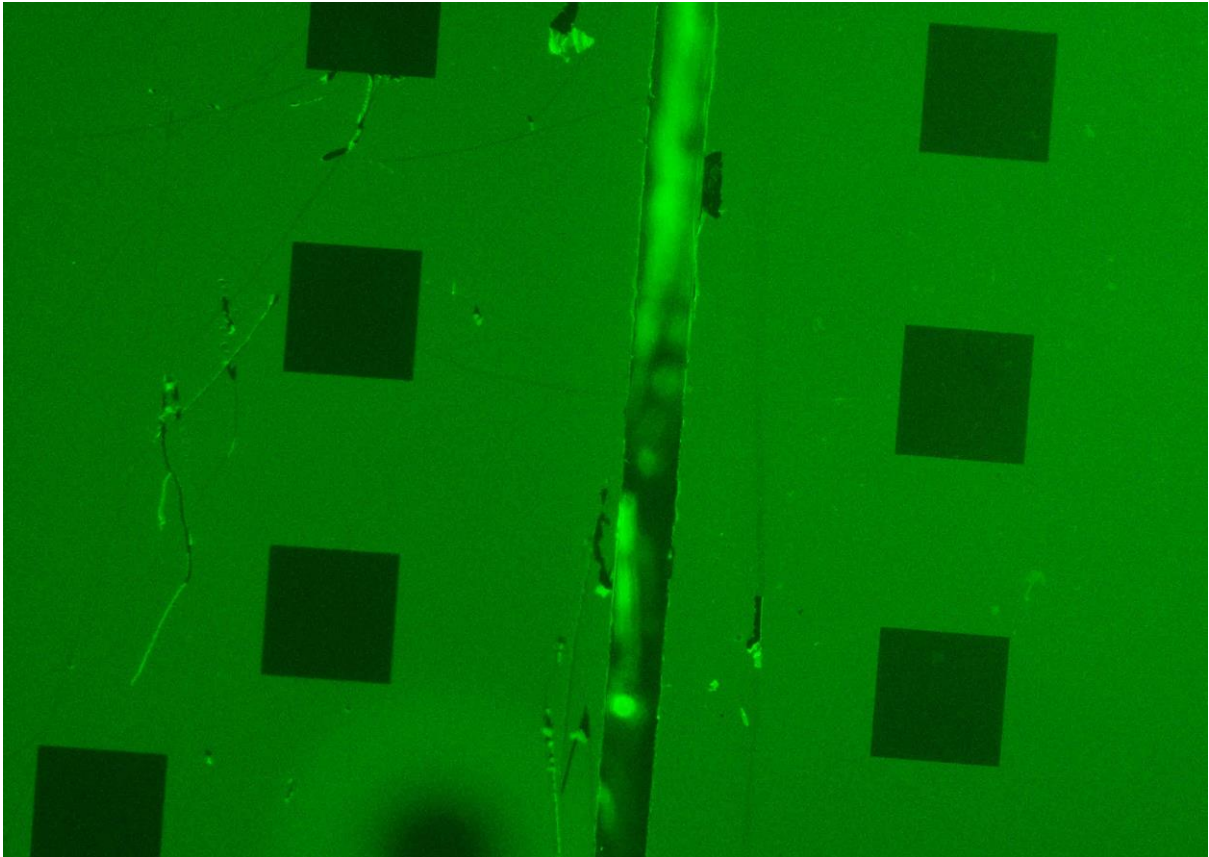
Process flow flowchart for substrates with motivation





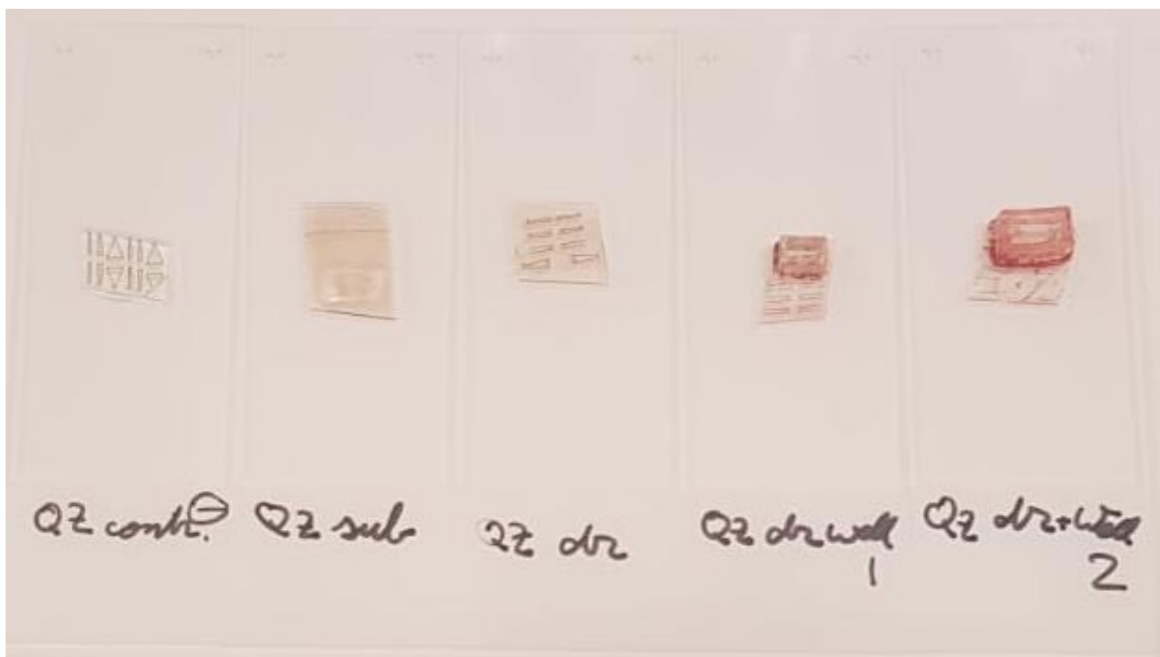
## Results

FITC



Submerged control right and anti-CD9 left. Control is negative, anti-CD9 is positive judged by slightly brighter colour. But poorly quantifiable.

HRP



The control is not showing any brown colour. All other samples do show colour caused by the HRP reacting with HR. The samples including a PMMA well show red colours after the 25% GA step.

	Fluorescence		HRP	
	submerged	drip	submerged	drip
MaCD9	1	-	1	1
control	0	-	0	-

Table shows the control never gave a positive and the MaCD9 all had colour changes indicating the presence of anti-CD9 on the sample surface.

## Conclusion

HMDS and GA treatment on PI can be used to successfully immobilise anti-CD9 on PI. The process also works well with epoxy wells. Problems arise when using PMMA wells.

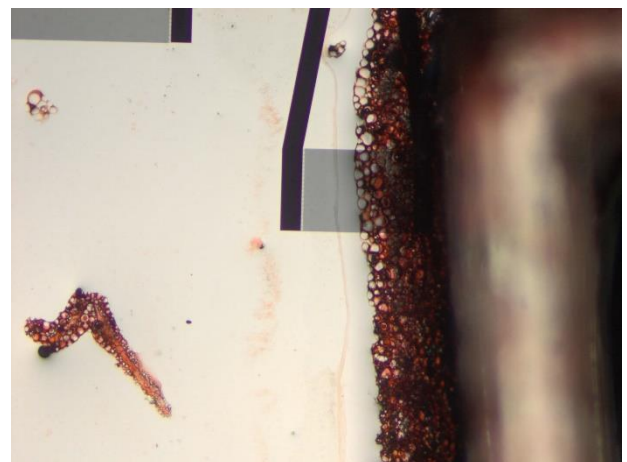
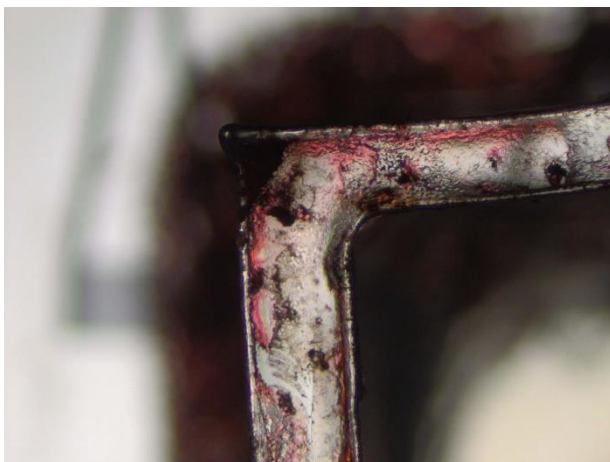
## Discussion

Fluorescence is often used to create a contrast on one sample. Using it on an entire sample makes it extremely difficult to quantify if a colour change has occurred due to background fluorescence. When samples are evaluated individually under the microscope, the quantification becomes even more troublesome as the microscope needs to be re-focussed after a sample change. A solution is to have a negative control and anti-CD9 sample on 1 microscopy plate for relative comparison. The resulting samples stay hard to interpret.

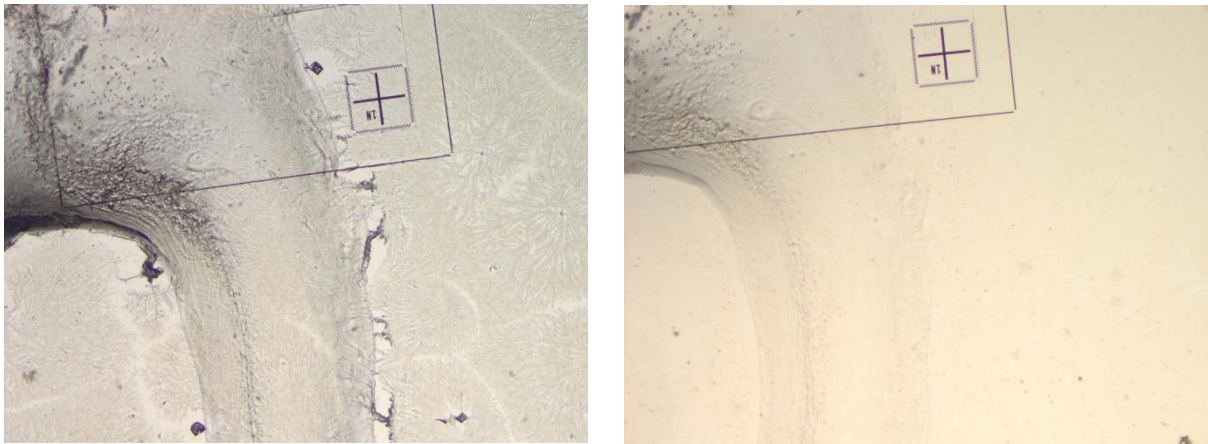
The process is time consuming. Some dry in steps might be shortened.

When optimising the process, it is worthwhile to investigate if sAvidin is strictly required. Maybe just dry in might be sufficient. This would be a big reduction in protocol execution time and material costs.

25% GA in water degrades the well material causing red colour changes and contamination on the sample surface. Though this does not influence the anti-CD9 immobilisation process, the particles might degrade the SAW.



When the samples dry out, salt crystals form on the surface. This is expected to be caused by salts in the PBS rinse that were not removed in a final DI water rinse. To avoid these salts to affect the surface mass, the SAW based CD9 measurements should be conducted using liquid samples.



Finally, there seems to be little influence by the method of application of all materials. Both submersion and dripping on the substrates lead to good anti-CD9 immobilisation.

# M | Functionalisation Protocol

Here the final functionalisation protocol is added. It was based on the work of Maaten Zeijlmans, then altered to accommodate a PI surface the protocol advised by Ayse Ogan, who was contacted through Alper Sissman. Then from 'avidin dry-in' onwards, it was updated by Joke Veldhoven and Natasja Dits who are in the group of Erasmus MC, in the Urology Lab from Guido Jenster, Martin van Royen and Chris Bangma.

## Functionalisation of on PCB samples for sensitivity measurement

The functionalisation protocol has been successfully verified and now the actual sensor can be characterised. For this purpose, the optimal device version and a backup version are used. Both versions are loaded with several concentrations of CD9 after functionalisation.

The loading with several concentrations can be done in serially or parallel as illustrated below. Here the serial method requires 1 device for characterisation, applying increasing concentrations of CD9-solutions over time. It is beneficial only one device is required but this comes at the cost of a less well-defined sensitivity.

In the parallel method, different devices are loaded with different concentration CD-9 solutions. This gives a better-defined figure for the concentration and is better reproducible, but comes at the cost of needing many devices and being subject to inter device variation.

For now, it is assumed to be best to start with the first method to demonstrate a proof of principle and get a first estimation of the sensitivity. The second method can be applied if the proof of principle has been successfully demonstrated.

If no response is found, it should be tested if any CD9 was attached at all.

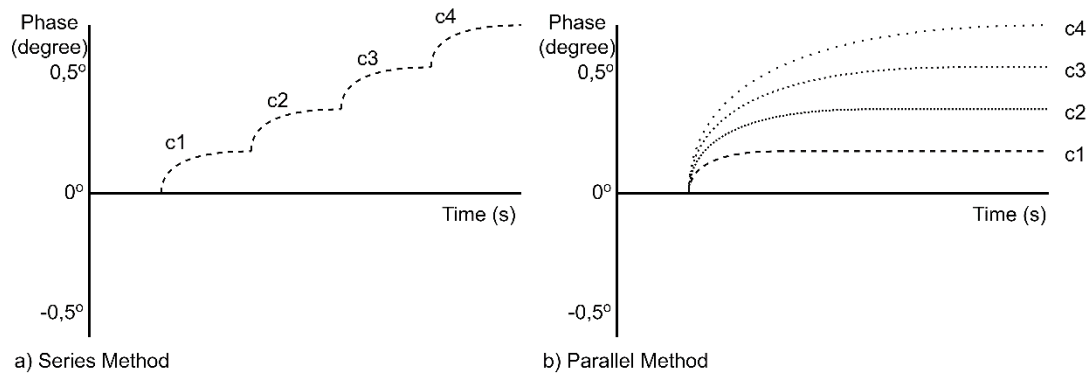
### Functionalisation Protocol

The protocol has 3 main steps, each with several sub-steps.

	Day and time planning
<ul style="list-style-type: none"> <li>- Amine functionalisation               <ul style="list-style-type: none"> <li>o Prepare 10ml 10% HMDA in methanol (1gr in 10ml)</li> <li>o Drip 80uL on to be sensitised area, soak for 30 minutes</li> <li>o 3x Wash with methanol to remove excess HMDA</li> <li>o Dry for 1 day</li> </ul> </li> </ul>	Tuesday 10.00-11.00
<ul style="list-style-type: none"> <li>- Glutaraldehyde activation               <ul style="list-style-type: none"> <li>o Drip 80uL GA 25% on to be sensitised area, soak for 1 hour</li> <li>o 3x Wash with distilled water to remove excess GA</li> <li>o Dry for 1 day</li> </ul> </li> </ul>	Wednesday 10.00-11.30
<ul style="list-style-type: none"> <li>- Covalent immobilization               <ul style="list-style-type: none"> <li>o Prepare 0.1mg/mL sAvidin in PBS solution. Drip 50uL per device</li> <li>o Dry for 12h at 25°C, finish drying in dry stove if still wet.</li> </ul> </li> </ul>	Thursday 10.00-11.00
<p>Now the surface can bind any biotinylated substance.</p> <ul style="list-style-type: none"> <li>- Antibody immobilisation and detection               <ul style="list-style-type: none"> <li>o 3x Phosphate buffered saline (PBS) rinse</li> <li>o Prepare 10ng/uL = 0.01mg/mL Biotinylated antibody anti-CD9 (normal is 1ng/uL)</li> <li>o Drip 50uL per sample on samples, soak for 1hour, make sure it does not dry out.</li> </ul> </li> </ul>	Friday 08.30-10.15
<ul style="list-style-type: none"> <li>o 3x PBS rinse</li> <li>o 0.5% BSA in PBS block, submerge samples in 80uL for 20 minutes</li> <li>o Wash with DI water, baseline VNA phase measurement (c0)</li> </ul>	10.15-11.45
<ul style="list-style-type: none"> <li>o Prepare CD9 solutions, concentration1 (c1) c2 c3 c4, 100uL per concentration</li> </ul>	Lab technician
<ul style="list-style-type: none"> <li>o Drip 15uL on sample, soak for 25 minutes, make sure does not dry out (shield sample from airflow).</li> <li>o VNA S12 phase measurement every 25 seconds, using NanoVNASaver 0.5.5</li> <li>o For serial measurement, 3x DI wash, pipette away fluid, next concentration</li> </ul>	12.45-20.00

## Mass loading protocol

- a) Increasing density solutions
- b) Single density solution per PCB

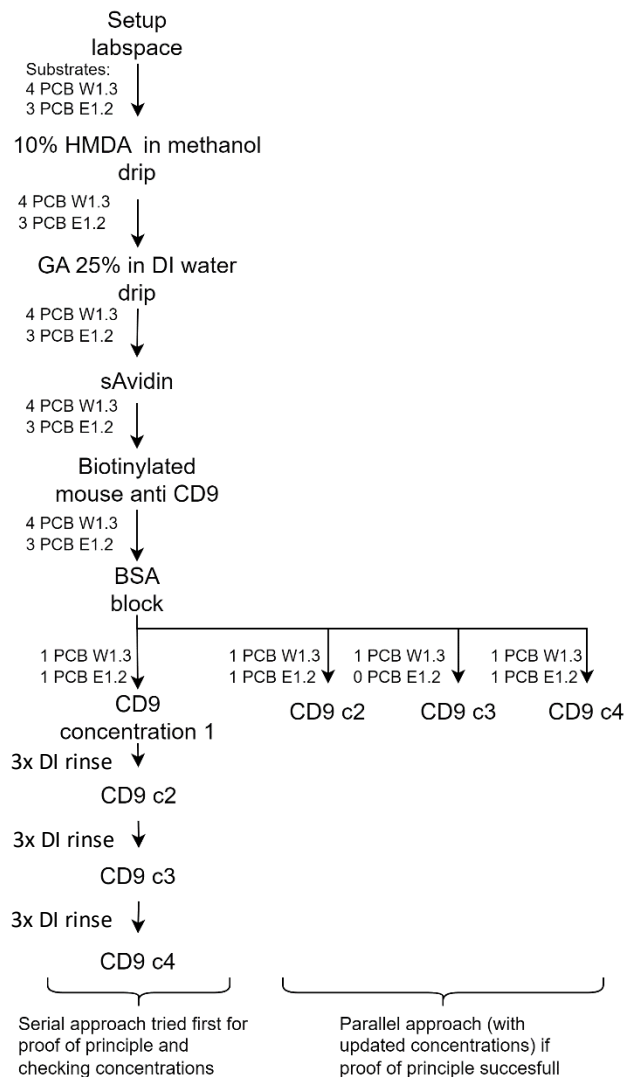


## Substrates

4 PCBs with optimal device, 3 PCBs with backup devices.

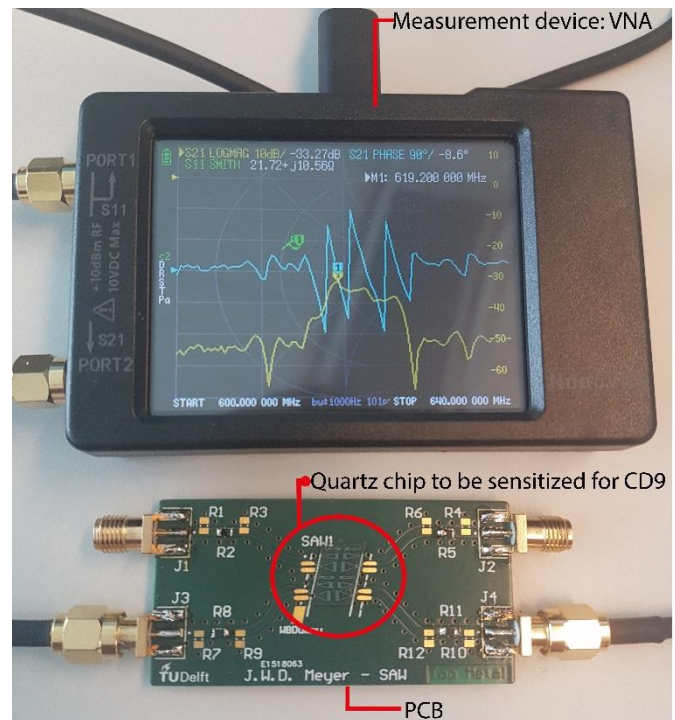
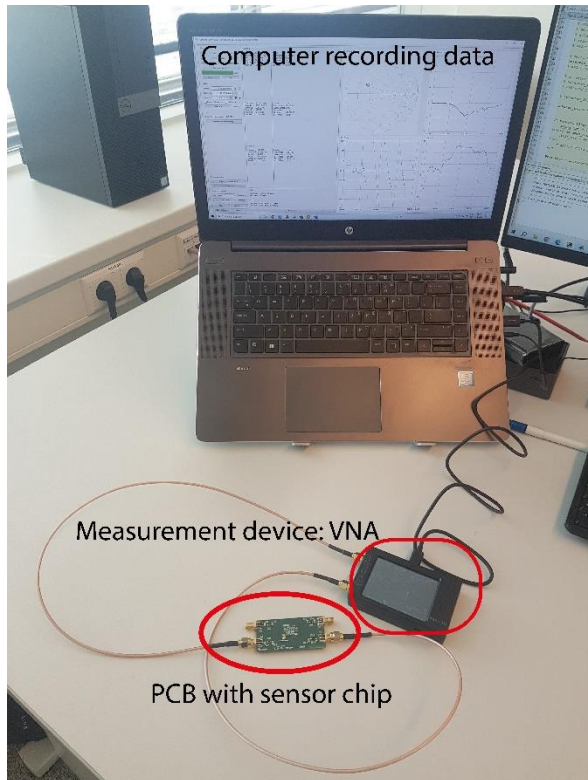
Null test: Loading with PBS at the start of the experiment

Functionilisation process flowchart  
PCB sensitivity



Make sure delay line area is dry as possible  
by pipetting away fluid to avoid sample dilution

## Setup



## Disposal

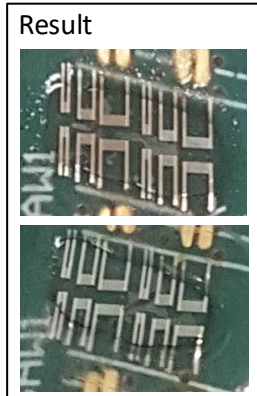
- HMDA collected in blue container with yellow lid. This container is destroyed.
- GA in black container
- sAvidin, Biotinylated-mouse-anti-CD9, goat-anti-mouse-HRP/fluorescence washed through drain
- Tools/glassware/materials, washed with plenty of water and soap.

## List of chemicals

- Methanol
- Hexamethyldiame (HMDA)  
(Sigma-Aldrich H11696, HMDS)  
[Hexamethylenediamine 98 124-09-4 \(sigmaaldrich.com\)](https://www.sigmaaldrich.com)
- GA  
(Sigma-Aldrich G6257, GA, grade II, 25% in H<sub>2</sub>O)  
<https://www.sigmaaldrich.com/NL/en/product/sial/g6257>
- DI water
- Stepto-Avidin  
(Sigma-Aldrich 189725 Avidin, Egg White)  
<https://www.sigmaaldrich.com/NL/en/product/mm/189725>
- PBS (gibco 1x DPBS)
- Biotinylated antigen  
Biotinylated Mouse-anti-CD9
- BSA
- VCaP concentrated extracellular fluid with 3e12 EVs/mL, 10%-20% CD9 positive

### Check successful M-a-CD9 immobilisation protocol

- Prepare 100uL 1/50 G-a-M-HRP in PBS
- Drip 20uL G-a-M-HRP on PCB 1, soak for 1 hour
- Wash 3x with PBS
- Prepare 2uL HR chromogen in 100uL substrate following supplier protocol (30uL/1.5mL)
- Put 50uL of chromogen + substrate per sample (PCB1 and PCB2)
- Check if PCB1 colours brown due to peroxidised HR and PCB2 stays clear as no HRP is present, so no brown peroxidised HR reaction product should show.
- Used biochemical materials:
  - o Dako polyclonal goat anti-mouse immunoglobins – HRP
  - o Dako REAL DAB+ chromogen
  - o Dako DAB+ Substrate buffer
  - o PBS



Result, above PCB1 showing brown colour. Below control PCB2, omitting GaM-HRP. Exactly same process otherwise. No colour, so colour must be due to GaM immobilisation on MaCD9, proving Biotinylated-aCD9-sAvidin immobilisation was successful.

### EV containing liquids at Erasmus MC

- VCaP, concentrated stock concentration  $10^{12}$  EVs per mL, 10%-20% CD9 positive
- COLO205, concentrated stock concentration  $10^{10}$  EVs per mL, 30%-40% CD9 positive
- CDU, concentrated stock concentration  $10^{12}$  EVs per mL, CD9 positive % lower than COLO205

Effectively, VCaP then has  $1.5 \times 10^{11}$  CD9-positive EVs/ml, whereas COLO205 has  $3.5 \times 10^9$  CD9-positive EVs/ml. Hence VCaP is used. Stock dilution is scarce, therefore not available. Dilutions of 10, 100, 1000, 10000 are made by the EV specialised lab technician Natasja Dits.

### EVQuant measurement of EVs per ml

Sample name:	Sample volume:	Particles/ml:	dilution corrected
PBS	40	0,00E+00	
PBS	40	0,00E+00	
liposomes	40	1,57E+14	
liposomes	40	1,59E+14	
VCaP Evs	5	3,43E+12	
VCaP Evs	5	3,65E+12	
VCaP Evs 1:10	5	2,45E+11	2,45E+12
VCaP Evs 1:10	5	3,00E+11	3,00E+12
VCaP Evs 1:100	5	2,64E+10	2,64E+12
VCaP Evs 1:100	5	1,29E+10	1,29E+12
VCaP Evs 1:1000	5	3,33E+10	3,33E+13
VCaP Evs 1:1000	5	2,95E+10	2,95E+13
VCaP Evs 1:10.000	5	1,41E+10	1,41E+14
VCaP Evs 1:10.000	5	9,04E+10	9,04E+14

EVs per mL measurement with microscopic colour staining method. The column 'dilution corrected', calculates back the concentration the stock should be to achieve the measured concentration. Dilutions of 1000 and 10000 give impossible stock concentrations showing these concentrations are too low for a reliable measurement.